Western Australian School of Mines

Department of Exploration Geophysics

Seismic Dispersion, Attenuation, and Frequency-Dependent Anisotropy of Fractured Reservoirs

Junxin Guo

This thesis is presented for the Degree of

Doctor of Philosophy

of

Curtin University

Mar 2018

Declaration

To the best of my knowledge and belief this thesis contains no material previously published by any other person except where due acknowledgment has been made.

This thesis contains no material which has been accepted for the award of any other degree or diploma in any university.

Signature: 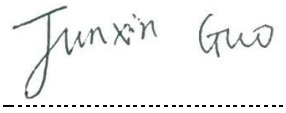

Date: 29/03/2018

Abstract

Fractures play an important role in controlling the fluid flow in the carbonate and unconventional reservoirs. Hence, the seismic detection and characterization of the fractures are of great importance for the oil and gas production in such reservoirs. When the seismic wave propagates through a fractured reservoir, it experiences the dispersion, attenuation, and frequency-dependent anisotropy, which in turn can serve as potential attributes for the fracture detection and characterization. For this purpose, in this thesis, I explore the mechanisms for these seismic signatures in fractured reservoirs. Two important mechanisms are investigated, one is the wave-induced fluid flow (WIFF), which causes the intrinsic attenuation and dispersion of the seismic wave. The other is the wave scattering by fractures, which is responsible for the apparent seismic attenuation and dispersion.

First, I study the WIFF between the fractures and the background medium (FB-WIFF) in the reservoirs with aligned fractures (Chapter 3), for which the characteristic frequency depends on the diffusivity of the background medium and the geometries of the fractures. Existing models for P-waves propagating in the direction perpendicular to the fracture plane are extended to take into account the effects of finite fracture thickness. To explore the frequency-dependent anisotropic properties of reservoirs with finite-thickness fractures, the results are further extended to the full stiffness matrix using the relaxation function interpolation and frequency-dependent fracture compliance matrix approaches. The 2D synthetic samples are then studied by the extended models, together with the numerical simulations based on the Biot's quasi-static equations of poroelasticity. The results show that the finite fracture thickness has significant influence on the seismic dispersion and attenuation. The theoretical predictions are in good agreement with the numerical simulations, even up to relatively high fracture density.

In the presence of the intersecting fractures, apart from FB-WIFF, the WIFF between fractures (FF-WIFF) can also become important and hence needs to be investigated. To study these effects, I consider seismic dispersion and attenuation in the saturated porous rocks with two perpendicular sets of fractures

(Chapter 4). Two cases are studied, one with intersecting fractures and the other with non-intersecting fractures. Based on the models for the aligned fractures, the models for the considered two cases are developed. The characteristic frequencies for the FB-WIFF and FF-WIFF in the studied cases are also given. For the FB-WIFF, the characteristic frequency is same with that for the aligned fracture case. However, for the FF-WIFF, the characteristic frequency depends on the geometries of the fractures, as well as the diffusivity of an effective background medium, for which the original saturated background acts as the solid phase and the pore space is composed of the fractures parallel to the wave propagation direction. The results show that the FF-WIFF can greatly reduce the seismic dispersion, attenuation, and frequency-dependent anisotropy caused by FB-WIFF. Furthermore, in the presence of FF-WIFF, there will be an additional frequency regime where the fractures are hydraulically isolated from the background medium, but are in hydraulic communications with each other. This additional frequency regime is well separated from the low- and high- frequency limits by the characteristic frequencies for the FB-WIFF and FF-WIFF respectively. To validate the theoretical predictions, the results are compared to the numerical simulations, which shows good agreement between them.

Another mechanism for the seismic dispersion and attenuation in fractured media is the wave scattering, which is of great importance in the fracture 'swarms' or 'corridors'. In these fractured zones, the fracture size is usually comparable to the seismic wavelength and hence the wave scattering can be significant. To explore this mechanism, the wave scattering by the fluid saturated fractures with finite thickness is studied using the Foldy approximation and representation theorem (Chapter 5). The wave scattering dispersion and attenuation is related to the displacement discontinuities across the fractures, which are then solved from the boundary conditions. The results show that the fracture thickness and saturating fluid properties have significant influence on the scattering dispersion and attenuation. The theoretical predictions are validated by the ultrasonic measurements on the fractured samples.

Finally, I study the interplay between the WIFF and the wave scattering (Chapter 6). By using the complex-valued and frequency-dependent fluid bulk modulus in the boundary conditions, the WIFF effects are incorporated into the scattering model. The results show the interactions between WIFF and wave scattering are significant when the characteristic frequencies for these two mechanisms are close

to each other. Hence, it is essential to consider the coupling between these two mechanisms under this condition. Comparing the theoretical predictions to the numerical simulations based on the low-frequency approximation of Biot's dynamic equations of poroelasticity shows good agreement between them.

In summary, the study in this thesis provides numerically validated theoretical models, which can be used as a basis for developing the seismic attributes for the detection and characterizations of fractured reservoirs. Various fracture properties can then be extracted from the seismic data, such as the fracture thickness, saturating fluid properties, and degree of fracture connectivity.

Acknowledgements

First of all, I would like to give my sincere gratitude to my supervisor, Professor Boris Gurevich, for his guidance, friendship, and help during my Ph. D. study. Without his support and tremendous input in this research, it would be much more difficult for me to complete my Ph. D. study. I am greatly impressed by his enthusiasm and immense knowledge, which inspired me and benefited me a lot. Whenever I need help and feel frustrated, he is always there for me. He always encourages me and gives me many insightful advices and comments. Under his guidance, I learned how to do research and enjoyed this procedure a lot. He is not only a supervisor for me, but also a great friend, who guides and helps me on the road to science.

I gratefully acknowledge the sponsors of Curtin Reservoir Geophysics Consortium (CRGC). Without the scholarship from this consortium, the study at Curtin University would be impossible.

Special thanks go to Dr. J. Germán Rubino for the valuable discussion with him and his great input in this research. Without his work in the numerical simulations, it would be very difficult to validate the theoretical models proposed in the thesis. Furthermore, he always gave very detailed review of the research results and provided many insightful advices and comments. This greatly improves the research quality and enables the smooth and fast publication of the research results. He is a tremendous mentor to me.

I would like to thank Dr. Stanislav Glubokovskikh, Dr. Nicolás D. Barbosa, Dr. Eva Caspari, Dr. Pinbo Ding, and Dr. Da Shuai, for their support in the theoretical modelling, numerical simulations, and also experimental study. I enjoyed the discussion with them, which inspired me and gave me many new ideas. Their valuable comments on my work are very beneficial to me. I also would like to thank all my friends at Curtin University. They made my life here interesting and colourful.

Finally, I would like to thank my parents, my wife, and my brother for their constant unending love and support. Without these, my life would lose its aim and driving force.

Contents

Chapter 1
Introduction

1.1 Background and motivation

Naturally fractured reservoirs constitute substantial part of oil and gas reserves worldwide. Importance of fractures was probably first understood in the context of carbonate reservoirs. In recent years, there has been a renewed interest in fractured unconventional reservoirs such as tight sands, shales, and coal. According to the contributions of the fractures to the overall porosity and permeability of the reservoirs, the fractured reservoirs can be classified into four types (Nelson, 2001). For the first type, the fractures contribute to both the porosity and permeability of the reservoirs and hence play an important role in controlling both the storage and transport of the oil and gas. For the second type, the fraction of the fractures is small compared to that of the pores in the background medium. Thus, most of the oil and gas are stored in the pores of the background medium. However, the permeability of the background medium is so low that no economic production is possible without natural fractures. Despite the small volume of the fractures, their existence can greatly improve the effective permeability of the reservoirs, and therefore, facilitate the flow of the oil and gas and make the economic production possible. In the third type of fractured reservoirs, the embedding background medium has relatively higher permeability than that of the second type. Hence, the oil and gas can also flow in the background medium. The fracture system under this condition, however, can further increase the overall permeability and thus enhance the oil and gas production. These three types of fractured reservoirs all have the open fractures embedded in the background medium. Conversely, in type IV fractured reservoirs, the fractures are usually filled with solids and hence are closed. In this case, the fractures will inhibit the fluid flow and thus decrease the reservoir productivity. For the oil and gas exploration, the detection and characterization of the fractures in the first three types of fractured reservoirs are of particular interest, which are the focus of this thesis.

The most direct method for fracture detection and characterization is the study of outcrops or core samples (e.g., Zeeb et al., 2013; Basquet and Wennberg, 2008), which provides first-hand information on the geometries and distribution of the fractures in the formation of interest. However, it can only provide such information for a very limited rock volume. Apart from these kinds of observations, well logging methods are also often applied in the characterization of fracture networks (e.g., Zazoun, 2013; Che et al., 2015). Detailed information on the fractures present around the borehole can be obtained, especially from imaging data. However, these methods also suffer from limited sampling of the affected rock volume, which is confined to the vicinity of the borehole. Furthermore, the accuracy of fracture detection and characterization through cores or logs is also influenced by the possible existence of coring- or drilling-induced fractures. For these reasons, non-invasive approaches that can offer fracture information on a larger scale are of significant interest. In this context, the seismic method presents a special value due to its ability to provide, in a non-invasive manner, information on the probed fractured volume on a relatively large scale (e.g., Wang et al., 2007; Liu and Martinez, 2012).

Very large fractures, or joints, can be detected with advanced seismic imaging techniques, such as ant-tracking and Tomographic Fracture Imaging (e.g., Basir et al., 2013; Lacazette et al., 2013; Zhang et al., 2015; Protasov et al., 2016; James et al., 2017). However, in most cases the resolution of the seismic data is insufficient to directly image fractures. Since the presence of many relatively small fractures can alter the apparent elastic properties of the rock, their presence can be detected using seismic attributes (e.g., Bakulin et al., 2000a, 2000b, 2000c; Vlastos et al., 2007; Sassen and Everett, 2009; Gao, 2013). In particular, when propagating through the fractured zones, seismic waves experience velocity dispersion and attenuation, as well as frequency-dependent anisotropy (e.g., Peacock et al., 1994; Maultzsch et al., 2003, 2007; Chapman et al., 2006; Clark et al., 2009). This in turn can serve as valuable signatures for fracture detection and characterization. In order to do so, it is essential to study the mechanisms for these phenomena. Hence, the objective of this thesis is to study such mechanisms in the fractured reservoirs.

1.2 Mechanisms for seismic wave dispersion, attenuation, and frequency-dependent anisotropy

In the seismic frequency band, the previous studies show that the wave-induced fluid flow (WIFF) and elastic wave scattering by fractures can play an important role on the seismic wave dispersion, attenuation, as well as the frequency-dependent anisotropy (e.g., Müller et al., 2010; Vlastos et al., 2003, 2006, 2007). Hence, in this thesis, we will focus on the study of these two mechanisms. In the following, I will briefly review the previous studies on them.

1.2.1 Wave-induced fluid flow (WIFF)

When a seismic wave propagates through a fractured reservoir fully saturated with a single fluid, its behaviour can be greatly affected by the properties of the fractures and their degree of hydraulic connectivity with the pore space of the background. This influence results from wave-induced fluid flow (WIFF) between these two regions, a phenomenon highly-dependent on the frequency of the elastic wave (e.g., Hudson, 1996; Chapman et al., 2002; Chapman, 2003; Gurevich, 2003; Jakobsen et al., 2003; Jakobsen and Hudson, 2003; Jakobsen, 2004; Brajanovski et al., 2005; Galvin and Gurevich, 2006, 2007). At low frequencies, the pore fluid has enough time to flow from the fractures into the background medium during the compression cycle of the seismic wave and vice versa during the extension cycle, hence reducing the fracture stiffness. Conversely, at higher frequencies, there is insufficient time for fluid flow between the fractures and the background medium. Thus, fractures are stiffer at higher frequencies than at lower frequencies. The variation of the fracture stiffness with frequency results in frequency-dependent effective elastic properties of the probed fractured material. In other words, fluid flow between the background medium and fractures manifests itself as seismic dispersion, which is accompanied with energy dissipation (seismic attenuation) due to viscous friction arising in the pore fluid.

Seismic dispersion and attenuation due to WIFF between fractures and the background medium (FB-WIFF) have been quantified by a number of theoretical models. Hudson et al. (1996) modelled fractures as penny-shaped cracks and quantified the WIFF effects induced by a single crack while neglecting potential interactions with neighbouring cracks. Chapman et al. (2002) and Chapman (2003) studied the seismic dispersion and attenuation of saturated rocks containing penny-shaped cracks by introducing spherical pores and compliant cracks as perturbations to an elastic non-porous background. Predictions

of this model were then compared with the experimental results and applied to seismic data analysis by Maultzsch et al. (2003, 2007) and Chapman et al. (2006). Another perturbation approach to model the effects of pores and fractures on elastic properties was proposed by Jakobsen et al. (2003), Jakobsen and Hudson (2003), and Jakobsen (2004) using a T-matrix formalism. This approach is very versatile as it allows modelling the effect of complex distributions of fractures; however it depends on many parameters, which are often unknown.

A different approach was proposed by Gurevich (2003), who studied the effect of fractures in the low frequency (Gassmann) limit by considering fractures as perturbation to a porous background medium described by Biot's equations of poroelasticity. This work was extended by Brajanovski et al. (2005) who modelled fractures as thin and highly-porous layers embedded in a porous background, based on which an analytical solution for P-wave dispersion and attenuation was obtained. The corresponding characteristic frequencies were also given by studying the asymptotes of the analytical solution at low, intermediate, and high frequencies (Brajanovski et al., 2006). Similarly, Galvin and Gurevich (2006, 2007) analysed seismic dispersion and attenuation in a medium with aligned sparsely-distributed penny-shaped cracks using a poroelasticity approach. A detailed review of these models is given by Gurevich et al. (2009), who also provide a unified formulation for several of these models by using the so-called branching function approach (Johnson, 2001; Pride and Berryman, 2003).

Besides FB-WIFF, WIFF can also occur between connected sets of mesoscopic fractures (FF-WIFF) (e.g., O'Connell and Budiansky, 1977; Guéguen and Sarout, 2009). In a series of papers, Rubino et al. (2013, 2014, and 2017) found that this manifestation of WIFF can have a significant influence on the dispersion, attenuation, and anisotropy of seismic waves at frequencies important for seismic reservoir characterisation. Since the fluid flow between fractures critically depends on the connectivity degree of the probed fracture network, these results suggest the potential to detect fracture connectivity and, hence, to quantify the effective permeability of fractured formations using seismic data. It is then of great importance to further explore this WIFF manifestation. However, to date, this task has been addressed mainly using numerical simulations (Rubino et al., 2013, 2014, 2017). Despite the versatility of this approach is, it is impractical to use numerical simulations routinely, especially for inversion. Thus, the

theoretical exploration of this manifestation of WIFF is needed. To this end, while some work has been done (e.g., O'Connell and Budiansky, 1977; Endres and Knight, 1997; Guéguen and Sarout, 2009; Sarout, 2012), most of them explored this by neglecting FB-WIFF effects. Hence, one of the objectives of this thesis is modelling the FB-WIFF and FF-WIFF effects together theoretically. It might be difficult to observe these effects in the field seismic data with current technology due to the limited acquisition bandwidth, but advances in broadband acquisition technology may enable observation of this phenomenon in the future.

1.2.2 Elastic wave scattering by fractures

In naturally fractured reservoirs, fracture 'swarms' or 'corridors' are usually of particular importance for oil and gas production (e.g., Questiaux et al., 2010), which are large zones of densely spaced fractures tens of meters in height and several hundred meters in length, up to several meters in width and with permeability on the order of several Darcies (Bush, 2010). As the size of fractures in such fractured zones is often comparable to or even larger than the seismic wavelength, the wave scattering by fractures can be significant (e.g., Wu and Aki, 1985; Gurevich et al., 1997; Vlastos et al., 2003, 2006, 2007; Sato et al., 2011). This will result in substantial apparent dispersion and attenuation of seismic wave. Due to the fact that the wave scattering depends critically on the fracture geometries and spatial distributions (e.g., Vlastos et al., 2003, 2006, 2007), it is possible to characterize such large fractures through the scattering attributes, such as scattering dispersion and attenuation (e.g., Landa et al., 1987; Kanasewich and Phadke, 1988; Vasconcelos and Jenner, 2005; Willis et al., 2006; Burns et al., 2007; Tsingas et al., 2010). This requires the theoretical modelling of the seismic wave scattering by fractures. However, the conventional scattering models, such as KT model (Kuster and Toksöz, 1974) and Hudson model (e.g., Hudson, 1981), usually assume that the seismic wavelength is much larger than the fracture size and hence only the Rayleigh scattering is considered. As stated above, in this thesis, we focus on a more general case where the fracture size is comparable to or even larger than the seismic wavelength and hence the scattering in the full frequency range (both Rayleigh and Mie scattering) needs to be studied. In the following, I briefly review the previous studies on this aspect.

For the wave scattering by dry fractures and the corresponding wave dispersion and attenuation in the full frequency range, many theoretical models have been proposed. Mal (1970a, b) studied the scattering of the normally incident P- and S- waves by a penny-shaped or Griffith fracture in an infinite isotropic elastic solid. The stress and displacement fields on the fracture and also those far away from the fracture were obtained by solving the associated integral equation numerically. Martin (1981) also modelled the interaction of the elastic wave with a penny-shaped fracture in the infinite elastic solid. A new method for solving the linear boundary value problem for the displacement field was developed by defining an 'elastic double layer'. Krenk and Schmidt (1982) solved the wave scattering by a penny-shaped crack in an elastic solid through the direct integral equation method. The advantage of this method was that it doesn't require any assumption of symmetry. Keogh (1986) analysed the scattering of the P-wave with the normal incidence by a penny-shaped fracture. The approximation for the far field at high frequencies was derived from the exact solution. Martin and Rizzo (1989) studied the scattering of the scalar waves by a 2D fracture with arbitrary smooth surface. The solution was obtained by solving a hypersingular boundary integral equation.

The above models all deal with the interactions of the elastic wave with a single dry fracture in the elastic solid. This provides the basis for studying the scattering of the elastic wave by multiple dry fractures. Foldy (1945) studied the multiple scattering of waves by a random distribution of scatterers (such as fractures) and gave an approximation for calculating the mean wave fields. This approximation was then used by numerous researchers to model the multiple scattering effects by the fractures. Kikuchi (1981) investigated the wave scattering in a medium with aligned randomly distributed fractures using the Foldy approximation and obtained an equation for the scattering-induced dispersion and attenuation. Similarly, Zhang and Achenbach (1991) considered the P-wave propagation in the solid containing randomly distributed aligned penny-shaped fractures. The interactions between the fractures were investigated and the analytical solutions for the wave dispersion and attenuation were given at low frequencies. This was then extended to the full frequency range by Zhang and Gross (1993a, b). For the 2D fractured medium, a similar problem was studied by Kawahara et al. (1992) and Kawahara (1992) using the Foldy approximation and the representation theorem (Achenbach, 1973). The scattering of

the P-, SH- and SV- waves were all studied and the corresponding solutions for the wave dispersion and attenuation were given. Their approach was then validated by the numerical simulations by Suzuki et al. (2006, 2013).

Instead of the application of Foldy approximation, Sabina et al. (1993) and Smyshlyaev and Willis (1993a, b) extended the static self-consistent approach to the dynamic regime, based on which the wave dispersion and attenuation due to the scattering by the aligned and randomly oriented fractures were analysed. Murai et al. (1995) and Murai (2007) considered the interactions between the fractures using a rigorous method and obtained the wave field of the SH wave in the medium with randomly distributed aligned fractures. The wave dispersion and attenuation were then estimated from the wave field. Yang and Turner (2005) used an anisotropic Green's dyadic approach to model the wave attenuations in the elastic solid with perfectly aligned penny-shaped fractures. It was then compared with the results of Hudson (1981) in the Rayleigh limit, which showed good agreement. Caleap et al. (2009) studied the SH wave scattering by the flat or open fractures with random or parallel orientations. Different formulas considering the multiple-scattering effects were used and compared.

While studies reviewed above have been carried out on the wave scattering by the dry fractures, scattering by the fluid saturated fractures has received relatively little attention. Yet, the fractures in the geological formations are usually saturated with fluids (e.g., Malin et al., 1988; Bush, 2010). Hence, it is essential to model the wave scattering by the fluid saturated fractures. To the authors' knowledge, however, only a few works have been devoted to this aspect. Kawahara et al. (1992) modelled the scattering by the aligned fluid saturated fractures, which focused on the effects of the viscous friction of the fluid on the wave dispersion and attenuation. This was then extended by Murai et al. (1995) by considering the fracture interactions. Sabina et al. (1993) and Smyshlyaev and Willis (1993a, b) applied the dynamic self-consistent approach to consider the wave propagation in the elastic solid with randomly distributed penny-shaped fractures saturated with a non-viscous fluid. This problem was also studied by Eriksson et al. (1995) using the T-matrix and Foldy approximation.

1.3 Objectives

While numerous models for WIFF and wave scattering have been proposed to explain the seismic dispersion, attenuation, and frequency-dependent anisotropy, there are still several problems remained that need to be explored as follows:

1) Effects of finite fracture thickness on the seismic signatures. Most of current models for WIFF and wave scattering assume that the fracture thickness is infinitesimal, whereas the fractures in reality have finite thickness. As the fracture thickness has significant influence on the fluid flow (e.g., Questiaux et al., 2010), it is essential to study its effects on the seismic dispersion, attenuation, and frequency-dependent anisotropy.

2) Influence of fracture interactions on the seismic signatures. It is assumed in most of current models that the fracture density is low enough that the interactions between the fractures can be ignored. However, in real reservoirs, the fracture density can be high enough that the interactions between the fractures cannot be neglected. Hence, the effects of the fracture interactions on the seismic responses also need to be investigated.

3) Influence of fracture intersections on the seismic signatures. While the numerical studies of Rubino et al. (2013, 2014, and 2017) showed that the FF-WIFF has significant influence on the seismic responses, little theoretical work has been done to study this manifestation of WIFF. Hence, this problem also needs to be explored.

4) Coupling effects between WIFF and wave scattering. Most of current studies investigate WIFF and wave scattering effects separately. However, when the characteristic frequencies for these two mechanisms are close to each other, the interplay between them can occur. Therefore, it is also important to study the coupling effects between WIFF and wave scattering on the seismic responses.

5) Validation of theoretical models by numerical simulations or experimental results. While numerous theoretical models for WIFF and wave scattering have been proposed, the corresponding validation of these models by numerical simulations or experimental results is rare. Hence, it is crucial to validate the proposed theoretical models, which is another objective of this thesis.

To study the problems presented above, the corresponding theoretical models are proposed, which are then validated by the numerical simulations or experimental results. Specifically, the effects of finite fracture thickness and fracture interactions on FB-WIFF and the corresponding seismic signatures are studied in Chapter 3. Then, the influence of fracture intersections on the seismic signatures due to FF-WIFF is explored in Chapter 4. After that, the effects of finite fracture thickness and fluid properties on the wave scattering are studied in Chapter 5. Finally, the coupling between the WIFF and wave scattering is investigated in Chapter 6.

1.4 Thesis outline and related publications

The detailed outline of this thesis is as follows:

Chapter 2: The theories and numerical simulation methodologies used in this thesis are introduced, based on which the problems discussed in the last section are studied.

Chapter 3: In this chapter, I extend existing models to the finite fracture thickness case for P-waves propagating perpendicular to the fracture plane using the so-called branching function approach. Three types of fractures are considered, namely, periodically- and randomly-spaced planar fractures, as well as penny-shaped cracks. The extended models with a unified form are then established, which is tested by comparing with corresponding numerical simulations based on Biot's quasi-static equations of poroelasticity. The seismic dispersion and attenuation are studied focusing on the effects of finite fracture thickness and fracture interactions. Furthermore, in order to study the frequency-dependent anisotropy, I propose two approaches to extend the results to the full stiffness matrix. The anisotropy of the velocities and attenuation can then be analysed theoretically, which is also verified by the numerical simulations.

Related publications:

1) Guo, J., J. G. Rubino, N. D. Barbosa, S. Glubokovskikh, and B. Gurevich, 2018, Seismic dispersion and attenuation in saturated porous rocks with aligned fractures of finite thickness: theory and numerical simulations – Part 1: P-wave perpendicular to the fracture plane: Geophysics, **83**, no. 1, WA49-WA62.

2) Guo, J., J. G. Rubino, N. D. Barbosa, S. Glubokovskikh, and B. Gurevich, 2018, Seismic dispersion and attenuation in saturated porous rocks with aligned fractures of finite thickness: theory and numerical simulations – Part 2: Frequency-dependent anisotropy: Geophysics, **83**, no. 1, WA63-WA71.

3) Guo, J., J. G. Rubino, B. Gurevich, and S. Glubokovskikh, 2017, Effects of finite fracture thickness on seismic dispersion and attenuation in saturated rocks with aligned penny-shaped cracks: theory versus numerical simulation: 6th Biot Conference on Poromechanics.

Chapter 4: In this chapter, I propose a theoretical approach to quantify seismic dispersion and attenuation, as well as frequency-dependent anisotropy, due to both the effects of FB-WIFF and FF-WIFF in saturated porous rocks permeated by two orthogonal sets of fractures. The methodology is based on existing theoretical models for rocks with aligned fractures, and I consider three types of fracture geometries, namely, periodic planar fractures, randomly spaced planar fractures, and penny-shaped cracks. Synthetic 2D rock samples with different degrees of fracture intersections are then explored by considering both the proposed theoretical approach and a numerical upscaling procedure that provides the effective seismic properties of generic heterogeneous porous media.

Related publications:

1) Guo, J., J. G. Rubino, S. Glubokovskikh, and B. Gurevich, 2017, Effects of fracture intersections on seismic dispersion: theoretical predictions versus numerical simulations: Geophysical Prospecting, **65**, no.5, 1264-1276.

2) Guo, J., J. G. Rubino, S. Glubokovskikh, and B. Gurevich, 2018, Dynamic seismic signatures of saturated porous rocks containing two orthogonal sets of fractures: Theory versus numerical simulations: Geophysical Journal International, **213**, 1244-1262.

3) Guo, J., J. G. Rubino, B. Gurevich, S. Glubokovskikh, A. V. Dyskin, and E. Pasternak, 2016, Effects of fracture intersections on seismic dispersion- Theoretical predictions versus numerical simulations: 78th EAGE Conference and Exhibition.

4) Guo, J., J. G. Rubino, B. Gurevich, S. Glubokovskikh, 2016, Fluid flow effects on Seismic Properties of Fractured medium: Theoretical / Numerical modelling: SEG-AGU Workshop: Upper Crust Physics of Rocks.

5) Guo, J., J. G. Rubino, S. Glubokovskikh, and B. Gurevich, 2017, Effects of fractures and background porosity on seismic dispersion and attenuation: theory versus numerical simulations: 4th International Workshop on Rock Physics.

6) Guo, J., S. Glubokovskikh, B. Gurevich, and J. G. Rubino, 2018, Seismic Signatures of fractured reservoirs: Theory versus numerical simulations: Extended Abstract, ASEG, https://doi.org/10.1071/ASEG2018abP070.

Chapter 5: In this chapter, I study the P-wave dispersion and attenuation due to the scattering by 2D fluid-saturated aligned fractures with finite thickness, which are embedded in an isotropic elastic background medium. Using the Foldy approximation and the representation theorem, the P-wave dispersion and attenuation are related to the displacement discontinuities across the fractures. Then, the fracture displacement discontinuities are obtained from the boundary conditions and the P-wave dispersion and attenuation can thus be calculated. The theoretical results are then illustrated by a numerical example. To validate the proposed model, the theoretical predictions are compared to ultrasonic measurements on fractured samples.

Related publications:

1) Guo, J., D. Shuai, J. Wei, P. Ding, and B. Gurevich, 2018, P-wave dispersion and attenuation due to scattering by aligned fluid saturated fractures with finite thickness: Theory and experiment: submitted to Geophysical Journal International.

Chapter 6: In this chapter, I investigate the coupling effects between WIFF and wave scattering. By representing the WIFF effects using the complex-valued and frequency-dependent fluid bulk modulus, I can incorporate the WIFF effects into the scattering model through the boundary conditions. To validate the proposed approach, we also perform the numerical simulations based on the low frequency

approximation of dynamic Biot's poroelastic equations. The theoretical predictions are then compared to the numerical simulations.

Chapter 7: The conclusions for this thesis are given in this chapter.

1.5 Author's contributions

The work presented in this thesis is done by collaborating with several other researchers from Curtin University, National Scientific and Technical Research Council of Argentina (CONICET), University of Lausanne, and China University of Petroleum (Beijing). The theoretical models in this thesis are developed by myself under the guidance of my supervisor (Boris Gurevich). The numerical simulations used to validate theoretical models were performed by my collaborators: J. Germán Rubino (Chapters 3 and 4), Nicolás D. Barbosa from (Chapter 3), and Eva Caspari (Chapter 6). The experiments in Chapter 5 were also carried out by several other collaborators: Da Shuai and Jianxin Wei. The analysis of the theoretical results and the comparison of these results to the numerical simulations and experimental data are primarily done by myself. Since all the publications arising from this research are results of teamwork, I use 'we' instead of 'I' in the following chapters where appropriate.

Chapter 2
Theoretical background and numerical simulation methodologies

2.1 Introduction

In this chapter, the theories and numerical simulation methodologies employed in this thesis are introduced. First, the theories for the quasi-static elastic properties of rocks with dry or hydraulically isolated fractures (linear-slip theory) are given (Sections 2.2). Then, the effects of the saturating fluid on the rock elastic properties in the low-frequency limit (Gassmann equations) and the influence of the macroscopic fluid flow at higher frequencies (Biot theory) are introduced (Section 2.3 and 2.4). After that, theoretical models for the seismic wave dispersion, attenuation, and frequency-dependent anisotropy caused by FB-WIFF in saturated porous rocks with aligned fractures are reviewed (Sections 2.5, 2.6, and 2.7). The models for the P-wave propagating perpendicular to the fracture plane is first considered for different types of fractures (Sections 2.5). Then, these models are unified and extended to the full stiffness coefficients case using the branching function approach (Section 2.6). The seismic wave dispersion and attenuation at any incidence angles, as well as the frequency-dependent anisotropic properties can thus be calculated (Section 2.7). These theories will be extended in the following chapters to study the effects of finite fracture thickness and fracture interactions (Chapter 3) and fracture intersections (Chapter 4).

The theories above all assume that the seismic wavelengths are much larger than the fracture size and hence the seismic wave scattering effects on dispersion and attenuation can be neglected. However, in the presence of large fractures, the effects of the seismic wave scattering can be significant, as discussed in Chapter 1. Hence, the seismic wave scattering theory for the dry open fractures is introduced in Section 2.8, which will be extended to the case with fluid saturated fractures in Chapter

5. Then, the characteristic frequencies for various mechanisms of seismic dispersion and attenuation are compared in Section 2.9. With these extended theoretical models for WIFF and wave scattering, the coupling effects between them can be studied, which are explored in Chapter 6. To validate these theoretical results, the corresponding numerical simulations are also performed, for which the methodologies are outlined in Section 2.10.

2.2 Linear-slip theory

To calculate the elastic properties of the porous rocks with dry or hydraulically isolated fractures, I use the linear-slip theory which was proposed and developed by several authors (e.g., Kachanov, 1980; Schoenberg, 1980; Schoenberg and Douma, 1988; Kachanov, 1992; Sayers and Kachanov, 1995; Schoenberg and Sayers, 1995). This theory does not require any assumption of the fracture geometry and hence can be used for any type of fractures, such as the planar fractures and penny-shaped cracks (e.g., Gurevich, 2003; Gurevich et al., 2009). According to this theory, the compliance matrix of the fractured rocks $\mathbf{S}$ can be expressed as the sum of the compliance matrix of the background medium $\mathbf{S}_b$ and the excess fracture compliance matrix $\mathbf{S}_f$ (e.g., Schoenberg and Sayers, 1995):

$$\mathbf{S} = \mathbf{S}_b + \mathbf{S}_f . \tag{2.1}$$

For a single set of aligned fractures with sparse and random distribution, the values of $\mathbf{S}_f$ can be calculated using the non-interaction Eshelby model as follows (Sevostianov and Kachanov, 1999):

$$\mathbf{F} = \phi_c \left[\left(\mathbf{T_c} - \mathbf{T_b} \right)^{-1} + \mathbf{Q} \right]^{-1}, \tag{2.2}$$

where $\mathbf{F}$ is the dry fracture excess compliance tensor; ϕ_c is the fracture porosity; $\mathbf{T_c}$ and $\mathbf{T_b}$ are the compliance tensors for the infill material (or saturating fluid) of the fractures and for the background medium, respectively; $\mathbf{Q}$ can be obtained from the stiffness tensor of the background medium $\mathbf{C}$ and the Eshelby's tensor $\mathbf{S}$ as follows:

$$Q_{ijkl} = C_{ijmn} \left(J_{mnkl} - S_{mnkl} \right), \tag{2.3}$$

where $\mathbf{J}$ is the unit fourth rank tensor; the expressions of Eshelby's tensor $\mathbf{S}$ can be found in Mura (1987, section 11). Once $\mathbf{F}$ is computed, it can be condensed into the Voigt matrix form $\mathbf{S}_f$ (Nye, 1985).

The main advantage of the non-interaction Eshelby model used here [equation (2.2)] is that it allows the ellipsoidal inclusions (fractures) which means the three principal axes of the inclusions can have any lengths. This is different from the conventional models (such as KT and Hudson models) which only consider the (strongly oblate) spheroidal inclusions. Furthermore, different from the popular KT model and other similar models, the Eshelby model also enables the investigation of the anisotropic elastic properties induced by the fractures.

When the fractures have infinitesimal thickness (flat fractures) and are rotationally invariant with respect to the fracture normal, the fracture compliance matrix only contains two elements: normal and tangential fracture compliances, Z_N and Z_T. Assuming the fracture normal lies along x_2-axis, $\mathbf{S}_f$ has the following simplified form (Schoenberg and Sayers, 1995):

$$\mathbf{S}_f = \begin{pmatrix} 0 & 0 & 0 & 0 & 0 & 0 \\ 0 & Z_N & 0 & 0 & 0 & 0 \\ 0 & 0 & 0 & 0 & 0 & 0 \\ 0 & 0 & 0 & Z_T & 0 & 0 \\ 0 & 0 & 0 & 0 & 0 & 0 \\ 0 & 0 & 0 & 0 & 0 & Z_T \end{pmatrix}, \tag{2.4}$$

Note that if the fractures are saturated with fluid, Z_N will vanish.

In the presence of multiple sets of fractures, the excess compliance induced by each set of fractures $\mathbf{S}_{fi}$ can be obtained using the Eshelby theory. Then, based on the assumption that there is no interactions between the fractures, we can calculate $\mathbf{S}_f$ by transforming $\mathbf{S}_{fi}$ into the same global coordinate system and summing them up:

$$\mathbf{S}_f = \sum_{i=1}^{M} \mathbf{S}_{fi}^1 , \tag{2.5}$$

where M is the number of the fracture sets, $\mathbf{S}_{fi}^1$ is the transformed excess compliance matrix for the i^{th} set of fractures.

If the fractures are densely distributed, the interactions between the fractures can occur. Under this condition, we can apply the Differential Effective Medium (DEM) (e.g., Nishizawa, 1982; Schoenberg

and Douma, 1988) or Self-Consistent Approximation (SCA) (e.g., Norris, 1985; Milton, 2002) schemes to take into account the effects of the fracture interactions on the fracture compliances.

2.3 Gassmann equations of poroelasticity

For the fluid saturated fractured and porous rock, when fractures are hydraulically isolated from the porous background medium, the elastic properties can be calculated using the linear-slip theory, as shown above. However, when fractures are hydraulically connected to the porous background medium, in the low frequency limit, the fluid in the fractures has enough time to communicate with that in the background medium, the fluid pressure will then be uniform throughout the rock and hence the rock elastic properties cannot be obtained by using the linear-slip theory directly. Under this condition, the Gassmann equations (Gassmann, 1951a, 1951b) can be used to calculate the saturated rock elastic properties from the corresponding dry ones. If the fractures are oriented and distributed randomly in the rocks, the rocks exhibit isotropic properties. In this case, the isotropic Gassmann equations can be used to compute the elastic moduli as follows:

$$K_{sat} = K_d + \alpha^2 M \,, \tag{2.6}$$

$$\boldsymbol{\mu}_{sat} = \boldsymbol{\mu}_d \,, \tag{2.7}$$

where K_{sat} and G_{sat} are the bulk and shear moduli of the saturated isotropic rock, respectively; K_d and G_d are the bulk and shear moduli of the dry isotropic rock, respectively; α and M are the Biot-Willis coefficient and the pore space modulus, which can be expressed as:

$$\alpha = 1 - \frac{K_d}{K_g} \,, \tag{2.8}$$

$$M = \frac{K_g}{\left(1 - K_d / K_g\right) - \phi\left(1 - K_g / K_f\right)} \,. \tag{2.9}$$

In equations (2.8) and (2.9), K_g and K_f are the grain and fluid bulk moduli, respectively; ϕ is the porosity of the rock.

It should be noted here that the shear modulus is not affected by the fluid saturation [equation (2.7)]. This is due to the fact that the fluid pressure decrease or increase in the randomly oriented fractures under the shear deformation is cancelled out in the low frequency limit. Hence, the shear deformation does not induce the overall fluid pressure variations in the rock, and therefore, the shear modulus is independent of the fluid saturation.

If the fractures are not randomly oriented in the rock, the rock will show anisotropic properties. Under this condition, the anisotropic Gassmann equations need to be used to calculate the elastic properties of the saturated rocks from the dry ones as follows:

$$c_{ij}^{sat} = c_{ij}^{d} + \alpha_i \alpha_j M_1, \; i, j = 1, \ldots 6, \tag{2.10}$$

where c_{ij}^{d} is the stiffness coefficients for the dry fractured rocks, the expressions for α_i are as follows:

$$\alpha_m = 1 - \frac{\sum_{n=1}^{3} c_{mn}^{d}}{3K_g}, \tag{2.11}$$

for m=1, 2, and 3, $\alpha_4 = \alpha_5 = \alpha_6 = 0$, and M_1 is the Biot's modulus:

$$M_1 = \frac{K_g}{\left(1 - K_0^* / K_g\right) - \phi\left(1 - K_g / K_f\right)}. \tag{2.12}$$

In equation (2.12), K_0^* represents the generalized drained bulk modulus:

$$K_0^* = \frac{1}{9}\sum_{i=1}^{3}\sum_{j=1}^{3} c_{ij}^{d}. \tag{2.13}$$

It should be noted here that equations (2.6), (2.7), and (2.10) assume that solid grains composing the rock are homogeneous and isotropic. When the solid grains are anisotropic or heterogeneous, the generalized Brown-Korringa equations need to be used (Brown and Korringa, 1975).

2.4 Biot's theory of dynamic poroelasticity

The Gassmann equations presented above is used when the fluid pressure is equilibrated throughout the rock in the low frequency limit. However, when the frequency becomes higher, the fluid pressure

gradient will be generated between the peak and trough of the seismic wave and hence the fluid flow on the scale of the wavelength (macroscopic flow) will occur. Due to the viscous friction between the pore fluid and the solid, the seismic wave will experience energy dissipation accompanied with velocity dispersion. To describe this phenomenon, the theory for dynamic poroelasticity was proposed by Biot (1956a, 1956b, 1962). According to this theory, the wave motion in the isotropic fluid saturated porous rock can be presented in the frequency – space domain as follows:

$$\nabla \cdot \tilde{\boldsymbol{\sigma}} = -\omega^2 \left(\rho \tilde{\mathbf{u}} + \rho_f \tilde{\mathbf{w}} \right), \tag{2.14}$$

$$\nabla \tilde{p} = \omega^2 \left(\rho_f \tilde{\mathbf{u}} + \tilde{\rho} \tilde{\mathbf{w}} \right), \tag{2.15}$$

where $\boldsymbol{\sigma}$ and p are the total stress tensor and fluid pressure, respectively; $\mathbf{u}$ and $\mathbf{w}$ are the displacement of the solid and that of the fluid relative to the solid; ρ and ρ_f are the density of the saturated rock and fluid, respectively; $\tilde{\rho}$ is called the effective filtration density which has the following expression:

$$\tilde{\rho} = \frac{i\eta}{\omega \kappa(\omega)}, \tag{2.16}$$

with η and $\kappa(\omega)$ being the dynamic fluid viscosity and permeability, respectively. $\kappa(\omega)$ describes the flow type of the pore fluid which can be written as (Johnson et al., 1987):

$$\kappa(\omega) = \kappa_0 \left[\sqrt{1 - i\frac{\omega}{2\omega_B}} - i\frac{\omega}{\omega_B} \right]^{-1}, \tag{2.17}$$

where $\omega_B = \dfrac{\phi\eta}{\kappa_0 \alpha_\infty \rho_f}$ is the Biot characteristic angular frequency, with ϕ the rock porosity, κ_0 steady-state permeability, and α_∞ tortuosity.

When the frequency is much lower than ω_B, $\kappa(\omega)$ can be approximated as the steady-state permeability κ_0 and hence the fluid flow is controlled by the viscous force. This type of fluid flow is called the Poiseuille flow. Conversely, the Poiseuille flow breaks down when the frequency is close to or larger than ω_B. The permeability then becomes frequency-dependent and complex-valued. The fluid flow under this condition is dominated by the inertial force.

The stress variables are related to the displacements by the constitutive relations (Biot, 1957)

$$\tilde{\boldsymbol{\sigma}} = \left[\left(C - 2\mu_d \right) \nabla \cdot \tilde{\mathbf{u}} + \alpha M \nabla \cdot \tilde{\mathbf{w}} \right] \mathbf{I} + \mu_d \left[\nabla \tilde{\mathbf{u}} + \left(\nabla \tilde{\mathbf{u}} \right)^T \right], \tag{2.18}$$

$$\tilde{p} = -\alpha M \nabla \cdot \tilde{\mathbf{u}} - M \nabla \cdot \tilde{\mathbf{w}}, \tag{2.19}$$

where the expressions for α and M are shown in equations (2.8) and (2.9), respectively; C is the saturated P-wave modulus:

$$C = K_{sat} + \frac{4}{3}\mu_d, \tag{2.20}$$

where K_{sat} is given by equation (2.6).

Combining equations of motion with the constitutive relations, we can obtain the dilatational and rotational (shear) wave equations by expressing **u** and **w** using the Helmholtz's potential theory (Achenbach, 1973) as follows:

$$\tilde{\mathbf{u}} = \nabla \phi_1 + \nabla \phi_2 + \nabla \times \boldsymbol{\psi}, \tag{2.21}$$

$$\tilde{\mathbf{w}} = \chi_1 \nabla \phi_1 + \chi_2 \nabla \phi_2 + \chi_3 \nabla \times \boldsymbol{\psi}, \tag{2.22}$$

where ϕ_1 and ϕ_2 denote the scalar potentials for the first and second kind of P-wave, respectively. Compared to the elastic medium, the additional P-wave mode (second kind of P-wave) is generated due to the relative movement between the pore fluid and the solid (Biot, 1956a, 1956b). $\boldsymbol{\Psi}$ is the vector potential for the S-wave. χ_1, χ_2, and χ_3 are the ratios of **w** to **u** for the corresponding wave mode, respectively.

Substituting equations (2.21) and (2.22) into equations (2.14), (2.15), (2.18), and (2.19) gives the P- and S- wave equations as follows:

$$\left(\nabla^2 + k_i^2 \right) \phi_i = 0, \ i = 1, 2 \tag{2.23}$$

$$\left(\nabla^2 + k_3^2 \right) \boldsymbol{\psi} = \mathbf{0}, \tag{2.24}$$

where k_1 and k_2 are the wavenumber for the first and second P-waves, respectively; k_3 is the wavenumber for the shear wave. The expressions for k_i are as follows (Berryman, 1985):

$$k_i = \omega s_i \text{ , } i = 1, 2, 3 \tag{2.25}$$

where s_i is the slowness of these waves as follows:

$$s_{1,2}^2 = b \mp \sqrt{b^2 - \frac{\rho\tilde{\rho} - \rho_f^2}{MC - \alpha^2 M^2}} \text{ , } \tag{2.26}$$

$$s_3 = \sqrt{\frac{\rho\tilde{\rho} - \rho_f^2}{\mu\tilde{\rho}}} \text{ , } \tag{2.27}$$

with

$$b = \frac{\rho M + \tilde{\rho} C - 2\rho_f \alpha M}{2\left(MC - \alpha^2 M^2\right)} . \tag{2.28}$$

Furthermore, the expressions for χ_1, χ_2, and χ_3 can also be obtained as follows:

$$\chi_{1,2} = -\frac{Cs_{1,2}^2 - \rho}{\alpha M s_{1,2}^2 - \rho_f} \text{ , } \tag{2.29}$$

$$\chi_3 = -\frac{\rho_f}{\tilde{\rho}} . \tag{2.30}$$

From the wavenumbers of the first and second kinds of P-waves, it can be found that the dispersion and attenuation of the first kind of P-wave are small, whereas those for the second kind of P-wave are very high at low frequencies ($\omega << \omega_B$). This is due to the fact that the wave equation for the second kind of P-wave will reduce to a diffusion-type equation in the low frequency regime. Comparing the phase velocities of the first and second kinds of P-waves, it can also be found that the first kind of P-wave is much faster than the second kind, especially at low frequencies. Hence, the first and second kinds of P-waves are usually called fast and slow P-waves respectively. The existence of the slow P-wave in the fluid saturated porous rock has been validated by the experiments (e.g., Plona, 1980). It should be noted that, in the low frequency limit, the slow P-wave will vanish and the Biot theory will be equivalent to Gassmann equations.

2.5 P-wave dispersion and attenuation due to FB-WIFF in saturated porous rocks with aligned mesoscopic fractures

Biot's theory of dynamic poroelasticity introduced above describes seismic dispersion and attenuation due to the macroscopic (global) WIFF between peaks and troughs of the wave. However, when a seismic wave propagates through the saturated rock with aligned mesoscopic fractures, besides the macroscopic WIFF, the fluid flow will also occur between the fractures and the background medium (FB-WIFF) due to the strong stiffness contrast between these two media. This will also result in the seismic dispersion and attenuation. As introduced in Chapter 1, extensive studies have been carried out on this mechanism. Due to the complexity of the geometries of the real fractures, in all these studies, for simplicity the fractures are usually approximated as planes of weakness or penny-shaped cracks.

If the radii of the considered fractures are much larger than the predominant seismic wavelengths and fracture spacing, the fractures can be treated as planes of weakness (Gurevich et al., 2009). This means that, in this case, fractures can be represented by highly-porous layers (Schoenberg, 1980), which can be called planar fractures. Then a porous rock with aligned planar fractures can be modelled as a layered porous medium of infinite lateral extent (Figure 2-1a). If the fractures are distributed periodically in an isotropic background medium, the frequency-dependent saturated P-wave modulus due to FB-WIFF effects in the direction perpendicular to the fracture plane, c^{sat}, can be obtained from a solution of Biot's equations of dynamic poroelasticity with 1-D periodic coefficients as follows (White et al., 1975; Norris, 1993; Brajanovski et al., 2005)

$$\frac{1}{c^{sat}}=\frac{1}{C_1}+\frac{2}{\sqrt{i\omega\eta}H}\frac{\left(\frac{\alpha_b M_b}{C_b}-\frac{\alpha_c M_c}{C_c}\right)^2}{\sqrt{\frac{M_b L_b}{C_b\kappa_b}}\cot\left(\sqrt{\frac{i\omega\eta C_b}{\kappa_b M_b L_b}}\frac{f_b H}{2}\right)+\sqrt{\frac{M_c L_c}{C_c\kappa_c}}\cot\left(\sqrt{\frac{i\omega\eta C_c}{\kappa_c M_c L_c}}\frac{f_c H}{2}\right)}, \tag{2.31}$$

where C_b and L_b are the P-wave modulus of the saturated and dry background, respectively; κ_b is the permeability of the background; f_b is the fraction of background with respect to the whole porous medium; $\alpha_b = 1\text{-}K_b/K_{gb}$ is the Biot's coefficient of the background, with K_b being the bulk modulus of the dry background and K_{gb} that of the solid grains composing the background; $M_b = K_{gb}/[(1\text{-}K_b/K_{gb})$-

$\phi_{bg}(1-K_{gb}/K_f)]$ is the Biot's modulus of the background, with K_f being the fluid bulk modulus and ϕ_{bg} the porosity of the background. It is interesting to notice that α_b and M_b determine the bulk modulus increment of the background medium due to the fluid saturation ($\Delta K_b = \alpha_b^2 M_b$). The subscript c represents the corresponding values for the fractures. In particular, the Biot-Willis coefficient and modulus for the fracture infill material are $\alpha_c = 1-K_c/K_{gc}$ and $M_c = K_{gc}/[(1-K_c/K_{gc})- \phi_{cg}(1-K_{gc}/K_f)]$ respectively, with K_c being the bulk modulus of the dry fracture infill material, K_{gc} that of the solid grains composing the fracture infill material, and ϕ_{cg} the porosity of the fracture infill material. In addition, C_1 is the saturated P-wave modulus of the fractured medium in the high-frequency limit of the WIFF, which is computed using the poroelastic Backus average applied to the saturated fractures and background medium [$C_1 = 1/(f_b/C_b + f_c/C_c)$]. Both the fractures and the background are saturated with the same fluid with shear viscosity η. In addition, ω is the angular frequency of the seismic wave and H represents the spatial period, which is the total thickness of a periodic unit (including the fractures and the background medium).

When the thickness of the planar fractures becomes infinitesimal, equation (2.31) can be simplified to the following form (Brajanovski et al., 2005; Gurevich et al., 2009):

$$\frac{1}{c^{sat}} = \frac{1}{C_b} + \frac{\Delta_N \left(\frac{\alpha_b M_b}{C_b} - 1 \right)^2}{L_b \left[1 - \Delta_N + \Delta_N \sqrt{i\Omega} \cot\left(\frac{C_b}{M_b} \sqrt{i\Omega} \right) \right]}, \tag{2.32}$$

where $\Delta_N = L_b Z_N / (1+L_b Z_N)$ is the normal fracture weakness, with Z_N being the excess normal compliance induced by the dry fractures; $\Omega = \omega H^2 M_b \eta/(4\kappa_b C_b L_b)$ is the normalized frequency. The characteristic angular frequency ω_{pl} then equals to $4\sqrt{2}\left(\frac{C_b}{M_b} \right)^2 \Delta_N^{-2} \frac{D_b}{H^2}$, with $D_b = M_b L_b \kappa_b / \eta C_b$ being the hydraulic diffusivity of the saturated background medium.

On the other hand, if the radii of the fractures are in similar size with or much smaller than their spacing but much larger than the pore size, the fractures can be treated as penny-shaped cracks, which

have an oblate spheroidal shape (Figure 2-1b). For saturated rocks containing aligned penny-shaped cracks, the corresponding seismic dispersion and attenuation due to the WIFF between the fractures and the background medium can be obtained by solving a mixed boundary value problem for Biot's equations of poroelasticity, which was studied by Galvin and Gurevich (2006, 2007) under the assumption that fracture thickness is infinitesimal. The resulting equation for P-waves propagating perpendicular to the fracture plane is an integral equation that requires a numerical solution. However, the asymptotic behaviour of the frequency-dependent P-wave modulus at low and high frequencies can be approximated analytically as follows (Galvin and Gurevich, 2006, 2007; Gurevich et al., 2009):

$$\frac{1}{c^{sat}} = \frac{1}{C_0}\left[1 + \frac{i\omega}{D_b}\frac{2M_b\left(C_b - \alpha_b M_b\right)^2\left(2 - 4\alpha_b g_b + 3\alpha_b^2 g_b^2\right)a^2\varepsilon}{15\mu_b g_b\left(1-g_b\right)^2 C_b^2}\right], \quad \omega << \omega_c \tag{2.33}$$

$$\frac{1}{c^{sat}} = \frac{1}{C_b}\left[1 + \frac{2\sqrt{D_b}\pi\varepsilon\left(C_b - \alpha_b M_b\right)^2}{L_b M_b\sqrt{-i\omega}a}\right], \ \omega >> \omega_c \tag{2.34}$$

where C_0 is the P-wave modulus in the low-frequency limit; μ_b is the dry background shear modulus and g_b is the ratio of μ_b to L_b; a is the radius of the penny-shaped cracks; $\varepsilon = (3/4\pi)\phi_c/\beta$ is the crack density with ϕ_c the crack porosity and β the aspect ratio; $\omega_{pe} = 4\pi D_b/a^2$ is the characteristic angular frequency in this case.

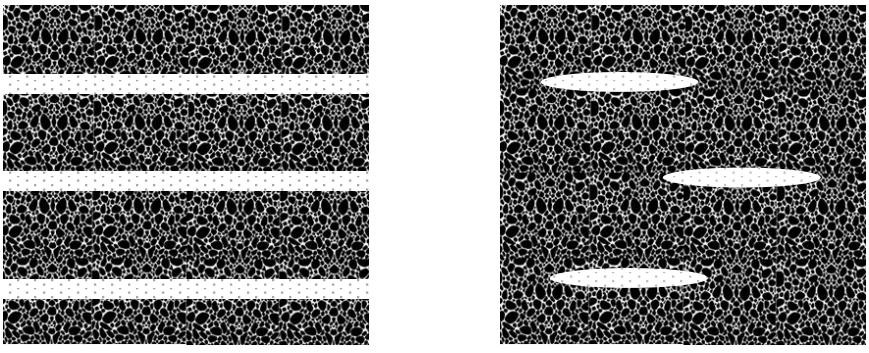

(a) (b)

Figure 2-1. Schematic representation of porous rocks with aligned planar fractures (a) and penny-shaped cracks (b).

It should be noted here that in all the above models and those that will be developed in the following chapters, the fractures are assumed to be in perfect hydraulic contact with the background medium and hence there is no fluid pressure jump across the boundary between the fractures and the background medium. This means the interface hydraulic permeability tends to infinity or the coupling coefficient between the fluid in the background pores and that in the fractures equals to 1 (e.g., Deresiewicz and Skalak, 1963; Rosenbaum, 1974; Gurevich and Schoenberg, 1999).

It is also important to point out that, while the shear moduli are not given in these models, they may also be affected by the fluid saturation and the FB-WIFF. For the shear moduli in the three principal planes of the fractured rocks, they are not affected by the fluid saturation and FB-WIFF due to the fact that the shear deformation in these planes does not induce fluid pressure which in turn has no effects on the values of these shear moduli. However, in other planes, the shear deformation may induce the fluid pressure and hence the shear modulus will be influenced by the fluid saturation and also FB-WIFF.

2.6 Unified model described by branching function and full stiffness coefficients

To describe the seismic dispersion and attenuation due to FB-WIFF in the rocks containing the above two types of fractures (Figure 2-1) in a unified form, Gurevich et al. (2009) employed the so-called branching function approach. This approach was first proposed in the context of WIFF by Johnson (2001) to approximate the frequency-dependent complex stiffness coefficients of porous rocks saturated with a mixture of two fluids. These simple approximations, which have similar behaviours as the asymptotic analytical solutions at low and high frequencies and satisfy causality, turned out to be very accurate and useful. Pride and Berryman (2003) also applied a very similar approach to a medium with a more general double porosity structure, which includes a periodically layered poroelastic medium as a special case (Pride, Berryman and Harris, 2004).

To describe the frequency-dependent P-wave modulus c^{sat} in the direction perpendicular to the fracture plane due to WIFF between the fractures and the background, Gurevich et al. (2009) use the branching function in the form

$$\frac{1}{c^{sat}}=\frac{1}{C_1}\left[1+\left(\frac{C_1-C_0}{C_0}\right)/\left(1-\varsigma+\varsigma\sqrt{1-i\frac{\omega\tau}{\varsigma^2}}\right)\right], \tag{2.35}$$

where C_0 and C_1 are the P-wave moduli in the low- and high-frequency limits, respectively; ζ and τ are parameters that shape the dispersion and attenuation curves of the elastic coefficient. $1/\tau$ denotes the characteristic frequency of the dispersion and attenuation.

At low and high frequencies, equation (2.35) has the following asymptotes:

$$\frac{1}{c^{sat}}=\frac{1}{C_0}\left(1+i\omega T\right), \qquad \omega\tau << \varsigma^2 \tag{2.36}$$

$$\frac{1}{c^{sat}}=\frac{1}{C_1}\left(1+\frac{G}{\sqrt{-i\omega}}\right), \qquad \omega\tau >> 1 \tag{2.37}$$

where T and G are related to ζ and τ as follows:

$$\tau=\left(\frac{C_1-C_0}{C_0G}\right)^2, \tag{2.38}$$

$$\varsigma=\frac{\left(C_1-C_0\right)^3}{2C_1C_0^2TG^2}. \tag{2.39}$$

Equations (2.38) and (2.39) show that seismic dispersion and attenuation caused by WIFF between the fractures and the background is controlled by the parameters T and G, together with the elastic properties in the low- and high-frequency limits, C_0 and C_1. Parameters T and G, are different for different fracture geometries but can be found by comparing the asymptotes of the exact analytical solution for a specific geometry against the asymptotes (2.36) and (2.37).

2.6.1 Parameters *T* and *G* for the infinitesimal fracture thickness case

For the infinitesimal fracture thickness case, Gurevich et al. (2009) derived expressions for the parameters T and G associated with the P-wave modulus in the direction perpendicular to the fracture plane. They are obtained by comparing equations (2.36) and (2.37) with the corresponding asymptotic

analytical solutions under the limit of infinitesimal fracture thickness. For periodically-spaced planar fractures, the low- and high- frequency asymptotes of equation (2.32) can first be obtained. Then, comparison of equations (2.36) and (2.37) with these asymptotes yields the following expressions for *T* and *G*:

$$T = \frac{1}{12}\left(C_b - C_0\right)\frac{Z_N H^2 \eta}{\left(C_b + Z_N L_b M_b\right)\kappa_b}, \tag{2.40}$$

$$G = \frac{2}{H}\left(C_b - \alpha_b M_b\right)^2 \sqrt{\frac{\kappa_b}{\eta C_b M_b L_b}}. \tag{2.41}$$

If spacing between planar fractures is random, rather than periodic, numerical simulations indicate that the seismic response at high frequencies is similar to that for the same rock containing the fractures periodically distributed. However, they are qualitatively different at low frequencies (Lambert et al., 2006). This is due to the fact that at high frequencies the fluid diffusion length is much smaller than fracture spacing, and hence, the distribution of the fractures has no influence on the seismic properties. Conversely, at low frequencies the fluid diffusion length is large and, thus, seismic dispersion and attenuation will be affected by the fracture distributions. Accordingly, it was found that τ for the random planar fracture spacing case is the same as for the periodic planar fracture case. However, in contrast to the periodic planar fracture case, ζ is zero as the effective fracture spacing tends to infinity for random distributions (Gurevich and Lopatnikov, 1995; Müller and Rothert, 2006; Gurevich et al., 2009). Taking this into account, the unified model [equation (2.35)] can be simplified for the random planar fracture spacing case as follows:

$$\frac{1}{c^{sat}} = \frac{1}{C_1} + \left(\frac{1}{C_0} - \frac{1}{C_1}\right) / \left(1 + \sqrt{-i\omega\tau}\right), \tag{2.42}$$

where τ is obtained from equation (2.38) with *G* shown in equation (2.41).

For sparsely distributed penny-shaped cracks, the expressions of *T* and *G* can be obtained by comparing equations (2.36) and (2.37) with equations (2.33) and (2.34), which yields:

$$T = \frac{2\left(C_b - \alpha_b M_b\right)^2 \left(2 - 4\alpha_b g_b + 3\alpha_b^2 g_b^2\right) a^2 \varepsilon \eta}{15\mu_b g_b \left(1 - g_b\right)^2 C_b L_b \kappa_b}, \tag{2.43}$$

$$G = \frac{2\pi\varepsilon}{a}\left(C_b - \alpha_b M_b\right)^2 \sqrt{\frac{\kappa_b}{\eta C_b M_b L_b}}. \tag{2.44}$$

Substituting the relation between the P-wave moduli of the saturated fractured rock in the low- and high- frequency limits (Gurevich et al., 2009), equation (2.43) can be rewritten as:

$$T = \frac{1}{5}\frac{C_1 - C_0}{C_0}\frac{\left(2 - 4\alpha_b g_b + 3\alpha_b^2 g_b^2\right) a^2 \eta}{g_b \left(1 - g_b\right) L_b \kappa_b}. \tag{2.45}$$

Hence, when the fracture thickness is infinitesimal, we can express the P-wave modulus in the direction perpendicular to the fracture plane using the unified model [equation (2.35)] for the three types of fractures considered (periodic planar fractures, penny-shaped cracks, and randomly distributed planar fractures). For different types of fractures, the corresponding expressions of T and G are different, as shown above. Gurevich et al. (2009) show that the results given by the unified model are almost the same with those calculated by the corresponding analytical solutions or numerical simulations, which validates the accuracy of this approach. Note that for the finite size fractures, no analytical solution is known for the entire frequency range, and hence for these fractures a simple all-frequency branching function solution is particularly useful.

It can be noted that for both planar fractures and penny-shaped cracks, G can be expressed in the same form as follows:

$$G = 2S\left(C_b - \alpha_b M_b\right)^2 \sqrt{\frac{\kappa_b}{\eta C_b M_b L_b}}, \tag{2.46}$$

where S is called the specific surface area of the fractures per unit volume (Gurevich et al., 2009). For periodic fractures, $S = 1/H$ and for penny-shaped cracks, $S = \pi\varepsilon/a$. Equation (2.46) implies that at high frequencies, the fluid diffusion length is much smaller than both the fracture size and spacing, and therefore, the fluid diffusion and energy dissipation occur in the immediate vicinity of the fracture

surfaces, which is controlled by the specific surface area *S*. This is also supported by numerical simulations (Rubino et al., 2014).

Note that the original equations in Gurevich et al. (2009) contain some typographical errors, which are corrected in the equations presented above.

2.6.2 Full stiffness coefficients

Equation (2.35) gives the frequency-dependent P-wave modulus in the direction perpendicular to the fracture plane. To obtain the full stiffness coefficients, Galvin and Gurevich (2015) assumed that the relaxation function for all the stiffness coefficients is the same. Hence, the frequency-dependent full stiffness coefficients are obtained as follows:

$$\frac{1}{c_{ij}^{sat}} = \frac{1}{c_{ij,hf}^{sat}}\left[1+\left(\frac{c_{ij,hf}^{sat}-c_{ij,lf}^{sat}}{c_{ij,lf}^{sat}}\right)f(\omega)\right], \quad i,j = 1,\ldots 6 \tag{2.47}$$

where c_{ij}^{sat} is the ij^{th} frequency-dependent stiffness coefficient; $c_{ij,lf}^{sat}$ and $c_{ij,hf}^{sat}$ are the values of the stiffness coefficients in the low- and high-frequency limits, respectively; ω is the angular frequency of the seismic wave; and $f(\omega)$ is the relaxation function, which has the following form:

$$f(\omega) = 1/\left(1-\varsigma+\varsigma\sqrt{1-i\frac{\omega\tau}{\varsigma^2}}\right). \tag{2.48}$$

It can be seen from equation (2.48) that the value of the relaxation function equals to one in the low-frequency limit and decays to zero in the high-frequency limit. Its shape is determined by the parameters ζ and τ. Since the relaxation function is the same for all stiffness coefficients, the values of ζ and τ in equation (2.48) are same with those in equation (2.35). Then, we can apply the obtained relaxation function to calculate the other frequency-dependent stiffness coefficients.

The assumption of the same relaxation function for all stiffness coefficients was proposed by Krzikalla and Müller (2011) and can be justified as follows. As the viscosity of the saturating fluid is assumed to be very low, the viscous shear relaxation is not considered here and hence only the WIFF

is responsible for the seismic wave dispersion and attenuation. When a fast compressional or shear wave strikes on a fracture surface, it generates WIFF between the fractures and the background medium, which can be considered as energy conversion into Biot's slow waves generated at the interface (Gurevich and Lopatnikov, 1995). For frequencies much lower than the Biot's characteristic frequency, the velocities of the slow waves are usually two to three orders of magnitude smaller than that of the incident wave (Kong et al., 2017). According to Snell's law, the reflection or transmission angle of the slow waves will then be nearly zero regardless of the propagation angle of the incident wave. This means that the fluid will always flow in the direction perpendicular to the fracture plane for waves propagating in any directions, thus implying that all the stiffness coefficients can be described by a single relaxation function. A detailed discussion on this topic can be found in Kong et al. (2017). Apart from the above theoretical justification, the single relaxation behaviour of the stiffness coefficients is also verified by the numerical simulations in Lambert et al. (2005), Krzikalla and Müller (2011), and Rubino et al. (2016).

2.6.3 Elastic properties in the low- and high- frequency limits

To obtain the frequency-dependent stiffness coefficients, the elastic properties in the low- and high-frequency limits are needed, as shown in equation (2.47). In the low-frequency limit, the fluid pressure is uniform throughout the fractured rock and hence the anisotropic Gassmann equation can be used to calculate the elastic properties. In order to do so, we can first obtain the elastic properties of the dry rock using the linear slip theory, as shown in Section 2.2. It should be noted that, due to the infinitesimal fracture thickness considered here, when using the Eshelby model to calculate the dry fracture compliance matrix $\mathbf{Z}_0$, only one normal and two tangential non-zero dry fracture compliances are obtained, while the other components are equal to zero [equation (2.4)]. Then, the anisotropic Gassmann equation (2.10) can be applied to calculate the rock elastic properties in the low-frequency limit. As the fracture thickness is infinitesimal, the porosity of the rock used in the anisotropic Gassmann equation is equal to that of the background medium.

In the high-frequency limit, the fractures are hydraulically isolated from the saturated background medium. Hence, the saturated fractured medium can be treated as the saturated background permeated

by the hydraulically-isolated saturated fractures. The elastic properties of the saturated background can be obtained using the isotropic Gassmann's equations (2.6) and (2.7). The compliance matrix of the hydraulically isolated fractures $\mathbf{Z}_1$ has the same values of the tangential fracture compliances as those of the dry fracture matrix $\mathbf{Z}_0$. However, the normal fracture compliance reduces to zero due to the infinitesimal fracture thickness (Galvin and Gurevich, 2015). Hence, $\mathbf{Z}_1$ can be obtained and the elastic properties of the saturated rocks with aligned fractures of infinitesimal thickness in the high-frequency limit can be calculated using the linear slip theory as follows:

$$\mathbf{S}_{hf}^{sat} = \mathbf{S}_{b}^{sat} + \mathbf{Z}_1, \tag{2.49}$$

where $\mathbf{S}_{hf}^{sat}$ is the compliance matrix of the saturated fractured rocks in the high-frequency limit; $\mathbf{S}_{b}^{sat}$ is the compliance matrix of the saturated background medium, which can be obtained by taking the inverse of $\mathbf{C}_{b}^{sat}$. The stiffness matrix $\mathbf{C}_{hf}^{sat}$ of the saturated fractured rocks can then be computed from $\mathbf{S}_{hf}^{sat}$.

With the expressions obtained for the parameters involved in the branching function presented above, the frequency-dependent full stiffness coefficients of the saturated porous rocks with aligned periodically- or randomly- spaced planar fractures, as well as penny-shaped cracks can be calculated.

2.7 Seismic wave dispersion, attenuation, and anisotropic properties

After obtaining the frequency-dependent full stiffness coefficients, the seismic wave dispersion, attenuation, and anisotropic properties can be calculated. As the resulting effective elastic properties for the rocks with aligned fractures are transversely isotropic (e.g., Schoenberg and Sayers, 1995; Galvin and Gurevich, 2015), assuming the symmetry axis (fracture normal) lies along x_2-axis, the complex velocities of the qP-wave, qSV-wave, and SH-wave can be calculated from the stiffness coefficients as follows (Mavko et al., 2009):

$$\tilde{V}_P = \left(c_{11}^{sat} \sin^2\theta + c_{22}^{sat} \cos^2\theta + c_{66}^{sat} + \sqrt{M} \right)^{1/2} \left(2\rho \right)^{-1/2}, \tag{2.50}$$

$$\tilde{V}_{SV} = \left(c_{11}^{sat} \sin^2\theta + c_{22}^{sat} \cos^2\theta + c_{66}^{sat} - \sqrt{M} \right)^{1/2} (2\rho)^{-1/2}, \tag{2.51}$$

$$\tilde{V}_{SH} = \left(\frac{c_{55}^{sat} \sin^2\theta + c_{44} \cos^2\theta}{\rho} \right)^{1/2}, \tag{2.52}$$

where ρ is the density of the saturated fractured rocks; θ is the incidence angle with respect to the fracture normal (x_2-axis); and M can be written as follows:

$$M = \left[\left(c_{11}^{sat} - c_{66}^{sat} \right) \sin^2\theta - \left(c_{22}^{sat} - c_{66}^{sat} \right) \cos^2\theta \right]^2 + \left(c_{12}^{sat} + c_{66}^{sat} \right)^2 \sin^2 2\theta. \tag{2.53}$$

Then, the seismic phase velocities and attenuations can be computed as follows (e.g., Carcione et al., 2013):

$$V = \left[\mathrm{Re}\left(\frac{1}{\tilde{V}} \right) \right]^{-1}, \tag{2.54}$$

$$\frac{1}{Q} = \left| \frac{\mathrm{Im}\left(\tilde{V}^2 \right)}{\mathrm{Re}\left(\tilde{V}^2 \right)} \right|, \tag{2.55}$$

where V and $1/Q$ is the phase velocity and attenuation of either qP-, qSV-, or SH- wave.

To investigate the anisotropic properties of fractured rocks, the anisotropy parameters can be used. For the phase velocities, the anisotropy parameters are defined as follows (Thomsen, 1986):

$$\varepsilon = \frac{\mathrm{Re}\left(c_{11}^{sat} - c_{22}^{sat} \right)}{2\,\mathrm{Re}\left(c_{22}^{sat} \right)}, \tag{2.56}$$

$$\delta = \frac{\left[\mathrm{Re}\left(c_{12}^{sat} + c_{66}^{sat} \right) \right]^2 - \left[\mathrm{Re}\left(c_{22}^{sat} - c_{66}^{sat} \right) \right]^2}{2\,\mathrm{Re}\left(c_{22}^{sat} \right) \mathrm{Re}\left(c_{22}^{sat} - c_{66}^{sat} \right)}. \tag{2.57}$$

For the attenuation, we use the anisotropy parameters defined by Collet and Gurevich (2016) as follows:

$$\varepsilon_Q = \frac{1}{2} \left(\frac{1}{Q_{11}} - \frac{1}{Q_{22}} \right), \tag{2.58}$$

$$\delta_Q = \left(\frac{1}{Q_{12}} - \frac{1}{Q_{22}} \right) + 2 \frac{\mathrm{Re}\left(c_{66}^{sat}\right)}{\mathrm{Re}\left(c_{22}^{sat}\right)} \left(\frac{1}{Q_{66}} - \frac{1}{Q_{12}} \right), \tag{2.59}$$

where Q_{ij} is the anisotropic attenuation matrix, which is given by:

$$Q_{ij} = \frac{\mathrm{Re}\left(c_{ij}^{sat}\right)}{\mathrm{Im}\left(c_{ij}^{sat}\right)}. \tag{2.60}$$

2.8 Seismic scattering dispersion and attenuation by aligned dry open fractures

Apart from WIFF, the wave scattering by the fractures is another important source of seismic dispersion and attenuation, especially in the carbonate or unconventional reservoirs which often contain fractures with similar or even larger size than seismic wavelength. Hence, it is also important to consider the scattering effects in the fractured reservoirs. In Chapter 5, I will develop the theoretical model for the P-wave dispersion and attenuation due to the scattering by the fluid saturated aligned fractures. This model is an extension of the model for dry open fractures, which was proposed by Kawahara (1992). In the following, I will briefly introduce this model.

In Kawahara model, aligned 2D dry slit fractures are assumed to be distributed randomly and sparsely in an infinite elastic isotropic background medium, as shown in Figure 2-2. The coordinate system is established, such that the fracture plane is perpendicular to the X_2-axis, and the fracture length along X_3-axis is infinity. Hence, the plane strain condition in $X_1 - X_2$ plane is satisfied and the 3D problem can be reduced to a 2D problem. It is assumed that all the fractures have an identical rectangular shape with a thickness β along X_2-axis and a length $2a$ along X_1-axis. The number density of the fractures (number of fractures in per unit of area) is v. We consider a longitudinal plane wave (P-wave) propagating in the fractured rock at an incidence angle of θ with respect to the fracture normal (X_2-axis).

The incident P-wave is assumed to be a plane time-harmonic wave with an angular frequency ω and displacement :

$$\mathbf{u}_{\mathbf{A}}^{\mathbf{0}} = A_0 e^{ik_p X_1 \sin\theta + ik_p X_2 \cos\theta} \left(\sin\theta, \cos\theta\right), \tag{2.61}$$

where A_0 is the displacement amplitude, $k_p = \omega/V_p$ the wave number, and V_p the P-wave velocity in the background medium (for brevity, the time factor $e^{-i\omega t}$ is omitted).

Due to the scattering of the randomly distributed fractures, the total wave field $\mathbf{u_A}$ is the sum of the incident wave plus the scattered wave. The ensemble average of this total field is called the mean field $\langle \mathbf{u_A} \rangle$ and has the following form (Kawahara, 1992):

$$\langle \mathbf{u_A} \rangle = Ae^{ik_p X_1 \sin\theta + i\left(k_p \cos\theta + \kappa\right) X_2} \left(\sin\theta, \cos\theta + \kappa / k_p\right), \tag{2.62}$$

where A is the initial displacement amplitude of the mean wave field, κ is the coefficient that determines the attenuation and dispersion of the mean wave.

Since the fractures are distributed sparsely and randomly in the solid, the relationship between the incident wave field and the ensemble averaging can be replaced by spatial averaging using the Foldy (1945) approximation as follows:

$$\langle \mathbf{u_A} \rangle = \mathbf{u_A^0} + v \int S_A \langle \mathbf{u_i} \rangle d\mathbf{r}_i, \tag{2.63}$$

where $S_A \langle \mathbf{u_i} \rangle$ is the scattered displacement caused by the ith fracture due to the incidence of the mean wave $\langle \mathbf{u_i} \rangle$ on the fracture; $\mathbf{r}_i$ denotes the central location of the ith fracture. By integrating over the entire volume of the fractured rock, the total scattered displacement is obtained, which is added to the incident displacement field to obtain the displacement field of the mean wave.

From equation (2.62), the mean incident wave $\langle \mathbf{u_i} \rangle$ on the ith fracture can be written as follows:

$$\langle \mathbf{u_i} \rangle = Ae^{ik_p (x_1 + p_1) \sin\theta + i\left(k_p \cos\theta + \kappa\right)(x_2 + p_2)} \left(\sin\theta, \cos\theta + \kappa / k_p\right), \tag{2.64}$$

where (p_1, p_2) is the location of the centre of the ith fracture in the global coordinate system (X_1, X_2). (x_1, x_2) defines the location in the local coordinate system with the origin at the centre of the ith fracture with the x_1-axis and x_2-axis parallel and perpendicular to the fracture plane, respectively (Figure 2-2).

Using the representation theorem, we can present the scattering wave field by the *i*th fracture as follows (e.g., Achenbach, 1973; Kawahara and Yamashita, 1992):

$$\left[S_i\left\langle \mathbf{u_i}\right\rangle\right]_j = -\int_{-a}^{a}\left[\Delta\mathbf{u_i}\left(\zeta_1, p_1, p_2\right)\right]_l \Gamma_{jl}\left(x_1, x_2 \mid \zeta_1, 0\right) d\zeta_1, \quad j,l = 1, 2, \tag{2.65}$$

where $\left[\cdot\right]_j$ represents the *j*th component of the vector field, the summation convention is employed for the repeated subscripts in the right hand side of the equation. $\Delta\mathbf{u_i}$ is the displacement discontinuity across the fracture. Γ_{jl} has the following form:

$$\Gamma_{jl}\left(x_1, x_2 \mid \zeta_1, \zeta_2\right) = \frac{i}{4}\left[\delta_{l2}\left(1-2\frac{k_p^2}{k_s^2}\right)\frac{\partial}{\partial x_j}H_0^{(1)}\left(k_p R\right) + \left(\delta_{jl}\frac{\partial}{\partial x_2} + \delta_{j2}\frac{\partial}{\partial x_l}\right)H_0^{(1)}\left(k_s R\right)\right.$$

$$\left. -\frac{2}{k_s^2}\frac{\partial^3}{\partial x_j \partial x_l \partial x_2}\left(H_0^{(1)}\left(k_p R\right) - H_0^{(1)}\left(k_s R\right)\right)\right], \; j, l = 1, 2, \tag{2.66}$$

where $k_s = \omega/V_s$ is the *S*-wave number in the background medium, with V_s being the *S*-wave velocity in this medium; δ_{jl} is the Kronecker's delta; $H_0^{(1)}\left(\cdot\right)$ is the zero order Hankel function of the first kind; *R* has the following expression:

$$R^2 = \left(x_1 - \zeta_1\right)^2 + \left(x_2 - \zeta_2\right)^2. \tag{2.67}$$

According to Hooke's law for the isotropic elastic medium (Timoshenko and Goodier, 1934), the stress field induced by $\left\langle \mathbf{u_i}\right\rangle$ and $S_i\left\langle \mathbf{u_i}\right\rangle$ can be represented as follows (Kawahara and Yamashita, 1992):

$$\sigma_{jk}^E = \lambda\delta_{jk}\frac{\partial}{\partial x_l}\left[\left\langle \mathbf{u_i}\right\rangle\right]_l + \mu\left(\frac{\partial}{\partial x_k}\left[\left\langle \mathbf{u_i}\right\rangle\right]_j + \frac{\partial}{\partial x_j}\left[\left\langle \mathbf{u_i}\right\rangle\right]_k\right), \; j, k, l = 1, 2, \tag{2.68}$$

$$\sigma_{jk}^S = \lambda\delta_{jk}\frac{\partial}{\partial x_l}\left[S_i\left\langle \mathbf{u_i}\right\rangle\right]_l + \mu\left(\frac{\partial}{\partial x_k}\left[S_i\left\langle \mathbf{u_i}\right\rangle\right]_j + \frac{\partial}{\partial x_j}\left[S_i\left\langle \mathbf{u_i}\right\rangle\right]_k\right), \; j, k, l = 1, 2, \tag{2.69}$$

where σ_{jk}^{E} and σ_{jk}^{S} are the stress field induced by $\langle \mathbf{u_i} \rangle$ and $S_i \langle \mathbf{u_i} \rangle$, respectively. λ and μ are the Lamé constants of the fractured rock.

Substituting equations (2.65) and (2.66) into equation (2.69) yields:

$$\sigma_{jk}^{S} = -\mu \int_{-a}^{a} \left[\Delta \mathbf{u_i} \left(\zeta_1, p_1, p_2 \right) \right]_l T_{jkl} \left(x_1, x_2 \,|\, \zeta_1, 0 \right) d\zeta_1 \text{, } j, k, l = 1, 2, \tag{2.70}$$

where the expressions of T_{jkl} are shown in the Appendix B.

For the dry open fractures, the normal and shear stresses applied on the fracture surface equal to zero and hence:

$$\sigma_{12}^{E} + \sigma_{12}^{S} = 0 \text{, } -a < x_1 < a, \; x_2 = 0, \tag{2.71}$$

and

$$\sigma_{22}^{E} + \sigma_{22}^{S} = 0 \text{, } -a < x_1 < a, \; x_2 = 0. \tag{2.72}$$

Substituting equations (2.64), (2.68) and (2.70) into equations (2.71) and (2.72) yields:

$$\int_{-a}^{a} D_1 \left(\zeta_1 \right) T_{121} \left(x_1, 0 \,|\, \zeta_1, 0 \right) d\zeta_1 - e^{ik_p x_1 \sin\theta} = 0 \text{, } -a < x_1 < a, \tag{2.73}$$

and

$$\int_{-a}^{a} D_2 \left(\zeta_1 \right) T_{222} \left(x_1, 0 \,|\, \zeta_1, 0 \right) d\zeta_1 - e^{ik_p x_1 \sin\theta} = 0 \text{, } -a < x_1 < a, \tag{2.74}$$

where

$$D_1 \left(\zeta_1 \right) = \frac{\left[\Delta \mathbf{u_i} \left(\zeta_1, p_1, p_2 \right) \right]_1}{2i \left(k_p \cos\theta + \kappa \right) \sin\theta A e^{ik_p p_1 \sin\theta + i\left(k_p \cos\theta + \kappa \right) p_2}} \text{,} \tag{2.75}$$

and

$$D_2\left(\zeta_1\right)=\frac{\left[\Delta\mathbf{u}_{\mathbf{i}}\left(\zeta_1,p_1,p_2\right)\right]_2}{ik_pAe^{ik_pp_1\sin\theta+i\left(k_p\cos\theta+\kappa\right)p_2}\left[\left(k_s^2/k_p^2-2\right)\sin^2\theta+k_s^2/k_p^2\left(\cos\theta+\kappa/k_p\right)^2\right]}. \quad (2.76)$$

Hence, the normal and shear displacement discontinuities across the fracture can be obtained by solving integral equations (2.73) and (2.74). The coefficient κ can then be calculated from the displacement discontinuities. To do so, we can first obtain $S_A\left\langle\mathbf{u}_{\mathbf{i}}\right\rangle$ by rewriting $S_i\left\langle\mathbf{u}_{\mathbf{i}}\right\rangle$ using the global coordinate system. Then, by substituting $S_A\left\langle\mathbf{u}_{\mathbf{i}}\right\rangle$ and equations (2.75) and (2.76) into equation (2.63) and comparing the result with equation (2.62), we can obtain the expression for κ (Kawahara, 1992):

$$\kappa=v\phi_1\gamma k_p\sin2\theta\sin\theta+v\phi_2\frac{k_p}{2\gamma\cos\theta}\left(1-2\gamma\sin^2\theta\right)^2, \quad (2.77)$$

where $\gamma=V_s^2/V_p^2$, and ϕ_j has the following form:

$$\phi_j\left(k_p,\theta\right)=\int_{-a}^{a}D_j\left(\zeta_1\right)e^{-ik_p\zeta_1\sin\theta}d\zeta_1,\ j=1,2. \quad (2.78)$$

After obtaining κ, the frequency dependency of the phase velocity V_{pe} and attenuation factor Q_p^{-1} of the P-wave can be calculated as (Kawahara and Yamashita, 1992):

$$V_{pe}/V_p=1-\frac{\cos\theta}{k_p}\mathrm{Re}\,\kappa, \quad (2.79)$$

and

$$Q_p^{-1}=2\frac{\cos\theta}{k_p}\mathrm{Im}\,\kappa, \quad (2.80)$$

where V_{pe} and Q_p^{-1} are the phase velocity and attenuation of the P-wave, respectively.

The numerical examples presented by Kawahara (1992) show that the maximum dispersion and attenuation occur when the wavelength is close to the fracture radius and hence the characteristic angular frequency ω_s approximately equals to V_p/a.

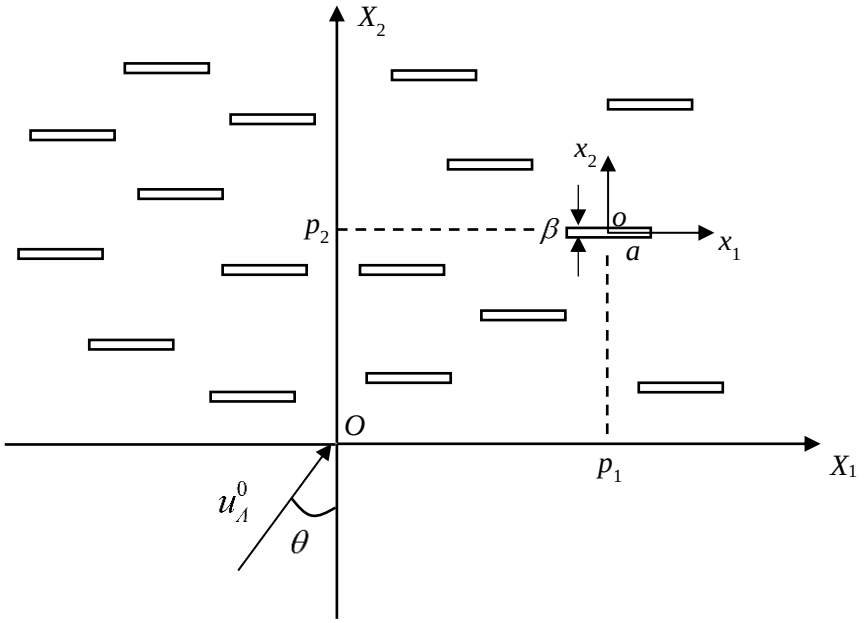

Figure 2-2. Infinite elastic background medium embedded with randomly and sparsely distributed aligned 2D slit fractures. The length and thickness of the fracture is $2a$ and β, respectively. Both the global and local coordinate system are established with the X_1- (or x_1-) and X_2- (or x_2-) parallel and perpendicular to the fracture plane, respectively. The origin of the local coordinate system is located at the centre of the ith fracture with a global coordinate (p_1, p_2).

2.9 Comparison of characteristic frequencies for various mechanisms of seismic dispersion and attenuation

In the above sections, I have described several mechanisms for the seismic dispersion and attenuation, which include the effects of Biot macroscopic fluid flow and FB-WIFF, as well as the influence of the wave scattering. To understand the frequency regime in which these mechanisms can play a role and possible interplay between them, it is crucial to compare the characteristic frequencies for these mechanisms. For ease of comparison, I select a set of parameters for the typical sandstone reservoirs (Mavko et al., 2009). The parameters are taken as follows: dry background bulk modulus K_m = 21 GPa, shear modulus G_m = 14 GPa, porosity ϕ = 0.16, permeability $\kappa = 10^{-15}$ m^2, and tortuosity α_∞ = 1; grain bulk modulus K_s = 38 GPa, and density ρ_s = 2.65 g/cm^3; fluid bulk modulus K_f = 2.25 GPa, density ρ_f = 1 g/cm^3, and viscosity η = 0.001 Pa.s. Using these parameters, the characteristic frequency

for Biot effects can be estimated using the formula introduced in Section 2.4. The value for this characteristic frequency is on the order of 10^7 Hz in this case, which is far beyond the seismic frequency band. Hence, the effects of Biot macroscopic fluid flow in the seismic frequency range is usually negligible, and therefore, is not considered in this thesis.

To estimate the characteristic frequencies for the FB-WIFF effects and wave scattering, the geometries of the fractures are also needed. As introduced above, for the randomly and sparsely distributed aligned fractures, the characteristic frequency for FB-WIFF is around D_b / a^2, whereas for wave scattering it is approximately $V_p / (2\pi a)$. Since the fracture size can vary in a wide range from millimetres to more than several meters (Narr et al., 2006), the corresponding characteristic frequencies for these two mechanisms can also vary substantially. For instance, if the fracture radius is 0.1 m, the characteristic frequency for FB-WIFF will be on the order of 10 Hz and that for wave scattering is around 10^3 Hz in the above studied case. When the fracture radius increases to 1 m, the characteristic frequency for FB-WIFF will change to ~10^{-1} Hz and that for wave scattering becomes ~10^2 Hz. Hence, both these two mechanisms can play a role in the seismic frequency range and thus will be studied in this thesis. Furthermore, if the characteristic frequencies for these two mechanisms are close to each other, the interplay between them may occur, which will be investigated in Chapter 6.

2.10 Numerical simulation schemes for elastic properties of fluid saturated porous and fractured rocks

To validate the theoretical models developed in this thesis, I also compare the theoretical predictions against numerical simulations. For this purpose, I use two types of numerical simulations. The first type of numerical simulations employs the Biot's quasi-static equation of poroelasticity (Biot, 1941), which can be used to investigate the WIFF effects and hence can validate the corresponding theoretical models (Chapter 3 and 4). The second type of numerical simulations simulates the wave propagation in the fluid saturated fractured porous rock using the low frequency approximation of Biot's dynamic poroelastic equations and hence the influence of both the scattering and WIFF can be taken into account.

The coupling between these two mechanisms can then be studied, and is compared to the corresponding theoretical model proposed in Chapter 6.

2.10.1 Quasi-static numerical simulation in saturated fractured and porous rocks

The quasi-static numerical simulations for the saturated fractured and porous rocks were proposed by Rubino et al. (2009, 2016). In this numerical simulation scheme, fractures are represented as highly compliant and permeable heterogeneities embedded in a stiffer porous background, and the behavior of fractured media is modeled in the framework of Biot's (1941) theory of quasi-static poroelasticity. Fluid-pressure communication between fractures and their embedding background as well as within connected fractures can take place, which allows to account for the effects produced by the manifestations of both FB-WIFF and FF-WIFF.

In order to estimate the effective seismic properties of fractured rocks, a numerical upscaling procedure is employed based on the application of three oscillatory relaxation tests on a square sample that is representative of the formation of interest (Rubino et al., 2016). First, homogeneous oscillatory vertical displacements are applied on the top and bottom boundaries of the representative sample, while it is not allowed to have horizontal displacements on the lateral boundaries. Moreover, it is not allowed for the fluid to flow into the sample or out of it. Next, a second test similar to the previous one is applied, but the normal displacements are applied on the lateral boundaries. Finally, a third test consisting of a simple shear is applied to the probed sample.

The solid and relative fluid displacements in response to the three tests are obtained by numerically solving, under corresponding boundary conditions, the Biot's (1941) quasistatic poroelastic equations in the space-frequency domain:

$$\nabla \cdot \boldsymbol{\sigma} = \mathbf{0}, \tag{2.81}$$

$$i\omega \frac{\eta}{\kappa} \mathbf{w} = -\nabla p_f , \tag{2.82}$$

where $\boldsymbol{\sigma}$ is the total stress tensor, p_f is the fluid pressure, $\mathbf{w}$ is the average relative fluid displacement, η is the shear viscosity of the pore fluid, κ is the rock permeability, and ω is the angular frequency.

Next, for each test, we compute the volume averages of the stress and strain components, which are needed for performing the upscaling:

$$\left\langle \varepsilon_{ij}^{k} \right\rangle = \frac{1}{V}\int_{\Omega} \varepsilon_{ij}^{k} dV \,, \tag{2.83}$$

$$\left\langle \sigma_{ij}^{k} \right\rangle = \frac{1}{V}\int_{\Omega} \sigma_{ij}^{k} dV \,, \tag{2.84}$$

where $\boldsymbol{\varepsilon}$ is the strain tensor, Ω is the domain of volume V that represents the probed sample, and k= 1,2,3 denotes the kth oscillatory test described above.

Assuming that the average responses of the probed sample can be represented by an equivalent homogeneous anisotropic viscoelastic solid, the average strain and stress components are then connected through a complex-valued frequency-dependent equivalent Voigt stiffness matrix **C**:

$$\begin{pmatrix} \left\langle \sigma_{11}^{k} \right\rangle \\ \left\langle \sigma_{22}^{k} \right\rangle \\ \left\langle \sigma_{12}^{k} \right\rangle \end{pmatrix} = \begin{pmatrix} c_{11} & c_{12} & c_{16} \\ c_{12} & c_{22} & c_{26} \\ c_{16} & c_{26} & c_{66} \end{pmatrix} \begin{pmatrix} \left\langle \varepsilon_{11}^{k} \right\rangle \\ \left\langle \varepsilon_{22}^{k} \right\rangle \\ \left\langle 2\varepsilon_{12}^{k} \right\rangle \end{pmatrix}. \tag{2.85}$$

Please notice that the stiffness coefficients in equation (2.85) are similar to those of the corresponding 3D samples under the plane strain condition.

Equation (2.85) holds for the three oscillatory tests described above. Therefore, 9 equations are established, and the 6 unknown stiffness coefficients are obtained by using a classic least-square algorithm. More details on the quasi-static numerical upscaling procedure can be found in Rubino et al. (2016). From the above procedures, we can see that this quasi-static numerical simulation approach allows the simulations on a small representative sample volume. This means that the grid size in the numerical simulations can be very small and hence the numerical dispersion effects at high frequencies can be avoided. Hence, this approach enables the investigation of the frequency-dependent rock elastic properties in a wide frequency range.

2.10.2 Dynamic wave propagation numerical simulation in saturated fractured rocks

To perform the dynamic wave propagation numerical simulations, the approach of Masson et al. (2006) and Caspari et al. (2017) is employed. This approach uses the low frequency approximation of

Biot's dynamic equations of poroelasticity, which can be derived from equations (2.14) and (2.15). Instead of using the solid and relative fluid displacements, the motion equations can also be expressed through the solid and relative fluid displacement velocities, $\tilde{\mathbf{v}}$ and $\tilde{\mathbf{q}}$, as follows:

$$\nabla\cdot\tilde{\boldsymbol{\sigma}} = -i\omega\left(\rho_f\tilde{\mathbf{q}} + \rho\tilde{\mathbf{v}}\right), \tag{2.86}$$

$$\nabla\tilde{p} = i\omega\left(\tilde{\rho}\tilde{\mathbf{q}} + \rho_f\tilde{\mathbf{v}}\right), \tag{2.87}$$

In order to transform equations (2.86) and (2.87) into the time – space domain, the dynamic permeability can be approximated at low frequencies ($\omega << \omega_B$) as follows:

$$\frac{1}{\kappa(\omega)} \approx \frac{1}{\kappa_0}\left(1 - \rho_f\frac{\kappa_0}{\eta}\frac{\alpha_\infty}{\phi}i\omega\right). \tag{2.88}$$

Hence, $\tilde{\rho}$ has the following approximation:

$$\tilde{\rho} \approx \frac{i\eta}{\omega\kappa_0}\left(1 - \rho_f\frac{\kappa_0}{\eta}\frac{\alpha_\infty}{\phi}i\omega\right). \tag{2.89}$$

Substituting equation (2.89) into equation (2.87) yields:

$$\nabla\tilde{p} = -\frac{\eta}{\kappa_0}\tilde{\mathbf{q}} + \frac{\rho_f\alpha_\infty}{\phi}i\omega\tilde{\mathbf{q}} + i\omega\rho_f\tilde{\mathbf{v}}. \tag{2.90}$$

Then equations (2.86) and (2.90) can be transformed into the time - space domain as follows:

$$\nabla\cdot\boldsymbol{\sigma} = \rho_f\frac{\partial\mathbf{q}}{\partial t} + \rho\frac{\partial\mathbf{v}}{\partial t}, \tag{2.91}$$

$$-\nabla p = \rho_f\frac{\alpha_\infty}{\phi}\frac{\partial\mathbf{q}}{\partial t} + \rho_f\frac{\partial\mathbf{v}}{\partial t} + \frac{\eta}{\kappa_0}\mathbf{q}, \tag{2.92}$$

The above two equations are the low frequency approximations of Biot's dynamic equations of poroelasticity. To carry out the numerical simulations, we also need the constitutive equations in time – space domain, which can be obtained from equations (2.18) and (2.19) as follows:

$$\frac{\partial\boldsymbol{\sigma}}{\partial t} = \left[\left(C - 2\mu_d\right)\nabla\cdot\mathbf{v} + \alpha M\nabla\cdot\mathbf{q}\right]\mathbf{I} + \mu_d\left[\nabla\mathbf{v} + \left(\nabla\mathbf{v}^{\mathbf{T}}\right)\right], \tag{2.93}$$

$$\frac{\partial p}{\partial t} = -\alpha M\nabla\cdot\mathbf{v} - M\nabla\cdot\mathbf{q}, \tag{2.94}$$

Using equations (2.91) – (2.94), the wave propagation simulations in the saturated fractured rock can be performed through the finite-difference method. The seismic waveforms before and after transmitting the fractured rock are recorded. Then, the phase velocities of the seismic wave can be picked from the recorded waveforms and the attenuation can be estimated using the spectral ratio method (e.g., Mavko et al., 2009).

Chapter 3

Dispersion, attenuation, and anisotropy due to WIFF in porous rocks with aligned fractures of finite thickness

3.1. Introduction

While numerous theoretical models have been proposed for quantifying seismic dispersion and attenuation due to WIFF as presented in Chapter 1, all of them have simplifying assumptions. For instance, in all the models introduced in Chapter 1, fracture thickness (or fracture volume) is considered infinitesimal. In addition, in some of them fracture density should be low enough to ensure that interactions between neighbouring fractures are negligible (Hudson et al., 1996; Galvin and Gurevich, 2006, 2007). These assumptions might not hold in real reservoirs, which may limit the applicability of the available models. Some of the assumptions can be overcome by generalising the existing models, such as in the case of infinitesimal fracture thickness. However, other assumptions, such as dilute fracture concentration, are difficult to overcome. One way to deal with these limitations is to test them using numerical simulations for a given fracture distribution. Indeed, recently Rubino et al. (2016) proposed a numerical upscaling approach based on Biot's (1941) quasi-static theory of poroelasticity to model seismic dispersion and attenuation of rocks containing arbitrary distributions of fractures. This creates an opportunity to test theoretical models and, in particular, the validity of underlying assumptions.

To expand the applicability of the theoretical models to real fractured reservoirs, two objectives are set in this chapter. First, we extend the existing models for infinitesimal-thickness fractures to the case of fractures having finite thickness. Second, numerical simulations are performed to explore the limits of applicability of the derived models. Two 2D numerical rock samples with aligned fractures are studied, one with sparse fracture distribution and the other with dense fracture distribution. The influence of fracture thickness is investigated by comparing the results given by the original models and the extended ones. By contrasting the predictions of the extended models with numerical simulations, we check the correctness of the former and, in addition, we assess the applicability of the theoretical models in rocks with relatively dense fracture concentration. Furthermore, the full stiffness matrix and hence the anisotropic properties of such rocks are also studied.

The contents of this chapter have been published in Geophysics (Guo et al., 2018b, 2018c).

3.2 Extended unified model for the case with finite fracture thickness

In Chapter 2, we have introduced the unified model for the saturated rocks with aligned fractures of infinitesimal thickness. However, all fractures have finite thickness in reality, especially large joints and fracture corridors, which have a particular significant effect on fluid flow (e.g., Questiaux et al., 2010). Hence, it would be useful to extend the unified model to the general case of finite fracture thickness. In order to do so, we can first obtain the P-wave modulus in the direction perpendicular to the fracture plane. Then, we can extend it to the full stiffness coefficients. For the P-wave modulus in the direction perpendicular to the fracture plane, we can still use the general expression (2.31). However, we need to obtain the new expressions for T and G, as well as the elastic properties in the low- and high-frequency limits.

3.2.1 Extension of T and G for the finite fracture thickness case

For periodic planar fracture distributions, the extension of T and G can be done by comparing equations (2.36) and (2.37) with the low- and high-frequency asymptotes of the analytical solution for the finite fracture thickness case [equation (2.31)]. The low-frequency asymptote of equation (2.31) is as follows:

$$\frac{1}{c^{sat}}=\frac{1}{C_0}\left[1+i\omega\frac{1}{12}\frac{C_1-C_0}{C_1}\frac{\left(\frac{f_b}{\kappa_b}+\frac{f_c}{\kappa_c}\right)\eta H^2}{\frac{M_bL_b}{C_bf_b}+\frac{M_cL_c}{C_cf_c}}\right]. \tag{3.1}$$

Comparing equation (2.36) with equation (3.1), we can obtain the expression for T for the finite fracture thickness case,

$$T=\frac{1}{12}\frac{C_1-C_0}{C_1}\frac{\left(\frac{f_b}{\kappa_b}+\frac{f_c}{\kappa_c}\right)\eta H^2}{\frac{M_bL_b}{C_bf_b}+\frac{M_cL_c}{C_cf_c}}. \tag{3.2}$$

On the other hand, the high-frequency asymptote of equation (2.31) has the following form:

$$\frac{1}{c^{sat}}=\frac{1}{C_1}\left[1+\frac{1}{\sqrt{-i\omega}}\frac{2C_1\left(\frac{\alpha_bM_b}{C_b}-\frac{\alpha_cM_c}{C_c}\right)^2}{H\left(\sqrt{\frac{M_bL_b\eta}{C_b\kappa_b}}+\sqrt{\frac{M_cL_c\eta}{C_c\kappa_c}}\right)}\right], \tag{3.3}$$

thus, giving the expression for G for the finite fracture thickness case as follows:

$$G=\frac{2SC_1\left(\frac{\alpha_bM_b}{C_b}-\frac{\alpha_cM_c}{C_c}\right)^2}{\left(\sqrt{\frac{M_bL_b\eta}{C_b\kappa_b}}+\sqrt{\frac{M_cL_c\eta}{C_c\kappa_c}}\right)}, \tag{3.4}$$

where $S = 1/H$ is the specific fracture surface area per unit volume for the planar fractures.

If planar fractures are distributed randomly, we can obtain the corresponding expressions for T and G by comparing to the periodic planar fracture distribution case. As the seismic dispersion and attenuation at high frequencies are independent of the fracture distribution, the parameter G for the random planar fracture distribution case is the same with that for the periodic case [equation (3.4)]. At low frequencies, due to the large fluid diffusion length, seismic dispersion and attenuation will be affected by the fracture distribution, thus making the parameter T for random distribution different from

that for the periodic case. As the effective fracture spacing tends to infinity for random distribution of planar fractures, the parameter T will tend to infinity, which corresponds to the zero value for ζ (Gurevich and Lopatnikov, 1995; Müller and Rothert, 2006; Gurevich et al., 2009).

For penny-shaped cracks with finite thickness, due to the fact that at high frequencies energy dissipation only occurs in the immediate vicinity of the fracture surfaces, it is reasonable to assume that the expression for the parameter G has the same form with that for the planar fracture case, as shown in equation (3.4). However, the specific fracture surface area per unit volume S equals to $\pi\varepsilon/a$ for penny-shaped cracks. Furthermore, Furthermore, it can be noted that the properties of the fracture infill material are directly involved in equation (3.4). Accounting for different geometries between penny-shaped cracks and planar fractures, and considering that the energy dissipation amount is dominated by the compliance contrast between the background and fractures, an equivalent fracture infill material needs to be used in equation (3.4) for the penny-shaped crack case with finite thickness. This equivalent infill material has the same porosity and permeability with the original infill material of penny-shaped cracks, but has different elastic properties as follows (Brajanovski et al., 2005):

$$L_{ce} = \frac{f_c}{Z_N}, \tag{3.5}$$

$$\mu_{ce} = \frac{f_c}{Z_T}, \tag{3.6}$$

where Z_N and Z_T are the normal and tangential excess compliances of the dry fractures, respectively; μ_c is the effective shear modulus of the dry fracture infill material. L_{ce} and μ_{ce} can then be used to calculate the Biot's coefficient and modulus α_{ce} and M_{ce}, and also the saturated P-wave modulus C_{ce} for the equivalent fracture infill material. The values of G for the penny-shaped cracks with finite thickness can then be calculated as follows:

$$G = \frac{2S_2C_1\left(\frac{\alpha_b M_b}{C_b} - \frac{\alpha_{ce} M_{ce}}{C_{ce}}\right)^2}{\sqrt{\frac{M_b L_b \eta}{C_b \kappa_b}} + \sqrt{\frac{M_{ce} L_{ce} \eta}{C_{ce} \kappa_{ce}}}}. \tag{3.7}$$

At low frequencies, Galvin and Gurevich (2009) show that the attenuation of saturated rocks with a sparse distribution of aligned penny-shaped cracks is not sensitive to the crack thickness. Even the differences between the attenuation for saturated rocks with aligned penny-shaped cracks of infinitesimal thickness and that for the rocks with spheres of the same radius are very small at low frequencies. Since the attenuation at low frequencies is determined by the parameter T as shown in equation (2.36), the crack thickness should have little effect on this parameter. Hence, we can use the same expression of T for the penny-shaped cracks with finite thickness as that for infinitesimal thickness [equation (2.43) or (2.45)].

Thus, we have extended the expressions of T and G to the case with finite fracture thickness for both rocks with planar fractures (periodically or randomly distributed) and penny-shaped cracks. It can be noted that, when the fracture thickness tends to infinitesimal, these extended expressions will reduce to those for the infinitesimal thickness case, which supports the goodness of our extension.

3.2.2 Elastic properties in the low- and high- frequency limits

Apart from the extension of the expressions for T and G, the elastic properties in the low- and high-frequency limits for the finite fracture thickness case are also needed. In the low-frequency limit, similarly to the infinitesimal thickness case (Section 2.6.3), we can first use the linear-slip theory [equation (2.1)] to calculate the elastic properties of the dry fractured rock with the fracture compliances computed by Eshelby model [equation (2.2)]. Then, the effect of fluid saturation on elastic properties of the fractured and porous rock can be modelled using anisotropic Gassmann equation [equation (2.10)] due to the uniform fluid pressure distribution throughout the fractures and background pores. It should be noted that, in the calculated dry fracture compliance matrix, besides the normal and tangential compliances, the other components also have small values due to the effects of finite fracture thickness. Furthermore, the total porosity used in the anisotropic Gassmann equation should include both the porosity of the background medium and that of the fractures in the finite fracture thickness case.

In the high-frequency limit, as in the infinitesimal thickness case, we can treated the saturated fractured rock as the saturated background permeated by the hydraulically isolated saturated fractures.

This is due to the fact that the fluid in the fractures does not have time to communicate with that in the background medium and hence the fractures are hydraulically isolated from the saturated background medium. Therefore, we can first obtain the elastic properties of the saturated background medium using the isotropic Gassmann equations (2.6) and (2.7). Then, we can calculate the compliance matrix of the saturated background medium permeated by the dry fractures $\mathbf{S}_{hf}^{1}$ using the linear slip theory:

$$\mathbf{S}_{hf}^{1} = \mathbf{S}_{b}^{sat} + \mathbf{Z}_{0}\,. \tag{3.8}$$

Finally, the stiffness coefficients of the saturated fractured rock $c_{ij,hf}^{sat}$ can be obtained by saturating the dry fractures with fluid using the anisotropic Gassmann equation (Gurevich, 2003):

$$c_{ij,hf}^{sat} = c_{ij,hf}^{1} + \alpha_{i}^{1}\alpha_{j}^{1}M_{2}\,, \quad i,j = 1,\ldots 6 \tag{3.9}$$

where $c_{ij,hf}^{1}$ is obtained by taking the inverse of $\mathbf{S}_{hf}^{1}$, α^{1} is the corresponding Biot's coefficient, which has non-zero values for i=1,2,3 and can be expressed as follows:

$$\alpha_{i}^{1} = 1 - \frac{\sum_{j=1}^{3} c_{ij,hf}^{1}}{3K_{b}^{sat}}, \tag{3.10}$$

M_2 is the corresponding Biot's modulus, which can be written as follows:

$$M_{2} = \frac{K_{b}^{sat}}{\left(1 - K_{1}^{*}/K_{b}^{sat}\right) - \phi_{c}\left(1 - K_{b}^{sat}/K_{f}\right)}, \tag{3.11}$$

where K_{1}^{*} is the generalized bulk modulus, which can be calculated from equation (2.13) by replacing c_{ij}^{d} with $c_{ij,hf}^{1}$; ϕ_c is the fracture porosity.

3.2.3 Full stiffness coefficients

With the extended expressions of T and G and the corresponding elastic properties in the low- and high- frequency limits, we can compute the frequency-dependent P-wave modulus in the direction perpendicular to the fracture plane for the finite fracture thickness. In order to study the anisotropic

properties of the fractured rock, we need to extend the results to the full stiffness coefficients. Besides using the interpolation method proposed by Galvin and Gurevich (2015) which assumes the same relaxation function for all stiffness coefficients (Section 2.6.2), we also propose another method to calculate the full stiffness coefficients. In this method, we express the full stiffness matrix using a complex-valued and frequency-dependent fracture compliance matrix. This can be done by first obtaining the fracture compliance matrix for the saturated fractured rock in the low- and high- frequency limits and then interpolating between these two ends using the relaxation function.

3.2.3.1 High-frequency limit

In the high-frequency limit, there is no sufficient time during a half wave cycle for fluid exchange between fractures and background. Hence, the saturated fractured rocks can be treated as the saturated background medium permeated by the hydraulically isolated saturated fractures. The compliance matrix of saturated fractured rocks in the high-frequency limit $\mathbf{S}_{hf}^{sat}$ can therefore be computed using the linear slip theory (Schoenberg and Douma, 1988; Schoenberg and Sayers, 1995; Gurevich, 2003):

$$\mathbf{S}_{hf}^{sat} = \mathbf{S}_{b}^{sat} + \mathbf{Z}_{hf}^{sat}, \tag{3.12}$$

where $\mathbf{S}_{b}^{sat}$ is the compliance matrix of the isotropic saturated background medium and $\mathbf{Z}_{hf}^{sat}$ is that of the hydraulically isolated fractures. Assuming that the fracture plane is normal to the *y*-axis, the fracture compliance matrix can be written as follows:

$$\mathbf{Z}_{hf}^{sat} = \begin{pmatrix} 0 & 0 & 0 & 0 & 0 & 0 \\ 0 & Z_{N,hf}^{sat} & 0 & 0 & 0 & 0 \\ 0 & 0 & 0 & 0 & 0 & 0 \\ 0 & 0 & 0 & Z_T & 0 & 0 \\ 0 & 0 & 0 & 0 & 0 & 0 \\ 0 & 0 & 0 & 0 & 0 & Z_T \end{pmatrix}, \tag{3.13}$$

where $Z_{N,hf}^{sat}$ and Z_T are the normal and tangential compliances of the hydraulically isolated fractures, respectively. It should be noted here that, due to the effect of finite fracture thickness, other components

besides the normal and tangential fracture compliances in $\mathbf{Z}_{hf}^{sat}$ can be different than zero; however, these values are expected to be rather small (Sevostianov and Kachanov, 1999).

The fracture compliance matrix can be computed taking into account that Z_T has the same value as the tangential compliance of the considered fractures in the dry case, whereas $Z_{N,hf}^{sat}$ can be obtained as follows. First, we calculate the values of the stiffness coefficients of the saturated fractured rock in the high-frequency limit using the linear slip theory and Gassmann's equation, as shown in Section 3.2.2. Then, by comparing the resulting stiffness coefficient $c_{22,hf}^{sat}$ with the corresponding value computed by taking the inverse of the matrix $\mathbf{S}_{hf}^{sat}$, we obtain:

$$Z_{N,hf}^{sat} = \frac{C_b - c_{22,hf}^{sat}}{c_{22,hf}^{sat} C_b}, \tag{3.14}$$

where C_b is the P-wave modulus for the saturated background medium.

3.2.3.2 Low-frequency limit

In the low-frequency limit, we can also express the compliance matrix of the saturated fractured rocks $\mathbf{S}_{lf}^{sat}$ as follows (Thomsen, 1995; Cardona, 2002):

$$\mathbf{S}_{lf}^{sat} = \mathbf{S}_{b}^{sat} + \mathbf{Z}_{lf}^{sat}, \tag{3.15}$$

where $\mathbf{Z}_{lf}^{sat}$ is the compliance matrix of the saturated fractures. We assume that the structure of this matrix is similar to that given by equation (3.13), that is,

$$\mathbf{Z}_{lf}^{sat} = \begin{pmatrix} 0 & 0 & 0 & 0 & 0 & 0 \\ 0 & Z_{N,lf}^{sat} & 0 & 0 & 0 & 0 \\ 0 & 0 & 0 & 0 & 0 & 0 \\ 0 & 0 & 0 & Z_T & 0 & 0 \\ 0 & 0 & 0 & 0 & 0 & 0 \\ 0 & 0 & 0 & 0 & 0 & Z_T \end{pmatrix}, \tag{3.16}$$

with $Z_{N,lf}^{sat}$ and Z_T being the normal and tangential compliances of the saturated fractures in the low-frequency limit. It is important to notice here that for very low frequencies, a significant amount of fluid has enough time during the compression cycle of the seismic wave to flow from the fractures into the background, and vice versa during the extension cycle. This implies that in addition to the effect of finite fracture thickness, the wave-induced fluid pressure diffusion can also cause that some of the components considered to be zero in equation (3.16) become non-negligible, especially the component $Z_{12,lf}^{sat}$ (Cardona, 2002; Gurevich, 2003). While these non-zero components are still small compared to the normal and tangential fracture compliances, they are larger than the corresponding values in the high-frequency limit. Hence, ignoring them may induce some errors, which we will analyse in the following sections.

For computing the components of the compliance matrix of the saturated fractures, we take into account, as before, that Z_T has the same value as the tangential compliance of the dry fractures. In addition, following similar steps as for the high-frequency limit case, $Z_{N,lf}^{sat}$ can be obtained from the stiffness coefficients of the saturated fractured rocks in the low-frequency limit:

$$Z_{N,lf}^{sat} = \frac{C_b - c_{22,lf}^{sat}}{c_{22,lf}^{sat} C_b}, \tag{3.17}$$

where $c_{22,lf}^{sat}$ is the P-wave modulus in the direction perpendicular to the fracture plane in the low-frequency limit, which can be calculated using linear slip theory and Gassmann's equation, as shown in Section 3.2.2.

3.2.3.2 Frequency-dependence of the stiffness coefficients

From equations (3.12) and (3.15), it can be seen that the elastic properties of saturated fractured rocks in the low- and high-frequency limits can be expressed using a similar mathematical expression. At intermediate frequencies, the normal fracture compliance becomes frequency-dependent due to WIFF. Hence, we propose to express the compliance matrix of saturated fractured rocks as a function of frequency as follows:

$$\mathbf{S}^{sat}\left(\omega\right)=\mathbf{S}_{b}^{sat}+\mathbf{Z}^{sat}\left(\omega\right), \tag{3.18}$$

where $\mathbf{Z}^{sat}(\omega)$ is the frequency-dependent compliance matrix of the considered saturated fractures, which has the following form:

$$\mathbf{Z}^{sat}\left(\omega\right)=\begin{pmatrix}0 & 0 & 0 & 0 & 0 & 0\\ 0 & Z_{N}^{sat}\left(\omega\right) & 0 & 0 & 0 & 0\\ 0 & 0 & 0 & 0 & 0 & 0\\ 0 & 0 & 0 & Z_{T} & 0 & 0\\ 0 & 0 & 0 & 0 & 0 & 0\\ 0 & 0 & 0 & 0 & 0 & Z_{T}\end{pmatrix}. \tag{3.19}$$

In equation (3.19), $Z_{N}^{sat}\left(\omega\right)$ is a complex-valued frequency-dependent normal fracture compliance of the saturated fractures that takes into account the WIFF effects, while Z_T is the tangential compliance of the fractures. The latter is frequency-independent and equal to the tangential compliance of the dry fractures, as it is not affected by WIFF. The frequency-dependent stiffness matrix $\mathbf{C}^{sat}$ can thus be obtained by taking the inverse of $\mathbf{S}^{sat}$.

To obtain the expression for $Z_{N}^{sat}\left(\omega\right)$, we can compare the P-wave modulus in the direction perpendicular to the fracture plane in $\mathbf{C}^{sat}$ with the corresponding value given by the method of Galvin and Gurevich (2015), which yields:

$$Z_{N}^{sat}\left(\omega\right)=Z_{N,hf}^{sat}+\left(Z_{N,lf}^{sat}-Z_{N,hf}^{sat}\right)f\left(\omega\right). \tag{3.20}$$

Hence, the dynamic nature of the stiffness coefficients of saturated fractured rocks is a result of the variation of the fracture normal compliance with frequency, which is controlled by the relaxation function $f(\omega)$ [equation (2.48)]. In this context, it is important to mention that a similar expression for the complex-valued and frequency-dependent fracture normal compliance was obtained by Rubino et al. (2015) for a porous medium permeated by regularly-distributed planar fractures.

Using the full stiffness coefficients, the wave velocities and attenuation at any incidence angles as well as the anisotropic parameters for the velocities and attenuation can be calculated, as shown in Section 2.7.

3.3 Numerical example

3.3.1 Parameters of the investigated sample

We first study one synthetic 2D rock sample with low fracture density, as shown in Figure 3-1a. Both the theoretical predictions and numerical simulations will be performed. The numerical simulations are based on the Biot's quasi-static equation of poroelasticity, for which the methodology is introduced in Section 2.10.1. The sample is a square rock of 16 cm sidelength and contains 4 parallel regularly distributed fractures, that is, the fracture density considered in this case is around 0.06. The coordinate system is chosen such that the fractures are parallel to the *x*-axis and perpendicular to the *y*-axis (Figure 3-1). The length of the sample along the *z*-axis is long enough to make sure that the normal and shear strains along this direction are negligible compared to those along *x*- and *y*- axis. Thus, the plane strain condition is satisfied which simplifies the 3D problem into a 2D problem.

The properties of the background medium are as follows (Rubino et al., 2015): grain bulk modulus K_{gb} = 37 GPa, dry background bulk modulus K_b = 26 GPa, shear modulus μ_b = 31 GPa, porosity ϕ_{bg} = 0.1, and permeability $\kappa_b = 10^{-4}$ mD (10^{-19} m^2). Both the fractures and the embedding background are fully saturated with water, with bulk modulus K_f and viscosity η of 2.25 GPa and 0.001 Pa.s, respectively. The fractures have elliptical shapes in the *x*-*y* plane, and are represented with a highly porous and permeable material, with a major axis (length) d_c of ~4cm and a minor axis (aperture) h_c of 0.06 cm. The bulk and shear moduli of the dry porous fracture infill material, K_c and μ_c, are 0.04 GPa and 0.02 GPa, respectively, which are obtained from a drained normal compliance η_N of 10^{-11} m/Pa and a shear compliance η_T of 3×10^{-11} m/Pa for a compliant fracture in a "typical" sandstone (Nakagawa and Schoenberg, 2007). The permeability κ_c of this highly porous infill material is taken to be 100 D (10^{-10} m^2) and its porosity ϕ_{cg} is 0.8. It should be noted that the permeability given here is much lower than that given by the cubic law for the considered fracture parameters (Witherspoon et al., 1980), which is

consistent with the fact that fractures are not entirely empty and their walls are not smooth. We assume that the physical properties of the solid grains composing the fracture infill material are similar to those of the background, thus having the same bulk modulus of 37 GPa.

It should be noted here that, when performing the numerical simulations, the fractures are fully characterized by the physical properties of the infill material described above. However, due to the differences between the geometries of the planar and elliptical fractures, an effective fracture infill material has to be considered when using the theoretical predictions for comparisons with the numerical simulations. To do this, first we compute the normal and tangential excess compliances of the dry fractures, Z_N and Z_T, using equation (2.2) with the Eshelby tensor for an elliptical cylinder (infinite height along *z*-axis) (shown in Appendix A). Then, the effective elastic properties of the fracture infill material to be used in the theoretical approach can be calculated using equations (3.5) and (3.6). The use of these effective properties allow the comparison between the theoretical and numerical results.

It is important to notice here that, as the dry fracture compliances are related to the elastic properties of both the background medium and the material infilling the fractures [equation (2.2)], the effective elastic properties of the fracture infill material in the theoretical model defined by equations (3.5) and (3.6) will depend on both the properties of the background and of the fracture infill material.

Furthermore, the specific surface area S of the 2D fractures is also needed in the theoretical predictions, which can be obtained according to its definition as follows:

$$S = \frac{4 f_c}{\pi h_c}. \tag{3.21}$$

Using this value of S, the effective distance between the fractures H can also be calculated according to the expression of the specific surface area for the planar fractures ($S = 1/H$). In addition, the fracture density for the 2D sample is defined as follows (e.g., Kachanov and Sevostianov, 2005):

$$\varepsilon = \frac{n a^2}{A}, \tag{3.22}$$

where *n* is the total fracture number of the 2D sample, *a* is the major radius of the elliptical 2D fractures, and *A* is the area of the sample.

Thus, using these properties of the 2D fractures (effective elastic properties, specific surface area, and fracture density), combined with the other known parameters of the sample stated above, the frequency-dependent elastic properties of the 2D samples can be calculated through the unified theoretical model for the three considered fracture geometries (periodic planar fractures, randomly spaced fractures, and penny-shaped cracks).

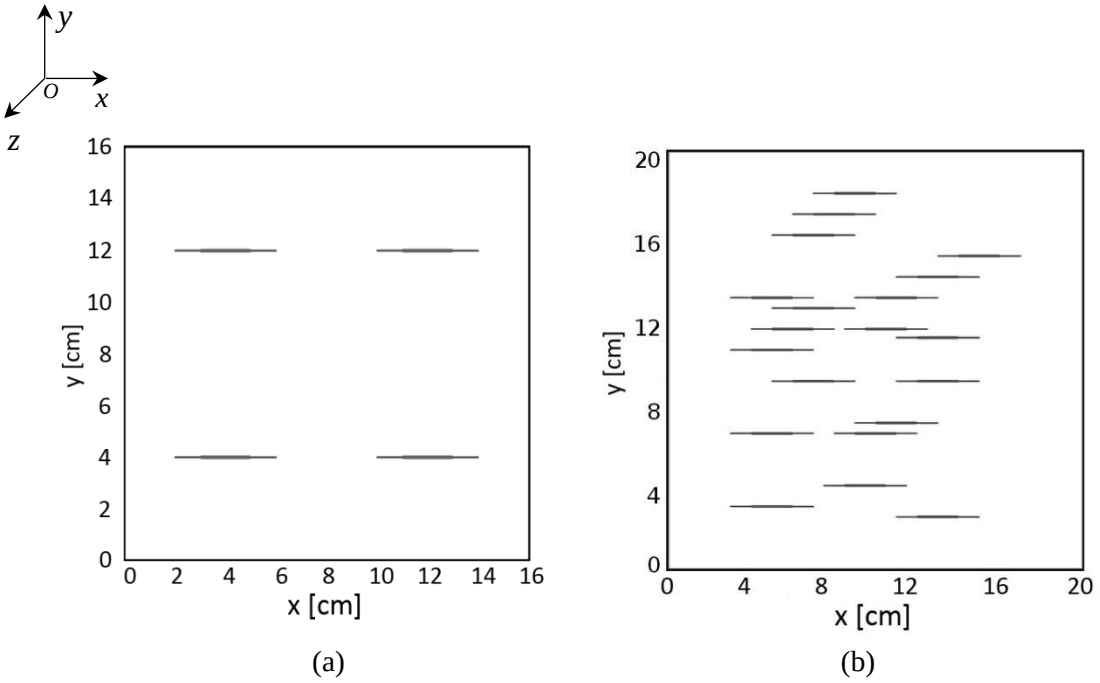

Figure 3-1. 2D synthetic rock samples investigated. a) Sample with 4 parallel fractures. b) One realization of samples with 20 parallel fractures randomly distributed.

3.3.2 Results and comparison

3.3.2.1 Numerical simulations

Using the numerical upscaling procedure described in Section 2.10.1 and the parameters of the sample, we compute the frequency-dependent stiffness coefficients. Here, we define the variation of the real part as the dispersion of the stiffness cofficients and the absolute value of the ratio of imaginary part to the corresponding real part as the attenuation of the stiffness coefficients. The numerical

simulation results show that the coefficients C_{16} and C_{26} are negligibly small compared to the other four coefficients C_{11}, C_{12}, C_{22}, and C_{66}. Thus, we only analyze these four coefficients (C_{11}, C_{12}, C_{22}, and C_{66}), as shown in Figure 3-2. Since the considered fractures are normal to the *y*-axis, the dispersion and attenuation for C_{22} are much larger than for the other three coefficients. The values of the other three coefficients keep nearly constant with the frequencies. Their corresponding attenuation is also negligible, especially for C_{11}. Furthermore, it can be clearly seen from C_{22} that the stiffness coefficients reach the low- and high- frequency limits at around 10^{-4} Hz and 10 Hz, respectively. The low frequency limit means the fluid pressure is uniform throughout the sample, whereas the high frequency limit indicates that no fluid flow occurs at such frequencies and the fractures are hydraulically isolated from the background medium. It should be noted that, as the characteristic frequency for the fluid flow between the fractures and the background medium is proportional to the background permeability (Gurevich et al., 2009; Guo et al., 2016), the high frequencies here are actually small compared to the seismic frequency band due to the low background permeability of the sample (10^{-4} mD).

Comparing the shape and characteristic frequency of the attenuation for the four stiffness coefficients, it can be found that they are similar to each other. This is due to the fact that the induced fluid flow between the fractures and the background is normal to the fractures due to its low velocity and, hence, all the frequency-dependent stiffness coefficients are controlled by the same relaxation function (Krzikalla and Müller, 2011; Galvin and Gurevich, 2015; Kong et al., 2016). For this reason and the fact that the dispersion and attenuation of C_{22} are much higher than that for the other three coefficients, we first focus on explorying the characteristics of the coefficient C_{22}, obtained from both theoretical predictions and numerical simulations. The full stiffness matrix and the anisotropic properties of fractured rocks will then be considered.

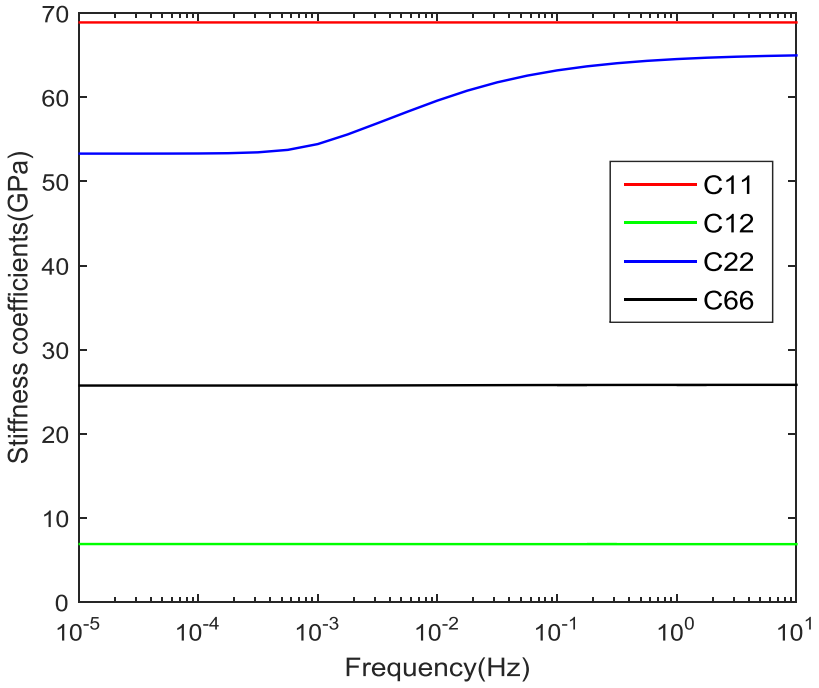

(a)

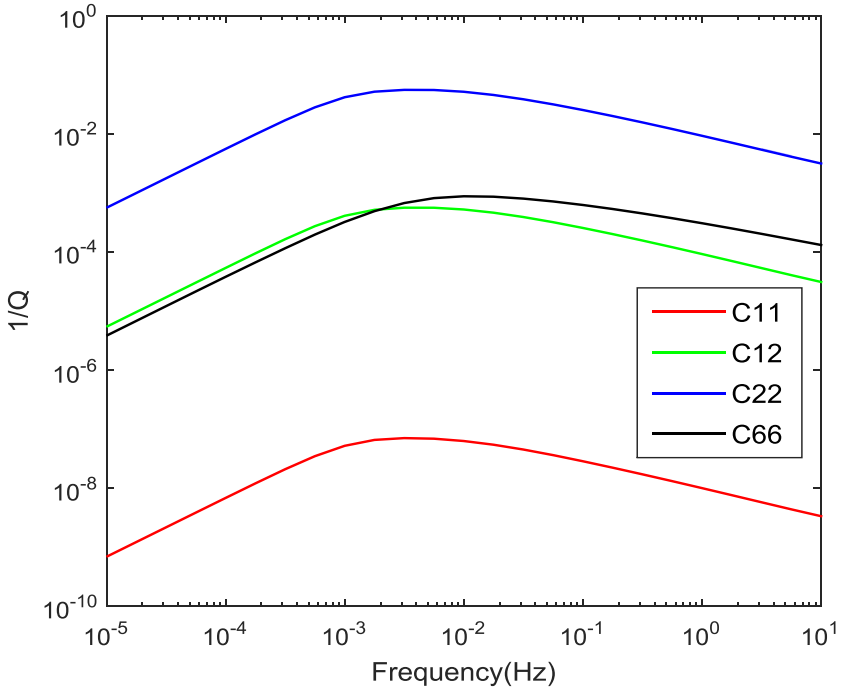

(b)

Figure 3-2. (a) Dispersion and (b) attenuation of the stiffness coefficients given by the numerical simulations for the sample with 4 parallel fractures.

3.3.2.2 Effects of finite fracture thickness

In order to analyse the effects of the finite thickness of fractures, we compare the results obtained using the original unified model (Section 2.6, considering fracture thickness as infinitesimal) and the extended unified model (Section 3.2, considering finite fracture thickness effect), as shown in Figure 3-3. To validate the accuracy of the extended unified model, we also show the results given by the analytical solution for rocks with periodically-spaced planar fractures of finite thickness [equation (2.31)]. It can be seen that they are almost the same with the corresponding results calculated by the extended unified model proposed in this paper. For the other two types of fractures (randomly-spaced planar fractures and penny-shaped cracks), while we do not have the corresponding analytical solutions, the accuracy of the extended unified model can be verified through its relations with the periodic planar fracture case and also by comparison with the numerical simulations in the following section.

For the dispersion of C_{22}, Figure 3-3a indicates that at low frequencies the response is not highly sensitive to the finite thickness of the fractures. More in detail, we observe that the infinitesimal fracture thickness model provides slightly higher values of C_{22} compared to those for finite thickness. However, the discrepancies are rather negligible. This is due to the fact that fracture porosity is small (only 0.0037) and, thus, its contribution to the rock overall porosity is negligible. This, in turn, implies that when using the anisotropic Gassmann's equation to saturate the dry rocks in the low-frequency limit, ignoring this small fracture porosity merely increases the resulting modulus slightly. However, at high frequencies the situation is drastically different. The influence of this small fracture porosity (or finite fracture thickness) becomes significant, and the values of C_{22} for the infinitesimal fracture thickness models get higher than those corresponding to finite thickness fracture models. The reason is that even a small fracture porosity will result in a non-zero fracture normal compliance in the high-frequency limit, which can significantly decrease the value of C_{22}. Hence, the effects of the small fracture porosity (or the finite fracture thickness) cannot be ignored at high frequencies. In this context, it is important to notice that in the case of low-permeability backgrounds, for frequencies within the seismic band there is no time for fluid pressure exchange between this region and the fractures. This implies that the seismic properties are given by the corresponding high-frequency limits, which, according to our results, can

be significantly affected by the finite thickness of the fractures. The incapability of the existing models for dealing with these situations may therefore have important implications in the seismic characterization of low-permeability reservoirs containing fractures.

A comparison of the attenuation of C_{22} given by the theoretical models with and without considering the finite fracture thickness effects is shown in Figure 3-3b. We observe that the influence of the finite fracture thickness on attenuation at low frequencies is small for all the fracture types considered, which is consistent with the observations of Galvin and Gurevich (2009). However, at high frequencies, the attenuation for finite thickness fractures is lower than that for infinitely thin fractures, which is consistent with the lower dispersion of C_{22} at high frequencies observed for fractures of finite thickness (Figure 3-3a). It is important to note that the attenuation for the three types of fractures merge together at high frequencies (Figure 3-3b). This is due to the fact that the energy dissipation at high frequencies only occurs in the immediate vicinity of the fracture surfaces. For the three types of fractures considered in the extended unified model, we use the same specific fracture surface area obtained from the real fracture geometry of the sample [equation (3.21)]. Hence, the attenuation for the three types of fractures becomes the same at high frequencies. In summary, the finite fracture thickness has small influence on the dispersion and attenuation of the stiffness coefficients of fractured rocks at low frequencies. However, this effect becomes significant at high frequencies.

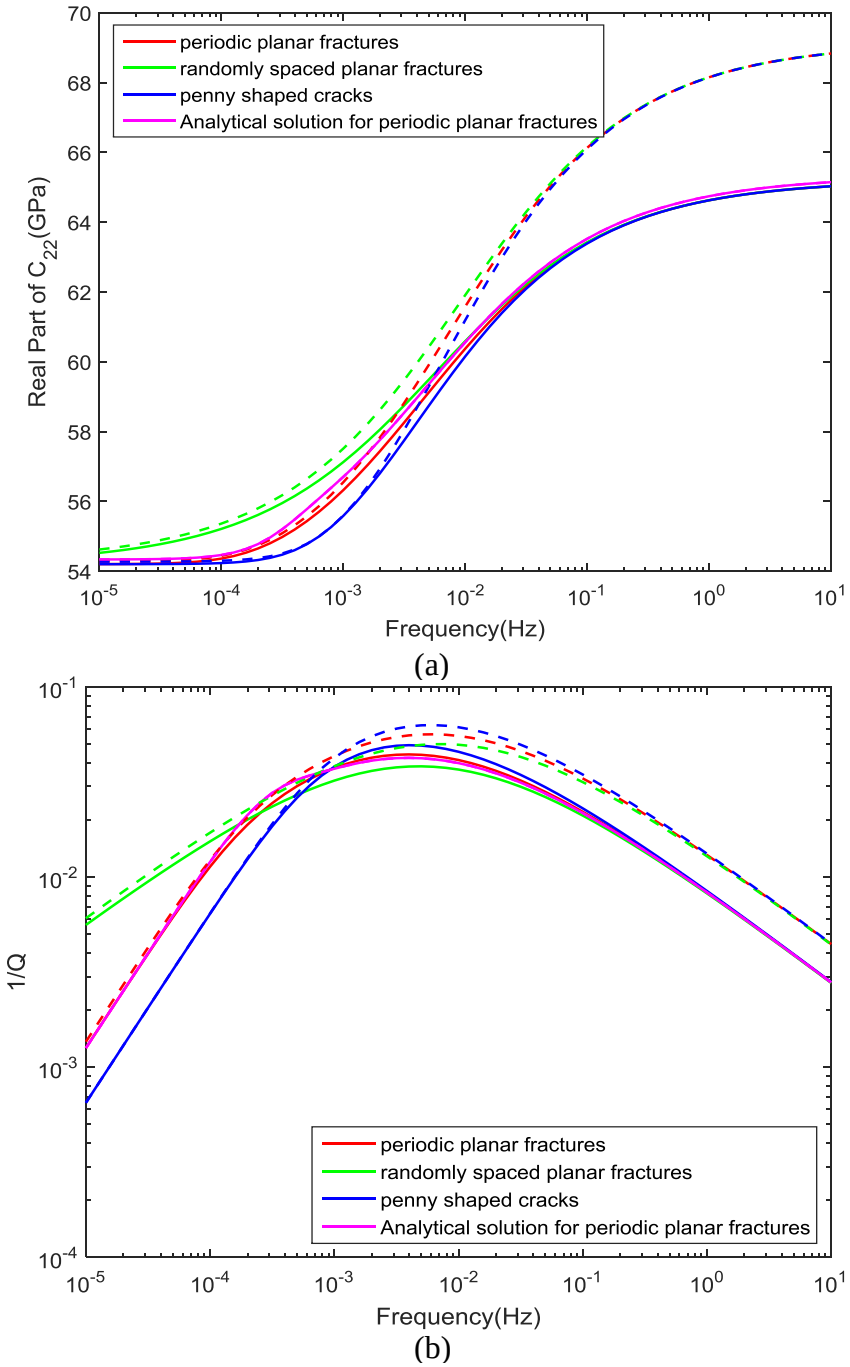

Figure 3-3. (a) Dispersion and (b) attenuation of C_{22} calculated using the unified model for the sample with 4 parallel fractures. Note that the solid lines are the results provided by the extended unified model (for fractures with finite thickness), while the dashed lines indicate the ones corresponding to the original unified model (for fractures with infinitesimal thickness). To validate the accuracy of the extended unified model, the results given by the analytical solution for the periodic planar fracture case with finite thickness [equation (2.31)] are also shown (pink solid line).

3.3.2.3 Theoretical predictions versus numerical simulations

To compare the theoretical predictions of the extended model and the results of the numerical simulations, we consider two cases which have low and relatively high fracture densities, respectively (Figure 3-1). For the low fracture density case, we use the sample with 4 regularly-distributed parallel fractures, which has a fracture density of 0.06. The properties of this sample are presented above. For the high fracture density case, we consider a set of samples, which have dimensions of 20 cm × 20 cm and contain 20 parallel fractures randomly distributed. Each sample corresponds to one realization of a random fracture distribution of interest (Figure 3-1b). By considering 20 realizations of the random fracture distributions in the numerical simulations, the standard deviations of the P-wave moduli C_{22} as functions of the number of realizations become nearly constant both at the low and high frequencies. Hence, we can take the mean value of the P-wave moduli C_{22} of these 20 samples to represent the results of numerical simulations for the random fracture distribution case with relatively high fracture density (0.20). The other properties of these samples remain the same as for the sample with 4 parallel fractures. This case allows us to study the influence of fracture interactions on the seismic signatures as well as the applicability of the extended model under the high fracture density condition.

The results of the numerical simulations and the theoretical predictions are shown in Figure 3-4. It is found that the theoretical predictions given by the penny-shaped crack model match the numerical simulation results best for both cases. This is expected since the shape of the 2D cracks is closer to that of penny-shaped cracks. At high frequencies, good agreement can be found between the theoretical predictions of the penny-shaped crack model and the numerical simulations, even for the case with 20 fractures. However, we can find some small discrepancies at low frequencies, which are probably due to fracture interactions. This is supported by the normal stress distributions computed in the low- and high-frequency limits (~10^{-4} Hz and ~10 Hz, respectively) in response to the vertical numerical relaxation test, as shown in Figure 3-5 for the sample with 4 fractures. In the low-frequency limit, we can observe some overlap between the stress shielding zones (blue) of adjacent fractures, indicating the interactions between the fractures. However, in the high-frequency limit, due to the diminished stiffness

contrast between background and fractures, the overlap between the stress shielding zones tends to vanish, and therefore, there is nearly no interactions between the fractures. This result conforms with the findings of Milani et al. (2016). Thus, we can see the good agreement between the theoretical predictions and the numerical simulations at high frequencies, but some small discrepancies are observed at low frequencies.

It can be noticed that, even for the case with relatively high fracture density (0.20), the discrepancies between the theoretical predictions and the numerical simulations are small. Indeed, Grechka and Kachanov (2006) carried out a number of numerical simulations for rocks with dense fracture densities and compared the results with the non-interactive theoretical approach to study the effects of fracture interactions. They found that, in rocks with random distributions of fractures, the influence of fracture interactions is rather small due to the cancellation of the competing effects of stress shielding and amplification. This implies that the non-interactive approach is still valid even for rocks with relatively high fracture densities. For the case with relatively high fracture density (0.20) investigated in this paper, due to the random distribution of the fractures, the stress shielding and amplification effects can be effectively cancelled out, which results in the overall good agreement between the theoretical predictions of the non-interactive penny-shaped crack model and the numerical simulation results.

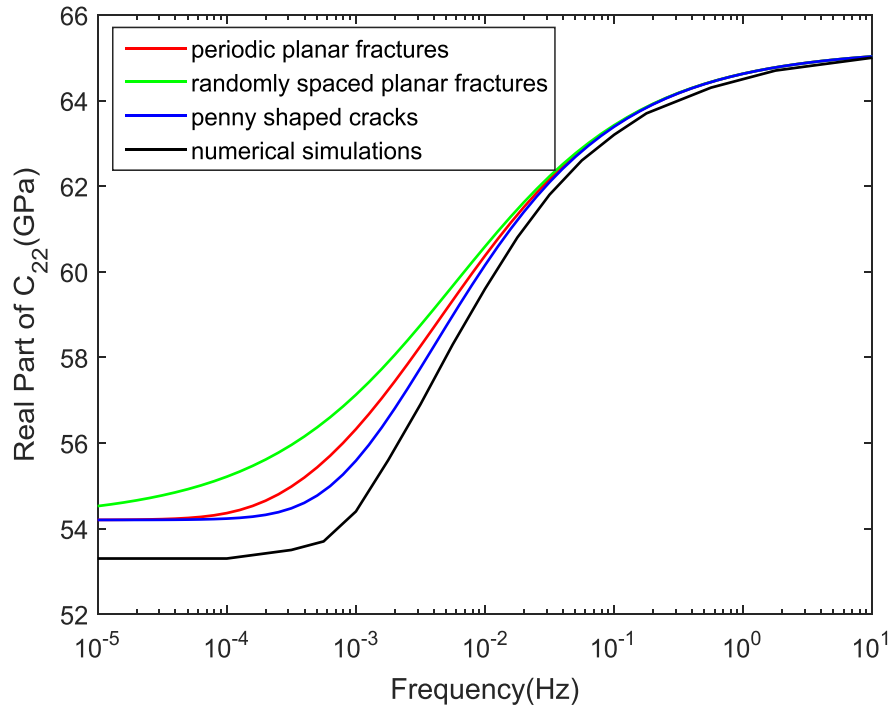
periodic planar fractures
randomly spaced planar fractures
penny shaped cracks
numerical simulations
Real Part of C_{22}(GPa)
Frequency(Hz)

(a)

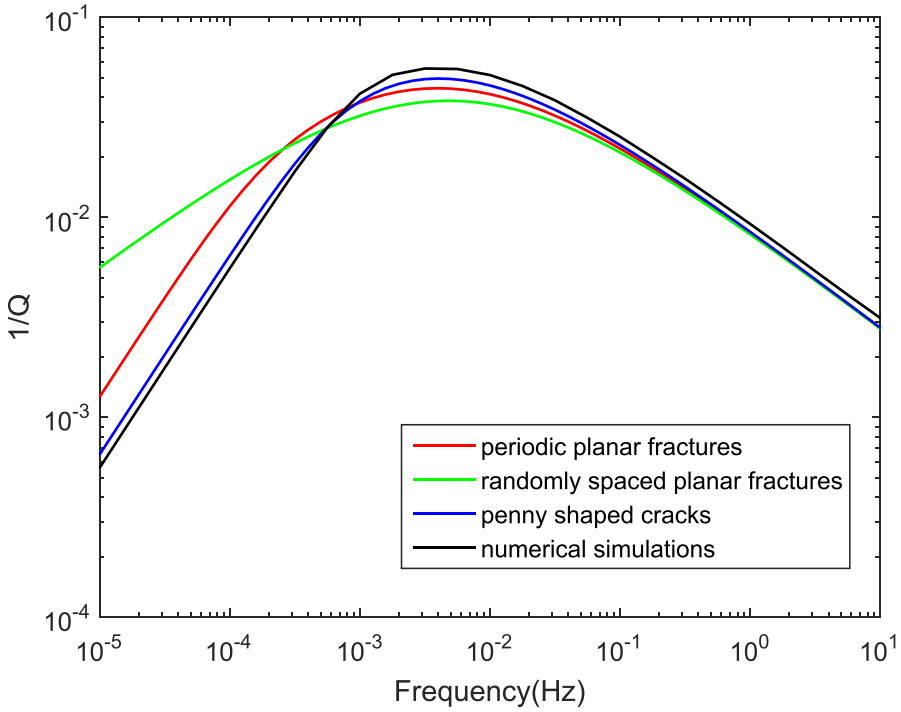
periodic planar fractures
randomly spaced planar fractures
penny shaped cracks
numerical simulations
1/Q
Frequency(Hz)

(b)

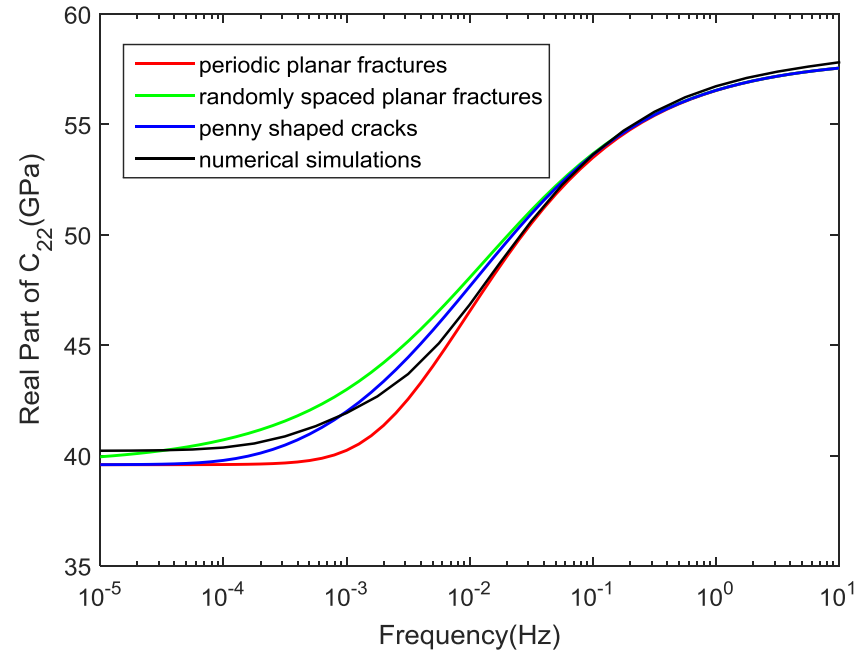

(c)

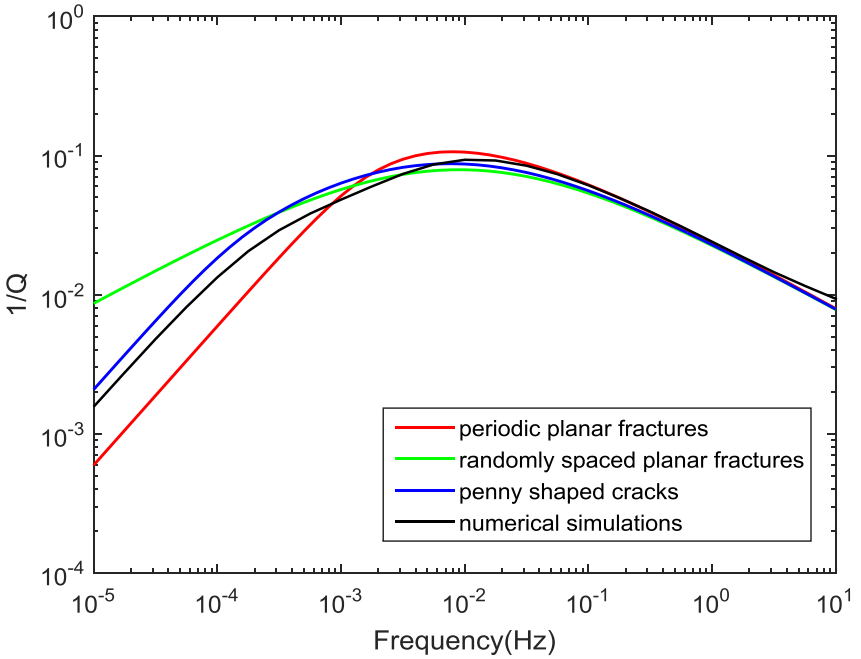

(d)

Figure 3-4. Numerical simulation results of dispersion and attenuation of C_{22} and those predicted by the extended unified model. a) and b) show the dispersion and attenuation, respectively, for the case with low fracture density (the sample with 4 parallel fractures), whereas c) and d) include the corresponding results for the case with high fracture density (mean value of 20 realizations of the samples with 20 parallel fractures which are randomly distributed).

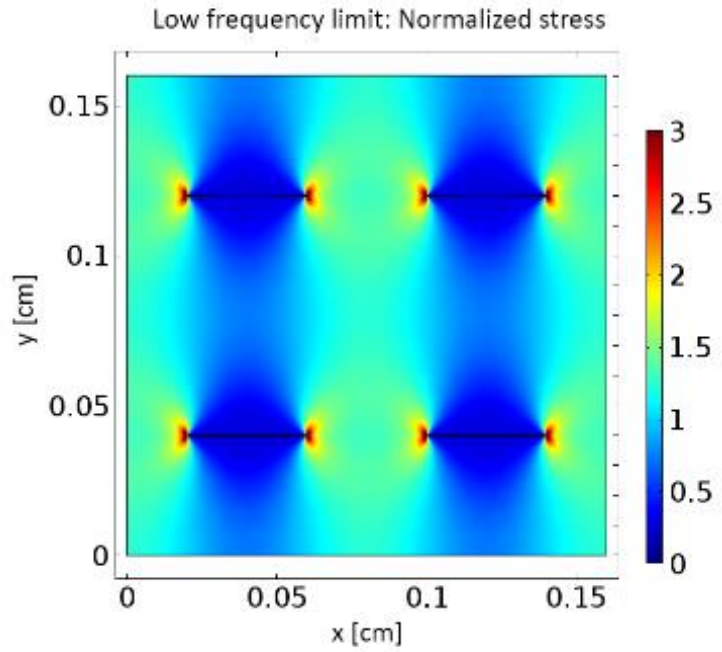

(a)

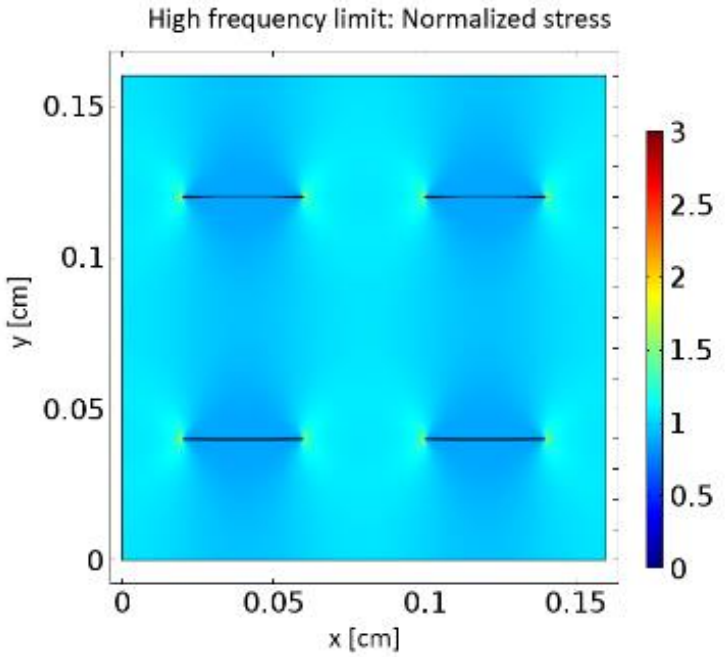

(b)

Figure 3-5. Spatial distribution of the real part of the normal stress in response to the vertical numerical relaxation test for the sample with 4 fractures. The upper and lower panels correspond to the low- and high-frequency limits (~10^{-4} Hz and ~10Hz), respectively. The values are normalized by the average stress and, hence, values smaller than 1 represent stress shielding and those larger than 1 represent stress amplification.

3.3.2.4 Seismic wave dispersion and attenuation at different incidence angles

The above results show that the results given by the penny-shaped crack model are in best agreement with the numerical simulations for both the samples with low and relatively high fracture densities. Hence, for brevity and clarity, we only employ the rock sample with low fracture density (4 fractures) for the investigation of the anisotropic properties. Here, we use both the interpolation approach of Galvin and Gurevich (2015) and the frequency-dependent fracture compliance approach proposed above to calculate the full stiffness coefficients of the saturated fractured rock. Then, the seismic wave velocities and attenuation at any incidence angles, as well as the anisotropic parameters for velocities and attenuation can be calculated (Section 2.7).

Figure 3-6 shows the P-wave phase velocity and attenuation as functions of frequency for different incidence angles measured with respect to the fracture normal. The numerical simulation results (solid lines) show that the greatest dispersion and attenuation occur when the P-wave propagates along the fracture normal. This is expected as for this direction of propagation the P-wave can easily compress the fractures, thus generating the largest amount of WIFF between the fractures and the background medium. When the incidence angle increases, the P-wave dispersion and attenuation decrease and they become negligible at incidence angles close to 90º. This is due to the fact that the fluid pressure gradient generated by a P-wave propagating parallel to the fractures is negligible and, hence, there is nearly no WIFF.

Comparing in Figure 3-6 the theoretical predictions given by the interpolation approach (dashed lines) and the frequency-dependent fracture compliance approach (stars), it can be seen that they are in good agreement. Some discrepancies can be found for P-waves propagating at incidence angles of 45º. The reason for these discrepancies is that the frequency-dependent fracture compliance approach only considers three non-zero components of the saturated fracture compliance matrix, located in its diagonal [see equation (3.19)], that is, those given by the normal and tangential fracture compliances. Conversely, the interpolation approach implicitly considers additional non-negligible components (especially Z_{12}^{sat}) related to the impact of finite fracture thickness and WIFF. Indeed, the observed discrepancies arise

mainly for low frequencies, which is due to the fact that the neglected components in the saturated fracture compliance matrix get larger for low frequencies (Cardona, 2002; Gurevich, 2003). It can also be noted that there are discrepancies between the attenuation of P-waves propagating at incidence angle of 90º, which in principle appears to be large. However, this is a visual artifact produced by the logarithmic scale used to present the result, as attenuation is negligibly small in this case. To assess the applicability of the two theoretical approaches, we compare their results with those provided by the numerical simulations (solid lines). We observe that the theoretical predictions given by these two approaches match very well with the numerical simulations. The small discrepancies found between the theoretical predictions and the numerical simulations are probably due to fracture interaction effects. It can be noticed that the theoretical predictions given by the frequency-dependent fracture compliance approach for Vp (45º) are in slightly better agreement with the numerical simulations than the interpolation approach. This is probably due to the fact that the error caused by neglecting the small non-zero components in the saturated fracture compliance matrix when using the frequeny-dependent fracture compliance approach coincidently cancelled out the discrepancies related to fracture interactions.

Figure 3-7 shows the SV-wave velocity and attenuation as functions of frequency for different incidence angles. The numerical simulation results (solid lines) show that the largest dispersion and attenuation for SV-waves occur for an incidence angle of around 45º. This can be confirmed by exploring the behavior of the SV-wave velocities and attenuation with incidence angle for different frequencies (not shown here for brevity). This means that the SV-wave induces the largest amount of WIFF between the fractures and the background when propagating at incidence angles of around 45º. It can also be noted that, SV-wave velocities at incidence angles of 0º and 90º are the same, as they are both controlled by the shear modulus C_{66}.

Comparing the theoretical prediction results given by the interpolation approach (dashed lines) and those based on the frequency-dependent fracture compliance (stars), it can be found that they are in good agreement with each other. The largest discrepancies are found for SV-wave velocities at low frequencies. The reason for the discrepancy is the same as for the P-wave, that is, the neglect of the

small non-zero components of the saturated fracture compliance matrix. As these components are larger at low frequencies than at high frequencies, the discrepancies at low frequencies get more significant. It can be noted that according to the two considered theoretical predictions, there is no dispersion and attenuation for SV-waves at incidence angles of 0º and 90º. This means that the theoretically-predicted shear modulus C_{66} is independent of frequency.

To assess the applicability of the theoretical approaches in the case of SV-waves, we compare them with the numerical simulations (solid lines). We observe in Figure 3-7 that the theoretical predictions given by both approaches match the numerical results very well. Further inspection indicates that the interpolation approach is in better agreement than that based on the frequency-dependent fracture compliance. This is due to the fact that the former takes into account all the non-zero components of the saturated fracture compliance matrix, whereas the latter only considers the normal and tangential fracture compliances. The observed discrepancies between the theoretical predictions and the numerical simulations are primarily due to fracture interaction effects.

It is interesting to note here that, according to the numerical simulations, there is very small dispersion and attenuation for SV-waves at incidence angles of 0º or 90º. This means that the shear modulus C_{66} is frequency-dependent in the numerical simulations, which is different from the theoretical predictions. The reason for the frequency dependency of C_{66} is the dilation and compression of the finite-length fractures when an SV-wave propagates through the medium at an incidence angle of 0º or 90º, which induces a smooth fluid pressure gradient and, hence, fluid flow (Caspari et al., 2016). However, this is not considered in the theoretical predictions. Since the induced seismic dispersion and attenuation are negligibly small, the theoretical predictions provide good approximations of the numerical simulation results.

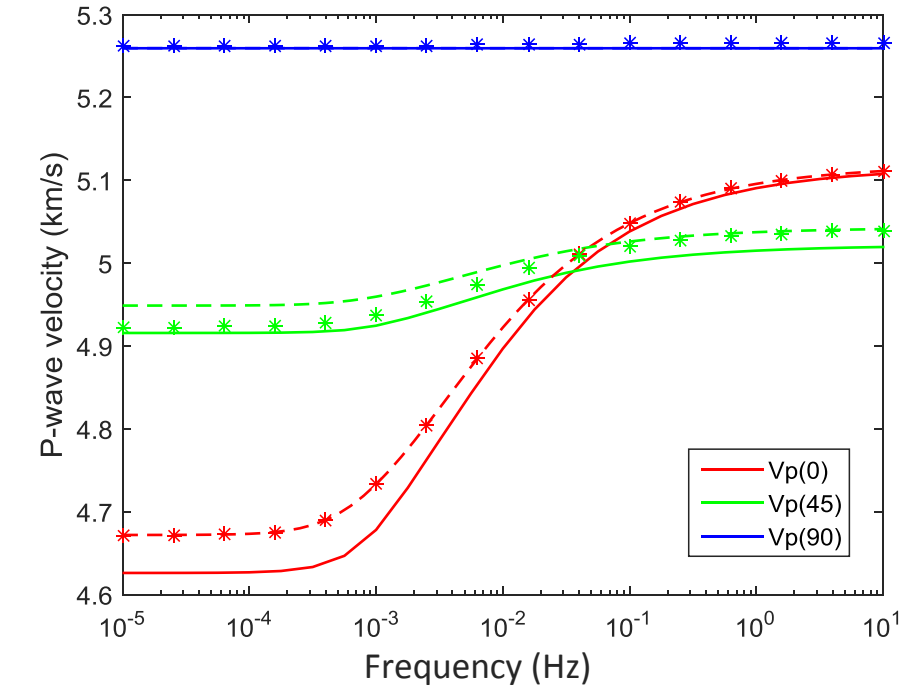

(a)

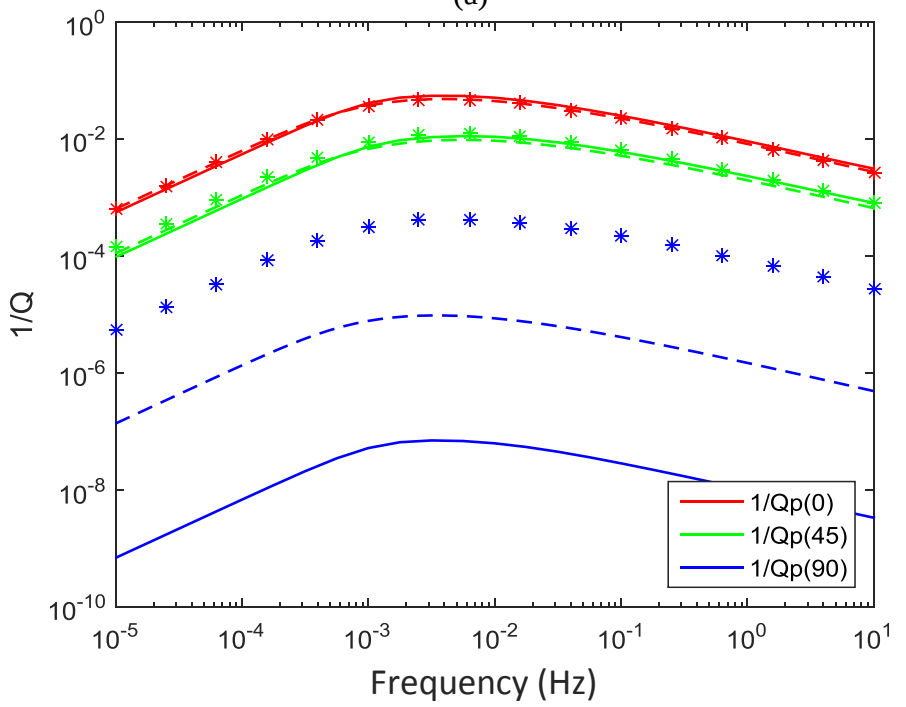

(b)

Figure 3-6. (a) P-wave velocity and (b) attenuation as functions of frequency for different incidence angles. Solid lines, dashed lines, and stars denote the results obtained from numerical simulations, interpolation approach, and frequency-dependent fracture compliance approach, respectively.

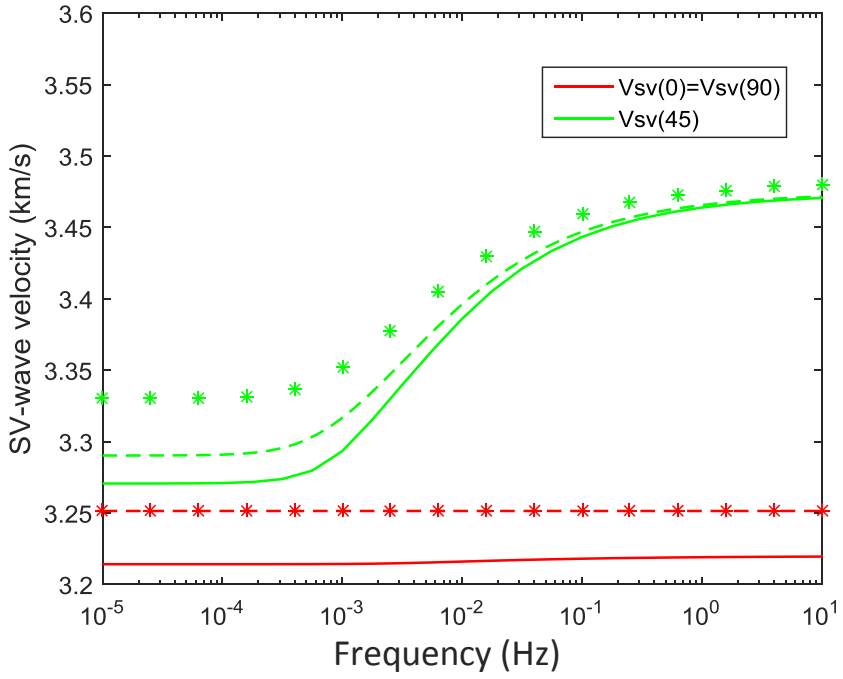

(a)

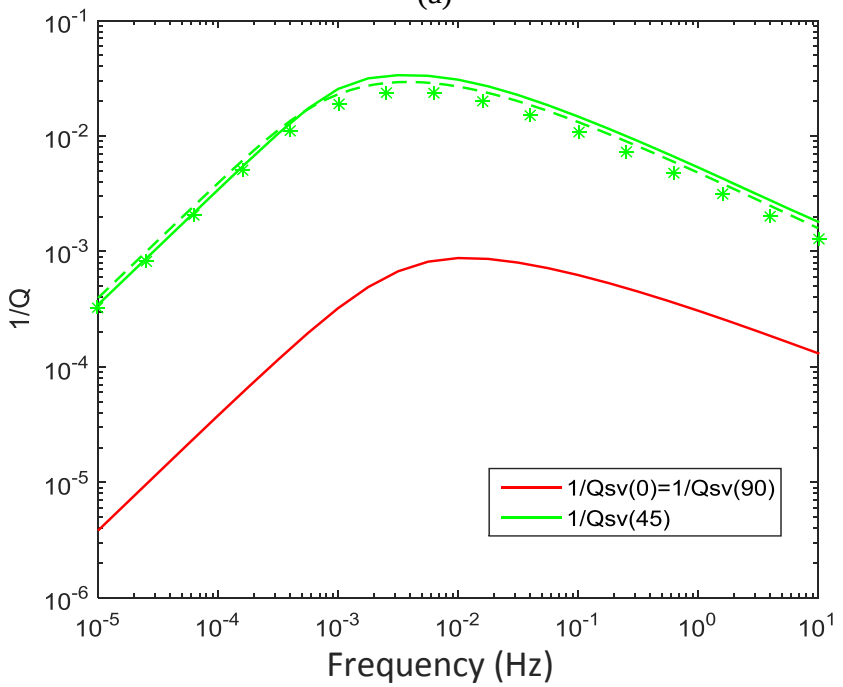

(b)

Figure 3-7. (a) SV-wave velocity and (b) attenuation as functions of frequency for different incidence angles. Solid lines, dashed lines, and stars denote the results obtained from numerical simulations, interpolation approach, and frequency-dependent fracture compliance approach, respectively. Note that the theoretical predictions for 1/Qsv (0°) and 1/Qsv (90°) are not shown in (b) as they are equal to zero.

3.3.2.5 Anisotropic parameters

An alternative approach for studying the anisotropic properties of the considered fractured sample consists in plotting the anisotropy parameters. They can be calculated through their definitions [equations (2.56) to (2.59)] from the stiffness coefficients provided by the developed theoretical models or the numerical simulations (Figure 3-8). In the case of the velocity anisotropy (Figure 3-8a), the numerical simulations show that ε and δ are relatively close to each other at low frequencies. This implies that the sample behaves as nearly elliptical for these frequencies. However, as the frequency increases, δ becomes negative and ε reaches a small positive value. Thus, the sample exhibits a strong anelliptical property at high frequencies. It should be noted here that the parameter ε does not vanish in the high-frequency limit due to the non-zero normal compliance of fractures with finite thickness, in contrast to the results obtained for fractures with infinitesimal thickness (Galvin and Gurevich, 2015).

Figure 3-8a also shows that in the case of ε there is good agreement between the two theoretical approaches, but some discrepancies for δ arise at low frequencies. As in the case of the behaviors of P- and SV-waves, the reason for the discrepancies is related to the small components of the saturated fracture compliance matrix (especially Z_{12}^{sat}), that are neglected in the approach based on the frequency-dependent fracture compliance. Comparisons of the theoretical predictions for ε against the numerical simulations indicate that there is a good agreement between them at high frequencies, but some discrepancies arise at low frequencies. This is caused by the slightly different values for C_{22} obtained theoretically and numerically. In the case of δ, the numerical simulations and the theoretical predictions given by the interpolation approach match well, whereas some discrepancies are observed when compared with the approach based on the frequency-dependent fracture compliance. Again as before, this is mainly due to errors in the value of C_{12} provided by the frequency-dependent fracture compliance approach associated with the neglected small components of the saturated fracture compliance matrix.

The results for the attenuation anisotropy parameters are shown in Figure 3-8b. It can be seen that ε_Q and δ_Q have similar trends with frequency. They are negligibly small in both the low- and high-frequency limits, and reach their maxima at a characteristic frequency for which the fluid diffusion

length in the background is close to the crack radius (Galvin and Gurevich, 2015). This means that the attenuation anisotropy is largest at the characteristic frequency. Comparing the two theoretical predictions, it is found that they are in good agreement with each other. These curves also match with the numerical simulations, thus supporting the validation of the theoretical models.

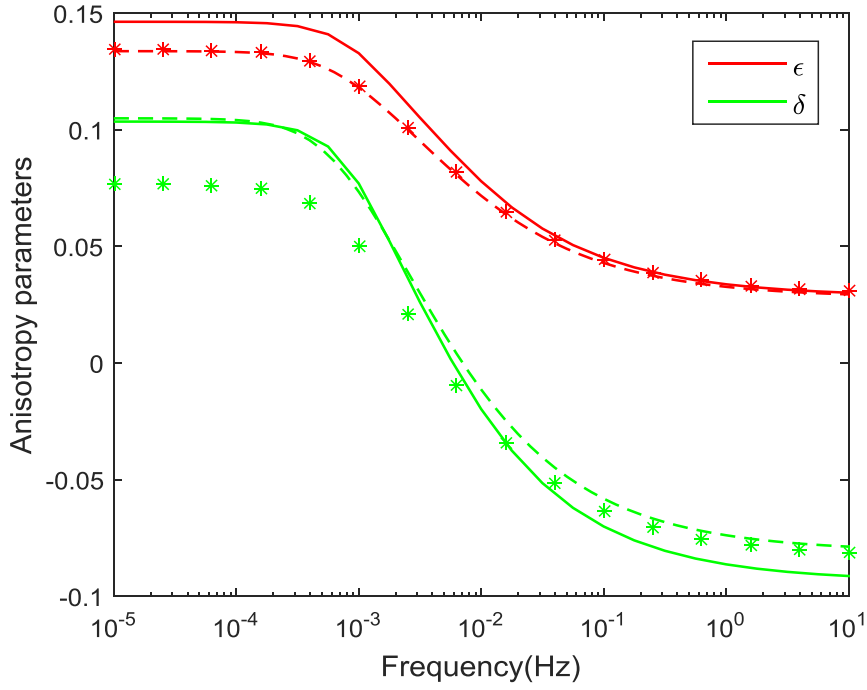

(a)

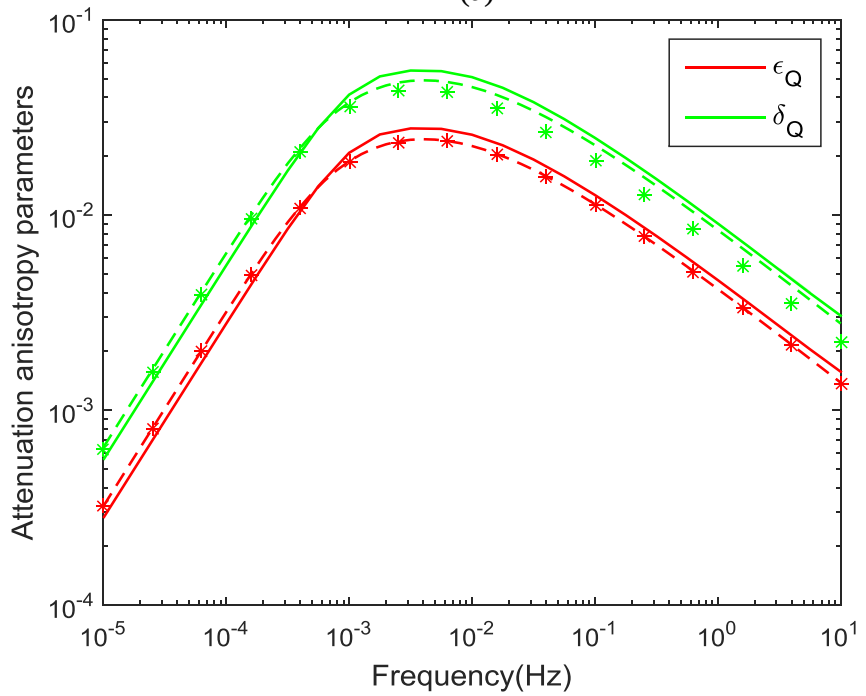

(b)

Figure 3-8. (a) Velocity and (b) attenuation anisotropy parameters as functions of frequency. Note that the solid lines, dashed lines, and stars denote the results obtained from numerical simulations, interpolation approach, and frequency-dependent fracture compliance approach, respectively.

3.4 Discussion

In this chapter, we considered the seismic dispersion and attenuation in the saturated porous rock with aligned fractures due to WIFF. Due to the very high computational cost of 3D numerical simulations, we only compared the predictions of the 3D theoretical model with 2D numerical results. However, the current computational capabilities allow us to consider the simple case of a regular distribution of penny-shaped cracks embedded in a 3D sample. In this case, we observe good agreement between the theoretical predictions and the numerical simulations, which suggests the applicability of the theoretical model in the 3D context (Figure 3-9). An exhaustive 3D analysis will be carried out in the future with improved computational capabilities. Moreover, the good agreement of our 3D theoretical model with the results of the 2D numerical simulations itself has indicated the robustness of our theoretical model. This implies that a model designed for axisymmetric penny-shaped cracks is also valid for 2D fractures (Figure 3-10). Recall that in the theoretical model, the crack diameter controls the characteristic frequency of the dispersion and attenuation (e.g., Gurevich et al., 2009). For the 2D fractures modelled in numerical simulations (Figure 3-10), the corresponding length scale parameter is fracture length d_c, while fracture 'depth' D is infinite. Thus, the agreement between theory and simulations means that the characteristics of the dispersion and attenuation are controlled by the smaller of the two fracture length parameters d_c, and are relatively insensitive to the larger of these parameters D. A similar observation was made by Barbosa et al. (2017) through comparisons of 2D and 3D numerical simulations for the rock with aligned fractures.

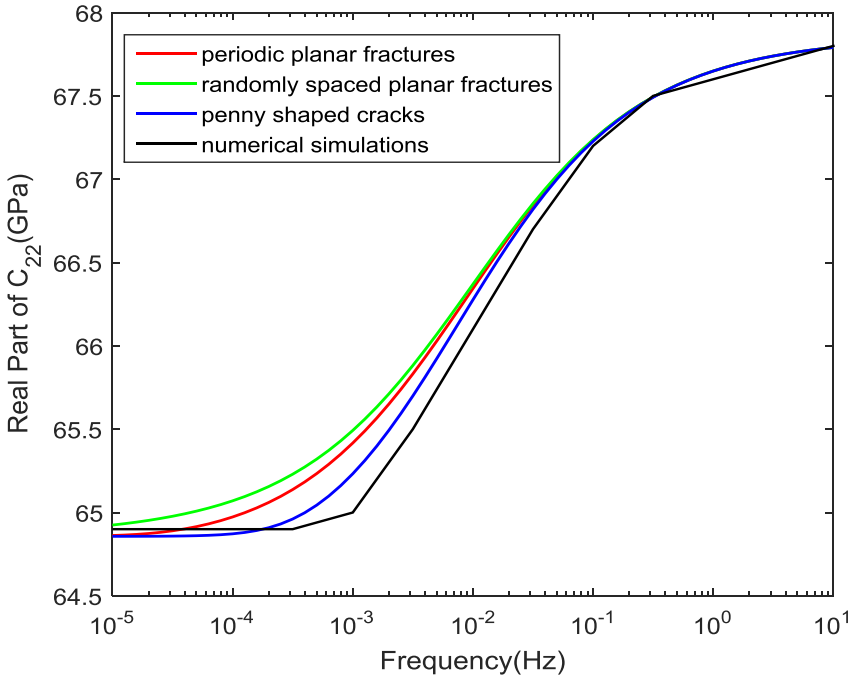

(a)

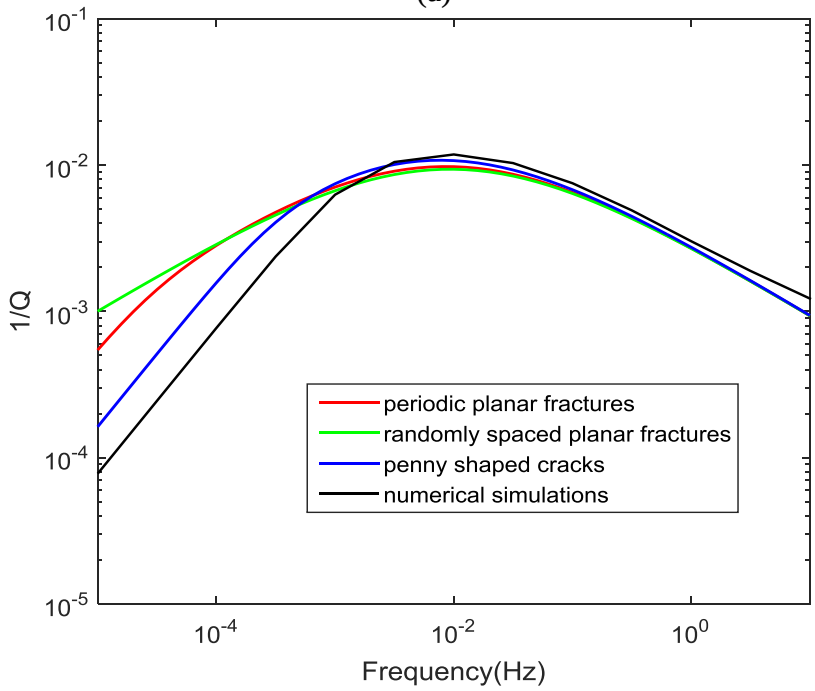

(b)

Figure 3-9. Comparison of theoretical predictions with numerical simulations for the 3D sample with regularly distributed aligned penny-shaped cracks.

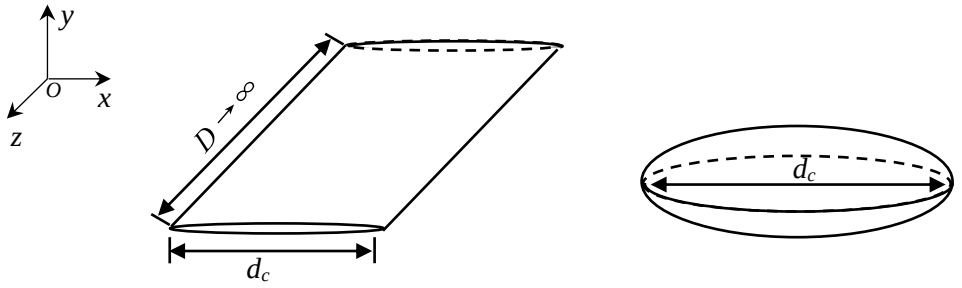

Figure 3-10. Schematic representation of the 2D fractures considered in the numerical simulations (a), and the penny-shaped cracks (oblate spheroid) considered in the theoretical predictions (b).

To extend the results for the P-wave modulus in the direction perpendicular to the fracture plane to the full stiffness coefficients, we apply both the interpolation method proposed by Galvin and Gurevich (2015) and the frequency-dependent fracture compliance matrix approach. The results show that there are some discrepancies between the two theoretical approaches, especially at low frequencies. This is due to the fact that, besides the three saturated fracture compliance components present in equation (3.16), the other components in the compliance matrix of the saturated fractures can be non-zero. At high frequencies, these non-zero components are caused by the effects of the finite fracture thickness, which can be easily estimated using the full Eshelby's solution [equation (2.2)]. For the sample investigated in this work, these non-zero components are negligibly small and hence the results given by the two theoretical approaches are nearly the same at high frequencies, as shown in Figure 3-6 and 3-7. At low frequencies, apart from the finite fracture thickness effects, due to the fluid communication between the fractures and the background medium, these non-zero components become much larger than at high frequencies (Cardona, 2002; Gurevich, 2003). The frequency-dependent fracture compliance approach neglects these non-zero components while the interpolation approach takes into account all these non-zero components. Therefore, much larger discrepancies between the two theoretical approaches can be found at low frequencies than at high frequencies. However, these discrepancies are still not large as shown in Figure 3-6 and 3-7. Hence, the results given by these two theoretical approaches are both in good agreement with the numerical simulation results.

It is important to remark here that both the two approaches proposed in this chapter make use of the interpolation to obtain the frequency-dependent elastic properties. The first approach provides the full stiffness coefficients at intermediate frequencies through an interpolation of the elastic moduli computed in the low- and high-frequency limits by using a relaxation function. The second approach, on the other hand, first obtains the fracture compliance matrix at intermediate frequencies through interpolation using the relaxation function and then calculates the frequency-dependent stiffness matrix using the linear-slip theory. While the first approach can give more accurate results in the low- and high- frequency limits, it is not as convenient as the second approach in the context of practical applications. The second approach is particularly attractive as it is simpler and is based on a fracture compliance matrix with a structure similar to that commonly employed in elastic frameworks, but with complex-valued and frequency-dependent components. By applying standard analyses of seismic data in the frequency domain, the frequency-dependent fracture compliance matrix can be estimated. Hence, this approach has great potential to be applied in the seismic characterization of real fractured reservoirs.

3.5 Conclusions

The objective of this chapter was to improve the applicability of theoretical models in the prediction of seismic dispersion and attenuation in reservoirs with aligned fractures. In order to do so, we extended the existing unified theoretical model for three fracture types, namely, periodically and randomly distributed planar fractures, and penny-shaped cracks, to the case of finite fracture thickness for P-waves propagating perpendicular to the fracture plane. To extend the results to the full stiffness coefficients, two theoretical models were used to obtain the full stiffness matrix. The first approach provides the frequency-dependent stiffness coefficients through an interpolation based on a relaxation function obtained from the normal-incidence solution. In contrast, the second approach makes use of a complex-valued and frequency-dependent fracture compliance matrix, whose behaviour is described by the relaxation function. The derived full stiffness matrix allows to compute P- and SV-wave velocity and attenuation as functions of frequency and incidence angle. Furthermore, the velocity and attenuation anisotropy parameters can also be obtained. In addition, we carried out numerical simulations to explore the validity of the extended theoretical model for given fracture configurations. Two 2D rock samples

with aligned fractures were studied, one with low fracture density (0.06) and the other with relatively high fracture density (0.20). The results show that the influence of fracture thickness on seismic dispersion and attenuation is rather small at low frequencies. However, it gets significant at high frequencies. This is an important result that should be taken into account when characterizing low-permeability formations containing fractures, for which the seismic properties typically correspond to the high-frequency limit.

Comparing theoretical predictions of the extended models with corresponding numerical simulations, it is found that the penny-shaped model matches the numerical simulation results best. Furthermore, the study indicates that this theoretical model is applicable even in the case of rocks with relatively high fracture density. Analyses of stress distributions in response to numerical vertical relaxation tests suggest that the small discrepancies observed between the theoretical predictions and the numerical simulations are probably due to fracture interactions.

For the anisotropic properties of the velocities and attenuation, the results show that the predictions given by the two theoretical approaches are in good agreement with each other. However, small discrepancies between them arise, especially for low frequencies, which are caused by small, but non-negligible components of the saturated fracture compliance matrix that are neglected by the approach based on a frequency-dependent fracture compliance matrix. The theoretical predictions are also in good agreement with corresponding numerical simulations. The small discrepancies are probably due to the fracture interactions.

The theoretical models proposed in this chapter are easy to apply and, hence, can be used in inversion schemes aimed at characterizing fractured reservoirs. The approach based on a frequency-dependent fracture compliance matrix is particularly attractive, as in practice the compliances of the probed saturated fractures could be estimated from seismic data by applying standard analyses in the frequency domain.

Chapter 4
Dispersion, attenuation, and anisotropy due to WIFF in porous rocks containing two orthogonal sets of fractures

4.1. Introduction

In the last chapter, we studied the seismic wave dispersion, attenuation, and frequency-dependent anisotropy due to WIFF in the saturated rock with aligned fractures. However, the fractures in the real reservoirs are not always aligned, which can intersect each other forming the fracture network. This fracture network is crucial for the fluid flow, which is of particular importance in the carbonate and unconventional reservoirs. Hence, it is of great interest to study the seismic signatures of the intersected (connected) fracture network for the seismic exploration.

As discussed in Chapter 1, in the presence of multiple sets of intersected fractures, the significant effects of FF-WIFF on the seismic dispersion, attenuation, and frequency-dependent anisotropy have been validated by the numerical studies (Rubino et al., 2013, 2014, and 2017). However, little theoretical work has been done on this aspect up until now. Hence, in this chapter, we study these effects theoretically in the saturated rocks with two perpendicular sets of fractures. In order to do so, two cases are considered, one with intersecting fractures and the other with non-intersecting fractures. The corresponding theoretical models are developed based on those for the aligned fracture case. To validate the proposed theoretical models, the numerical simulations based on the Biot's quasi-static equations of poroelasticity are also performed.

The contents of this chapter have been published in Geophysical Prospecting (Guo et al., 2017a) and Geophysical Journal International (Guo et al., 2018d).

4.2 Theory

To study the effects of fracture intersections (FF-WIFF) on seismic dispersion and attenuation, we consider a simple case consisting of a rock with two sets of perpendicular fractures, having all the fractures the same geometrical characteristics. We assume that the two fracture sets are perpendicular to the *x*- and *y*- axis, respectively, and we take into account the presence of intersecting and non-intersecting fracture networks, such as those shown in Figure 4-1. Furthermore, we consider three types of fractures, namely, periodically- and randomly-spaced planar fractures, as well as penny-shaped cracks. In the following, we will first develop the method for calculating the frequency-dependent P-wave moduli in the direction perpendicular to the fracture plane (c_{11} and c_{22}). Based on this, the full stiffness coefficients can then be obtained.

4.2.1 Non-intersecting fracture case

For rocks with two orthogonal sets of non-intersecting fractures, a P-wave propagating perpendicular to one of the fracture sets will induce oscillatory fluid flow between such fractures and the background pores (FB-WIFF). The fractures parallel to the propagation direction, on the other hand, are not expected to affect significantly the behaviour of the seismic wave (Rubino et al., 2014). Hence, the two P-wave moduli in the directions perpendicular to the two fracture sets, c_{11} and c_{22}, can be directly obtained in a similar way as for rocks with aligned fractures [equation (2.35)]. That is, the expressions for T and G for the cases with orthogonal non-intersecting planar fractures as well as for non-intersecting penny-shaped cracks can be calculated using the same formulas as for the corresponding aligned fracture case. As the fractures considered here have the same geometrical characteristics, at least one of the non-intersecting fracture sets will have the fracture spacing that is larger than the fracture radii under the periodical distributions. This violates the definition of planar fractures. Hence, the non-intersecting periodic planar fracture case is not realizable and we only consider the randomly spaced planar fracture and penny-shaped crack cases here. For randomly-spaced planar fractures, T tends to infinity and G can be calculated using equation (3.4). For penny-shaped cracks, T and G can be calculated using equation

(2.47) and (3.7), respectively. However, it should be noted that, for calculating c_{11}, the properties of the aligned fracture set in these equations correspond to those of the fracture set perpendicular to the *x*-axis, whereas for calculating c_{22} the properties of the fracture set perpendicular to the *y*-axis should be used. Furthermore, the P-wave moduli in the low- and high- frequency limits C_0 and C_1 need to be replaced by the corresponding values of c_{11} or c_{22}.

It is important to remark here that, due to Poisson ratio effects, a small amount of fluid flow also occurs between the fracture set parallel to the wave propagation direction and the background pores. The corresponding effects on the P-wave moduli are expected to be negligible and, therefore, are not accounted for in the approach proposed here. This is in agreement with the results of Rubino et al. (2014) and is supported by the numerical analysis considered in this work.

4.2.2 Intersecting fracture case

In the case of rocks with two perpendicular sets of intersecting fractures, a P-wave propagating perpendicular to one of the fracture sets will not only induce FB-WIFF, but also FF-WIFF (e.g., Rubino et al., 2014). Hence, the P-wave modulus in the direction perpendicular to one fracture set will experience two stages of dispersion and attenuation, which are due to these two manifestations of WIFF. The characteristic frequencies for these two stages of dispersion and attenuation are proportional to the permeability of the background medium and that of the material composing the fractures, respectively (Rubino et al., 2014). Consequently, since typically the permeability of the background medium is much lower than that of the fractures, the dispersion and attenuation due to FB-WIFF occur at much lower frequencies than in the case of FF-WIFF.

To obtain the frequency-dependent P-wave moduli c_{11} and c_{22} for the first stage of dispersion and attenuation (FB-WIFF), the corresponding expressions for T and G are needed. For rocks with two orthogonal sets of fractures having the same geometries, when a P-wave propagates perpendicular to one of the fracture sets, the resulting FB-WIFF is expected to be primarily controlled by the stiffness contrast between such fracture set and the background medium. Hence, it is reasonable to approximate the expressions for T and G using the same form as those for aligned fracture case [equations (3.2) and (3.4) for planar fractures, and equations (2.45) and (3.7) for penny-shaped cracks]. However, even in

the high frequency limit of FB-WIFF, connected fractures will be in pressure communication with each other, and hence, the system will be softer than in the case of only one set of aligned fractures. This implies that the dispersion and attenuation due to FB-WIFF will also be weaker in presence of connected fractures, as shown by Rubino et al. (2014). As the dispersion and attenuation at low and high frequencies are controlled by the parameters T and G, respectively [equations (2.36) and (2.37)], weaker dispersion and attenuation means smaller values of T and G for the intersecting fracture case in comparison with the aligned fracture case. Hence, the values of T and G need to be scaled down here. Since the amplitude of the dispersion and attenuation are dominated by the elastic properties in the low- and high- frequency limits (Mavko et al., 2009), the scaled values of T and G can be easily obtained by replacing the P-wave moduli in the low- and high- frequency limits C_0 and C_1 in equations (3.2), (3.4), (2.45), and (3.7) with the corresponding limiting values of c_{11} or c_{22} due to FB-WIFF for the intersecting fracture case. It should be noted that T for the randomly spaced planar fracture case still tends to infinity (corresponding to the zero value of ζ). Similar to the non-intersecting fracture case, the parameters of the fracture set perpendicular to the x-axis should be used when calculating T and G for c_{11}, whereas those of the other fracture set for computing c_{22}. In the numerical examples, we will see that the theoretical predictions using the scaled values of T and G are in good agreement with the numerical simulations.

For computing the P-wave moduli c_{11} and c_{22} for the second stage of dispersion and attenuation (FF-WIFF), it is important to take into account that if the frequency of the propagating wave is above the high-frequency limit of FB-WIFF, the fluid in the fractures does not have enough time to communicate with that of the background and, therefore, the fractures are hydraulically isolated. However, the fluid can still communicate between connected fractures. Hence, if a P-wave propagates perpendicular to one of the fracture sets, the fluid from such fractures will be injected into (or withdrawn from) the connected ones during the compression (or extension) cycle. This indicates that the fluid in the fracture set perpendicular to the wave propagation direction is communicating with an effective medium, for which the other fracture set acts as the porosity and the saturated background medium acts as the solid phase. This implies that this process can be represented by aligned fractures embedded in an effective medium and, again as before, the equations (3.2), (3.4), (2.45), and (3.7) can be used to compute the required

parameters T and G. In order to do so, the properties of the effective medium are needed. The elastic properties of the dry effective medium are obtained by adding the dry fractures into the saturated background medium using the linear slip theory (Schoenberg and Sayers, 1995). The saturated elastic properties of this effective medium are then obtained by using the anisotropic Gassmann equation (Gurevich, 2003). Furthermore, the permeability of the effective medium along x-axis (or y-axis) κ_e can be obtained based on the definition of permeability:

$$\kappa_e = \kappa_c \phi_e , \tag{4.1}$$

where κ_c is the permeability of the material composing the fracture set parallel to x- or y- axis, and ϕ_e is the volume fraction that the corresponding fracture set occupies.

With the properties of the effective medium and the fracture sets, the expressions of T and G for c_{11} and c_{22} for the second stage of dispersion and attenuation can be calculated through equations (3.2), (3.4), (2.45), and (3.7) by replacing the properties of the background medium with those of the effective medium and the properties of the aligned fractures with those of the fracture set perpendicular to the x- and y-axes, respectively. Also, we need to replace the elastic properties in the low- and high-frequency limits C_0 and C_1 with the corresponding values for the stage of dispersion and attenuation due to FF-WIFF. It should be noted that T for randomly spaced planar fractures still tends to infinity here.

It is important to remark here that, different from the case of an isotropic background, the effective medium is anisotropic. Hence, strictly speaking, the expressions for T and G should be derived for fractures in an anisotropic background. However, the resulting equations may get very complicated. To keep our approach easy to apply, we still use equations (3.2), (3.4), (2.45), and (3.7) to calculate T and G. However, the background porosity in these equations is replaced by the fraction that the fracture set along x-axis occupies in the rock for c_{11} and that occupied by the fracture set along y-axis for c_{22}. And also, the background permeability and elastic properties are replaced by those of the effective medium along x-axis for c_{11} and those along y-axis for c_{22}. This may cause some errors, which we will discuss in the numerical example section of this work. In addition, in our current approach, we assume that all the fractures are connected to at least one orthogonal fracture and, hence, the fluid pressure increase induced by the seismic wave can be released. If there are isolated fractures, the rock will behave in a

stiffer manner due to the unreleased fluid pressure. This will also be analysed in the numerical example section.

4.2.3 Elastic properties in the low- and high- frequency limits for the two manifestations of WIFF

To obtain the frequency-dependent P-wave moduli c_{11} and c_{22}, the elastic properties in the low- and high-frequency limits for each manifestation of WIFF are needed. For rocks with non-intersecting fractures, only FB-WIFF occurs. Hence, we only need to obtain the elastic properties in the low- and high- frequency limits for this WIFF manifestation in this case. In the low-frequency limit, the fluid in the fractures has enough time to communicate with that in the background pores, and therefore, the fluid pressure is uniform throughout the rock. Under this condition, we can first add the two sets of dry fractures into the dry background medium using the linear slip theory to obtain the elastic properties of the dry fractured rock:

$$\mathbf{S}_d = \mathbf{S}_b + \sum_{i=1}^{2} \mathbf{S}_{fi}\,, \tag{4.2}$$

where $\mathbf{S}_d$ and $\mathbf{S}_b$ are the compliance matrix of the dry fractured rock and background medium, respectively; $\mathbf{S}_{fi}$ is the excess compliance matrix of the i^{th} dry fracture set, which can be calculated using equation (2.2).

The elastic properties of the saturated fractured rock can then be calculated by using the anisotropic Gassmann's equation [equation (2.10)]. This procedure of obtaining elastic properties in the low-frequency limit of FB-WIFF for the rock with non-intersecting fractures is schematically illustrated in Figure 4-1.

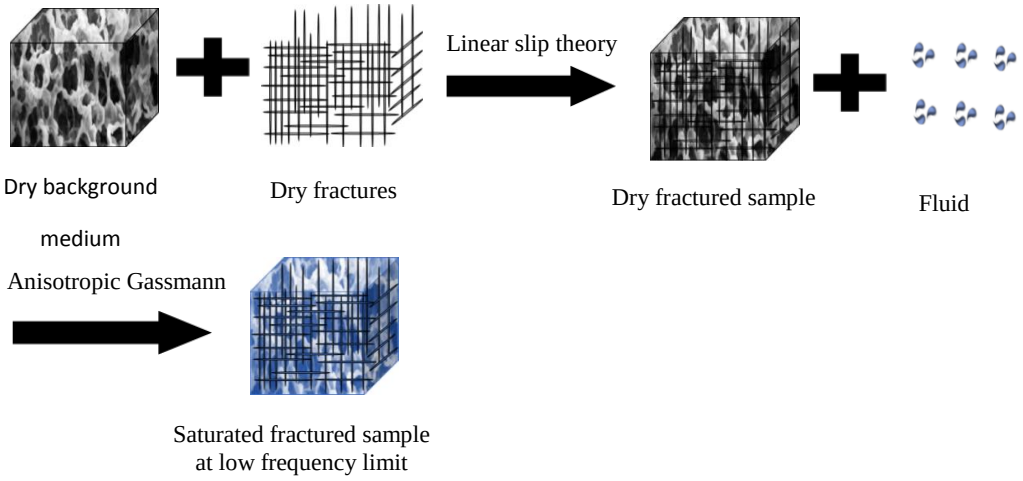

Figure 4-1. Schematic illustration of the procedure proposed to obtain the stiffness coefficients of the saturated fractured rock with non-intersecting fractures in the low frequency limit of FB-WIFF.

Conversely, in the high-frequency limit, the fluid in the fractures does not have enough time to communicate with that in the background pores. Hence, the fractures are hydraulically isolated from the saturated background medium. In this case, we first obtain the compliances of the hydraulically isolated fractures from the dry fracture compliances using a theory for isolated fluid-filled fractures (Hudson, 1981; Schoenberg and Douma, 1988; Gurevich, 2003):

$$Z_{Ni}^{sat} = \frac{Z_{Ni}}{1+\frac{Z_{Ni}K_f}{\phi_{fi}}\left(1-\frac{K_f}{K_g}\right)^{-1}}, \tag{4.3}$$

where Z_{Ni}^{sat} and Z_{Ni} are the saturated and dry normal compliances for the i^{th} fracture set while the saturated tangential fracture compliances are same with the dry case; ϕ_{fi} is the fraction of the i^{th} fracture set in the saturated rock (fracture porosity); K_f and K_g are the fluid and grain bulk moduli, respectively.

Then, the compliance matrix of the saturated fractured rock **S** can be obtained by adding the hydraulically isolated fractures into the saturated background medium using the linear slip theory:

$$\mathbf{S} = \mathbf{S}_b^{sat} + \sum_{i=1}^{2} \mathbf{S}_{fi}^{sat}, \tag{4.4}$$

where $\mathbf{S}_b^{sat}$ is the compliance matrix of the saturated background, which can be obtained by using the isotropic Gassmann's equation [equations (2.6) and (2.7)], $\mathbf{S}_{fi}^{sat}$ is the excess compliance matrix of the i^{th} saturated fracture set. This procedure of obtaining elastic properties in the high-frequency limit of FB-WIFF for the rock with non-intersecting fractures is schematically illustrated in Figure 4-2.

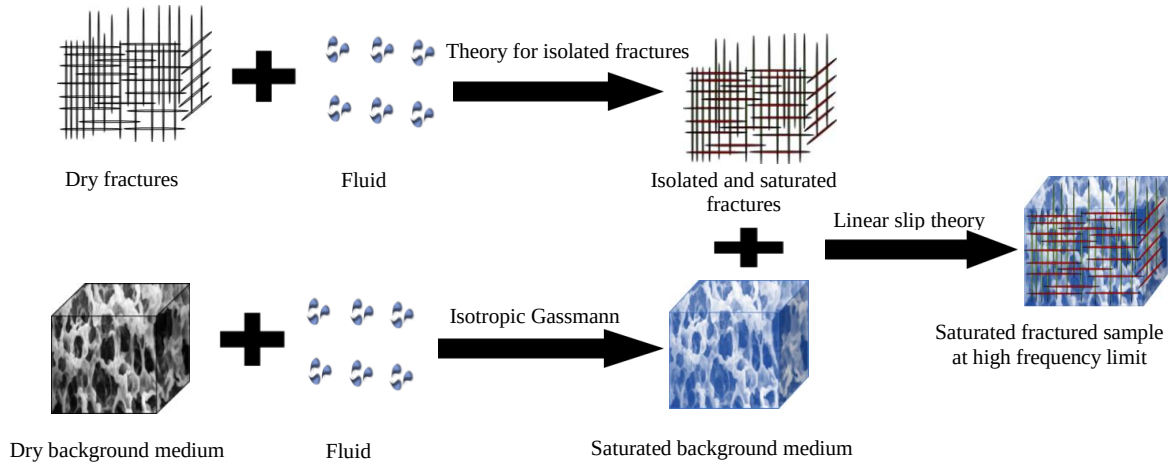

Figure 4-2. Schematic illustration of the procedure proposed to obtain the stiffness coefficients of the saturated fractured rock with non-intersecting fractures in the high-frequency limit of FB-WIFF.

For rocks with intersecting fractures, apart from FB-WIFF, FF-WIFF can also occur. For the FB-WIFF, the elastic properties in its low-frequency limit can be obtained by using the linear slip theory and the anisotropic Gassmann's equation since the fluid pressure is uniform throughout the rocks. This procedure is similar to that for the non-intersecting fracture case (Figure 4-1). On the contrary, in its high-frequency limit, the fluid in the fractures does not have enough time to communicate with that of the background pores due to its low permeability. However, as the permeability of the fractures is much higher than that of the background, the fluid can still communicate within connected fractures. Hence, the fluid pressure will be uniform inside the system of connected fractures, but with a value different from that of the saturated background medium. Under this condition, we can obtain the elastic properties of the saturated fractured rock by first adding the dry fractures into the saturated background medium using the linear slip theory:

$$\mathbf{S}^1 = \mathbf{S}_b^{sat} + \sum_{i=1}^{2} \mathbf{S}_{fi} \ . \tag{4.5}$$

Then, the dry fractures can be saturated using the anisotropic Gassmann's equation, with the saturated background medium acting as the solid phase and the fracture porosity acting as the porosity:

$$c_{ij}^{sat} = c_{ij}^1 + \alpha_i^1 \alpha_j^1 M_1 , \tag{4.6}$$

where C_{ij}^1 is the components of $\mathbf{C}^1$ inversed from $\mathbf{S}^1$; $\alpha_m{}^1$ takes the form:

$$\alpha_m^1 = 1 - \frac{\sum_{n=1}^{3} c_{mn}^1}{3K_b^{sat}} ; \tag{4.7}$$

and M_1 is expressed as:

$$M_1 = \frac{K_b^{sat}}{\left(1 - K_1^* / K_b^{sat}\right) - \phi_f \left(1 - K_b^{sat} / K_f\right)} \ , \tag{4.8}$$

$K_1{}^*$ is obtained from equation (2.13) by replacing c_{ij}^d with c_{ij}^1, and ϕ_f is the total volume fraction of the fractures in the rock.This procedure for obtaining the elastic properties in the high-frequency limit of FB-WIFF for the rock with intersecting fractures is schematically illustrated in Figure 4-3.

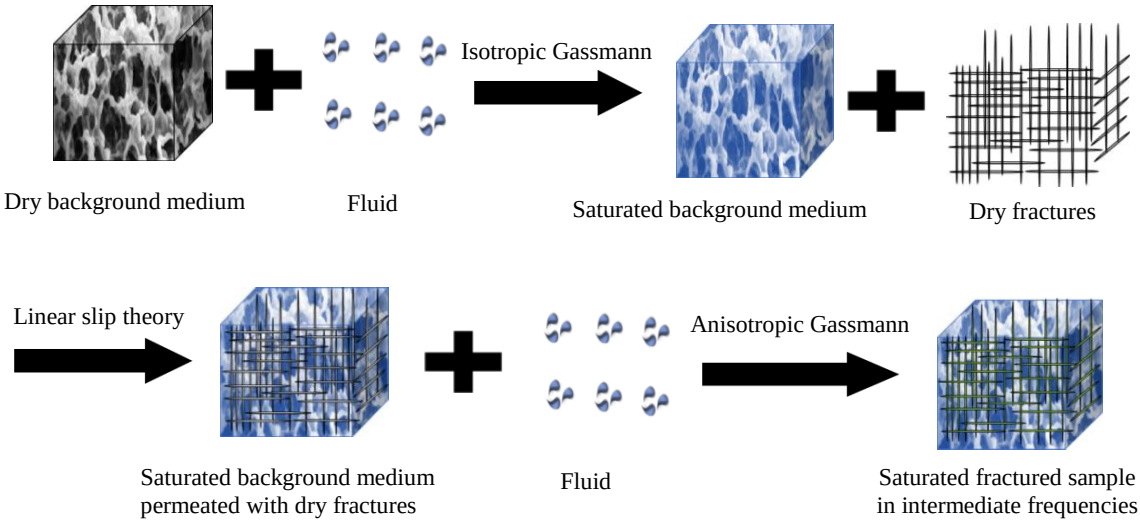

Figure 4-3. Schematic illustration of the procedure proposed to obtain the stiffness coefficients of the saturated fractured rock with intersecting fractures in the high-frequency limit of FB-WIFF.

For FF-WIFF, the elastic properties in its low-frequency limit coincide with those in the high-frequency limit of FB-WIFF. However, in the high-frequency limit of the FF-WIFF, the fractures will be hydraulically isolated from both the background medium and the other fractures. Hence, similar to the non-intersecting fracture case, we can calculate the corresponding elastic properties by adding the hydraulically isolated fractures into the saturated background medium using the linear slip theory (Figure 4-2).

4.2.4 Full stiffness coefficients

With the values of T and G obtained for the P-wave moduli in the directions along the x- and y-axes (c_{11} and c_{22}), and the corresponding elastic properties in the low- and high-frequency limits, the frequency-dependent P-wave moduli c_{11} and c_{22} can be calculated. For rocks with non-intersecting fractures, c_{11} and c_{22} can be written as follows:

$$\frac{1}{c_{ii}} = \frac{1}{c_{ii}^{hf}}\left[1+\left(\frac{c_{ii}^{hf}-c_{ii}^{lf}}{c_{ii}^{lf}}\right)\Big/\left(1-\zeta_i+\zeta_i\sqrt{1-i\frac{\omega\tau_i}{\zeta_i^2}}\right)\right], \quad i = 1, 2 \tag{4.9}$$

where c_{ii}^{lf} and c_{ii}^{hf} are the corresponding P-wave moduli in the low- and high- frequency limits, respectively; and ζ_i and τ_i are the shape parameters for c_{ii}, which can be calculated from T_i, G_i, c_{ii}^{lf}, and c_{ii}^{hf} using equations (2.38) and (2.39).

For rocks with intersecting fractures, there are two stages of seismic dispersion and attenuation which are due to the FB- and FF-WIFF. For each stage, we can calculate the frequency-dependent P-wave moduli c_{11} and c_{22} through the use of equation (4.9), with the involved parameters evaluated for the considered WIFF manifestation. We can then combine these two stages of seismic dispersion and attenuation as follows:

$$\frac{1}{c_{ii}} = \frac{1}{c_{ii}^{hf-2}}\left\{1+\left[\frac{c_{ii}^{hf-2}-c_{ii}^{1}(\omega)}{c_{ii}^{1}(\omega)}\right]\Big/\left(1-\zeta_{2i}+\zeta_{2i}\sqrt{1-i\frac{\omega\tau_{2i}}{\zeta_{2i}^2}}\right)\right\}, i = 1, 2 \tag{4.10}$$

where c_{ii}^{hf-2} is the P-wave moduli along x- or y- axis in the high-frequency limit for the second stage of seismic dispersion and attenuation (due to FF-WIFF) and ζ_{2i} and τ_{2i} are the corresponding shape

parameters; and $c_{ii}^{1}(\omega)$ is the frequency-dependent P-wave moduli calculated from equation (4.9) for the first stage of seismic dispersion and attenuation (due to FB-WIFF).

Hence, we have obtained the frequency-dependent P-wave moduli c_{11} and c_{22} for both rocks with non-intersecting and intersecting fractures. For the other stiffness coefficients, we can also obtain their frequency-dependent values from equations (4.9) and (4.10). Following Gurevich et al. (2009), for all the stiffness coefficients, each stage of dispersion and attenuation (due to FF- or FB-WIFF) is expected to be controlled by two crossover frequencies:

$$f_P = \frac{\varsigma^2}{\pi\tau}, \tag{4.11}$$

$$f_M = \frac{C_1}{C_0}\frac{1}{2\pi\tau}. \tag{4.12}$$

These two crossover frequencies separate each stage of dispersion and attenuation in three regimes where the seismic velocities and attenuation, or stiffness coefficient, vary with frequency in a different manner.

Numerical simulations (Rubino et al., 2015) show that all the stiffness coefficients have similar frequency-dependent behaviours for rocks with relatively high symmetry (equal number of horizontal and vertical fractures). For FB-WIFF, the characteristic frequency is controlled by the fracture geometries and the properties of the background medium (Galvin and Gurevich, 2006, 2007; Rubino et al., 2014), similarly, that for FF-WIFF should be determined by the fracture geometries and the properties of an effective background medium. Hence, for rocks with relatively low symmetry, the crossover frequencies for FB-WIFF for all the stiffness coefficients should still be similar as both the properties of the background medium and the fracture geometries do not change with the incidence angle of the seismic wave. However, for FF-WIFF, while the fracture geometries remain unchanged with the wave incidence angle, the properties of the effective background medium can vary. This may result in some shifts of the corresponding crossover frequencies for different stiffness coefficients. Nevertheless, since we consider fractures having identical shapes and physical properties, these frequency shifts should be rather small unless the number of horizontal and vertical fractures are

drastically different. Hence, for the general case, ω_P and ω_M for c_{11} and c_{22} for a given stage of dispersion and attenuation (FB- or FF-WIFF) are expected to be similar, and close to the crossover frequencies of the remaining stiffness coefficients. Based on this fact, the shape parameters for the other stiffness coefficients can be obtained as follows:

$$\tau' = \frac{C_0}{C_0'}\frac{C_1'}{C_1}\tau, \tag{4.13}$$

$$\varsigma' = \sqrt{\frac{\tau'}{\tau}}\varsigma, \tag{4.14}$$

where, for the first or second stage of dispersion and attenuation, τ and ζ are the shape parameters for c_{11} or c_{22} with C_0 and C_1 being the values of c_{11} or c_{22} in the low- and high- frequency limits respectively, and τ', ζ', C_0', and C_1' are the corresponding values for a different stiffness coefficient of interest.

Using the thus obtained shape parameters τ' and ζ' and also the elastic properties in the low- and high-frequency limits for each stage of dispersion and attenuation (Section 4.2.3), the frequency-dependent values of the other stiffness coefficient can be obtained from equation (4.9) for the non-intersecting fracture case and from equation (4.10) for the intersecting fracture case. It should be noted here that the τ' and ζ' can be estimated from either c_{11} or c_{22} using equations (4.13) and (4.14), as the resulting values are expected to be close. Here, we use the average values of τ' and ζ' obtained from both c_{11} and c_{22}.

4.2.5 Seismic wave velocity and attenuation as functions of incidence angle and associated anisotropic parameters

Once the full stiffness coefficients are computed, we can calculate the seismic wave velocity and attenuation as functions of incidence angle. Rubino et al. (2015) show that the effective elastic properties of saturated rocks containing two sets of orthogonal fractures correspond to those of an orthorhombic medium. Hence, the complex velocities of the qP-, qSV-, and SH-waves can be calculated from the stiffness coefficients using the formulas for orthorhombic media. The complex velocities in the *x-y* plane can then be calculated as follows (Mavko et al., 2009):

$$\tilde{V}_{qP}=\left(c_{66}+c_{22}\cos^2\theta+c_{11}\sin^2\theta+\sqrt{\left(c_{66}+c_{22}\cos^2\theta+c_{11}\sin^2\theta\right)^2-4M}\right)^{1/2}\left(2\rho\right)^{-1/2}, \quad (4.15)$$

$$\tilde{V}_{qSV}=\left(c_{66}+c_{22}\cos^2\theta+c_{11}\sin^2\theta-\sqrt{\left(c_{66}+c_{22}\cos^2\theta+c_{11}\sin^2\theta\right)^2-4M}\right)^{1/2}\left(2\rho\right)^{-1/2}, \quad (4.16)$$

$$\tilde{V}_{SH}=\left(\frac{c_{55}\sin^2\theta+c_{44}\cos^2\theta}{\rho}\right)^{1/2}, \quad (4.17)$$

where ρ is the density of the saturated fractured rock, θ is the incidence angle measured with respect to the *y*-axis, and the expression for M is as follows:

$$M=\left(c_{66}\cos^2\theta+c_{11}\sin^2\theta\right)\left(c_{22}\cos^2\theta+c_{66}\sin^2\theta\right)-\left(c_{12}+c_{66}\right)^2\sin^2\theta\cos^2\theta. \quad (4.18)$$

The complex velocities for seismic waves propagating in the *x*-*z* and *y*-*z* planes can be calculated in a similar way, as can be seen in Mavko et al. (2009). After obtaining the complex velocities, the corresponding phase velocities and attenuations for the qP-, qSV-, and SH-waves can be computed as follows (e.g., Carcione et al., 2013):

$$V=\left[\mathrm{Re}\left(\frac{1}{\tilde{V}}\right)\right]^{-1}, \quad (4.19)$$

$$\frac{1}{Q}=\left|\frac{\mathrm{Im}\left(\tilde{V}^2\right)}{\mathrm{Re}\left(\tilde{V}^2\right)}\right|, \quad (4.20)$$

where $\tilde{V}$ represents the complex velocities of either qP-, qSV-, or SH-waves, and V and $1/Q$ are the corresponding phase velocities and attenuations.

To study the anisotropic properties of fractured rocks, it is convenient to plot Thomsen's style anisotropic parameters. For orthorhombic media, the velocity anisotropic parameters in the *x*-*y* plane can be computed as follows (Tsvankin, 1997; Collet et al., 2014):

$$\varepsilon^{(3)}=\frac{\mathrm{Re}\left(c_{22}-c_{11}\right)}{2\,\mathrm{Re}\left(c_{11}\right)}, \quad (4.21)$$

$$\delta^{(3)}=\frac{\left[\mathrm{Re}\left(c_{12}+c_{66}\right)\right]^2-\left[\mathrm{Re}\left(c_{11}-c_{66}\right)\right]^2}{2\,\mathrm{Re}\left(c_{11}\right)\mathrm{Re}\left(c_{11}-c_{66}\right)}, \quad (4.22)$$

$$\gamma^{(3)} = \frac{\mathrm{Re}\left(C_{44} - C_{55}\right)}{2\,\mathrm{Re}\left(C_{55}\right)}. \tag{4.23}$$

The velocity anisotropic parameters in the other planes (*x*-*z* and *y*-*z* planes) can be calculated in a similar way (Tsvankin, 1997; Collet et al., 2014).

4.2.6 Characteristic frequencies

As discussed above, the characteristic frequencies for all frequency-dependent stiffness coefficients should be similar, which means the characteristic frequencies for the seismic waves at any incidence angles should also be similar. For each stage of seismic dispersion and attenuation (FB-WIFF or FF-WIFF), the behaviours are controlled by two characteristic frequencies, f_P and f_M, as shown in equations (4.11) and (4.12). Here, we focus on analysing the value of f_M as it represents the frequency for the largest attenuation and dispersion (Gurevich et al., 2009). Apart from using equation (4.12), we can also estimate the value of f_M from the diffusivity of the (effective) background medium and the fracture geometries, which is shown in the following.

For FB-WIFF, the fluid diffusion length can be written as follows (Gurevich et al., 2009):

$$l = \sqrt{\frac{\gamma D_b}{f}}, \tag{4.24}$$

where f is the frequency of the seismic wave; γ is a coefficient which depends on the shape of the fractures, for the penny-shaped cracks, $\gamma = 2$, whereas for the planar fractures, γ can be written as follows:

$$\gamma = \frac{\sqrt{2}}{2\pi}\left(\frac{C_b}{M_b}\right)^2\left(1+\frac{1}{L_b Z_N}\right)^2, \tag{4.25}$$

with C_b and L_b the saturated and dry P-wave modulus of the background medium, respectively, M_b the Biot's modulus of the background medium, and Z_N the dry normal fracture compliance of any set of fractures; D_b is the hydraulic diffusivity of the background medium, which has the following form:

$$D_b = \frac{M_b L_b \kappa_b}{\eta C_b}, \tag{4.26}$$

where κ_b is the permeability of the background medium; η is the fluid viscosity.

For the penny-shaped cracks, maximum attenuation due to FB-WIFF occurs when the diffusion length l is of the similar size as the radius of the cracks a (Galvin and Gurevich 2006, 2007). On the other hand, for the planar fractures, the attenuation caused by FB-WIFF is largest when the diffusion length is close to the average half-distance between the consecutive fractures $H/2$. Therefore, the characteristic frequency f_M^{FB} for FB-WIFF has the following form:

$$f_M^{FB} = \frac{\gamma D_b}{L^2}, \tag{4.27}$$

where L is the characteristic diffusion length, which equals to a for the penny-shaped cracks and $H/2$ for the planar fractures.

For FF-WIFF, the fractures are hydraulically isolated from the background medium. However, as discussed in Section 4.2.2, the fluid in the fractures perpendicular to the wave propagation direction can still communicate with the effective background medium, for which the pore space is composed of the fractures parallel to the wave propagation direction and the original saturated background medium acts as the solid phase. The diffusivity for this effective background medium D_e can be written as follows:

$$D_e = \frac{M_e L_e \kappa_e}{\eta C_e}, \tag{4.28}$$

where L_e and C_e are the dry and saturated P-wave moduli of the effective background medium in the wave propagation direction, respectively; κ_e is the effective permeability, as shown in equation (4.1); M_e is the Biot's modulus for this effective background medium, which can be written as follows:

$$M_e = \frac{K_b^{sat}}{\left(1 - K_e / K_b^{sat}\right) - \phi_e \left(1 - K_b^{sat} / K_f\right)}, \tag{4.29}$$

where K_b^{sat} is the saturated bulk modulus for the background medium; ϕ_e is the fraction of the fractures in this effective background medium; K_f is the fluid bulk modulus; K_e denotes the generalized

bulk modulus, which can be calculated using equation (2.13) by replacing C_{ij}^{d} with the corresponding elements of the dry stiffness matrix for this effective background medium.

The energy dissipation due to FF-WIFF occurs primarily in the fractures of this effective medium as for these frequencies fluid only flows within connected fractures (Rubino et al., 2013, 2014). Maximum attenuation thus occurs when the fluid penetrates into the largest possible depth inside connected fractures or, in other words, when the effective diffusion length l computed using the diffusivity D_e is comparable to the radius of the fractures a for the penny-shaped crack case or the average half-distance between the consecutive fractures $H/2$ for the planar fracture case (Gurevich et al., 2009). The characteristic frequency f_M^{FF} for FF-WIFF is then given by:

$$f_M^{FF} = \frac{\gamma D_e}{L^2}. \tag{4.30}$$

It should be noted here that, the characteristic frequencies f_M^{FF} can be calculated for both the P-waves propagating along *x*- and *y*- axis, which should have similar values. Here, we take their average value.

4.3 Numerical example

4.3.1 Sample parameters

Following Rubino et al. (2014), we consider 2D synthetic square samples of side length 20 cm containing 2 orthogonal sets of fractures (Figure 4-4), which are representative of different geological formations of interest. The samples shown in Figs 4-4a and 4-4b contain 20 horizontal and 20 vertical fractures. The major difference between them is that the two perpendicular fracture sets are non-intersecting for one sample, but mostly intersecting for the other one. On the other hand, the samples included in Figures 4-4c and 4-4d also have 20 horizontal fractures and are characterized by contrasting degrees of fracture connectivity, but they only have 10 vertical fractures.

The coordinate system for the samples is established in Figure 4-4, such that the *x*-axis is along the horizontal direction and the *y*-axis is along the vertical direction. The *z*-axis is perpendicular to the *x*-*y*

plane and the samples are long enough along this direction to ensure that they satisfy the plane strain condition. The properties of the fractures and backgrounds remain unchanged for all the samples considered in the analyses. For the background we consider a porosity of 0.1 and, for the solid grains, we use a bulk modulus of 37 GPa and a density of 2.65 g/cm^3. In addition, the dry bulk and shear moduli for this region are 26 GPa and 31 GPa, respectively, whereas its permeability is 10^{-4} mD. The fractures, on the other hand, have a rectangular geometry with a constant length of ~4 cm and a thickness of 0.06 cm. We represent them with a highly compliant porous material having a porosity of 0.8 and a permeability of 100 D. The solid grains composing this porous infill material have the same properties as those of the background medium, whereas the dry bulk and shear moduli are 0.04 GPa and 0.02 GPa, respectively (Nakagawa and Schoenberg, 2007; Rubino et al., 2014). Both the background medium and the fractures are assumed to be fully saturated with water, with a bulk modulus of 2.25 GPa, a shear viscosity of 0.001 Pa*s, and a density of 1.09 g/cm^3.

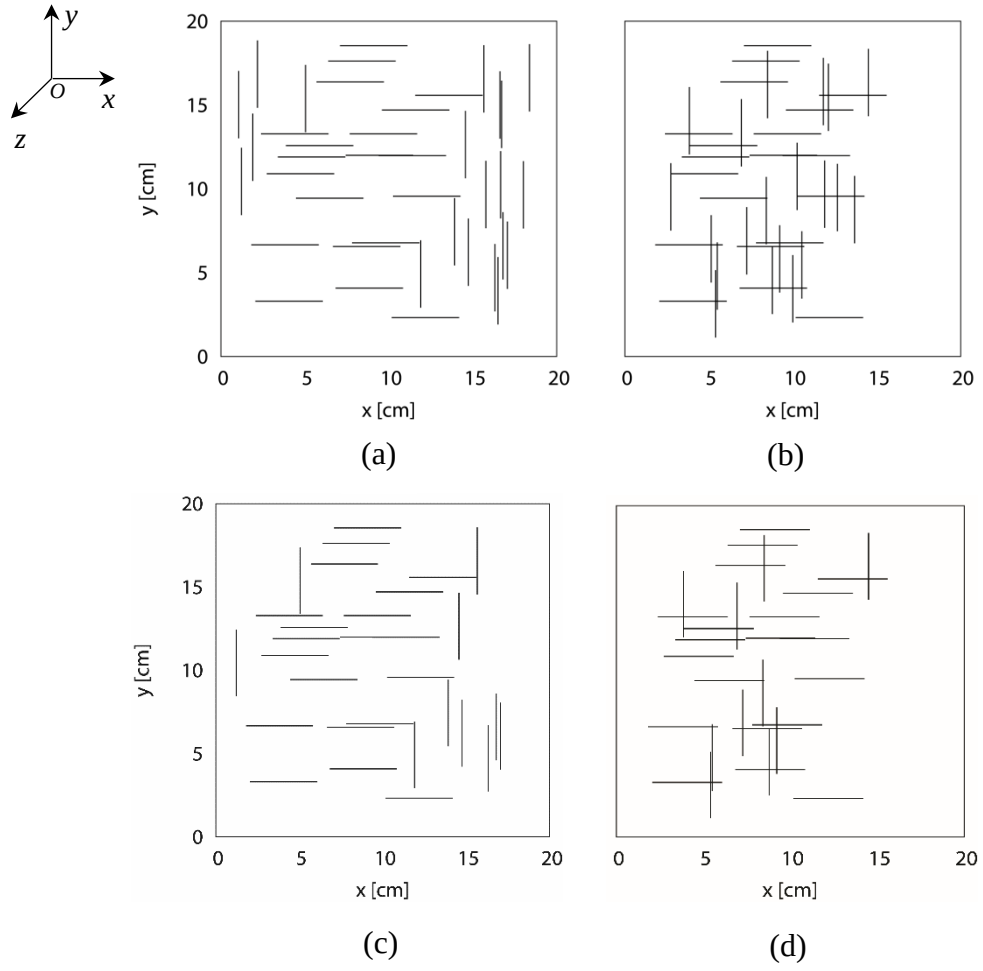

Figure 4-4. Geometries of the investigated 2D synthetic rock samples. Samples (a) and (b) have 20 horizontal and 20 vertical fractures, whereas samples (c) and (d) also have 20 horizontal fractures but 10 vertical fractures. In addition, while samples (a) and (c) contain non-intersecting fractures, in samples (b) and (d) all vertical fractures have at least one intersection.

Apart from obtaining the stiffness coefficients for the described samples using the theoretical approach presented in this work, for comparison we also compute these parameters employing a numerical upscaling procedure (Rubino et al., 2016). To do so, three numerical oscillatory relaxation tests are applied on a given sample of interest, and the responses are obtained by solving the Biot's (1941) quasistatic poroelastic equations. The volume average responses of the probed sample allow us to define an equivalent anisotropic viscoelastic solid which, in turn, provide us with the stiffness coefficients of interest. This numerical approach is briefly outlined in Section 2.10.1 of Chapter 2.

To predict the frequency-dependent stiffness coefficients theoretically, we need to calculate the dry fracture compliance matrixes for the fracture sets perpendicular to the *x*-axis ($\mathbf{S}_{c1}$) and *y*- axis ($\mathbf{S}_{c2}$):

$$\mathbf{S}_{c1} = \begin{pmatrix} Z_{N1} & 0 & 0 & 0 & 0 & 0 \\ 0 & 0 & 0 & 0 & 0 & 0 \\ 0 & 0 & 0 & 0 & 0 & 0 \\ 0 & 0 & 0 & 0 & 0 & 0 \\ 0 & 0 & 0 & 0 & Z_{T3} & 0 \\ 0 & 0 & 0 & 0 & 0 & Z_{T1} \end{pmatrix}, \tag{4.31}$$

$$\mathbf{S}_{c2} = \begin{pmatrix} 0 & 0 & 0 & 0 & 0 & 0 \\ 0 & Z_{N2} & 0 & 0 & 0 & 0 \\ 0 & 0 & 0 & 0 & 0 & 0 \\ 0 & 0 & 0 & Z_{T4} & 0 & 0 \\ 0 & 0 & 0 & 0 & 0 & 0 \\ 0 & 0 & 0 & 0 & 0 & Z_{T2} \end{pmatrix}. \tag{4.32}$$

Here, each fracture set has two different tangential fracture compliances due to the fact that the fracture lengths along *x*- and *z*- axis are different for our 2D samples (Far et al., 2013). Hence, there are six dry fracture compliances in total for these two sets of fractures. However, for the calculation of the elastic properties of the 2D samples, we only need to know four fracture compliances: Z_{N1}, Z_{N2}, Z_{T1}, and Z_{T2}.

The dry fracture compliances Z_{N1}, Z_{N2}, Z_{T1}, and Z_{T2} can be calculated by using the theoretical formulas for 2D fracture compliances or the general Eshelby's model [equation (2.2)]. However, we find that the values obtained from these theoretical models have notable discrepancies with respect to the ones inverted from the stiffness coefficients of the dry samples computed from the numerical simulations. One possible reason for the observed discrepancies is the effect of fracture interactions, which are not considered in the theoretical models. To quantify the effects of fracture interactions on the theoretical models, we employ the schemes of the Differential Effective Medium (DEM) and Self-consistent Approximation (SCA). However, contrary to our expectation, there is nearly no improvement in the agreement between the theoretically predicted and numerically inverted dry fracture compliances. This is consistent with the work of Grechka and Kachanov (2006), who found that in rocks with random distributions of fractures, the influence of fracture interactions is rather small due to the cancellation of the competing effects of stress shielding and amplification, which is also confirmed by the studies in Chapter 3. Hence, there should be another reason for the discrepancies. Since the 2D fractures considered in the theoretical models have elliptical shapes whereas those in the numerical simulations are rectangular, the differences in fracture geometry can be responsible for the discrepancies. To confirm this, we use elliptical fractures in the numerical simulations and compare the results with the theoretical predictions. We observe that the agreement between the theoretically predicted and numerically inverted dry fracture compliances improves greatly. This verifies that the difference in the fracture geometry considered in the theoretical models and numerical simulations is the primary reason for the discrepancies. However, as it is more convenient to use the 2D rectangular fractures for the multiple fracture sets case in the numerical simulations, we keep on using rectangular fractures here. To compare the theoretical predictions with the numerical simulations, we then compute the dry fracture compliances based on the linear slip theory from the stiffness coefficients of the dry samples obtained from the numerical simulations (shown in Table 4-1) as follows:

$$Z_{Ni} = S_{ii} - 1/E_b^{2D},\ i=1, 2, \tag{4.33}$$

$$Z_{T1} + Z_{T2} = S_{66} - 2(1+\nu_b^{2D})/E_b^{2D}, \tag{4.34}$$

where **S** is the dry compliance matrix of the 2D samples, which can be inverted from the dry stiffness matrix provided by the numerical simulations; and E_b^{2D} and ν_b^{2D} are the Young's modulus and Poisson ratio of the 2D background medium, respectively, which have the following relations with the 3D parameters under the plane strain condition:

$$E_b^{2D} = \frac{E_b}{1-\nu_b^2}, \tag{4.35}$$

$$\nu_b^{2D} = \frac{\nu_b}{1-\nu_b}. \tag{4.36}$$

Table 4-1. Dry stiffness coefficients for the samples shown in Figure 4-4 provided by the numerical simulations

	Sample shown in Figure 4-4a	Sample shown in Figure 4-4b	Sample shown in Figure 4-4c	Sample shown in Figure 4-4d
c_{11} (GPa)	27.18	25.82	40.22	33.77
c_{12} (GPa)	0.27	2.07	0.81	2.38
c_{16} (GPa)	-0.14	-0.39	0.28	0.84
c_{22} (GPa)	33.01	32.57	33.86	34.06
c_{26} (GPa)	-0.49	1.06	0.11	0.87
c_{66} (GPa)	9.56	7.65	12.11	10.27

It should be noted that equation (4.34) only provides the sum of Z_{T1} and Z_{T2}. However, their individual values can be estimated based on the fact that the ratios of the normal to tangential compliance Z_N / Z_T for the considered sets of orthogonal fractures are expected to have close values since they are generated in the same fashion. Hence, Z_{T1} and Z_{T2} can be obtained as follows:

$$Z_{Ti} = Z_{Ni} \frac{Z_{T1} + Z_{T2}}{Z_{N1} + Z_{N2}}, \; i = 1, 2. \tag{4.37}$$

The use of the numerically inverted dry fracture compliances in the theoretical model guarantees that the normal and tangential compliances of the dry fractures considered in the numerical simulations and in the theoretical approach are equal, thus allowing the comparisons between the two methodologies. With the dry fracture compliances, the stiffness coefficients of the samples in the low- and high-

frequency limits for each manifestation of WIFF can be computed following the steps described above. To obtain the frequency-dependent behaviour of the stiffness coefficients, the values of T and G also need to be calculated, which requires the elastic properties of the fracture infill material. To compare the 3D theoretical predictions with the 2D numerical simulations, we calculate the effective elastic properties of the equivalent planar fracture infill material from the properties of the dry 2D fractures. For each set of the fractures, these properties are calculated through equations (3.5) and (3.6) using the fraction of the fracture set in the rock f_{ci} and the numerically inverted compliances for the dry 2D fractures Z_{Ni} and Z_{Ti}. Then, these effective fracture infill material properties are used in the calculation of the values of T and G for the planar fracture model, and the value of G for the penny-shaped crack model.

Furthermore, we also need to use the specific surface area and the fracture density of the 2D fractures in the calculations of T and G, which have the following forms for 2D rectangular fractures (Figure 4-4) (Kachanov and Sevostianov, 2005):

$$S_i^{2D} = \frac{f_{ci}}{h_{ci}}, \; i = 1, 2 \tag{4.38}$$

$$\varepsilon_i = \frac{n_i a^2}{A}, \; i = 1, 2 \tag{4.39}$$

where S_1^{2D}, f_{c1}, h_{c1}, ε_1, n_1 are the specific fracture surface area, fraction of fractures in the rock, fracture thickness, fracture density, and number of fractures for the fracture set perpendicular to x-axis. In addition, the subscript 2 represents the corresponding values for the other fracture set, whereas a and A are the fracture radius and area of the sample, respectively.

Using these effective properties of the dry fractures and the other known parameters, the theoretical predictions can be obtained for the three types of fractures (periodic planar fractures, randomly spaced planar fractures, and penny-shaped cracks). Since the samples satisfy the plane strain condition, the results of the 3D theoretical predictions for the stiffness coefficients can then be compared directly with the 2D numerical simulations.

4.3.2 Comparison and analysis

It can be found from the numerical simulation results for the considered samples that only four stiffness coefficients (c_{11}, c_{12}, c_{22}, and c_{66}) need to be considered for the saturated samples, as the other two stiffness coefficients (c_{16} and c_{26}) turn out to be rather negligible (not shown here for brevity). Hence, in this work we only compare these four stiffness coefficients obtained from the numerical simulations and the theoretical predictions. In addition, the numerical simulations also allow us to verify that all the stiffness coefficients have similar frequency-dependent behaviours for both samples with relatively low symmetry (Figures 4-4a and 4-4b) and high symmetry (Figures 4-4c and 4-4d). This validates our assumption that the frequency-dependent behaviours of all the stiffness coefficients should be similar, even for samples with relatively low symmetry. Hence, in the rest of the work we mostly focus the analysis on the stiffness coefficient c_{22}.

4.3.2.1 Dispersion and attenuation due to FB-WIFF

Figure 4-5 shows the dispersion (variation of the real part with frequency) and attenuation (ratio of the imaginary part to the real part) of c_{22} due to FB-WIFF for the samples shown in Figs 4-4a and 4-4b. As explained before, the non-intersecting periodic planar fracture case is not realizable, hence, we only consider the randomly spaced planar fracture and penny-shaped crack cases for the rock with non-intersecting fractures. It can be seen that, for such rock (Figure 4-4a), the theoretical predictions provided by the penny-shaped crack model are in better agreement with the numerical simulations than the randomly spaced planar fracture model (Figs 4-5a and 4-5b). This result is consistent with that obtained for samples with aligned fractures (Chapter 3), which is reasonable as when a seismic wave propagates along the *y*-axis, WIFF primarily occurs between the horizontal fractures and the background for both the non-intersecting and aligned fracture cases. It should also be noted that, even though the fractures in the sample have rectangular geometry (not penny-shaped) and they may interact with each other, good agreement can be found between the results given by the penny-shaped non-interaction crack model and the numerical simulations. This is due to the fact that the effects of the geometry of the fractures and the fracture interactions are taken into account in the theoretical approach, at least partially, by using the numerically-inverted dry fracture compliances.

For the sample with intersecting fractures (Figure 4-4b), it can be seen that, the theoretical predictions for FB-WIFF are also in good agreement with the numerical simulations (Figs 4-5c and 4-5d). Moreover, the results provided by the penny-shaped crack model match the numerical simulations best. Due to fluid pressure equilibration occurring between connected horizontal and vertical fractures, we use scaled values of T and G to calculate seismic dispersion and attenuation due to FB-WIFF, as explained before. The results depicted by Figures 4-5c and 4-5d demonstrate that this approach works well and only small discrepancies are observed between the results of the penny-shaped crack model and the numerical simulations.

It is interesting to notice that, for both samples, the attenuation curves at high frequencies given by the theoretical models are similar. This is because the energy dissipation at high frequencies only occurs in the immediate vicinity of the fractures, which implies that, regardless of the geometry of the fractures, the resulting attenuation is controlled by their specific surface area (Gurevich et al., 2009). As we use the same specific surface area obtained from the real geometries of the considered fractures for the theoretical models, their predictions of attenuation at high frequencies coincide.

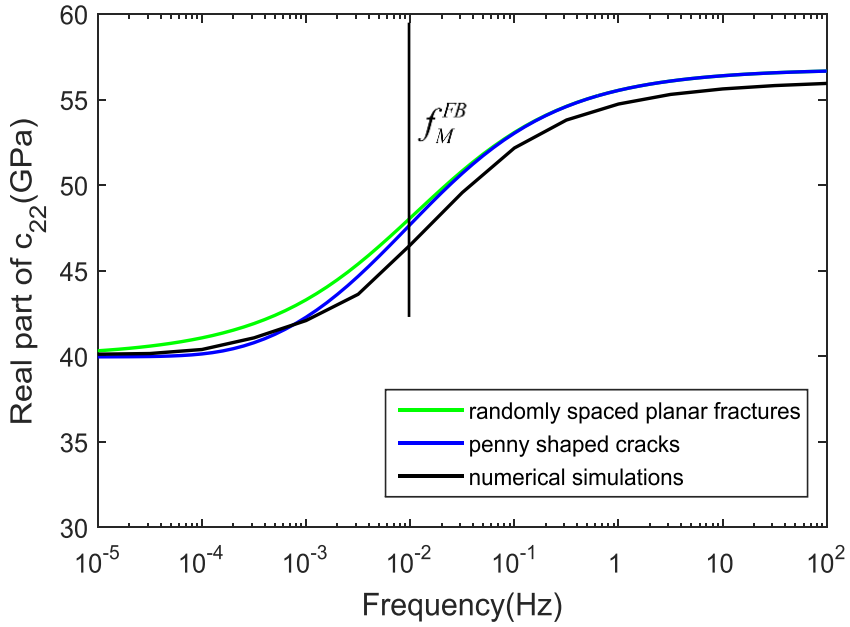
Real part of c_{22}(GPa)
60
55
50
45
40
35
30
f_M^{FB}
randomly spaced planar fractures
penny shaped cracks
numerical simulations
10^{-5}
10^{-4}
10^{-3}
10^{-2}
10^{-1}
1
10
10^{2}
Frequency(Hz)

(a)

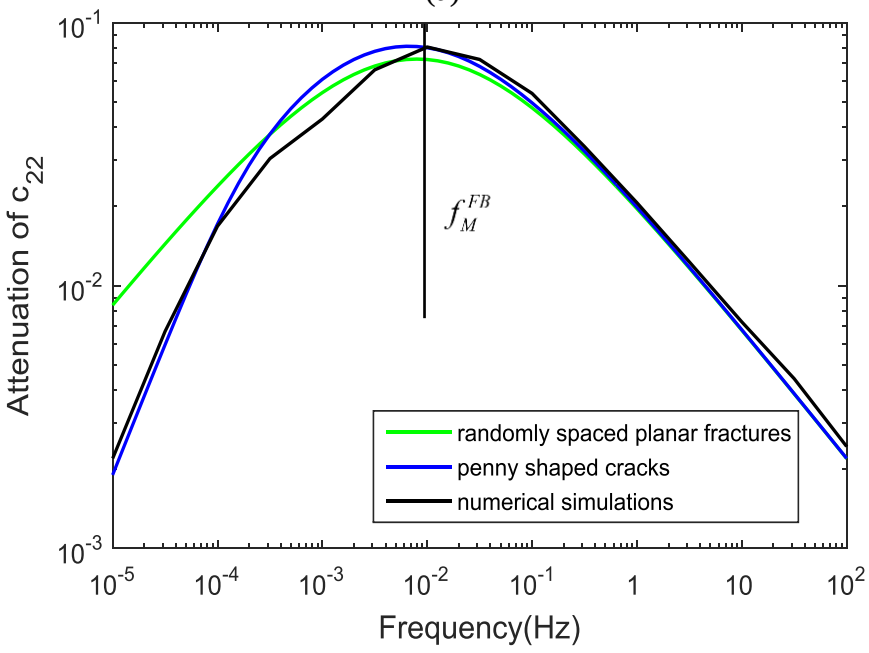
Attenuation of c_{22}
10^{-1}
10^{-2}
10^{-3}
f_M^{FB}
randomly spaced planar fractures
penny shaped cracks
numerical simulations
10^{-5}
10^{-4}
10^{-3}
10^{-2}
10^{-1}
1
10
10^{2}
Frequency(Hz)

(b)

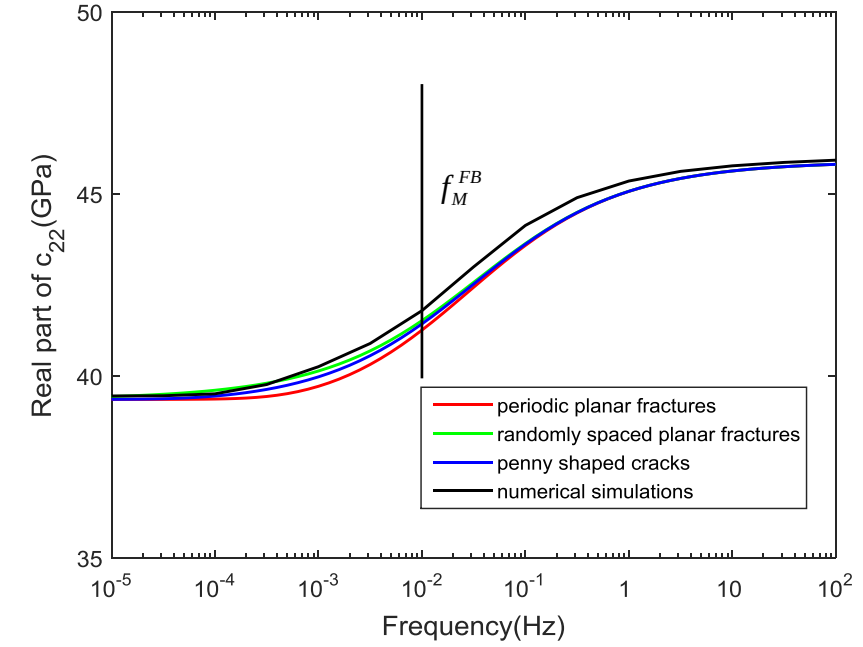

(c)

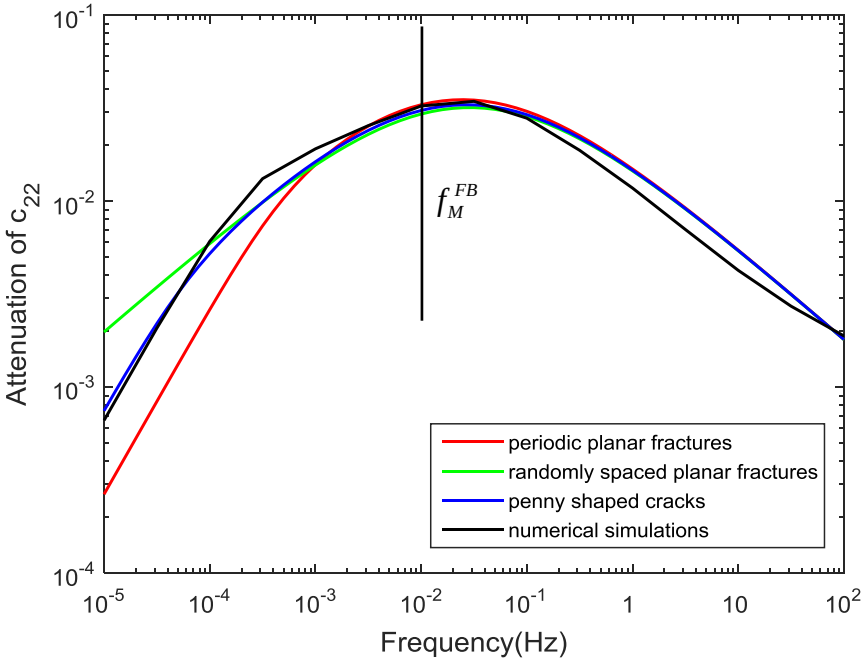

(d)

Figure 4-5. Dispersion and attenuation of c_{22} due to FB-WIFF for the samples containing 20 horizontal and 20 vertical fractures. Panels (a) and (b) show the results for the sample with non-intersecting fractures (Figure 4-4a), while (c) and (d) correspond to the sample with intersecting fractures (Figure 4-4b). The characteristic frequency f_M^{FB} is denoted as vertical lines.

The samples studied above have an equal number of horizontal and vertical fractures, which can be regarded as a special case characterized by a high degree of symmetry. In order to check if our theoretical models are valid in more general situations, we investigate two more samples with non-intersecting and intersecting fractures (Figures 4-4c and 4-4d). Similar to the samples depicted by Figures 4-4a and 4-4b, these new samples have 20 horizontal fractures; however, in order to reduce their degree of symmetry, they only have 10 vertical fractures. Figure 4-6 shows the theoretical results for c_{22} along with the numerical simulations. We can see that, again as before, the theoretical predictions given by the penny-shaped crack model match the numerical simulation results best. For the sample with non-intersecting fractures (Figure 4-4c), the results are very similar to those corresponding to the sample with 20 vertical fractures (compare Figures 4-5a and 4-5b with Figures 4-6a and 4-6b). This further demonstrates that the influence of vertical fractures on the dispersion and attenuation of c_{22} is rather small in absence of fracture intersections. For the sample with intersecting fractures (Figure 4-4d), we see that the value of c_{22} in the high-frequency limit of FB-WIFF is higher than that corresponding to the sample containing 20 vertical fractures (compare Figure 4-5c with Figure 4-6c). This is produced by an increase in the number of non-intersecting horizontal fractures, which do not release their fluid pressure into connected vertical fractures, thus behaving stiffer.

It can be noted that, in contrast to the case of the sample shown in Figure 4-4b, the theoretically predicted value of c_{22} in the high-frequency limit of FB-WIFF for the sample shown in Figure 4-4d is slightly lower than the numerical simulation result (Figure 4-6c). This is due to the fact that, for the sample shown in Figure 4-4b, nearly every fracture is intersected by at least one orthogonal fracture, and hence the fluid pressure is uniform throughout the whole fracture system. Therefore, the theoretical prediction obtained by saturating the fractures through the use of the anisotropic Gassmann's equation is in good agreement with the numerical simulation results. However, for the sample shown in Figure 4-4d, there are several horizontal fractures that are not intersected by any of the vertical fractures. Hence, the fluid pressure increase in these horizontal fractures cannot be released by flowing into the vertical ones, which results in the effective stiffening of the sample. Thus, the theoretical prediction in the high-frequency limit of this WIFF manifestation based on the anisotropic Gassmann's equation underestimates the numerical simulation results.

Since the penny-shaped crack model matches the numerical simulation results best, the characteristic frequency of FB-WIFF f_M^{FB} can be predicted by equation (4.27) with $\gamma = 2$. The results are shown in Figures 4-5 and 4-6 (solid vertical lines). It can be seen that the characteristic frequency is well estimated. Equation (4.27) shows this characteristic frequency depends on the diffusivity of the background medium and the fracture geometries. As all these samples have the same background diffusivity and fracture geometries, the estimated characteristic frequency is the same. However, it can be observed from the theoretical predictions and numerical simulations in Figures 4-5 and 4-6, this characteristic frequency actually shifts slightly between the non-intersecting and intersecting fracture cases. For the non-intersecting fracture case, when a seismic wave propagates in the direction perpendicular to one set of the fractures, fluid flow primarily occurs between this set of fractures and the background medium. However, in the intersecting fracture case, as the fluid pressure is equilibrated between connected horizontal and vertical fractures, the fluid flow between connected fractures that are parallel to the propagation direction and the background medium will also be significant (Rubino et al., 2014). Hence, the different fluid flow characteristics between the non-intersecting and intersecting fracture cases is expected to be responsible for the slight shift of the characteristic frequency of FB-WIFF between these two cases. Since the different fluid flow characteristics are not captured by equation (4.27), it gives identical estimation of the characteristic frequency for all these samples.

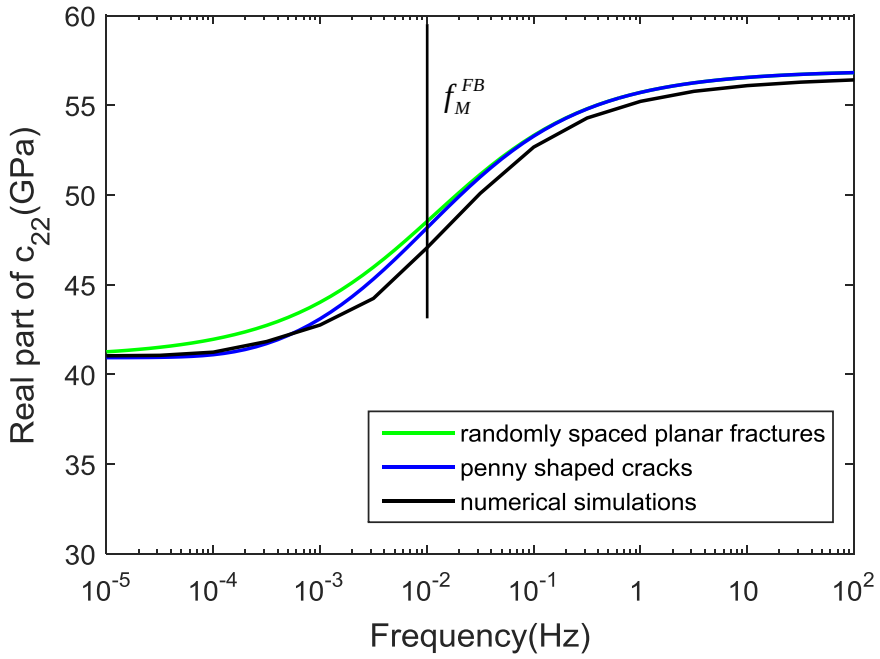
60
55
50
45
40
35
30
Real part of c_{22}(GPa)
f_M^{FB}
randomly spaced planar fractures
penny shaped cracks
numerical simulations
10^{-5}
10^{-4}
10^{-3}
10^{-2}
10^{-1}
1
10
10^{2}
Frequency(Hz)

(a)

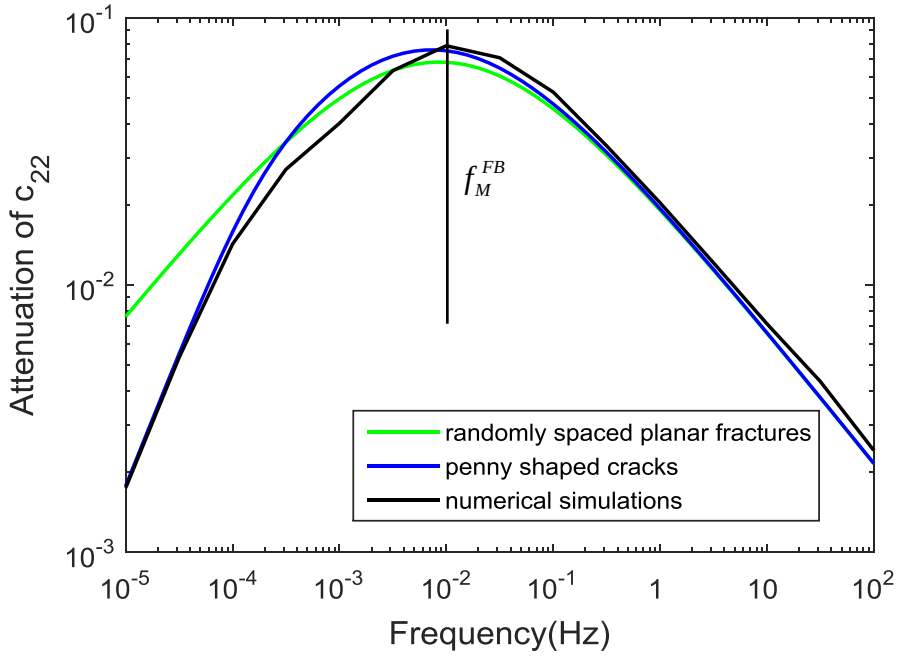
10^{-1}
10^{-2}
10^{-3}
Attenuation of c_{22}
f_M^{FB}
randomly spaced planar fractures
penny shaped cracks
numerical simulations
10^{-5}
10^{-4}
10^{-3}
10^{-2}
10^{-1}
1
10
10^{2}
Frequency(Hz)

(b)

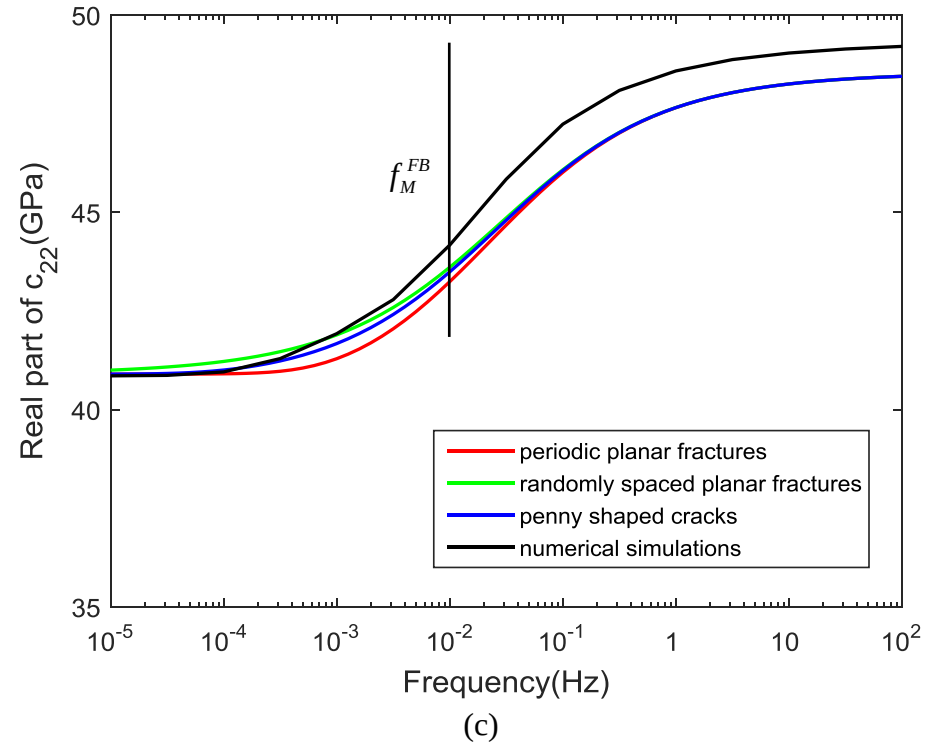

(c)

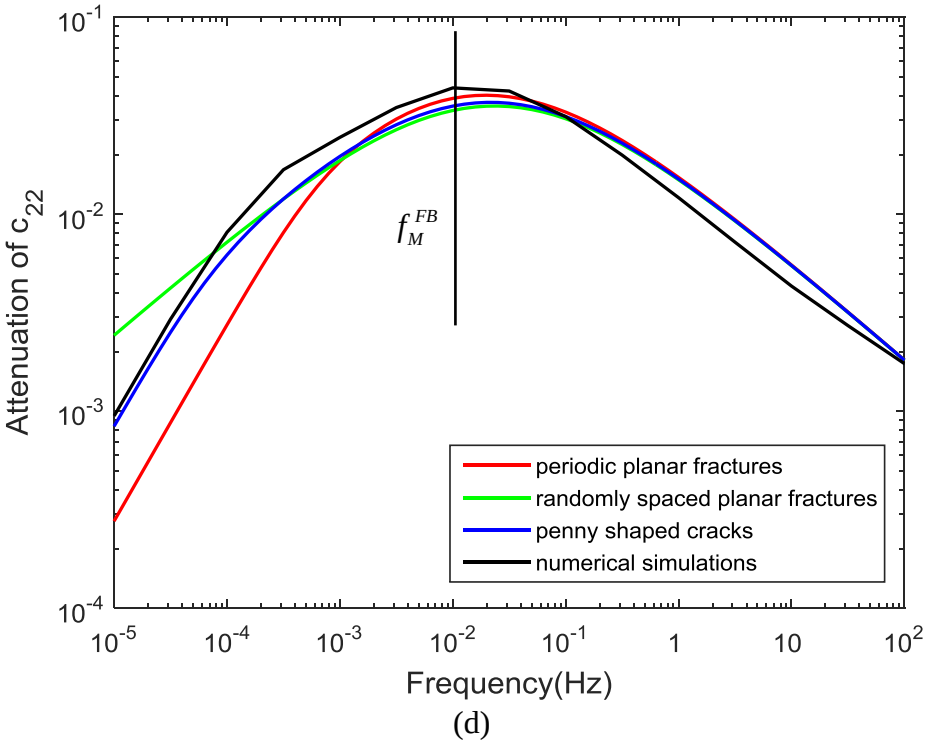

(d)

Figure 4-6. Dispersion and attenuation of c_{22} due to FB-WIFF for the samples containing 10 vertical and 20 horizontal fractures. Panels (a) and (b) show the results for the sample with non-intersecting fractures (Figure 4-4c), while (c) and (d) correspond to the sample with intersecting fractures (Figure 4-4d). The characteristic frequency f_M^{FB} is denoted as vertical lines.

4.3.2.2 Dispersion and attenuation due to FF-WIFF

Figure 4-7 shows the dispersion and attenuation of c_{22} due to FF-WIFF for the samples depicted by Figures 4-4b and 4-4d. We see that, in contrast to the case of FB-WIFF, the theoretical predictions given by the periodic planar fracture model match the numerical simulations best. As explained before, the theoretical predictions for FF-WIFF are based on an effective background medium approach. For c_{22}, the effective background medium is composed of the saturated background as the solid phase and the fractures along the *y*-axis as the pore space. The good agreement between the theoretical predictions provided by the periodic planar fracture model and the numerical simulations indicates that the behaviour of the fractures is largely consistent with that of periodic planar fractures in an effective background medium when FF-WIFF occurs. Hence, we can estimate the characteristic frequency for FF-WIFF f_M^{FF} using equation (4.30) for the planar fracture case. The results are shown in Figure 4-7 (Solid vertical lines). We can see good estimations of the characteristic frequencies f_M^{FF}. It can be noticed that f_M^{FF} for Sample 4-4d is smaller than that for Sample 4-4b, which is primarily due to the decreased permeability of the effective background medium for Sample 4-4d. Further inspection of the curves shown in Figure 4-7 indicates that the discrepancies between the theoretical predictions of the planar fracture model and the numerical simulations are primarily found at low frequencies. This is probably due to the fact that FB-WIFF does not vanish completely at the low frequencies of FF-WIFF. Hence, these two manifestations of WIFF interact with each other for such frequencies, an effect that is not considered in the theoretical predictions presented in this work.

It is important to remark that the effective background medium used here is anisotropic, whereas the background medium for FB-WIFF is isotropic. As discussed above, the theoretical models were originally developed for fractures embedded in an isotropic background medium. Hence, to take into account the anisotropic properties of the effective background medium and, at the same time, to keep our approach simple to apply, we use the properties of the anisotropic effective background medium in the considered direction of wave propagation to replace the original isotropic background properties. This ignores the influence of the properties of the anisotropic background medium in other directions on the FF-WIFF. This, in turn, may be another source of discrepancies between the theoretical

predictions and the numerical simulations. Furthermore, the porosity in the effective background medium is of the same order of magnitude as the fracture porosity. However, our theoretical models assume that the fracture porosity should be much smaller than the porosity in the effective background medium. Hence, this assumption is violated here. This can also cause some errors in the theoretical predictions. In addition, the fractures are assumed to be interconnected to each other in the theoretical model, whereas some fractures are not connected to other fractures in the investigated samples, especially for that shown in Figure 4-4d. This influences the fluid flow characteristics between fractures and hence can be another reason for the discrepancies observed between the theoretical predictions and numerical simulations. All these important points will require detailed analysis in the future.

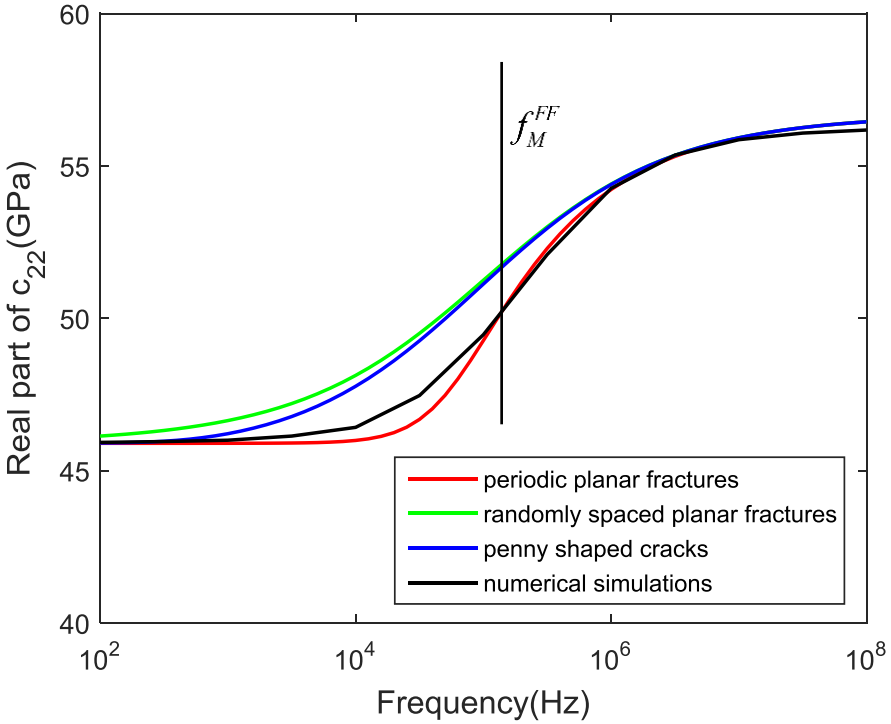
60
55
50
45
40
Real part of c_{22}(GPa)
f_M^{FF}
periodic planar fractures
randomly spaced planar fractures
penny shaped cracks
numerical simulations
10^2
10^4
10^6
10^8
Frequency(Hz)

(a)

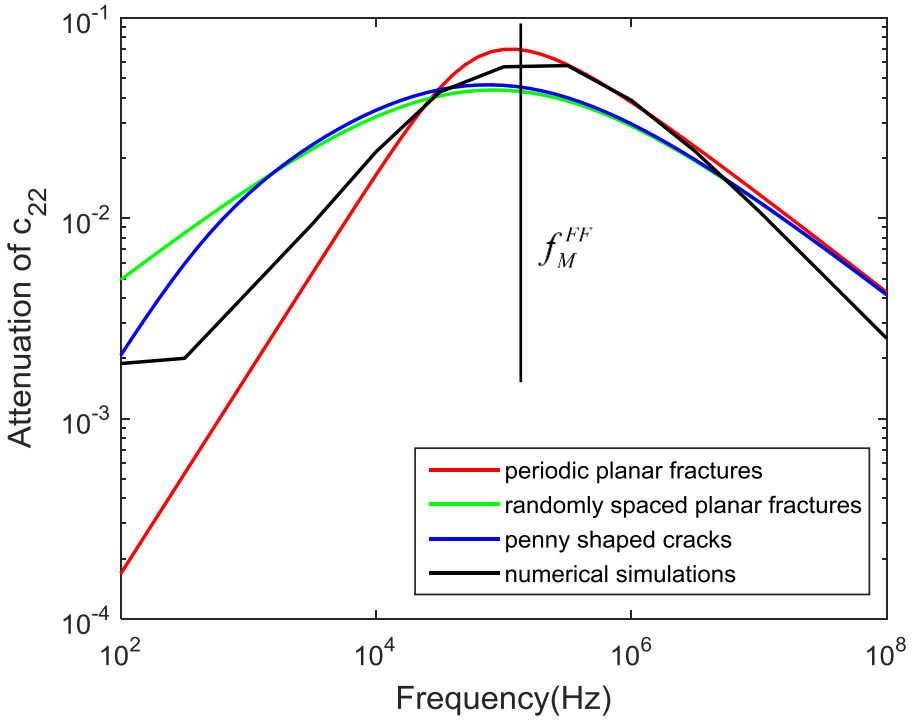
10^{-1}
10^{-2}
10^{-3}
10^{-4}
Attenuation of c_{22}
f_M^{FF}
periodic planar fractures
randomly spaced planar fractures
penny shaped cracks
numerical simulations
10^2
10^4
10^6
10^8
Frequency(Hz)

(b)

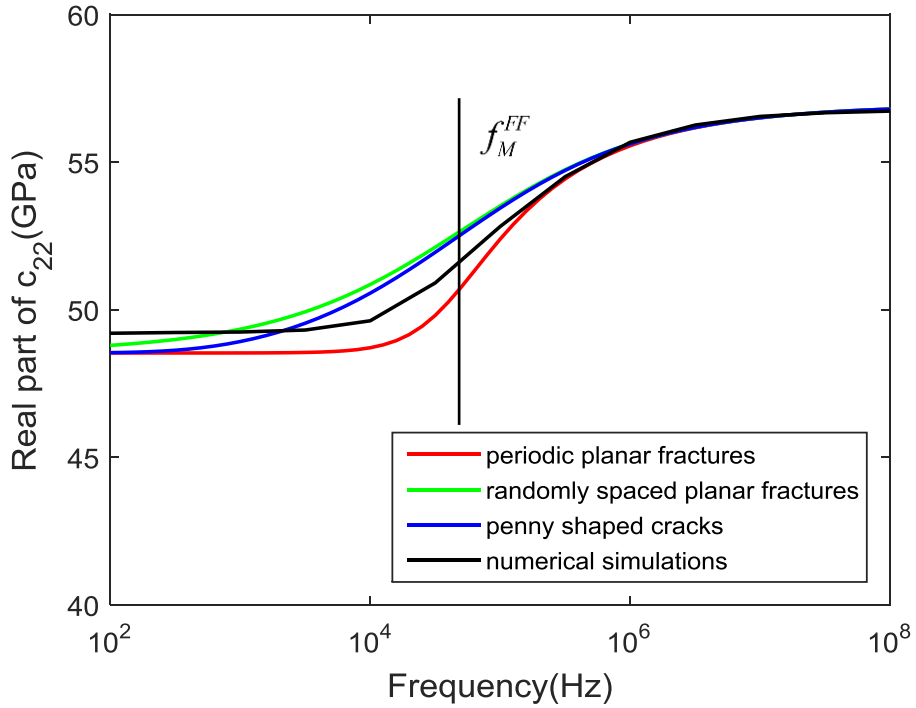
60
55
50
45
40
Real part of c_{22}(GPa)
f_M^{FF}
periodic planar fractures
randomly spaced planar fractures
penny shaped cracks
numerical simulations
10^2
10^4
10^6
10^8
Frequency(Hz)

(c)

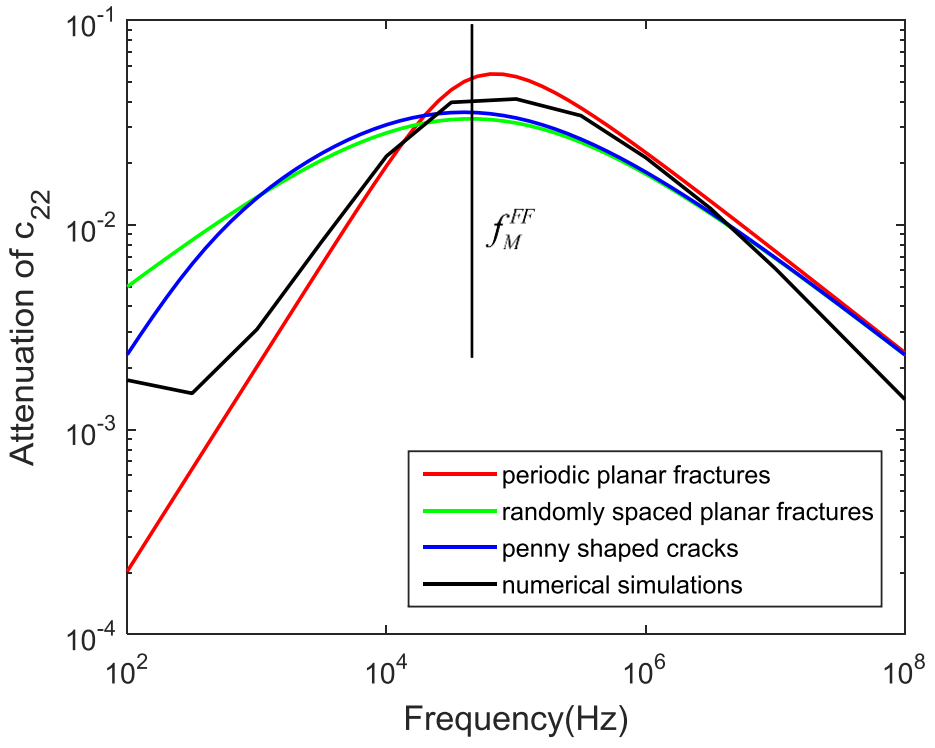
10^{-1}
10^{-2}
10^{-3}
10^{-4}
Attenuation of c_{22}
f_M^{FF}
periodic planar fractures
randomly spaced planar fractures
penny shaped cracks
numerical simulations
10^2
10^4
10^6
10^8
Frequency(Hz)

(d)

Figure 4-7. Dispersion and attenuation of c_{22} due to FF-WIFF. Panels (a) and (b) depict the results for the sample shown in Figure 4-4b, while (c) and (d) correspond to the sample shown in Figure 4-4d. The characteristic frequency f_M^{FF} is shown in vertical lines.

4.3.2.3 Dispersion and attenuation of all the stiffness coefficients for the full frequency range

In Figure 4-8, we compare the theoretical predictions and numerical simulations of the dispersion and attenuation of all the stiffness coefficients for the full frequency range for samples with non-intersecting (Figure 4-4a) and intersecting fractures (Figure 4-4b). The theoretical predictions for the effects caused by FB-WIFF are given by the penny-shaped crack model, whereas the periodic planar fracture model is used for representing those caused by FF-WIFF. For brevity, the results for the samples shown in Figures 4-4c and 4-4d are not included, as they are qualitatively similar to those corresponding to the chosen samples.

For the sample with non-intersecting fractures, we can see good agreement between the theoretical predictions and the numerical simulations (Figures 4-8a and 4-8b). We observe that, in contrast to c_{11} and c_{22}, the real part of c_{12} decreases with frequency, which corresponds to negative attenuation. However, c_{12} does not control any type of seismic wave by itself and, hence, the attenuation of seismic waves propagating through the probed medium remains positive even though that of c_{12} is negative. Furthermore, we can notice in the numerical simulations a small shift of the characteristic frequency of c_{12} compared to that of c_{11} and c_{22}. In the theoretical predictions, we assume that all the stiffness coefficients have nearly the same characteristic frequency. This inconsistency is probably due to fracture interactions, which are not taken into account by the theoretical predictions. In addition, small discrepancies can be found between the theoretical predictions and the numerical simulations for c_{11} at low frequencies. This is likely to be due to fluid diffusion interaction effects at low frequencies. As the vertical fractures tend to concentrate in small areas (Figure 4-4a), fluid diffusion interaction can easily occur between adjacent vertical fractures at low frequencies (Müller and Rothert, 2006). From the point of view of the diffusion process, adjacent vertical fractures tend to merge, which results in an apparent increase of the effective length of fractures at low frequencies. This is not considered in the theoretical predictions, which may cause the small discrepancies observed for c_{11} at low frequencies. To verify this,

we increase the radii of the vertical fractures by a factor of 1.5 when calculating the value of T needed for the theoretical approach. The resulting estimates, which are shown as circles in Figures 4-8a and 4-8b, improve the agreement with the numerical simulations for c_{11}.

It is interesting to note that the shear modulus c_{66} shows small dispersion and attenuation in the numerical simulations for the sample with non-intersecting fractures. In the theoretical predictions, it was assumed that SV-waves propagating along the x- or y- axis do not perturb the fluid pressure field. This, in turn, implies that the shear modulus c_{66} for the saturated sample is equal to that for the dry sample and is independent of frequency. However, in the numerical simulations, due to the heterogeneities of the fractured sample, a smooth fluid pressure gradient is induced and, hence, fluid flow occurs causing slight dispersion and attenuation of c_{66}. This phenomenon was also observed by Caspari et al. (2016).

For the sample with intersecting fractures, good agreement is also observed between the theoretical predictions and the numerical simulations. We see small discrepancies for c_{12}, especially for the dispersion and attenuation due to FF-WIFF. This is primarily due to the fact that the theoretically-predicted value of c_{12} in the high-frequency limit for this WIFF manifestation is slightly lower than the value given by the numerical simulations. Hence, the corresponding theoretically-predicted dispersion and attenuation are slightly larger than the numerical simulation results. In addition, it is interesting to notice that for this sample the dispersion and attenuation of c_{66} in the numerical simulations turned out to be higher than for the sample with non-intersecting fractures. This means that the fluid pressure gradient induced by SV-waves propagating along the x- or y- axis for samples with intersecting fractures is much larger than for samples with non-intersecting fractures.

Here, it is important to note that the investigated frequency range is wide in this case (10^{-5} Hz to 10^{8} Hz). This may violate the quasi-static condition, as the higher frequencies may be larger than the Biot's characteristic frequency (Biot, 1962; Dutta and Odé, 1979). In addition, effective seismic properties can be determined provided that the heterogeneities are much smaller than the considered seismic wavelengths, which is not satisfied for the higher frequencies analysed here. However, considering this wide frequency range is necessary for analysing the mechanisms of both FB-WIFF and FF-WIFF. In this case, the permeability of the background medium is much lower than that of the fractures and hence

the characteristic frequency for FB-WIFF is much lower than that for the FF-WIFF. Therefore, it is essential to investigate these two mechanisms in a wide frequency range. In addition, the frequency range where dispersion takes place is mainly controlled by the permeabilities of the involved materials. This implies that for materials with lower permeabilities, the features taking place above the mentioned threshold frequencies would shift towards lower frequencies, eventually below such threshold values (and can be in the seismic frequency band), thus showing that the results obtained here for unrealistically high frequencies may be useful in other situations.

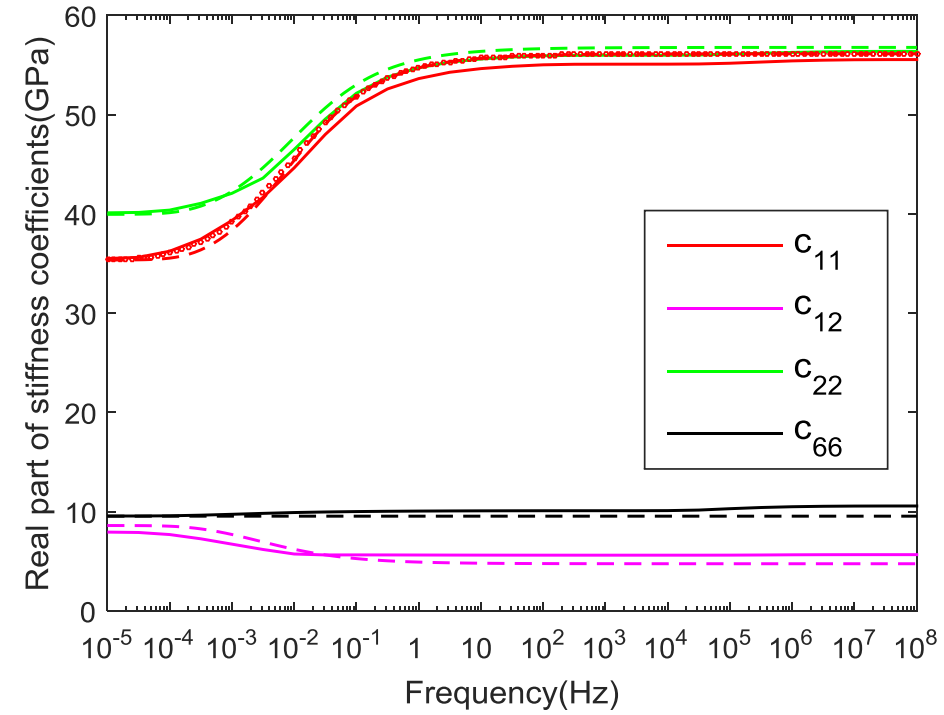
Real part of stiffness coefficients(GPa)
60
50
40
30
20
10
0
10^{-5} 10^{-4} 10^{-3} 10^{-2} 10^{-1} 1 10 10^{2} 10^{3} 10^{4} 10^{5} 10^{6} 10^{7} 10^{8}
Frequency(Hz)
c_{11}
c_{12}
c_{22}
c_{66}

(a)

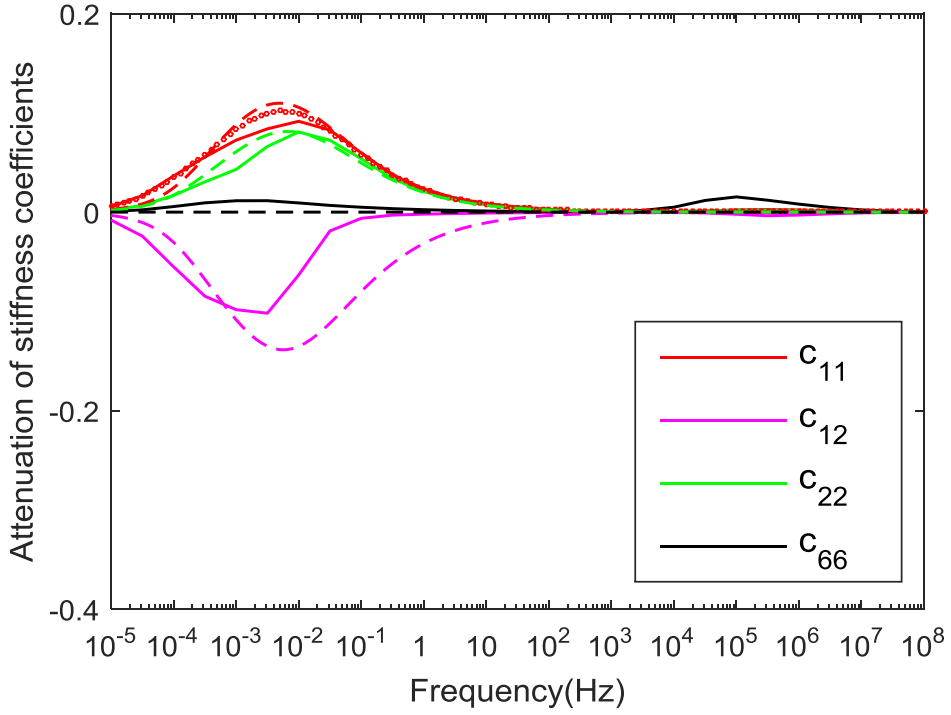
Attenuation of stiffness coefficients
0.2
0
-0.2
-0.4
10^{-5} 10^{-4} 10^{-3} 10^{-2} 10^{-1} 1 10 10^{2} 10^{3} 10^{4} 10^{5} 10^{6} 10^{7} 10^{8}
Frequency(Hz)
c_{11}
c_{12}
c_{22}
c_{66}

(b)

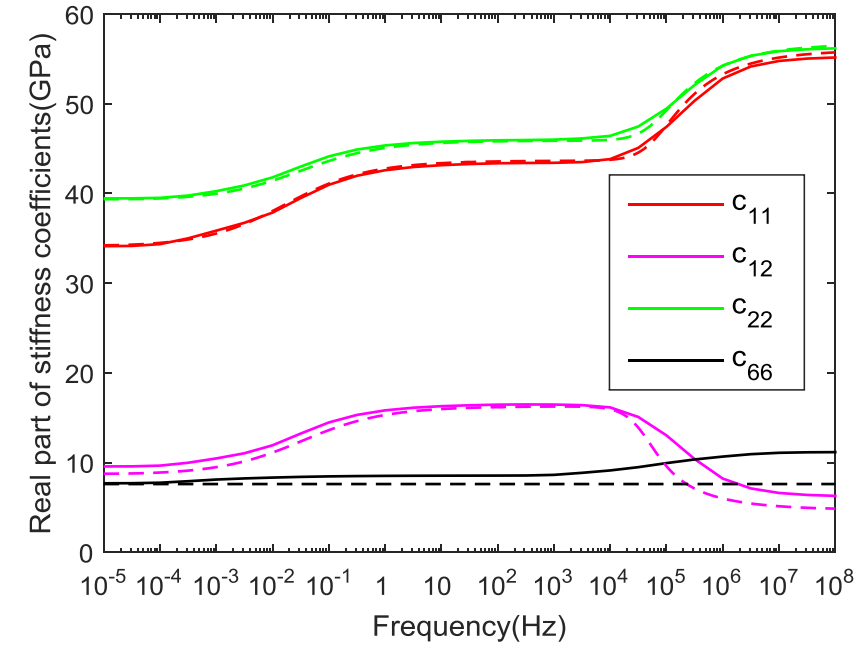

(c)

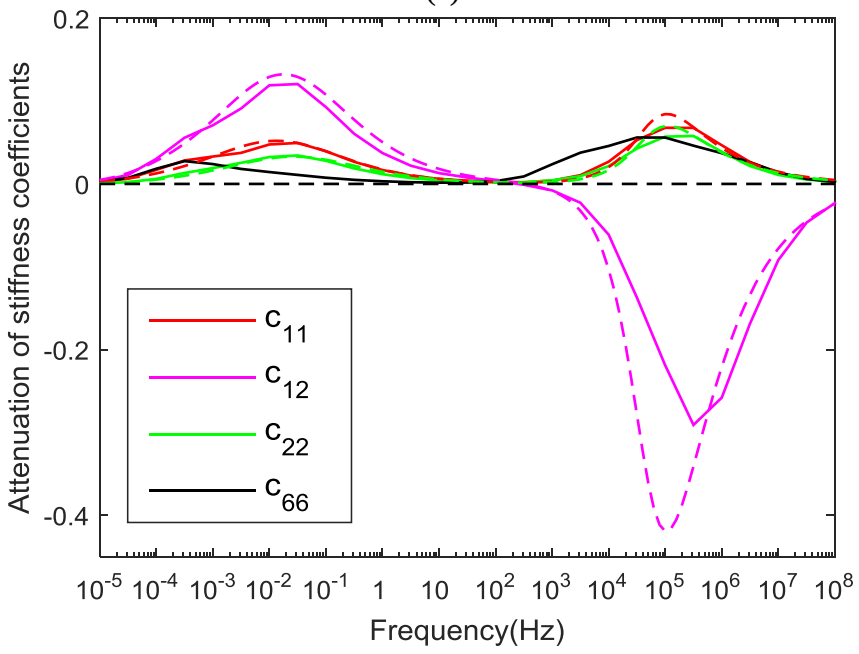

(d)

Figure 4-8. Theoretical predictions (dashed lines) and numerical simulations (solid lines) for all the stiffness coefficients and for the full frequency range. Panels (a) and (b) depict the results for the sample shown in Figure 4-4a, while (c) and (d) correspond to the sample shown in Figure 4-4b. The circles in panels (a) and (b) represent the results for c_{11} considering increased radii of the vertical fractures to account for fluid pressure diffusion interactions.

4.3.2.4 Anisotropic properties

Apart from the full stiffness coefficients, it is also interesting to compare Thomsen's style anisotropy parameters given by the theoretical predictions and the numerical simulations. Using the stiffness coefficients provided by the theoretical predictions and the numerical simulations, the anisotropy parameters $\varepsilon^{(3)}$ and $\delta^{(3)}$ are then calculated using equations (4.21) and (4.22) for the samples shown in Figures 4-4a and 4-4b. For the sample with non-intersecting fractures, Figure 4-9a shows that the theoretical predictions are in overall good agreement with the numerical simulations. Some small discrepancies can be seen, which are primarily caused by the inaccurate value of c_{11} given by the theoretical predictions. If we use the improved value of c_{11} (circles in Figure 4-8a) to calculate the anisotropy parameters (circles in Figure 4-9a), the discrepancies between the theoretical predictions and the numerical simulations get smaller, especially for $\varepsilon^{(3)}$. For the sample with intersecting fractures, we also see overall good agreement between the theoretical predictions of the anisotropy parameters and the numerical simulations (Figure 4-9b). In particular, we see that the theoretical prediction of $\varepsilon^{(3)}$ matches very well with the numerical simulations. On the other hand, while the theoretical prediction of $\delta^{(3)}$ is systematically slightly lower than the numerical simulations, their variations with frequency are similar. The observed differences are mainly due to the discrepancies in the coefficients c_{12} and c_{66}.

To further compare the anisotropic properties given by the theoretical predictions and the numerical simulations, we calculate the phase velocity and attenuation of qP- and qSV-waves as functions of incidence angle. For the sample with non-intersecting fractures (Figure 4-4a), we know from Figure 4-8 that the largest discrepancies between the theoretical predictions and the numerical simulations occur for frequencies close to the characteristic frequency of FB-WIFF (~0.01 Hz). Hence, we compare the predictions at this particular frequency. We observe in Figures 4-10a and 4-10b that the angle-dependent velocities provided by the theoretical prediction and the numerical simulations are in very good agreement, whereas some discrepancies arise in the case of attenuation. This is primarily due to the differences in c_{12} and c_{66} given by the two approaches. In the case of the sample with intersecting fractures (Figure 4-4b), we compare the angle-dependent predictions at a frequency of 10^5 Hz, for which the largest discrepancies took place (Figure 4-8). Figures 4-10c and 4-10d indicate that relatively good agreement between the theoretical predictions and the numerical simulations also occurs

in this case. However, significant discrepancies between the two approaches arise, especially for the qSV-wave at incidence angles of 0° and 90°. The observed discrepancies are also primarily due to the differences in c_{12} and c_{66}. In particular, the shear modulus c_{66} is frequency-independent in the theoretical predictions, whereas it shows some frequency-dependency in the numerical simulations due to the heterogeneity of the sample (Caspari et al., 2016). Indeed, if we assume no frequency-dependency for c_{66} in the numerical simulations, the agreement between theoretical predictions and numerical simulations improves greatly (not shown here for brevity). Hence, in the future, the theoretical model can be further developed to incorporate the frequency-dependency of the shear modulus c_{66}. This should greatly reduce the discrepancies between theoretical predictions and numerical simulations.

It is interesting to note here that the attenuation of P-waves propagating with an incidence angle of 45° vanishes in the theoretical predictions for the sample with intersecting fractures. This is due to the fact that, when the P-wave propagates in this direction, it will generate the same fluid pressure in the horizontal and vertical fractures and, hence, fluid flow within connected fractures is negligible. However, this attenuation value does not completely vanish in the case of the numerical simulations, which is also due to the frequency dependence of c_{66}.

Hence, we have compared the angle dependence of the phase velocity and attenuation of qP- and qSV- waves for the two samples (Figures 4-4a and 4-4b) at the frequencies that showed the largest discrepancies between the theoretical predictions and numerical simulations. For other frequencies, the discrepancies are expected to be much smaller. These results, combined with the comparison of the anisotropic parameters, allow us to conclude that the anisotropic properties given by the theoretical predictions and numerical simulations are in overall good agreement with each other.

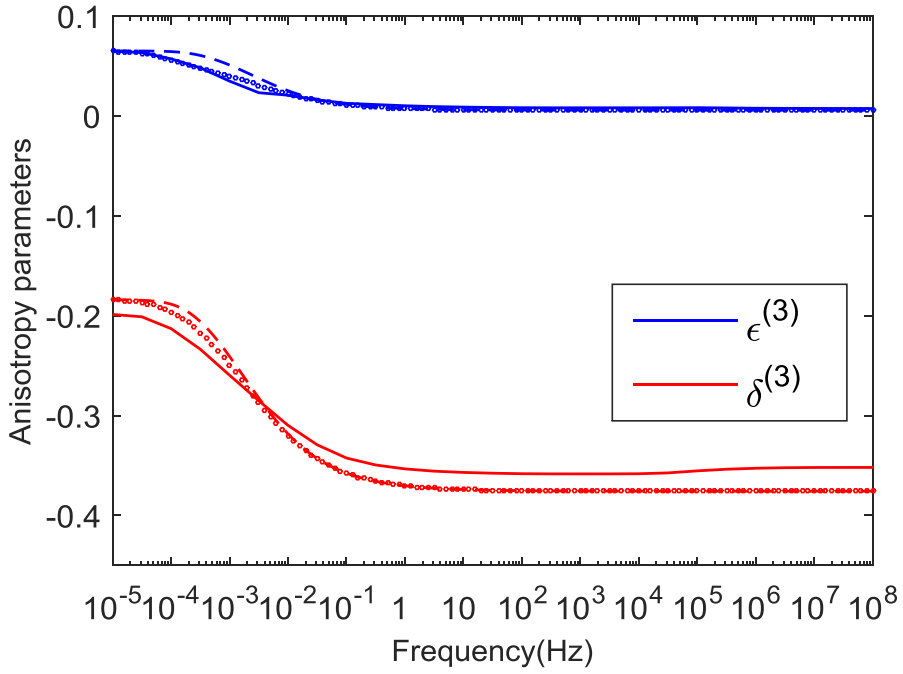

(a)

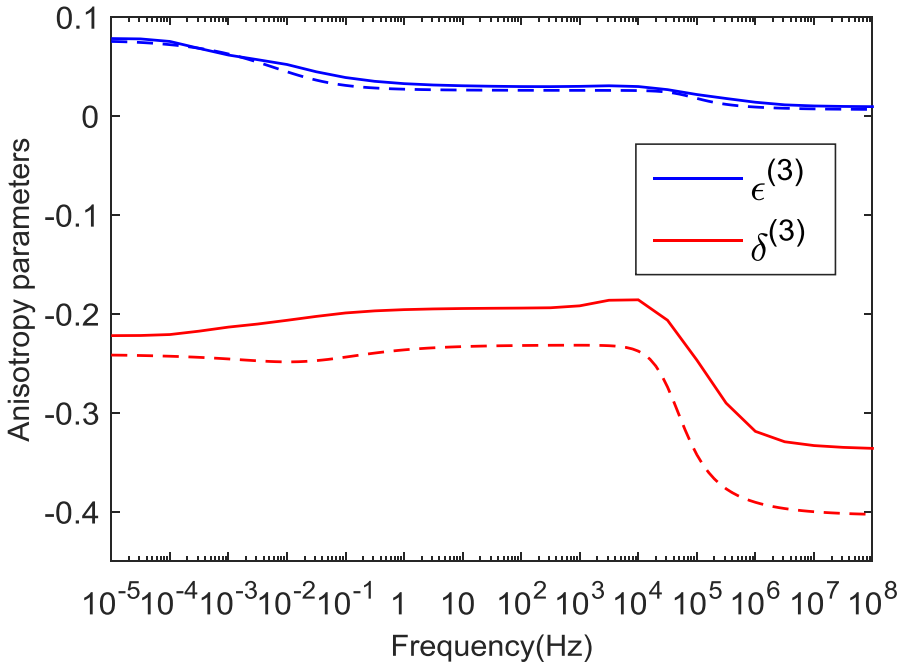

(b)

Figure 4-9. Anisotropic parameters calculated using the stiffness coefficients provided by the theoretical predictions (dashed lines) and the numerical simulations (solid lines). Panels (a) and (b) depict the results for the samples shown in Figure 4-4a and 4-4b, respectively. The theoretical predictions considering increased radii of the vertical fractures to account for fluid diffusion interactions are also given in panel (a) as circles.

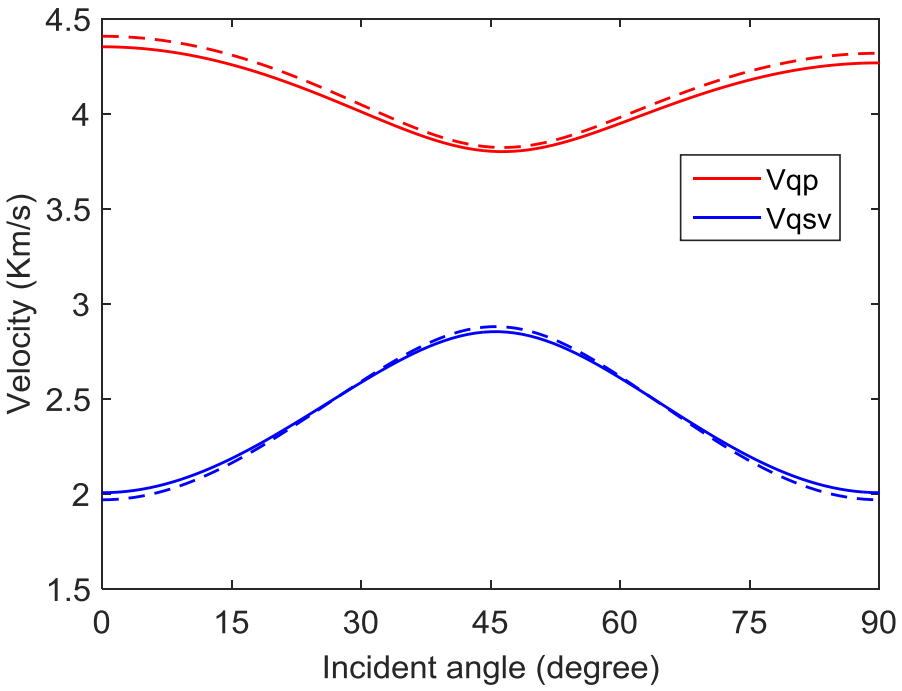
Velocity (Km/s)
Incident angle (degree)
Vqp
Vqsv
4.5
4
3.5
3
2.5
2
1.5
0
15
30
45
60
75
90

(a)

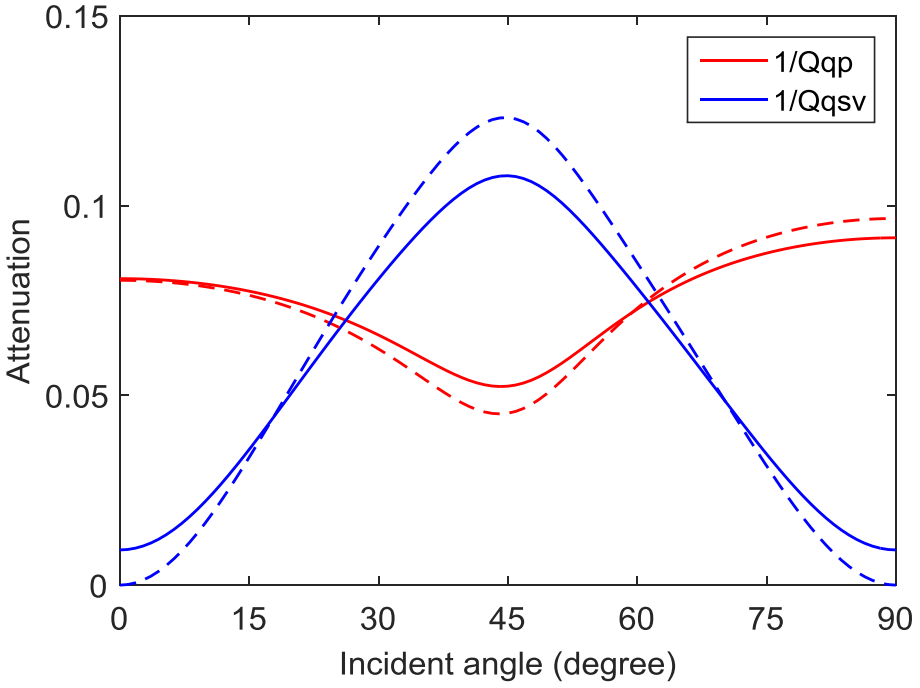
Attenuation
Incident angle (degree)
1/Qqp
1/Qqsv
0.15
0.1
0.05
0
0
15
30
45
60
75
90

(b)

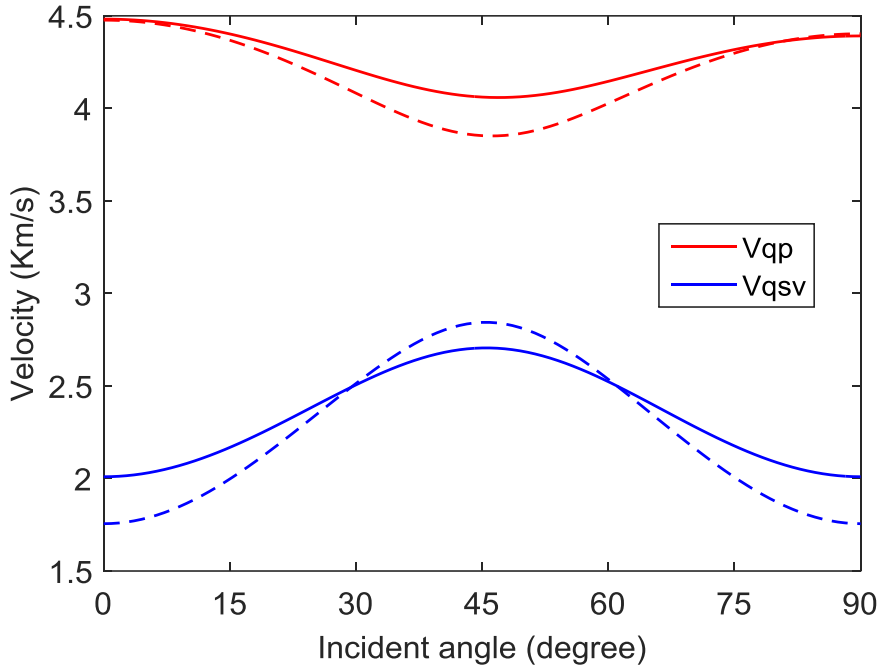

(c)

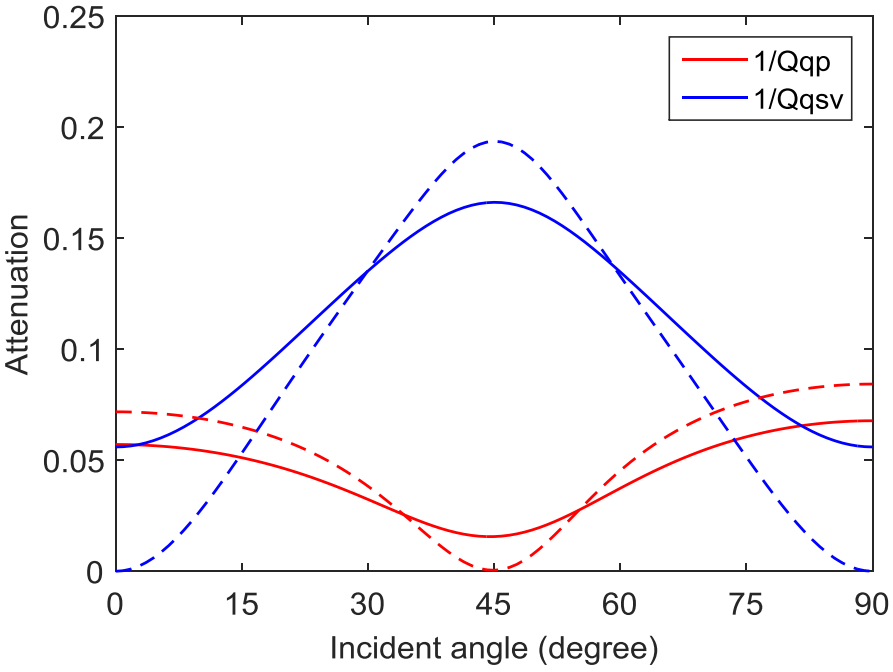

(d)

Figure 4-10. Phase velocity and attenuation of qP- and qSV-waves as functions of incidence angle given by the theoretical predictions (dashed lines) and the numerical simulations (solid lines). Panels (a) and (b) show the results for the sample with non-intersecting fractures (Figure 4-4a) at a frequency of 0.01 Hz, whereas panels (c) and (d) correspond to the sample with intersecting fractures (Figure 4-4b) and a frequency of 10^5 Hz.

4.4. Discussion

In this chapter, we consider seismic dispersion and attenuation in saturated porous rocks containing two orthogonal sets of non-intersecting and intersecting mesoscopic fractures. To validate our theoretical model, we compare its predictions with corresponding numerical simulations. However, due to the high computational cost of 3D numerical simulations, we only consider 2D cases and compare the results with 3D theoretical predictions. To enable this comparison, we obtain effective parameters for the 2D samples and then substitute them into the 3D theoretical model, as shown in Section 4.3.1. The good agreement between the theoretical predictions and the numerical simulations means that a model designed for axisymmetric penny-shaped cracks is also valid for slit 2D fractures (especially for the FB-WIFF effects), which is also verified in the last chapter for the study of the aligned fracture case.

Up until now, a number of theoretical models have been proposed to study seismic wave propagation in saturated porous rocks with multiple sets of fractures (e.g., Liu et al., 2006; Chapman, 2009). However, these models assume that the fractures are hydraulically connected to the background medium, but unconnected to each other. Hence, effects due to fluid flow between the background medium and the fractures (FB-WIFF) are considered, whereas those related to flow within connected fractures (FF-WIFF) are neglected (e.g., Liu et al., 2006; Chapman, 2009). Thus, these models should predict frequency-dependent elastic properties for the non-intersecting fracture cases similar to those provided by our theoretical model. However, in presence of connected fractures these models cannot account for the corresponding effects on both FB- and FF-WIFF effects. A detailed comparison between these models and the one proposed in this paper will be carried out in the future.

It is important to remark here that, in presence of intersecting fractures, the degree of seismic dispersion and attenuation caused by FB-WIFF is significantly reduced due to the fluid pressure communication within connected fractures, as shown in Figure 4-8. In addition, the velocity anisotropy of such rocks can also be significantly reduced due to variations of the stiffening effects of the fracture fluid in response to FF-WIFF (Rubino et al., 2017). Hence, it is of great importance to consider both manifestations of WIFF when interpreting seismic data from fractured reservoirs. This, in turn, may

provide the possibility to extract information on the connectivity degree of fracture networks from seismic recordings.

4.5 Conclusions

In this chapter, we proposed a theoretical approach to describe seismic dispersion and attenuation of saturated porous rocks containing two orthogonal sets of non-intersecting or intersecting fractures. The methodology is based on theoretical models for rocks with aligned fractures, and three types of fracture geometries are considered, namely, periodic planar fractures, randomly spaced planar fractures, and penny-shaped cracks. For rocks with non-intersecting fractures, seismic dispersion and attenuation are produced by FB-WIFF, a process similar to that arising in rocks containing aligned fractures. Hence, the theoretical models for aligned fractures can be directly extended to this case for computing the P-wave moduli in the directions perpendicular to the two fracture sets, from where the remaining elastic moduli are derived. For rocks with intersecting fractures, FF-WIFF also occurs at higher frequencies. Similar to the non-intersecting fracture case, the effects due to FB-WIFF can be computed by extending the theoretical models for aligned fractures. Conversely, for computing the effects caused by FF-WIFF, an effective background medium is introduced. The theoretical models for aligned fractures are then used, with the original background replaced by the effective medium, where the fractures perpendicular to the propagation direction are immersed.

2D synthetic rock samples containing two orthogonal sets of fractures with varying degrees of intersections are then explored. To do this, apart from the theoretical predictions, numerical simulations are also carried out, which consist of an upscaling method in the framework of Biot's quasi-static equations of poroelasticity. The results show that the theoretical predictions are in overall good agreement with the numerical simulations. For the effects caused by FB-WIFF, the theoretical model for penny-shaped cracks matches the numerical simulations best, whereas for those produced by FF-WIFF the model for periodic planar fractures is the most suitable one. Furthermore, we also observe good agreement between the theoretical predictions and the numerical simulations of the anisotropic properties. The proposed theoretical approach is convenient to apply in practice, and is applicable not

only to 2D but also to 3D fracture systems. Therefore, it has the potential to constitute a powerful tool to assist in the seismic characterization of fracture systems.

Chapter 5

Scattering of seismic waves by aligned fluid saturated fractures with finite thickness

5.1 Introduction

In Chapters 3 and 4, we have studied the dispersion and attenuation of seismic wave in fractured reservoirs due to WIFF. Besides this mechanism, as discussed in Chapter 1, the wave scattering by the fractures can also result in significant seismic dispersion and attenuation when the fractures have similar size with the seismic wavelength. These large fractures can form the fracture 'swarms' or fracture 'corridors', which is of great importance for the fluid flow (e.g., Questiaux et al., 2010), especially in the carbonate or unconventional fractured reservoirs. As the wave scattering depends critically on the fracture geometries and spatial distributions (e.g., Vlastos et al., 2003, 2006, 2007), it is possible to characterize such large fractures through the scattering attributes, such as scattering dispersion and attenuation (e.g., Landa et al., 1987; Kanasewich and Phadke, 1988; Vasconcelos and Jenner, 2005; Willis et al., 2006; Burns et al., 2007; Tsingas et al., 2010). In order to do so, it is essential to study the mechanism for the scattering dispersion and attenuation.

Up until now, while a few models have been proposed to study the wave scattering by the fluid saturated fractures (Chapter 1), most of them consider the fracture thickness to be infinitesimal. For dry fractures, the influence of the fracture thickness is negligible both in the quasi-static and dynamic regimes, provided that the fracture aspect ratio is not very large (usually smaller than 0.1) (e.g., Schoenberg and Douma, 1988; Sabina et al., 1993; Smyshlyaev and Willis, 1993b). However, for fluid saturated fractures, the fracture thickness has a significant influence on the elastic properties of the

fractured rocks and therefore, on wave propagation even in the quasi-static regime (e.g., Chapter 3; Kuster and Toksöz, 1974). Hence, in the dynamic regime, it is also essential to study the effects of the fracture thickness on wave scattering and the corresponding dispersion and attenuation for the case of fluid saturated fractures.

In this chapter, we develop a model for the P-wave scattering dispersion and attenuation by aligned fluid saturated 2D fractures with finite thickness, which are distributed randomly in an isotropic elastic background medium. The model is developed by extending the model for dry open fractures introduced in Chapter 2, which was proposed by Kawahara (1992). A numerical example is used to explore the effects of the fracture thickness and the saturating fluid properties on wave scattering dispersion and attenuation. To validate this model, the theoretical predictions are also compared to the ultrasonic measurements on fractured samples.

The contents of this chapter have been submitted to Geophysical Journal International (Guo et al., 2018e).

5.2 Theory for scattering by aligned fluid saturated fractures

Here, we assume the same model as Kawahara (1992), which was introduced in Chapter 2. In this model, the aligned 2D fractures are distributed randomly and sparsely in an infinite elastic isotropic background medium, as shown in Figure 2-2. The fracture geometries and elastic properties of the background medium in our model is same with those in Kawahara model. The only difference is that, in our model, we assume that the fractures are saturated with a single fluid, whereas the original model assumes the dry fractures.

When the fractures are saturated with a viscous fluid, the fracture displacement discontinuities will be influenced by the fluid. However, the relation between the scattered wave field and the fracture displacement discontinuities remains unchanged and hence equations (2.77) – (2.80) are still applicable (Kawahara, 1992). Therefore, to obtain the P-wave scattering dispersion and attenuation for fluid filled fractures, the corresponding displacement discontinuities (D_1 and D_2) across the fractures need to be

calculated. In this case, the fluid will apply both normal and shear stresses on the fracture surface as follows:

$$\sigma_{12}^{E}+\sigma_{12}^{S}=-i\omega\eta\frac{\left[\Delta\mathbf{u_i}\left(x_1,p_1,p_2\right)\right]_1}{\beta},\ -a<x_1<a,\ x_2=0, \tag{5.1}$$

$$\sigma_{22}^{E}+\sigma_{22}^{S}=K_f\frac{\left[\Delta\mathbf{u_i}\left(x_1,p_1,p_2\right)\right]_2}{\beta},\ -a<x_1<a,\ x_2=0, \tag{5.2}$$

where η and K_f are the shear viscosity and bulk modulus of the fluid, respectively. The shear stress is caused by the viscous friction between the fluid and the fracture surface (Kawahara and Yamashita, 1992), whereas the normal stress is equal to the fluid pressure in the fracture, which is generated due to the fracture volume compression (or extension). It should be noted that, as we consider the fluid with relatively high viscosity, the fluid flow inside the fracture is ignored and hence the fluid pressure is not equilibrated, and can vary with the location x_1.

By substituting equations (2.64), (2.68) and (2.70) into equations (5.1) and (5.2), we can obtain:

$$\int_{-a}^{a}D_1\left(\zeta_1\right)T_{121}\left(x_1,0\,|\,\zeta_1,0\right)d\zeta_1-e^{ik_px_1\sin\theta}=\frac{i\omega\eta}{\mu}\frac{D_1\left(x_1\right)}{\beta},\ -a<x_1<a, \tag{5.3}$$

$$\int_{-a}^{a}D_2\left(\zeta_1\right)T_{222}\left(x_1,0\,|\,\zeta_1,0\right)d\zeta_1-e^{ik_px_1\sin\theta}=-\frac{K_f}{\mu}\frac{D_2\left(x_1\right)}{\beta},\ -a<x_1<a, \tag{5.4}$$

where the relations between D_j and $\left[\Delta\mathbf{u_i}\right]_j$ are given by equations (2.75) and (2.76).

Hence, by solving equations (5.3) and (5.4), the values of D_1 and D_2 can be obtained. It is difficult to solve equations (5.3) and (5.4) analytically, however, it is straightforward to solve them numerically using the method proposed by Kawahara and Yamashita (1992). This can be done by first normalizing equations (5.3) and (5.4) as follows:

$$\int_{-1}^{1}\hat{D}_1\left(\hat{\zeta}_1\right)\hat{T}_{121}\left(s,0\,|\,\hat{\zeta}_1,0\right)d\hat{\zeta}_1-e^{i\hat{k}_ps\sin\theta}=\frac{i\omega\eta a}{\mu}\frac{\hat{D}_1\left(s\right)}{\beta},\ -1<s<1, \tag{5.5}$$

and

$$\int_{-1}^{1} \hat{D}_2\left(\hat{\zeta}_1\right)\hat{T}_{222}\left(s,0\,|\,\hat{\zeta}_1,0\right)d\hat{\zeta}_1 - e^{i\hat{k}_p s\sin\theta} = -\frac{K_f a}{\mu}\frac{\hat{D}_2(s)}{\beta},\ -1 < s < 1, \tag{5.6}$$

where $\hat{\zeta}_1, s, \hat{k}_p, \hat{D}_1, \hat{D}_2, \hat{T}_{121}$, and $\hat{T}_{222}$ are normalized values by the half of the fracture length a as follows:

$$\hat{\zeta}_1 = \zeta_1 / a, \tag{5.7}$$

$$s = x_1 / a, \tag{5.8}$$

$$\hat{k}_p = a k_p, \tag{5.9}$$

$$\hat{D}_j = D_j / a, j = 1, 2 \tag{5.10}$$

$$\hat{T}_{j2j} = a^2 T_{j2j}, j = 1, 2 \tag{5.11}$$

Then, equations (5.5) and (5.6) can be discretised as follows:

$$\sum_{n=1}^{M-1}\left(T_{mn}^{121} - \delta_{mn}\frac{i\omega\eta a}{\mu\beta}\right)\hat{D}_{1n} = e^{i\hat{k}_p s_m\sin\theta},\ m = 1, \ldots, M\text{-}1 \tag{5.12}$$

and

$$\sum_{n=1}^{M-1}\left(T_{mn}^{222} + \delta_{mn}\frac{K_f a}{\mu\beta}\right)\hat{D}_{2n} = e^{i\hat{k}_p s_m\sin\theta},\ m = 1, \ldots, M\text{-}1 \tag{5.13}$$

where $s_m = -1 + m\Delta s$, $\Delta s = 2/M$, T_{mn}^{121} and T_{mn}^{222} are calculated from $\hat{T}_{121}$ and $\hat{T}_{222}$ as follows:

$$T_{mn}^{j2j} = \int_{s_n-\Delta s/2}^{s_n+\Delta s/2}\hat{T}_{j2j}\left(s_m,0\,|\,\hat{\zeta}_1,0\right)d\zeta_1,\ j = 1, 2. \tag{5.14}$$

The expressions of T_{mn}^{121} and T_{mn}^{222} are given in Appendix B. Hence, $\hat{D}_1$ and $\hat{D}_2$ can be computed by solving the matrix equations (5.12) and (5.13) using the corresponding numerical algorithm. Then, ϕ_1 and ϕ_2 can be calculated as follows:

$$\phi_j = a^2 \hat{\phi}_j \, , j = 1, 2, \tag{5.15}$$

where

$$\hat{\phi}_j = \sum_{m=1}^{M-1} \hat{D}_{jm} e^{-i\hat{k}_p s_m \sin\theta} \Delta s \, , j = 1, 2. \tag{5.16}$$

Substituting equation (5.15) into equation (2.77) yields:

$$\kappa = \varepsilon \hat{\phi}_1 \gamma k_p \sin 2\theta \sin\theta + \varepsilon \hat{\phi}_2 \frac{k_p}{2\gamma \cos\theta} \left(1 - 2\gamma \sin^2\theta\right)^2 , \tag{5.17}$$

where $\varepsilon = va^2$ is called the fracture density for the slit fractures (e.g., Kachanov and Sevostianov, 2005). It can be seen from equation (5.17) that the expression for the fracture density is the same for the dry and saturated fractures, the saturating fluid only influences the normal and shear displacement discontinuities across the fractures. Furthermore, we can observe from equations (5.12) and (5.13) that in the low frequency limit, the normalized fracture displacement discontinuities for the saturated fractures are affected by the fracture aspect ratio, whereas those for the dry fractures are independent of the fracture aspect ratio. This is consistent with the Eshelby model (Mura, 1987; Sevostianov and Kachanov, 1999).

After the value of κ has been obtained, the P-wave scattering dispersion and attenuation for the fluid saturated fracture case can be obtained from equations (2.79) and (2.80). It can be noted that the scattering dispersion and attenuation are not controlled by the number density v, but the combination of the number density and half of the fracture length (i.e., fracture density ε).

5.3 Numerical example

5.3.1 Parameters

In this section, we give a numerical example to study the P-wave scattering dispersion and attenuation in the fractured reservoir. We consider a carbonate reservoir with negligible background porosity (e.g., Rashid et al., 2015). The properties of the isotropic elastic background medium are taken as follows: bulk modulus K_s = 63.7 GPa, shear modulus G_s = 31.7 GPa, and density ρ_s = 2.70 g/cm^3 (Mavko et al., 2009). Large 2D fractures (fracture corridors) are developed in the reservoir with their planes parallel to each other and centres distributed randomly and sparsely in the background medium. It is assumed that the size of the fractures is identical to a length 2a of 40 m and a thickness β of 0.4 m (aspect ratio α = 0.01). The fractures are assumed to be saturated with a viscous fluid, which has a bulk modulus K_f of 2.25 GPa (close to that of water) and a relatively high shear viscosity η of 0.1 Pa*s.

Using these parameters, we can first analyse the variations of the scattering dispersion and attenuation with frequency, fracture density, and incidence angle. Then, we can vary the fracture thickness and the saturating fluid properties to study their influence on the scattering dispersion and attenuation. Since the peak scattering attenuation occurs when the seismic wavelength is comparable to the fracture length (e.g., Kawahara and Yamashita, 1992), the frequencies studied here range from 10 Hz to 1000 Hz due to the large fracture length (40 m).

5.3.2 Variations of P-wave velocity and attenuation with frequency, fracture density, and incidence angles.

The variations of the P-wave velocity and attenuation with frequency f, fracture density ε, and incidence angle θ are shown in Figures 5-1 and 5-2, respectively. It can be seen that in the low frequency regime (Rayleigh scattering domain), the P-wave velocity decreases slightly with the frequency. Then it increases rapidly when the resonant (or Mie) scattering (e.g., Ishimaru, 1978) occurs at around 100 Hz, for which the incidence wavelength is on the same order of size with the fracture radius. In the high frequency regime, the P-wave velocity tends to the value of the background medium with some small fluctuations. These small fluctuations are probably due to the interference pattern variations of the scattered wave fields generated from the fracture tips (Kawahara and Yamashita, 1992). These behaviours of the P-wave velocity with the frequency are similar to the case with dry fractures (Kawahara, 1992). This is due to the assumptions in the model that the fluid is isolated in the fractures

and no fluid flow occurs, hence, the effects of the fluid are similar to those of the elastic solid. For the dry fractures, the fracture infill material can be treated as an elastic solid with zero moduli. Therefore, the P-wave velocity for the fluid saturated fracture case behaves similarly with the dry fracture case, but with a smaller dispersion magnitude due to the reduced stiffness contrast between the fractures and the background medium. In terms of the effects of the fracture density, it can be found from equations (2.77) and (2.79) that the P-wave velocity dispersion increases linearly with the fracture density due to the application of the Foldy approximation, which gives the solution to the accuracy of the first order in ε (Keller, 1964; Ishimaru, 1978). Comparing the wave dispersion at different incidence angles (Figs 2a, 2b, and 2c), we note that the magnitude of the dispersion decreases with the incidence angles to the smallest value at 90º. Note that while the dispersion at 90º is very small, it is not equal to zero. This is due to the fact that, when the P-wave propagates parallel to the fracture plane, the compaction and extension of the rock in this direction will also induce a small normal displacement discontinuity across the fractures due to the Poisson ratio effects. It can also be noted that, the characteristic frequency for the dispersion is found to shift slightly between the oblique incidence angles and the normal (or grazing) incidence angle (θ = 0° or 90°). The reason is that, the dispersion and attenuation at the normal (or grazing) incidence angle is only controlled by the normal fracture displacement discontinuity, whereas that at the oblique incidence angles are controlled by both the normal and shear displacement discontinuities across the fracture.

The scattering attenuation (Figure 5-2) first increases with the frequency and reaches the peak at around 100 Hz when the incidence wavelength has the similar size with the fracture radius. This corresponds to the resonant (or Mie) scattering domain, where the P-wave velocity increases rapidly with the frequency. The attenuation (inverse quality factor Q_p^{-1}) in the low and high frequency regime is approximately proportional to f^2 and f^{-1}, respectively. This is also observed by Yamashita (1990) and Kawahara and Yamashita (1992) for the dry fracture case. In the high frequency regime, the attenuation decreases with some small fluctuations, which is caused by interference pattern variations of the scattered wave fields from the fracture tips (Kawahara and Yamashita, 1992). Due to the assumption of random and sparse distributions of the fractures, similar with the dispersion, the

attenuation is also found to increase with the fracture density linearly. When changing the incidence angles from 0° to 90°, the attenuation decreases and reaches the smallest (but non-zero) value at 90°. Similarly to the dispersion, the characteristic frequency for the attenuation also shifts slightly between the normal (or grazing) incidence case and the oblique incidence case.

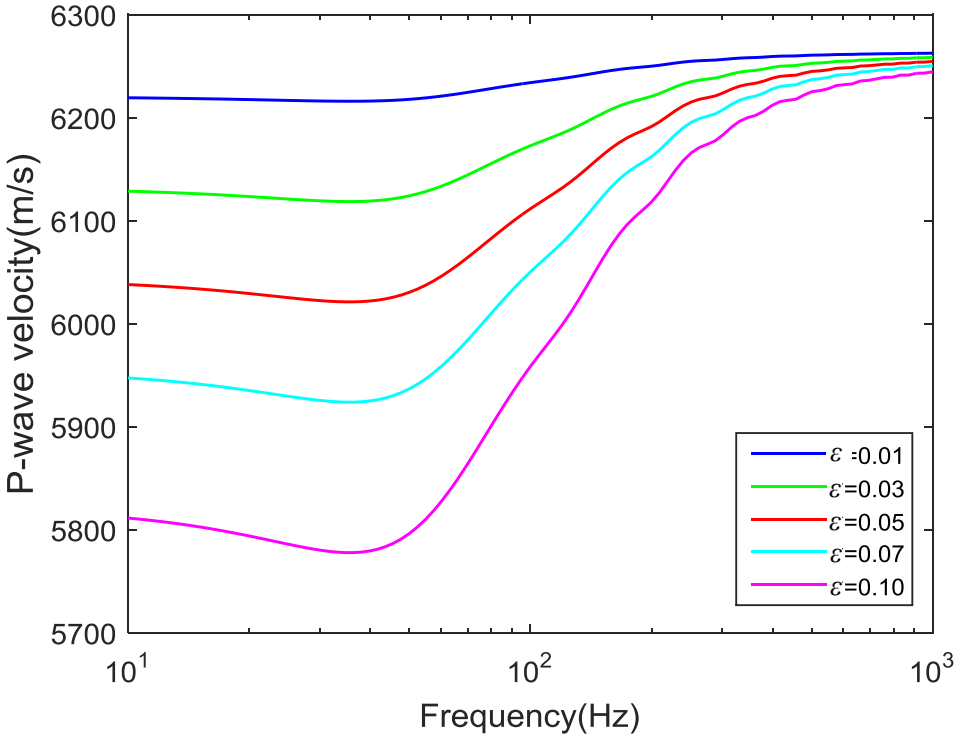
6300
6200
6100
6000
5900
5800
5700
P-wave velocity(m/s)
10^1
10^2
10^3
Frequency(Hz)
ε =0.01
ε=0.03
ε=0.05
ε=0.07
ε=0.10

(a)

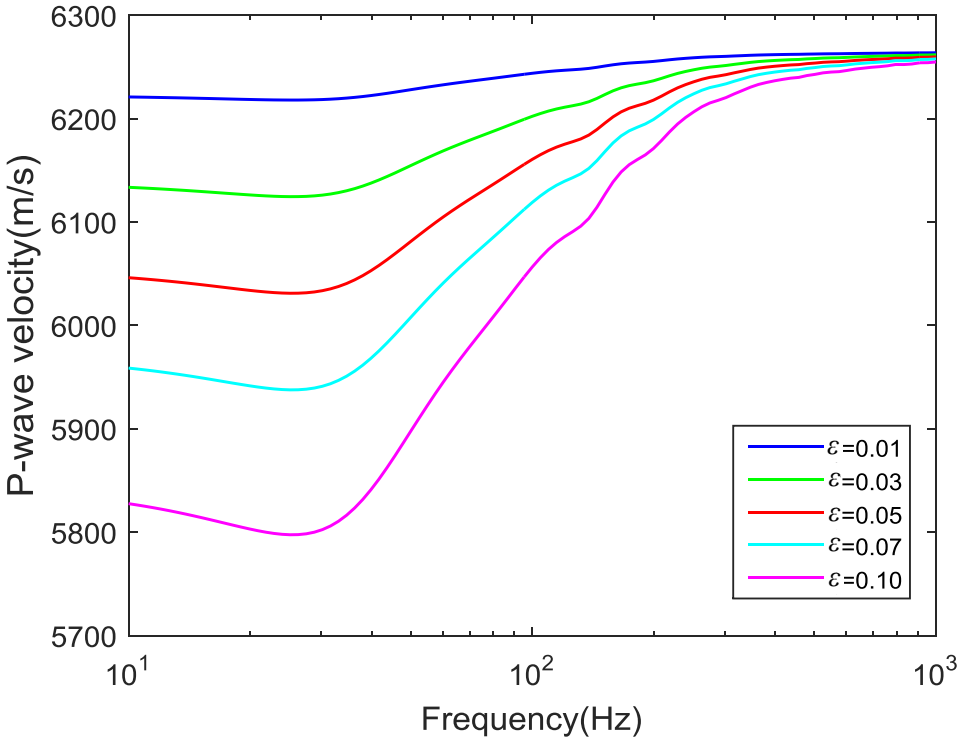
6300
6200
6100
6000
5900
5800
5700
P-wave velocity(m/s)
10^1
10^2
10^3
Frequency(Hz)
ε=0.01
ε=0.03
ε=0.05
ε=0.07
ε=0.10

(b)

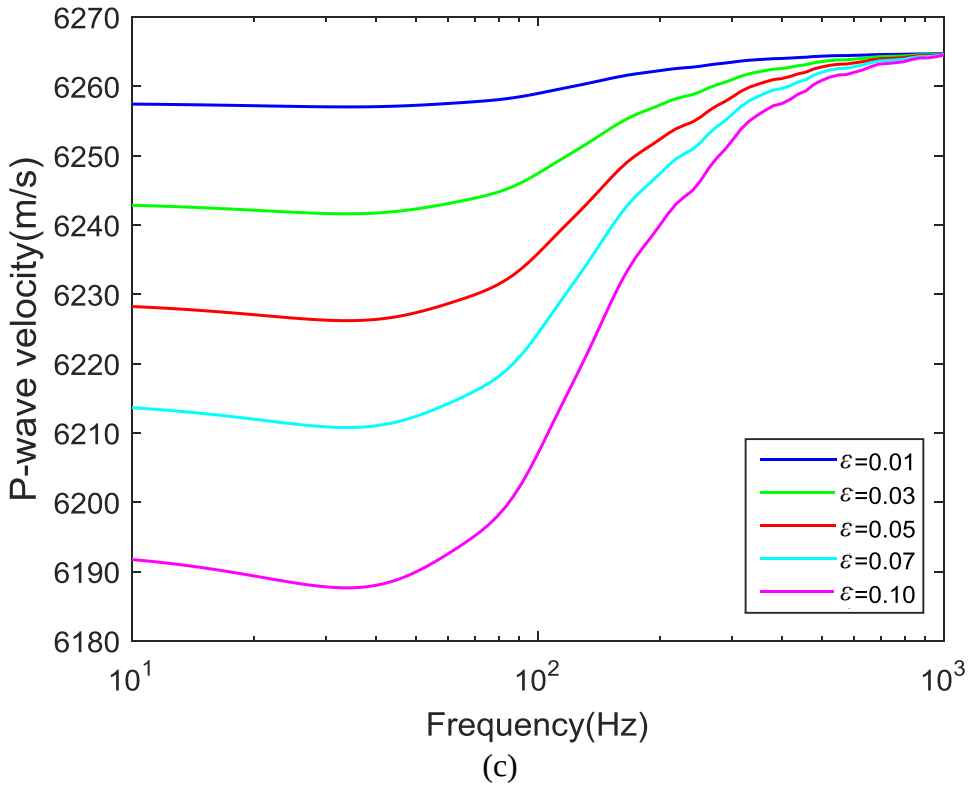

Figure 5-1. Variations of P-wave velocity with frequency f, fracture density ε, and incidence angle θ. (a) $\theta = 0°$ (normal incidence); (b) $\theta = 45°$; (c) $\theta = 90°$ (grazing incidence). Note the much smaller scale of the y-axis for case (c) to show the small velocity dispersion.

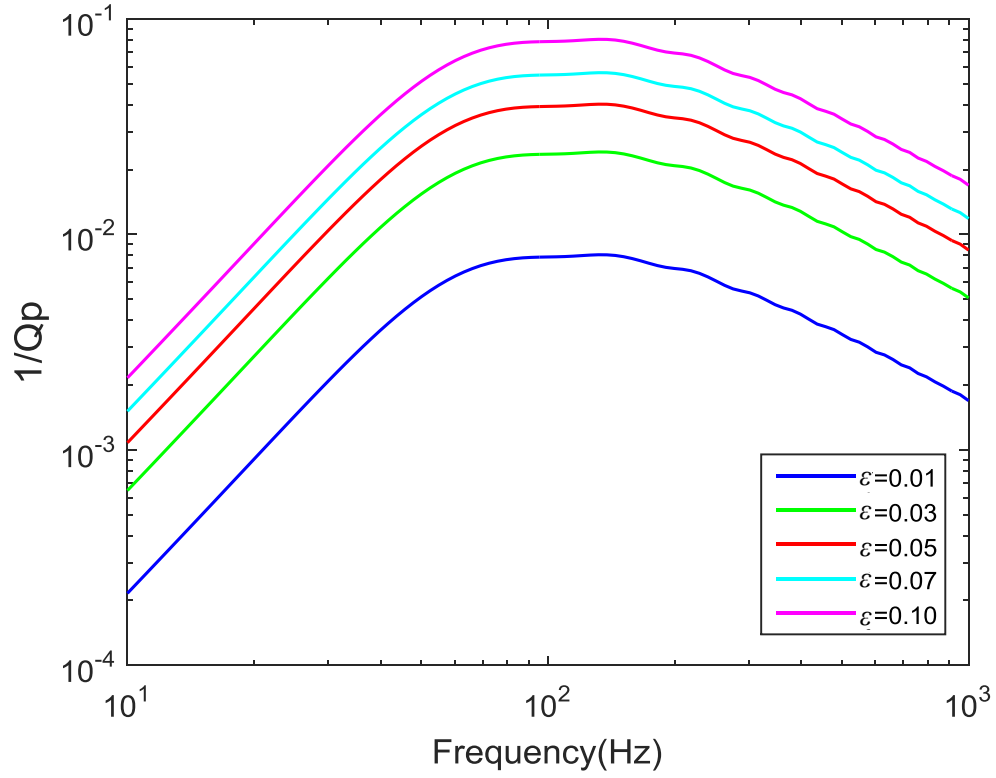
1/Qp
Frequency(Hz)
ε=0.01
ε=0.03
ε=0.05
ε=0.07
ε=0.10

(a)

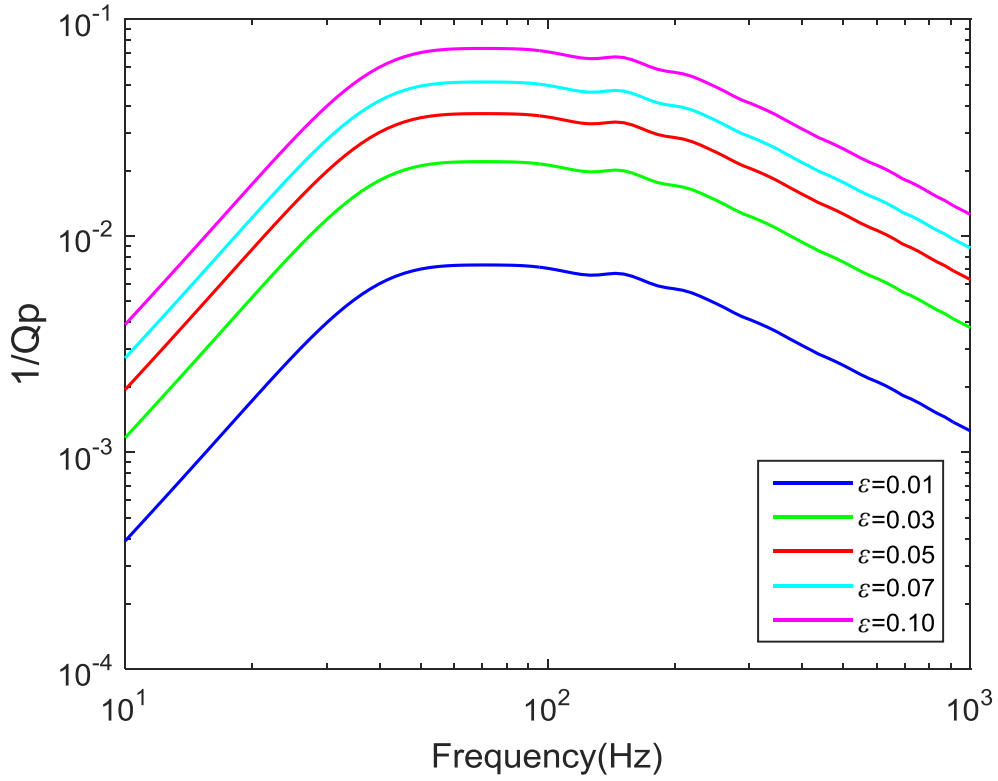
1/Qp
Frequency(Hz)
ε=0.01
ε=0.03
ε=0.05
ε=0.07
ε=0.10

(b)

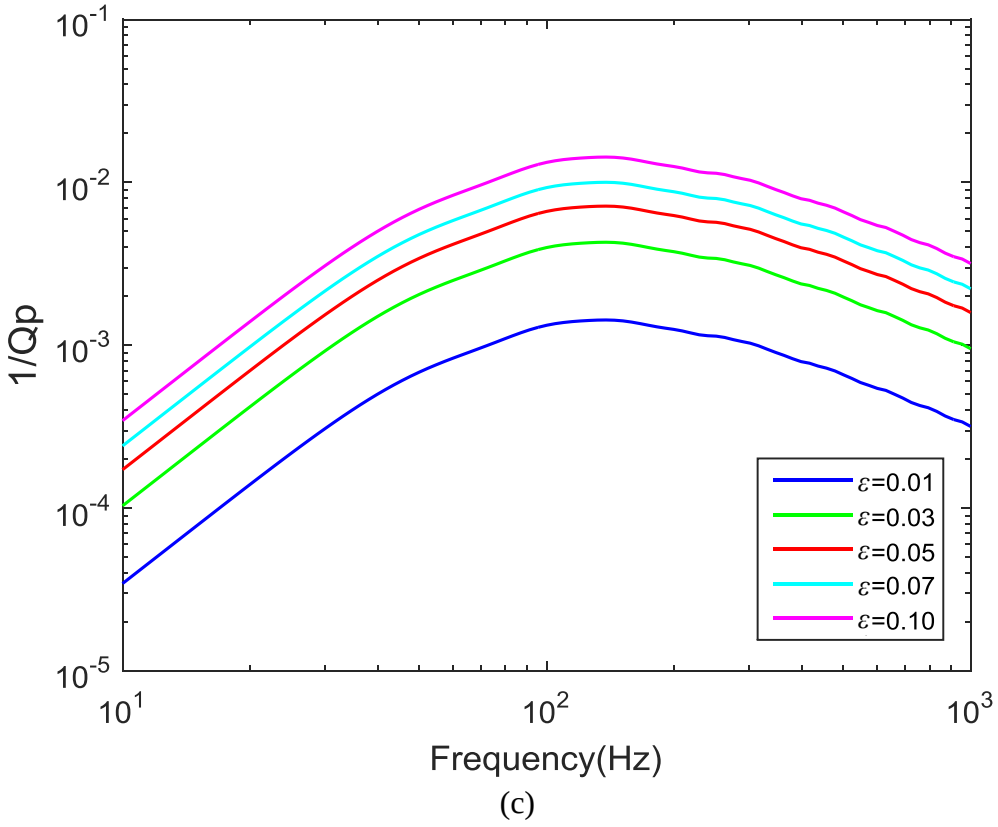

Figure 5-2. Variations of P-wave scattering attenuation with frequency f, fracture density ε, and incidence angle θ. (a) θ = 0° (normal incidence); (b) θ = 45°; (c) θ = 90° (grazing incidence). Note the different scale of the y-axis for case (c) to show the small attenuation.

5.3.3 Effects of fracture thickness on the scattering dispersion and attenuation

The effects of fracture thickness on the scattering dispersion and attenuation are found to be similar at different incidence angles, hence, we only show the results at the normal incidence (θ = 0°) in Figure 5-3 (ε = 0.05). In the low frequency regime, it is found that the fracture thickness has significant influence on the P-wave velocity. In agreement with the predictions by the static Eshelby model (Mura, 1987; Sevostianov and Kachanov, 1999), the P-wave velocity decreases with fracture thickness. However, in the high frequency regime, it is interesting to note that the P-wave velocity increases with the fracture thickness. This is due to the fact that the magnitude of the scattering dispersion increases with the fracture thickness, as shown in Fig. 4. Hence, the P-wave velocity in the Mie scattering regime increases more rapidly for the case with larger fracture thickness. This will thus result in the reversed

trend of the P-wave velocity with the fracture thickness in the high frequency regime. Note that the fracture thickness considered here is small. For the fractures with relatively large thickness, we may observe different phenomena. This will be studied in the future.

It can be noted here that there is no dispersion and attenuation for the infinitesimal fracture thickness case at the normal incidence. This is because both the normal and shear displacement discontinuities across the fracture vanish in this case. According to equations (2.77) to (2.80), the P-wave dispersion and attenuation will thus vanish. Similarly, at incidence angles other than 0°, the P-wave dispersion and attenuation also vanish if the fracture thickness is infinitesimal. Hence, the P-wave velocity equals to that of the background medium at all frequencies and remains unaffected by the incidence angle in this case. This is different from the predictions of Eshelby model (Mura, 1987; Sevostianov and Kachanov, 1999) in the low frequency limit, which predicts the largest velocity at the incidence angle of 0° or 90°, but smallest at 45°. The reason is that while the normal fracture displacement discontinuity given by our model and Eshelby both vanish for the infinitesimal thickness case, the shear displacement discontinuity is different in these two models. In our model, we consider the viscous fluid and hence the viscous friction between the fracture surface and the fluid leads to zero shear fracture displacement discontinuity for the infinitesimal thickness case, as indicated by equation (5.3). However, no viscous friction exists in Eshelby model and hence the shear fracture displacement discontinuity does not vanish at the incidence angles other than 0° and 90°, which is largest at 45°. It should be noted that, while not shown here, the results of our model are consistent with those given by Eshelby model when the fluid viscosity reduces to zero.

We also find that the attenuation increases with the fracture thickness. This is primarily due to the increase of the normal displacement discontinuity across the fracture with the fracture thickness. The effects of fracture thickness on the attenuation are found to be significant in the low frequency regime. However, in the high frequency regime, the effects of the fracture thickness are smaller, they decrease with the frequency and vanish when the seismic wavelength is much smaller than the fracture size. Furthermore, the peak of the attenuation (characteristic frequency) shifts towards the low frequency regime when the fracture thickness increases.

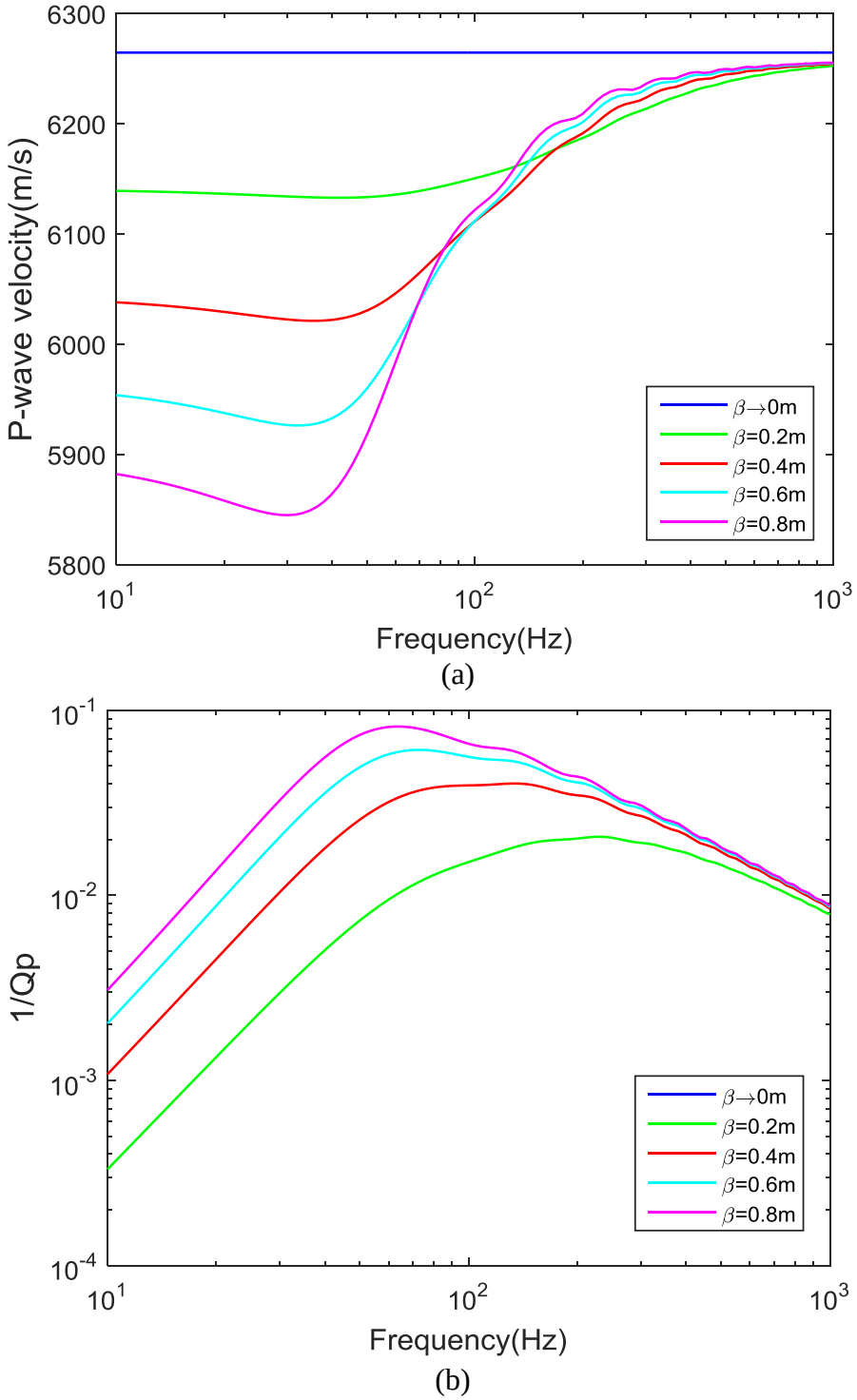

Figure 5-3. Effects of the fracture thickness on the P-wave scattering dispersion and attenuation at the normal incidence (θ = 0°) and different frequencies f (ε = 0.05). (a) P-wave dispersion; (b) attenuation. Note that the dispersion and attenuation for the infinitesimal thickness case are zero.

5.3.4 Effects of saturating fluid properties on the scattering dispersion and attenuation

Similar to the effects of fracture thickness, the effects of the bulk modulus of the saturating fluid on the scattering dispersion and attenuation are similar at different incidence angles. Hence, we only show the results at the normal incidence (θ = 0°) in Figure 5-4 (ε = 0.05). Significant influence of the fluid bulk modulus on the velocity dispersion is observed. The scattering dispersion decreases with the increase of the fluid bulk modulus and hence the largest dispersion occurs for the dry fracture case. The results for the dry fracture case in Figure 5-4 are the same as those given by the model of Kawahara (1992). In the low frequency regime, the P-wave velocity increases with the fluid bulk modulus, which agrees with the predictions of the static Eshelby model (Mura, 1987; Sevostianov and Kachanov, 1999). However, in the high frequency regime, the P-wave velocity decreases with the fluid bulk modulus. These different trends of the P-wave velocity with the fluid bulk modulus in the low and high frequency regimes were also observed by Sabina et al. (1993) and Smyshlyaev et al. (1993b). The reason is that the P-wave velocity increases more rapidly in the Mie scattering domain for the cases with lower fluid bulk modulus, which results in the reversal of the trends of the P-wave velocity with the fluid bulk modulus in the high frequency regime.

For the scattering attenuation, it decreases with the fluid bulk modulus. This effect is significant in the low frequency regime, whereas negligible in the high frequency regime. The peak of the attenuation (characteristic frequency) is found to shift towards the high frequency regime with the increase of the fluid bulk modulus. Here, we observe that the effects of the fluid bulk modulus on the scattering dispersion and attenuation are opposite to those of the fracture thickness. This can be explained by equation (5.4). From this equation, we can see that increasing the fluid bulk modulus has similar effects on the normal fracture displacement discontinuity as decreasing the fracture thickness.

Apart from the fluid bulk modulus, the fluid viscosity should also have some effects on the scattering dispersion and attenuation. This is expected because the viscous friction operating at the fracture surface affects the shear fracture displacement discontinuity and hence the scattering dispersion and attenuation. From the wave motion characteristics of the P-wave, it is expected that the shear displacement discontinuity should be largest at an incidence angle of around 45° (Kawahara and Yamashita, 1992). Hence, the effects of fluid viscosity should be most obvious at this angle, which is shown in Figure 5-

5. However, contrary to our expectation, the curves for different fluid viscosities nearly overlap each other and hence the effects of the fluid viscosity are negligible, even when the viscosity reaches 10 Pa.s. The reason can be found in equation (5.3), which shows the effects of fluid viscosity in the right hand side. As the term $\omega\eta/\mu$ is usually much smaller than 1, the shear displacement discontinuity across the fracture will be nearly unaffected by the fluid viscosity and hence its value will be close to the case with non-viscous fluid. Therefore, the fluid viscosity has little effects on the scattering dispersion and attenuation for the studied configurations. However, it should be noted that, when the fracture thickness is extremely small, the effects of fluid viscosity may be significant, as indicated by equation (5.3). Furthermore, for the case with low fluid viscosity, the non-uniform normal displacement discontinuity across the fracture may induce the fluid flow inside the fractures. This will affect the dispersion and attenuation of the P-wave, which is not considered in our current model. Its effects will be discussed in the discussion section.

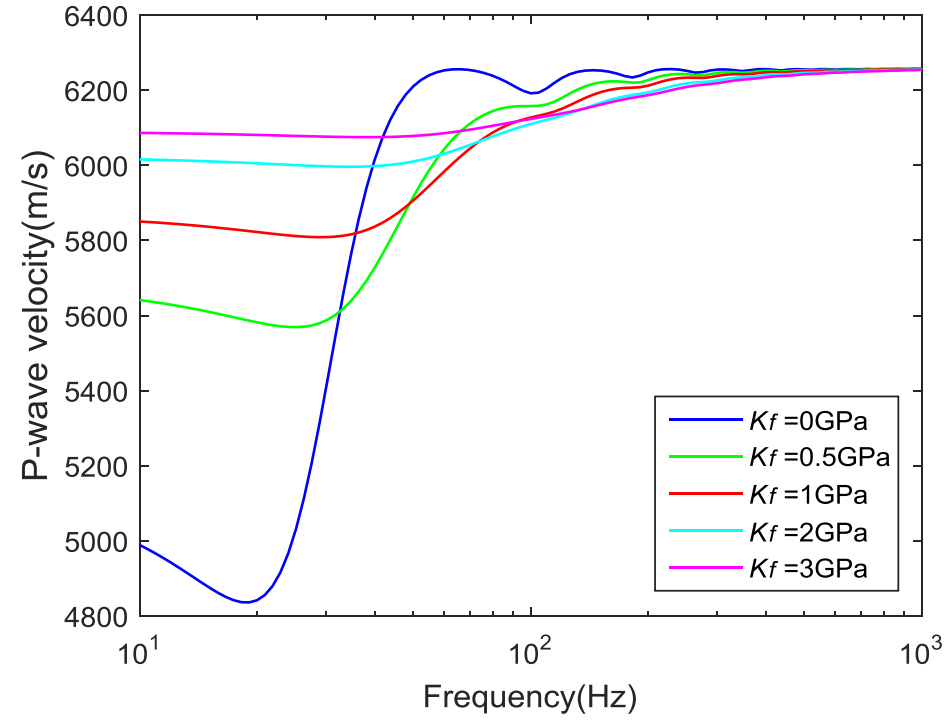

(a)

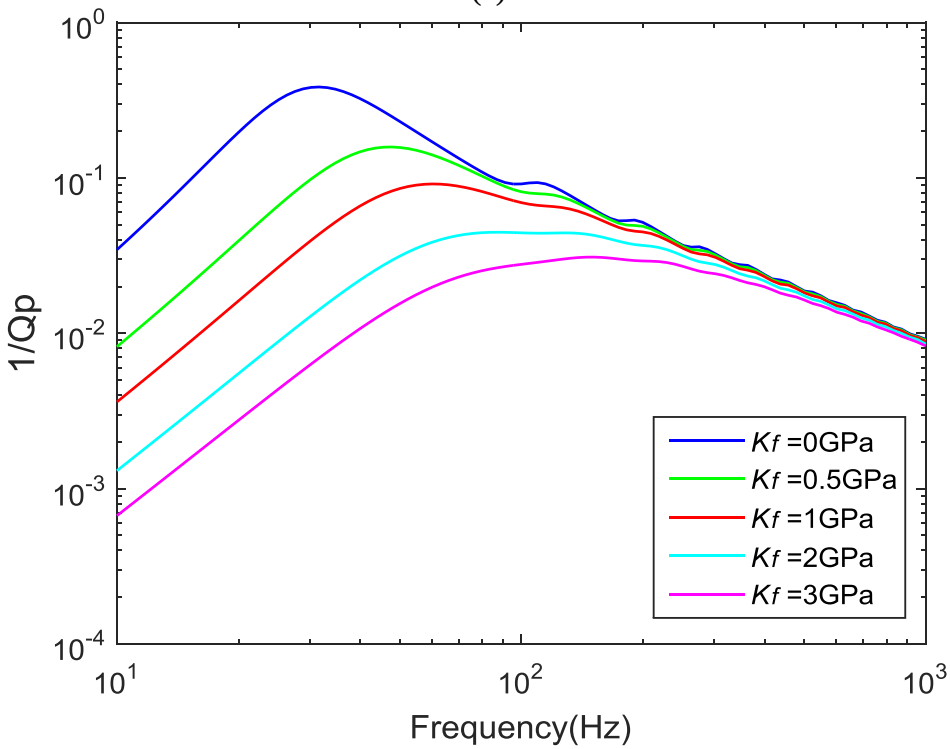

(b)

Figure 5-4. Effects of the fluid bulk modulus on the P-wave scattering dispersion and attenuation at the normal incidence (θ = 0°) and different frequencies f (ε = 0.05). (a) P-wave dispersion; (b) attenuation.

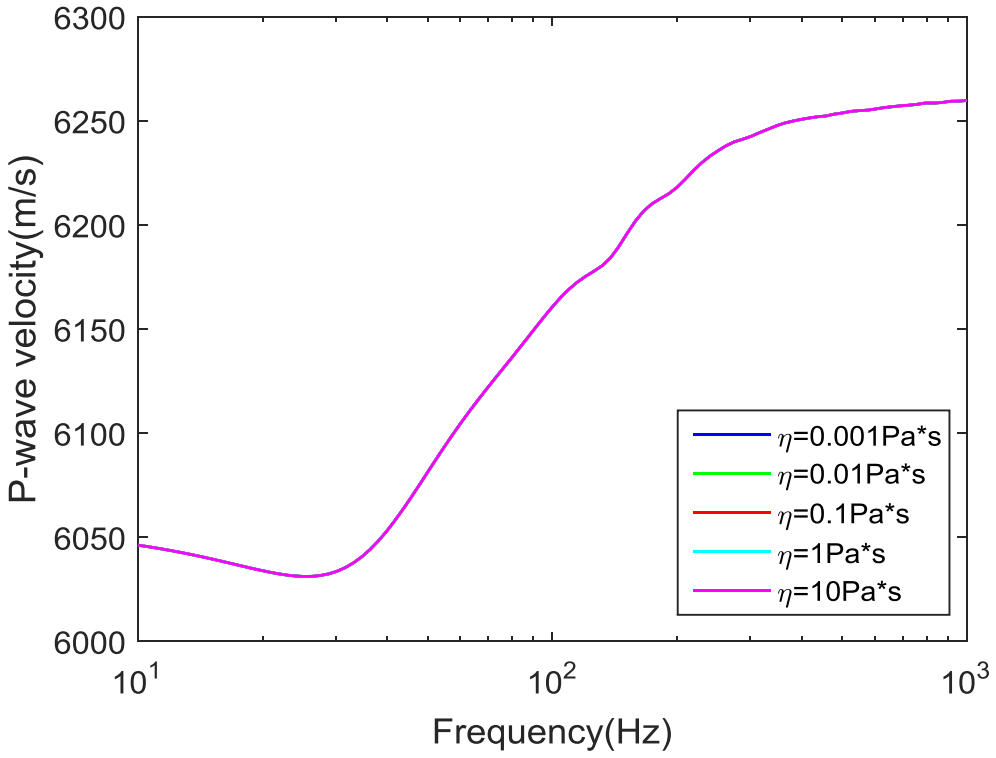

(a)

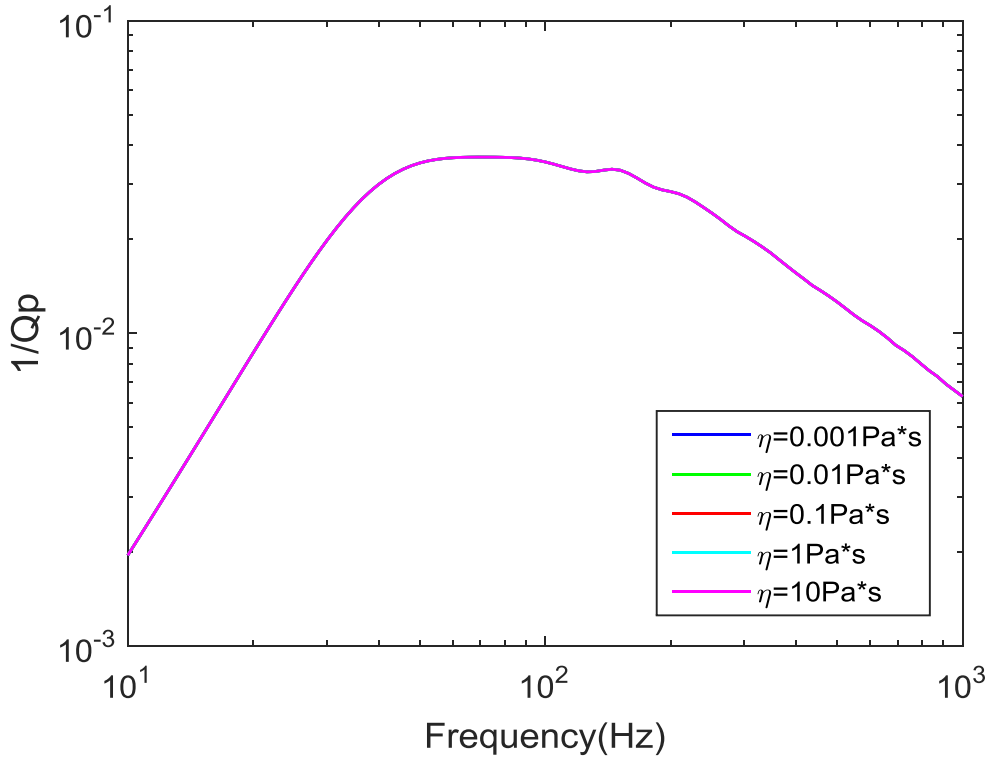

(b)

Figure 5-5. Effects of fluid viscosity on the P-wave scattering dispersion and attenuation under different frequencies *f* at the incidence angle of 45°. (a) P-wave dispersion; (b) attenuation.

5.4 Comparison with experimental data

5.4.1 Experiment configuration and sample parameters

To validate our theoretical model, we compare the theoretical predictions with the ultrasonic measurements on synthetic rock samples containing penny-shaped fractures performed by Wei et al. (2013). The background of the samples were constructed using a rock powder-epoxy mixture by a layering technique, which results in the layered medium with equal thickness for each layer. The background medium thus shows some degrees of anisotropy. However, this anisotropy is very weak (Wei et al., 2013) and hence can be treated as isotropic. The background medium has negligible porosity with a density of 1.66 g/cm^3. Fractures are added by placing randomly, on the surface of each layer, penny shaped inclusions made of a mixture of the silica rubber and epoxy, with a bulk modulus of 2.02 GPa and very small shear modulus. Thus, the fractures are aligned to each other and distributed randomly on the surface of each layer. The penny-shaped inclusions are punched out from a block sample made of a mixture of silica rubber and epoxy. The velocities of this mixture are measured giving an average P-wave velocity of 1350 m/s and a negligibly small S-wave velocity. The density of this mixture is 1.09 g/cm^3, and hence the bulk modulus is around 2.02 GPa while its shear modulus is very small. Hence, this mixture has similar elastic properties to a fluid. Furthermore, due to the very small but finite shear modulus of the mixture, the pressure (stress) will not be (fully) equilibrated within the fractures at ultrasonic frequencies (e.g., Glubokovskikh et al., 2016). Therefore, the properties of the fracture infilling mixture are similar to those of the saturating fluid assumed in the theoretical model (Section 5.2), which enables the application of the theoretical model in the predictions of the experimental results. The details on the sample microstructure and the procedure of constructing the samples are given in Wei (2004) and Wei et al. (2013). Seven synthetic rock samples (Figure 5-6) are then constructed: one reference sample (with no fractures) and six fractured samples with fixed fracture density (around 0.083) and radius (1.5 mm), but varying fracture thickness (Table 5-1).

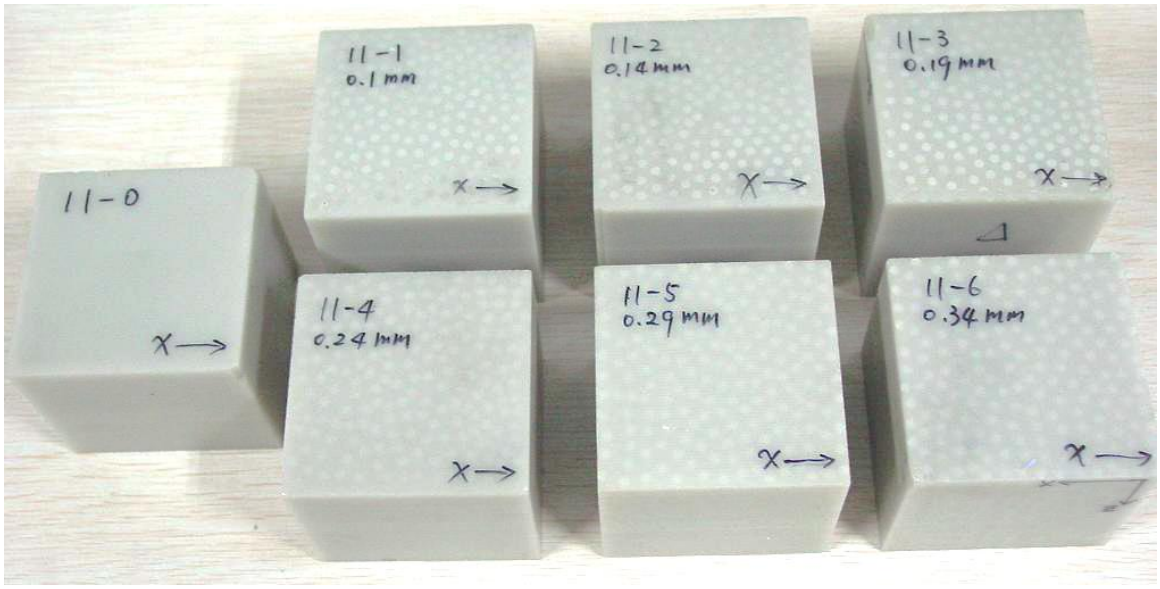

Figure 5-6. Synthetic rock samples containing penny-shaped fractures. The sample 11-0 is the reference sample with no fractures, whereas samples 11-1 to 11-6 have the same fracture density and radius, but with the increasing fracture thickness, as indicated in the figure (0.1 mm – 0.34 mm).

Table 5-1. Distribution of the fracture thickness of the samples

Sample No.	Fracture thickness (mm)	Sample No.	Fracture thickness (mm)
11-1	0.10	11-4	0.24
11-2	0.14	11-5	0.29
11-3	0.19	11-6	0.34

Due to the small fracture size, the wave scattering can occur in the ultrasonic frequency range and hence we measure the P-wave velocity and attenuation using the ultrasonic pulse transmission method in the direction perpendicular and parallel to the fracture plane. The measurement system consists of the Panametrics- NDT 5077PR Pulser-Receiver coonected to a TK-DPO3102 digital oscilloscope and a PC. To obtain the results at different frequencies, three pairs of transducers are used with the nominal frequencies of 1 MHz, 0.25 MHz, and 0.1 MHz, respectively. The physical parameters of the transducers are shown in Table 5-2. More information about the transducers can be accessed at the website of the manufacturer (www.olympus-ims.com/en/ultrasonic-transducers). By applying a Fourier

transform to the recorded waveforms of the transmitted P-waves through the reference sample, we can obtain the centroid frequencies of these transmitted P-waves, which are close to those of the incident P-waves. Hence, we can obtain the centroid frequencies of the incident P-waves for the three pairs of transducers, whose values are around 0.66 MHz, 0.21 MHz, and 0.097 MHz, respectively. At different centroid frequencies, the P- and S- wave velocities of the background medium (reference sample) are measured. Combining with the density of the background medium (1.66 g/cm^3), the elastic moduli of the background medium are obtained which vary slightly with the frequency, as shown in Table 5-3. This indicates that the background medium has slightly viscoelastic (or near-elastic) properties. Hence, apart from the P-wave scattering, a small intrinsic attenuation may also occur in the background medium. As the host medium of the fractured samples has nearly the same properties as the reference sample, the intrinsic attenuation should be similar between them. Hence, the intrinsic attenuation in the background can be excluded by comparing the results with the measurements on the reference sample, using the following expressions (e.g., Tang et al., 1990):

$$\ln\frac{|S_2(f)|}{|S_1(f)|}+\ln\frac{|G_1(f)|}{|G_2(f)|}=\frac{\pi L_1 f}{V_p}\frac{1}{Q_{int}}-\frac{\pi L_2 f}{V_{pe}}\left(\frac{1}{Q_{int}}+\frac{1}{Q_{sca}}\right), \tag{5.18}$$

with

$$G_i(f)=\frac{\gamma}{ik_p}\left[1-\left(1-\frac{\xi_i^2}{2k_p^2r^2}\right)\left[J_0(\xi_i)+iJ_1(\xi_i)\right]e^{-i\xi_i}-\frac{\xi_i^2}{k_p^2r^2}\left(\frac{iJ_1(\xi_i)}{\xi_i}\right)e^{-i\xi_i}\right],\ i=1,2, \tag{5.19}$$

$$\xi_i=\frac{k_p}{2}\left(\sqrt{4r^2+L_i^2}-L_i\right),\qquad i=1,2, \tag{5.20}$$

where $1/Q_{int}$ and $1/Q_{sca}$ are intrinsic and scattering attenuation, respectively; f is the measurement frequency; S_1 and S_2 are the amplitude spectra of the transmitted P-waves through the reference and fractured samples, respectively; L_1 and L_2 are the length of the reference and fractured samples in the wave propagation direction, respectively; r is the radius of the transducer; J_0 and J_1 are Bessel functions of the first kind with order zero and one, respectively. Note that the second term in the left hand side of equation (5.18) is the correction of the geometric spreading effects (Tang et al., 1990).

Table 5-2. Physical parameters of transducers used to record P- and S- wave seismograms

Nominal frequency (MHz)	P-wave		S-wave	
	Catalogue number	Transducer Diameter (mm)	Catalogue number	Transducer Diameter (mm)
1	V102-RB	25	V152-RB	25
0.25	V1012	39	V150-RB	25
0.1	V1011	39	V1548	25

Table 5-3. Elastic moduli of the background medium at different centroid frequencies of the incident P-waves

Centroid frequency	Bulk modulus (GPa)	Shear modulus (GPa)
0.66 MHz	9.39	3.81
0.21 MHz	9.15	3.76
0.097 MHz	9.30	3.61

In this experiment, the size for the reference and fractured samples is similar (~ 68 × 68 × 62 mm). Hence, the intrinsic attenuation $1/Q_{int}$ in equation (5.18) is cancelled and the following approximation is obtained:

$$\ln \frac{|S_2(f)|}{|S_1(f)|} = -\frac{\pi L_2 f}{V_{pe}} \frac{1}{Q_{sca}} . \tag{5.21}$$

Thus, we can estimate the P-wave scattering attenuation using equation (5.21) through the spectral ratio method (e.g., Bath, 1974; Ganley and Kanasewich, 1980; Mavko et al., 2009). The full measured data for the velocities and waveforms are given in Wei et al. (2013). An example of the amplitude spectra S_1 and S_2 is given in Figure 5-7.

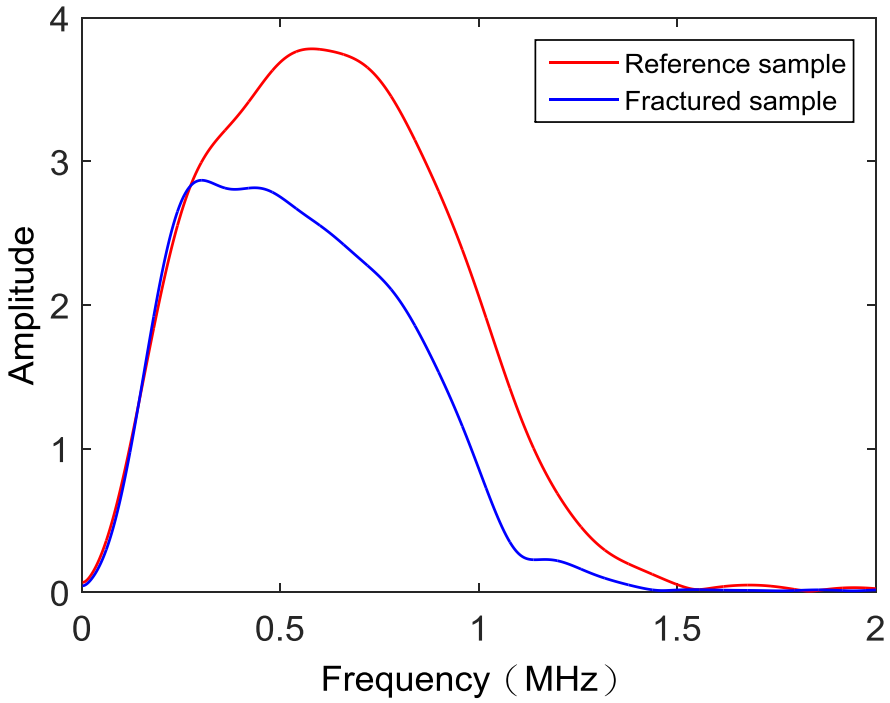

Figure 5-7. An example of the amplitude spectra of the transmitted P-waves through reference and fractured samples, respectively.

The results for the velocities and estimated scattering attenuation for the fractured samples are shown in Figure 5-8 and Figure 5-9. We can observe notable P-wave dispersion and attenuation. To validate our theoretical model, we can compute dispersion and attenuation theoretically, and compare the theoretical predictions with the experimental results. When carrying out the theoretical predictions, it should be noted that our model is for 2D fractures while experiments use penny-shaped fractures. As the wave scattering is controlled by the fracture density (e.g., Zhang et al., 1993a, 1993b), to compare the theoretical predictions with the numerical simulations, we use the same fracture density in the 2D model as for the 3D samples. Furthermore, as the primary component of the incident P-waves is that at the centroid frequencies, we use the centroid frequencies (instead of the nominal frequencies) as the inputs in the theoretical predictions. In addition, to account for the effects of the slightly viscoelastic properties of the background medium on the P-wave velocities, we use frequency-dependent elastic properties of the background medium (Table 5-3) in the theoretical predictions. Finally, the viscosity of the fluid-like mixture in the fractures is not measured as there is no shear displacement discontinuity

across the fractures for the wave propagating perpendicular and parallel to the fracture plane. Hence, it is not needed in the theoretical predictions.

5.4.2 Comparison of experimental results with theoretical predictions

Figure 5-8 shows the P-wave velocity measured at different frequencies and fracture thickness and the corresponding theoretical predictions. For the P-wave propagating parallel to the fracture plane, it can be seen that the measured and predicted velocities are in good agreement with each other. They both decrease with the fracture thickness and increase with the frequency. At higher frequency (0.66 MHz), the velocities are obviously larger than those at lower frequencies (0.097 MHz and 0.21 MHz), which should be due to the Mie scattering effects. At lower frequencies, if the elastic properties of the background medium are frequency-independent, the velocities given by the theoretical predictions will decrease slightly with the frequency due to the Rayleigh scattering effects. However, as the P-wave modulus of the background medium increases slightly with the frequency in this regime (Table 5-3), the trend of the velocities with the frequency is reversed.

When the wave propagates perpendicular to the fracture plane, the theoretical predictions are also in overall good agreement with the experimental results. Both of them show an increase of the velocity dispersion with the fracture thickness, which is consistent with the observation in the numerical example section. The primary discrepancy is the slightly different trends of the P-wave velocity with the frequency in the relatively low frequency regime (0.097 MHz and 0.21 MHz). In the theoretical predictions, the dispersion caused by Rayleigh scattering for samples with relatively low fracture thickness is small and hence the velocities increase slightly due to the small increase of the P-wave modulus of the background medium with the frequency. However, for samples with relatively large fracture thickness, the dispersion due to Rayleigh scattering becomes larger, the theoretical predictions thus give lower velocities at 0.21 MHz than those at 0.097 MHz. Different from the theoretical predictions, the experimental results show an increase trend of P-wave velocities with the frequency for all the samples measured. The possible reason for the discrepancy is that our theoretical model is based on the Foldy approximation, which neglects interactions between the fractures. This holds when the fracture density is low and the fractures are distributed randomly in the samples. However, the fracture

density of the samples (0.083) is close to 0.1 and hence is not very low (e.g, Grechka and Kachanov, 2006; Suzuki et al., 2013). Furthermore, while the fractures are distributed randomly on the surface of each layer of the background medium, they are not randomly distributed throughout the samples. Hence, the concentration of the relatively large number of fractures on each layer of the background medium may result in the interaction between the fractures (especially for the cases with relatively large fracture thickness), which may change the trend of the P-wave velocity with the frequency. In addition, it should also be noted that our theoretical model deals with the 2D slit fractures, whereas the fractures in the samples are 3D (penny-shaped). The difference in the geometries of the fractures may also lead to the discrepancies between the theoretical predictions and the experimental results.

The measured P-wave attenuation in the directions perpendicular and parallel to the fracture plane is shown in Figure 5-9, along with the corresponding theoretical predictions. It can be seen that the theoretical predictions are in overall good agreement with the measured results. Both the theoretical predictions and the measured results show that the attenuation increases with the fracture thickness at different measurement frequencies, which is consistent with the observations in the numerical example section. Moreover, the effects of the fracture thickness on the attenuation become smaller when the frequency increases. Again, this is also observed in the numerical example section. The discrepancies between the theoretical predictions and experimental results primarily occur in the direction parallel to the fracture plane at lower frequencies (0.21 MHz and 0.097 MHz). The theoretical predictions give lower values of attenuation than the experimental results. The discrepancies may be due to the transmission loss occurred on the surface of the sample and also the increased relative error in the measurement of the small attenuation, which is amplified by the logarithmic scale. Furthermore, the differences between the assumptions of the theory and the configuration of the experiment presented above can also be responsible for the discrepancies.

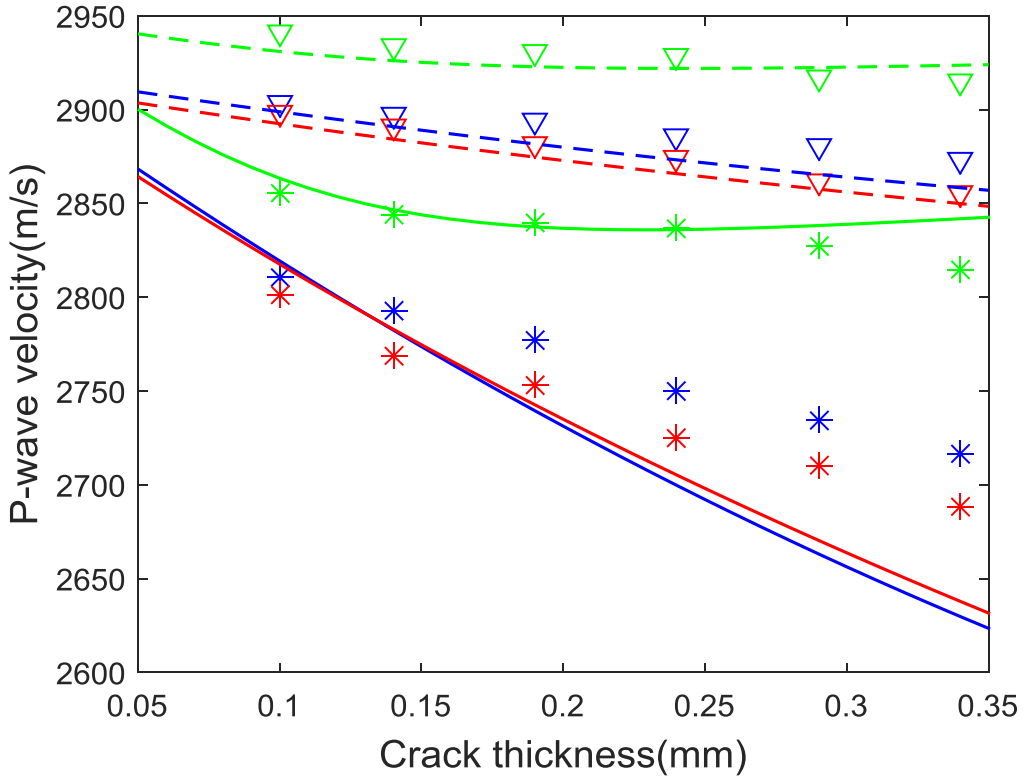

Figure 5-8. Measured and predicted P-wave velocities of the samples in the directions parallel and perpendicular to the fracture plane under different fracture thicknesses and centroid frequencies. The green, blue, and red colours represent the velocities measured at the centroid frequencies of 0.66 MHz, 0.21 MHz, and 0.097 MHz, respectively. The dashed and solid lines represent the theoretical predictions in the directions parallel and perpendicular to the fracture plane, respectively. The triangles and the stars are the corresponding experimental measurement results.

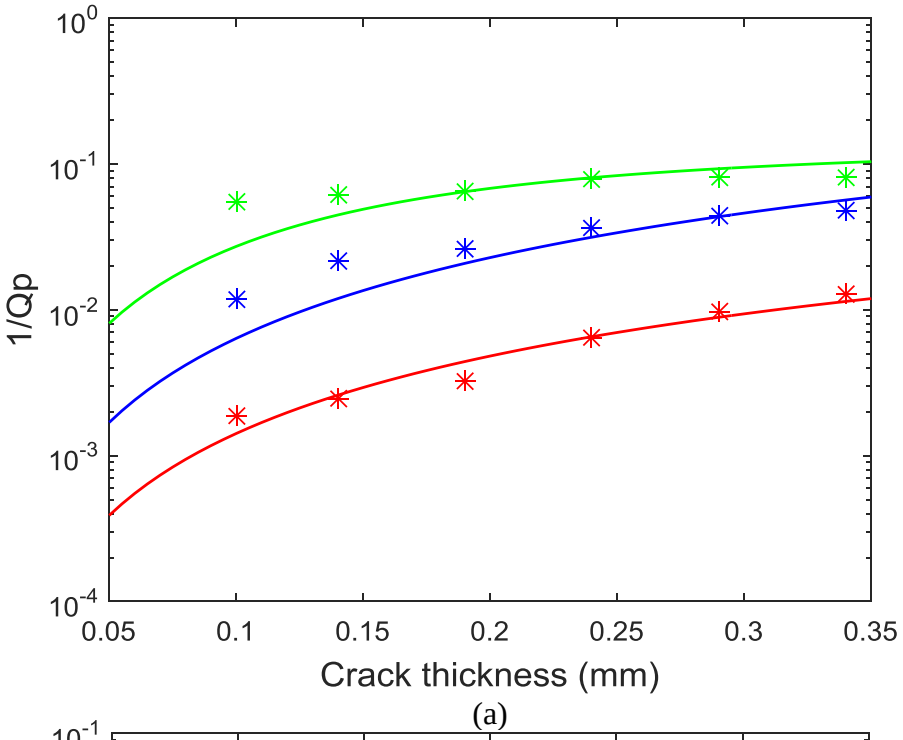

(a)

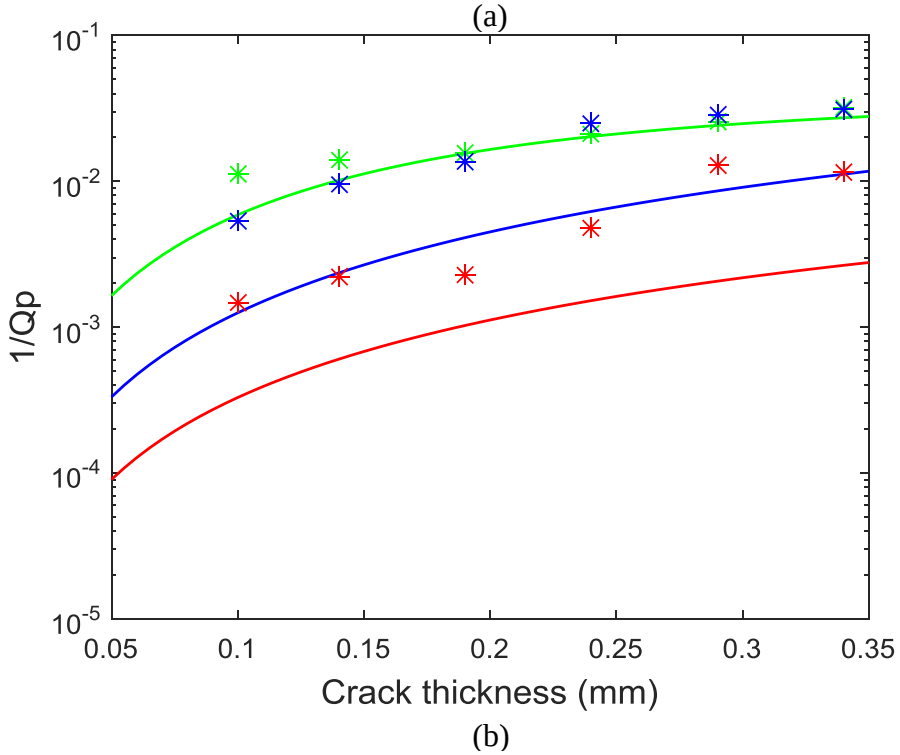

(b)

Figure 5-9. Measured and predicted P-wave attenuation in the directions perpendicular (a) and parallel (b) to the fracture plane under different fracture thicknesses and frequencies. The green, blue, and red colours represent the attenuation measured at the centroid frequencies of 0.66 MHz, 0.21 MHz, and 0.097 MHz, respectively. The solid lines and the stars are the theoretical predictions and the experimental measurement results, respectively.

5.5 Discussion

In this chapter, we considered fractures filled with the fluid with a relatively high viscosity and hence the fluid flow inside the fractures should be negligible in the scattering frequency regime. However, if the fluid has low viscosity, due to the non-uniform normal displacement discontinuity across the fractures, the fluid flow can be induced inside the fractures in the scattering frequency regime. The fluid flow will result in the intrinsic attenuation and also affect the scattering attenuation, which is not considered in our current model. To study this effect, we can consider the limiting case when the fluid pressure is uniform in the fractures. This can be done by changing the boundary condition for the normal stress as follows:

$$\int_{-a}^{a} D_2(\zeta_1) T_{222}(x_1, 0 \mid \zeta_1, 0)\, d\zeta_1 - e^{ik_p x_1 \sin\theta} = -\frac{K_f}{2a\beta\mu} \int_{-a}^{a} D_2(\zeta_1)\, d\zeta_1 . \tag{5.22}$$

Hence, using boundary conditions (5.3) and (5.22), the normal and tangential fracture displacement discontinuities can be computed by employing the same numerical method as before. Then, the P-wave dispersion and attenuation for this case can be calculated. The uniform fluid pressure case represents the situation where the fluid in the fractures is relaxed, whereas the no fluid flow case studied in Section 5.2 denotes the situation with unrelaxed fluid in the fractures. There is no intrinsic attenuation due to the fluid flow inside the fractures for both limiting cases. However, the differences in the velocities and attenuation at low frequencies (quasi-static regime) between these two cases can indicate the magnitude of the intrinsic attenuation. Furthermore, they can also show the largest possible effects of the fluid flow inside the fractures on the scattering dispersion and attenuation.

Fig. 5-10 shows the comparison between these two cases at the normal incidence (θ = 0°). The parameters used are the same with those in the numerical example section. The fracture density is assumed to be 0.1. Since the normal fracture displacement discontinuity is largest at the normal incidence, the differences between these two limiting cases should also be largest at this incidence angle. We find that the differences between these two cases are small at low frequencies, where the no fluid flow case has higher velocity and lower attenuation than the uniform fluid pressure case. However, the

differences are small even for a relatively large fracture density (0.1). The largest difference between the velocities does not exceed 35 m/s and for the attenuation is negligible. This indicates that the fluid flow inside the fractures induces negligible intrinsic attenuation and has very small effects on the scattering attenuation for the case with small aspect ratio (0.01). Tests for larger aspect ratios, (not presented here) show similar results even for the case with an aspect ratio of 0.1. Hence, we can conclude that the fluid flow inside the fractures has negligible effects on the seismic dispersion and attenuation for the studied fracture configuration.

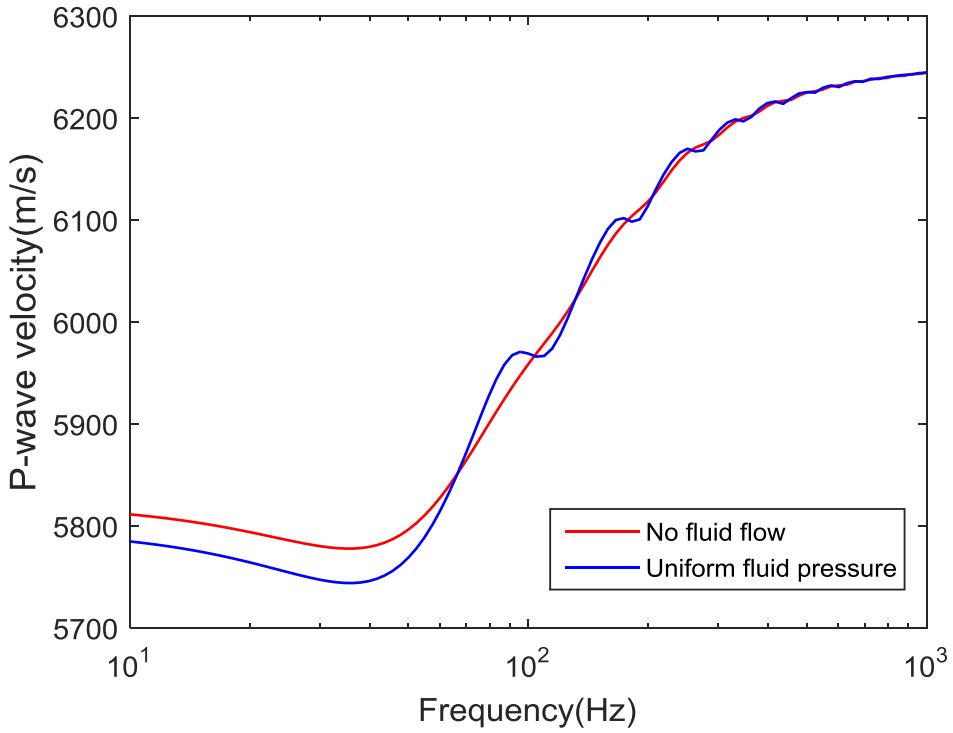

(a)

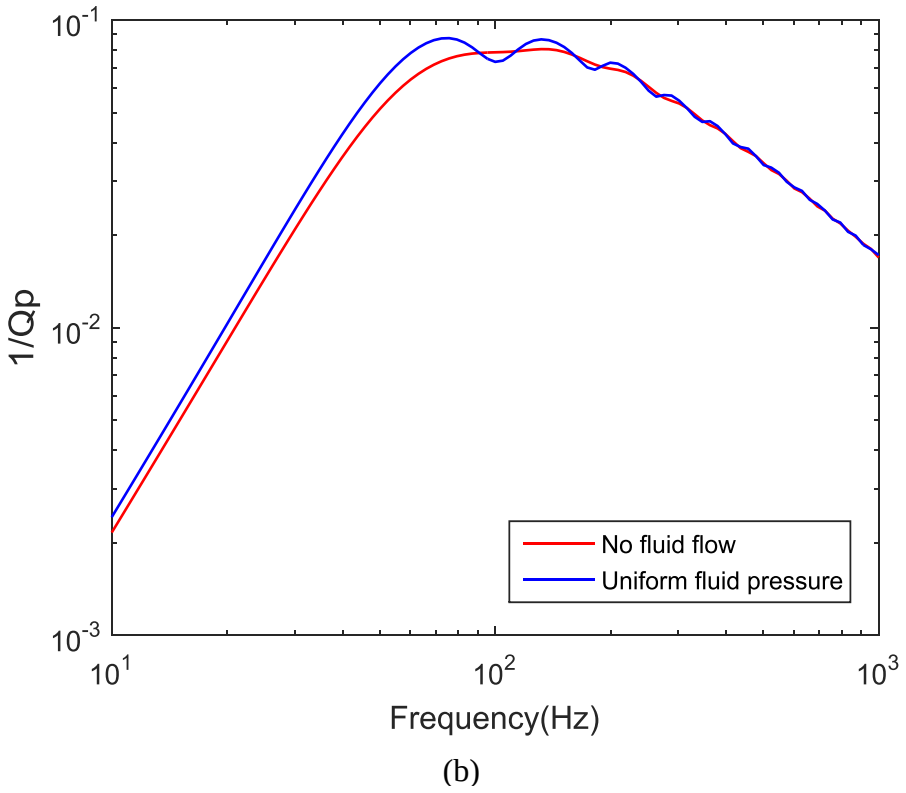

Figure 5-10. Comparison of the P-wave dispersion and attenuation between the no fluid flow case and the uniform fluid pressure case at the normal incidence (θ = 0°). (a) P-wave dispersion; (b) attenuation.

In addition, in our current model, we assume that fractures are embedded in an elastic background medium. This means that the rock is non-porous or the fractures are hydraulically isolated from the pores. For the saturated porous rock with aligned fractures, apart from the wave scattering effects and the fluid flow inside the fractures, the wave-induced fluid flow between the fractures and porous background medium can also occur, which will result in additional dispersion and attenuation of the seismic wave (e.g., Müller et al., 2010). Hence, it is also essential to incorporate this effect into our model for such rock. To this end, Galvin and Gurevich (2007) studied the scattering of a normal incident P-wave on a penny-shaped fracture in a fluid saturated porous medium. Both the scattering and fluid flow effects are formulated in their approach, however, the scattering effects were then neglected by assuming the incompressible fluid in the fracture. Hence, by taking into account the compressibility of the fluid in the fracture and using a similar approach as that of Galvin and Gurevich (2007), we can extend our model to consider the effects of the fluid flow between the fractures and the porous

background medium. This work will be carried out in the future. In the next chapter, we will develop a hybrid method to consider both the scattering and WIFF effects.

5.6 Conclusions

In this chapter, we studied the P-wave dispersion and attenuation due to the scattering by the 2D fluid saturated aligned fractures with finite thickness, which are embedded in an isotropic elastic solid. We assumed that the fractures are distributed randomly and sparsely, which allowed us to use the Foldy approximation, which, together with the representation theorem, gives the P-wave scattering dispersion and attenuation for the given displacement discontinuities across the fractures. Using the boundary conditions, the fracture displacement discontinuities can be computed numerically, which enables the calculation of P-wave dispersion and attenuation.

The behaviour of the theoretical results is illustrated using a numerical example. The analysis of this example shows that fracture thickness has significant influence on the P-wave dispersion and attenuation, especially in the low frequency regime. In this regime, the P-wave velocity decreases with the increasing fracture thickness. However, due to the increase of the dispersion and attenuation with the fracture thickness, the trend of the P-wave velocity with the fracture thickness is reversed in the high frequency regime. The fluid bulk modulus is also found to have significant effects on the dispersion and attenuation, but these effects are opposite to those of the fracture thickness. With respect to the fluid viscosity, its effects on the dispersion and attenuation are found to be negligible for the studied configurations.

To validate our 2D theoretical model, we compare the theoretical predictions with the ultrasonic measurements on the 3D fractured samples. The results show overall good agreement between the theoretical predictions and the experimental results. This work reveals the important effects of the fracture thickness and the properties of the saturating fluid on the P-wave scattering dispersion and attenuation. Hence, it provides a potential to extract these parameters from the seismic data.

.

Chapter 6
Coupling effects between WIFF and scattering on the seismic dispersion and attenuation

6.1 Introduction

In previous chapters, we have studied the effects of WIFF and wave scattering by fractures on the seismic dispersion and attenuation separately. However, in the real reservoirs, both mechanisms can contribute to the measured seismic dispersion and attenuation. Hence, in order to interpret the seismic data properly, it is essential to study the coupling effects between WIFF and scattering. This will allow a more accurate interpretation of the rock properties from the seismic dispersion and attenuation data. However, to the authors' knowledge, only a few studies have been reported on this aspect up until now. Gurevich et al. (1997) analysed the WIFF and scattering effects on the seismic attenuation separately using the corresponding theoretical solutions for the rocks composed of fine poroelastic layers. The results were then superposed and compared with the numerical simulations, which show good agreement between them. Masson et al. (2006) and Wenzlau and Müller (2009) implemented the wave propagation algorithms based on the low frequency approximation of Biot's dynamic equations of poroelasticity. The interference between the WIFF and scattering in the heterogeneous poroelastic medium can thus be studied. Recently, Caspari et al. (2017) employed a similar numerical approach to investigate these coupling effects. Furthermore, to separate the WIFF effects from those of scattering, the numerical simulations based on the quasi-static equations of poroelasticity were also performed. Besides these theoretical and numerical simulation studies, the estimation of the respective intrinsic

(WIFF) and apparent (scattering) attenuation from the real seismic data has also been done by several authors (e.g., Mangriotis et al., 2013; Gurevich and Pevzner, 2015; Alasbali et al., 2016).

In this chapter, we propose a hybrid method to combine the WIFF and scattering models developed in the previous chapters. Hence, the coupling effects between WIFF and scattering on the seismic dispersion and attenuation can be studied. For simplicity and clarity, we only consider the case with aligned fractures embedded in the porous isotropic background medium. A numerical example is then given to illustrate the coupling effects. Furthermore, the corresponding numerical simulations are also performed to validate the proposed method.

6.2 Theory

Here, we assume the same fracture geometries and distributions as the scattering model proposed in Chapter 5. The fractures are parallel to each other and distributed randomly in the isotropic background medium. The size of the fractures is finite in the $X_1 - X_2$ plane, whereas the length of the fractures along the X_3-axis is infinite. Hence, the plane strain condition is satisfied and we can simplify the problem to the 2D problem. The details of the configurations of the fractures are shown in Figure 2-2. In order to study the WIFF effects, different from the elastic background assumed in Chapter 5, we assume the porous background in this model and both the background and the fractures are saturated with the same fluid. Hence, when the seismic wave propagates through such saturated fractured medium, both the wave scattering by the fractures and the WIFF can occur. This allows us to study their coupling effects on the seismic dispersion and attenuation. Same with Chapter 5, we only consider the case for P-wave here.

Due to the elastic contrasts between the fractures and the background medium, different fluid pressure can be generated in the fractures and background medium when the seismic wave propagates through the fractured medium. Hence, the fluid flow between the fractures and the background medium will occur. To quantify these effects, we can treat the saturated fractured medium as the saturated background medium permeated by the saturated fractures with frequency-dependent normal compliance.

This approach was employed by Rubino et al. (2015) and was also used in Chapter 3. Following Chapter 3, the frequency-dependent fracture normal compliance can be written as follows:

$$Z_N^{sat}(\omega) = Z_{N,lf}^{sat} f(\omega) + Z_{N,hf}^{sat}\left[1 - f(\omega)\right], \tag{6.1}$$

where $Z_N^{sat}(\omega)$ is the frequency-dependent fracture normal compliance; $Z_{N,lf}^{sat}$ and $Z_{N,hf}^{sat}$ are the saturated fracture compliances in the low- and high- frequency limits of WIFF, respectively; $f(\omega)$ is the relaxation function, which decays from one to zero from the low-frequency limit to the high-frequency limit of WIFF. The method of calculating $f(\omega)$ is given in Chapter 3.

Alternatively, we can present the frequency-dependent fracture normal compliance using the complex-valued and frequency-dependent fluid bulk modulus (Gurevich et al., 2010; Collet and Gurevich, 2016):

$$Z_N^{sat}(\omega) = \frac{1}{1 + \frac{Z_N}{\phi_f}\left(\frac{1}{K_f(\omega)} - \frac{1}{K_{ms}}\right)^{-1}}, \tag{6.2}$$

where Z_N is the dry fracture compliance; ϕ_f is the fracture porosity; $K_f(\omega)$ is the frequency-dependent fluid bulk modulus; K_{ms} is the saturated bulk modulus of the background medium.

Substituting equation (6.2) into equation (6.1), the following expression for the fluid bulk modulus can be obtained:

$$K_f(\omega) = \frac{1}{\left(\frac{1}{K_{f0}} - \frac{1}{K_{f1}}\right) f(\omega) + \frac{1}{K_{f1}}}, \tag{6.3}$$

where K_{f0} is the equivalent fluid bulk modulus in the low-frequency limit of WIFF; K_{f1} is the real fluid bulk modulus. K_{f0} can be calculated from the saturated fracture normal compliance in the low-frequency limit as follows:

$$K_{f0} = 1/\left(\frac{1}{\frac{\phi_f}{Z_{N,lf}^{sat}} - \frac{\phi_f}{Z_N}} + \frac{1}{K_{ms}} \right), \tag{6.4}$$

where the value of $Z_{N,lf}^{sat}$ can be calculated from equation (3.17).

Hence, the effects of FB-WIFF on the seismic dispersion and attenuation in this model can be quantified by the complex-valued and frequency-dependent fluid bulk modulus. As the permeability of the fractures is usually much higher than that of the background medium, the fluid pressure in the fractures is normally equilibrated in the considered frequencies. Thus, we can write the boundary condition on the fracture surface as follows:

$$\int_{-a}^{a} D_1(\zeta_1) T_{121}(x_1, 0 \mid \zeta_1, 0)\, d\zeta_1 - e^{ik_p x_1 \sin\theta} = \frac{i\omega\eta}{\mu} \frac{D_1(x_1)}{\beta}, \; -a < x_1 < a, \tag{6.5}$$

$$\int_{-a}^{a} D_2(\zeta_1) T_{222}(x_1, 0 \mid \zeta_1, 0)\, d\zeta_1 - e^{ik_p x_1 \sin\theta} = -\frac{K_f(\omega)}{2a\beta\mu} \int_{-a}^{a} D_2(\zeta_1)\, d\zeta_1, \; -a < x_1 < a. \tag{6.6}$$

It can be seen that the boundary condition for the shear stress remain unchanged compared to that for the scattering model proposed in Chapter 5. This is due to the fact that the fluid pressure only affects the normal stress and has no influence on the shear stress. By introducing the frequency-dependent fluid bulk modulus in boundary condition (6.6), the WIFF effects can be incorporated into the scattering model and hence the coupling between WIFF and scattering can be studied. After calculating normal and shear displacement discontinuities across the fractures by solving equations (6.5) and (6.6) numerically, we can compute the dispersion and attenuation of seismic waves due to both WIFF and scattering using equations (2.77) - (2.80).

6.3 Numerical example

6.3.1 Sample parameters

To study the coupling effects between the WIFF and wave scattering, we consider a P-wave propagating through a saturated porous sandstone with aligned fractures, as shown in Figure 6-1. The properties for the dry background medium are as follows: bulk modulus K_m = 26 GPa, shear modulus G_m = 31 GPa, porosity ϕ_b = 0.1, permeability κ_b = 10^{-13} m^2, tortuosity τ_b = 1.83, grain bulk modulus K_s = 37 GPa, and grain density ρ_s = 2.65 g/cm^3. The 2D fractures have a rectangular shape with a length of 30 mm and a thickness of 4 mm. The fraction of the fractures with respect to the whole rock (fracture porosity) is 0.0625. These fractures are filled with a high porous material which has the following properties: bulk modulus K_f = 0.02 GPa, shear modulus G_f = 0.01 GPa, porosity ϕ_f = 0.9, permeability κ_f =10^{-9} m^2, and tortuosity τ_b = 1.1. The grains composing the fracture infill material are assumed to be same with those for background medium. Both the fractures and the background medium are saturated with water with the following properties: bulk modulus K_f = 2.25, shear viscosity η_f = 0.001 Pa.s, and density ρ_f = 1.09 g/cm^3.

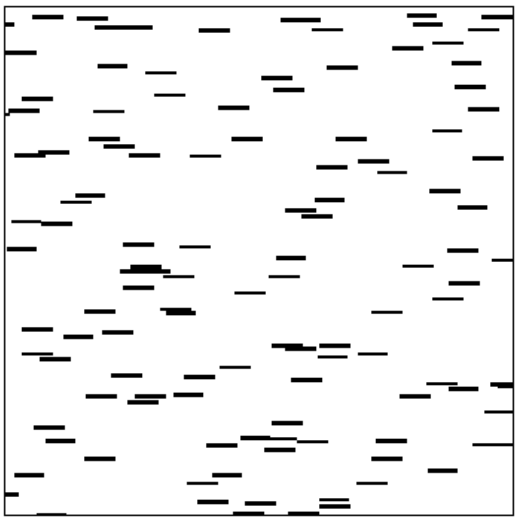

Figure 6-1. Saturated porous sandstone with aligned fractures.

Using the above parameters, the P-wave dispersion and attenuation due to both WIFF and scattering can be predicted by the proposed model. It should be noted that, when calculating the frequency-dependent fluid bulk modulus, the dry normal fracture compliance is needed. Since there is no exact theoretical solution for the dry normal compliance of rectangular fractures, we approximate its value by that for the elliptical fractures which have the same length and width. Then, the Eshelby model can be

used to calculate the dry fracture normal compliance [equation (2.2)]. Furthermore, the fracture density ε can be calculated from the fracture porosity as follows:

$$\varepsilon = \frac{\phi_f a}{2\beta}. \tag{6.7}$$

Apart from the theoretical predictions, we also performed the wave propagation numerical simulations based on the low-frequency approximation of Biot's dynamic poroelastic equations. The details for the numerical simulations are introduced in Section 2.10.2. The incident wave is generated in the host rock which has the same properties with the background medium of the fractured sandstone (Figure 6-2). Then, using the recorded waveforms before and after transmitting through the fractured sandstone, the velocity and attenuation of P-wave can be estimated. The theoretical predictions then can be compared to and validated by the numerical simulations. Due to the fact that the WIFF and wave scattering effects are both largest when the P-wave propagates in the direction perpendicular to the fracture plane (Chapters 3 and 5), their coupling should also be largest in this direction and hence we only consider the normal incidence case here.

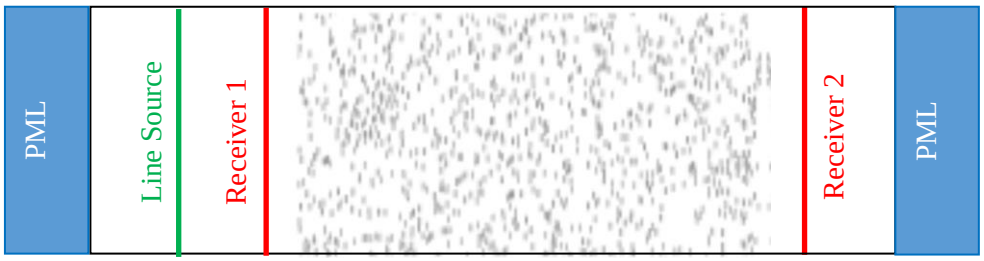

Figure 6-2. Sample configuration for numerical wave propagation simulation (Caspari et al., 2017).

6.3.2 Results

Figure 6-3 shows the theoretical predictions (red line) and numerical simulation results (blue line) for the P-wave dispersion and attenuation in the direction perpendicular to the fracture plane. In order to show the coupling effects between WIFF and scattering, we also show the theoretical predictions of pure scattering (green line). Comparing the results with and without considering the WIFF effects (red and green lines), it can be seen that the interplay between WIFF and scattering is significant in the

Rayleigh scattering regime, especially between 10^2 Hz and $2.5*10^4$ Hz. In the low-frequency limit, the equilibration of the fluid pressure significantly decreases the P-wave velocity. Then, due to the WIFF effects, the velocity start to increase slightly with the frequency. However, before it reaches the quasi-static value for the saturated rock with hydraulically isolated fractures, the effects of Rayleigh scattering become dominant and hence the velocity begin to decrease. It can be noted that the predicted velocity considering both the effects of WIFF and scattering is always smaller than that which only takes into account scattering effects in the Rayleigh regime. This is due to the fact that, the WIFF occurs in this regime which weakens the stiffness of the fractures. As a result, the velocity decreases compared to the pure scattering case. With the increase of the frequency, the size of the fractures becomes comparable to the seismic wavelength and hence the Mie scattering occurs. We observe that the velocity in this regime is almost the same between the cases with and without considering WIFF effects. This means that the WIFF effects are negligible in this regime and the fractures are hydraulically isolated from the background medium. Comparing the theoretical predictions with the numerical simulations, we can find the excellent agreement between them. This verifies the goodness of the proposed approach. Furthermore, the good agreement between the theoretical predictions and the numerical simulations imply that the effects of the Biot's global flow in the numerical simulations are negligible. This is probably due to the much higher characteristic frequency for Biot's global flow than the considered frequencies in the numerical simulations, which results in the negligible Biot's global flow.

By comparing the theoretical predictions with and without considering WIFF effects, we can note that the attenuation is primarily due to the effects of WIFF before 10^2 Hz. The attenuation is proportional to ω in this frequency regime instead of ω^2 for the scattering model. This is the typical characteristic of the attenuation at low frequencies caused by WIFF (Chapter 3), which further validates the major role of the WIFF in this frequency regime. When the frequency lies between 10^2 Hz and $2.5 * 10^4$ Hz, the interaction between the WIFF and scattering become significant, which is consistent with the results for the velocity dispersion. In this regime, the attenuation continue to increase with the frequency, whereas the shape becomes complex due to the interplay between the WIFF and the scattering. At high frequencies ($> 2.5 *10^4$ Hz), the fracture size becomes comparable to the seismic wavelength and hence

Mie scattering occurs. We can see that the WIFF effects are negligible in this regime because the theoretical predictions with and without considering these effects (red and green lines) are almost the same.

Comparing the numerical simulations with the theoretical predictions, the variation of the attenuation with the frequency obtained from numerical simulations has the same shape as that predicted by theory. However, the numerically estimated value is slightly higher than the theoretically predicted value. This is probably due to the transmission loss. In the wave propagation numerical simulation, the incident wave is generated in the host rock and then transmitted into and out of the fractured sandstone. Due to the different acoustic impedance between the host rock and the fractured sandstone, some energy will be reflected back on the surface between these two media. Hence, the transmission loss will occur, which will result in additional energy attenuation in the numerical simulations (Caspari et al., 2007). Furthermore, the magnitude of the transmission loss depends on the acoustic impedance contrast between the host rock and the fractured sandstone. It can be seen from Figure 6-3a that the acoustic impedance of the fractured sandstone varies with the frequency due to the effects of WIFF and scattering. However, this variation is small and hence the transmission loss should be almost independent of the frequency. From Figure 6-3b, we can note a nearly constant shift of the attenuation between the theoretical predictions and numerical simulations. This means that this additional attenuation in the numerical simulations is nearly frequency-independent, which agrees with the characteristics of the energy attenuation caused by transmission loss.

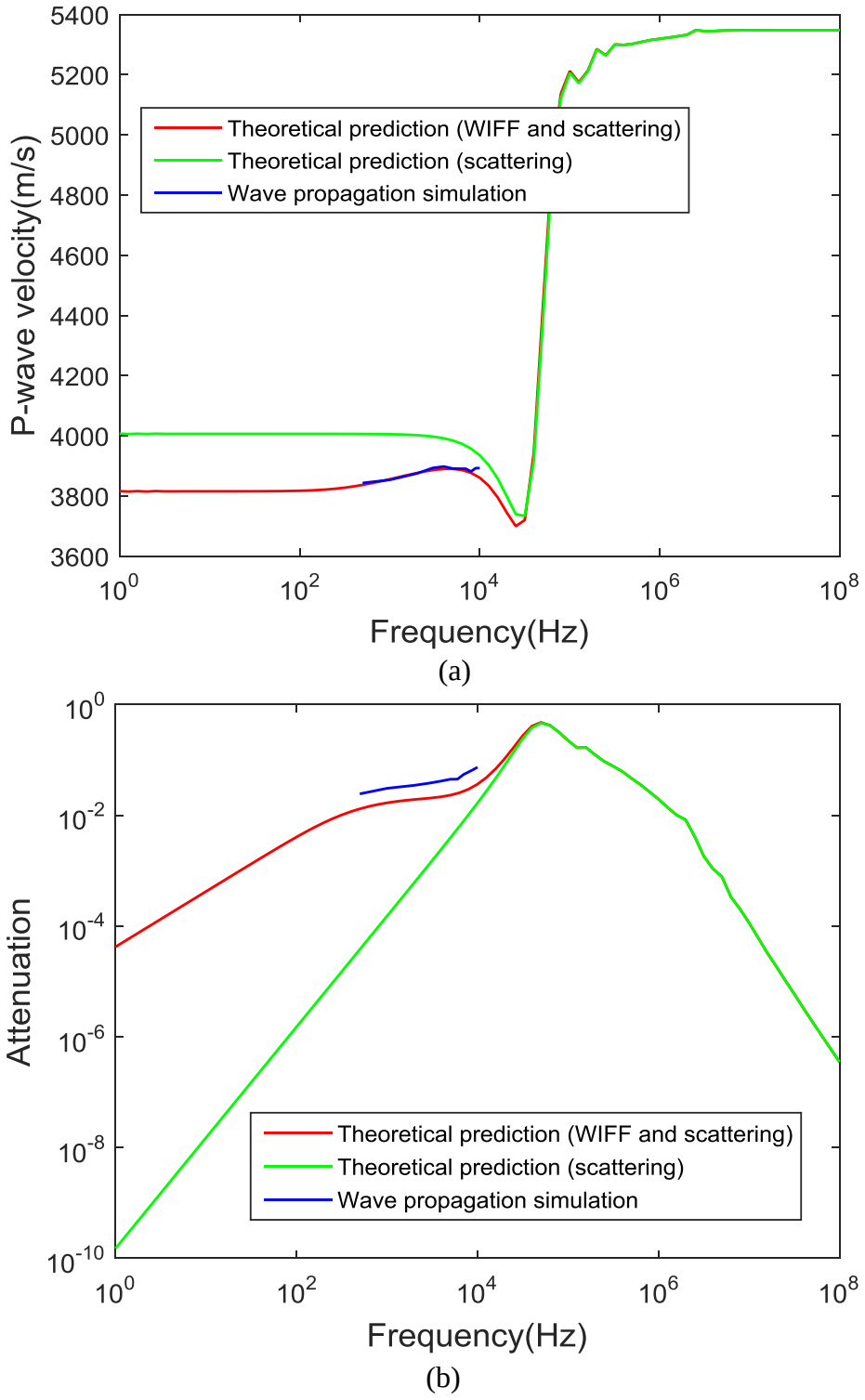

Figure 6-3. Comparison between theoretical predictions and numerical simulations.

As discussed before, we use the frequency-dependent fluid bulk modulus to quantify the WIFF effects in this approach. Hence, it is interesting to analyse the results for the frequency-dependent fluid

bulk modulus, as shown in Figure 6-4. Here, we define the ratio of the imaginary part to the real part of the fluid bulk modulus as the attenuation and the variation of the real part as the dispersion. We can note that the equivalent fluid bulk modulus in the low-frequency limit of WIFF is around half value of that in the high-frequency limit, which indicates the large effects of WIFF on the P-wave dispersion and attenuation. It can be seen that, the equivalent fluid bulk modulus in the high-frequency limit approaches its real value. This means the fractures are hydraulically isolated from the saturated background medium. For the attenuation, the value is proportional to ω and $\omega^{-1/2}$ at low and high frequencies, respectively. This is consistent with the characteristics of the attenuation caused by WIFF (Chapter 3). Furthermore, it can be observed that the peak frequency for WIFF is around 10^3 Hz, whereas that for the wave scattering can be found to be on the order of 10^4 Hz from Figure 6-3b. Hence, the characteristic frequencies for these two mechanisms are close to each other and thus the interplay between them occurs, as shown above. Due to the interactions between these two mechanisms, the peak for WIFF cannot be seen clearly in Figure 6-3b, but becomes an inflection point.

It is interesting to note here that while there may be some errors when using the Eshelby model to calculate the dry normal compliance of the 2D rectangular fractures (Chapter 4), the resulting equivalent fluid bulk modulus can still give good theoretical predictions (Figure 6-3). This is probably due to the fact that both the dry and saturated fracture normal compliances are influenced by the fracture geometries and hence this influence can be cancelled out when calculating the equivalent fluid bulk modulus, as indicated in equation (6.4). In summary, we can conclude that the WIFF effects are well quantified by using the frequency-dependent fluid bulk modulus.

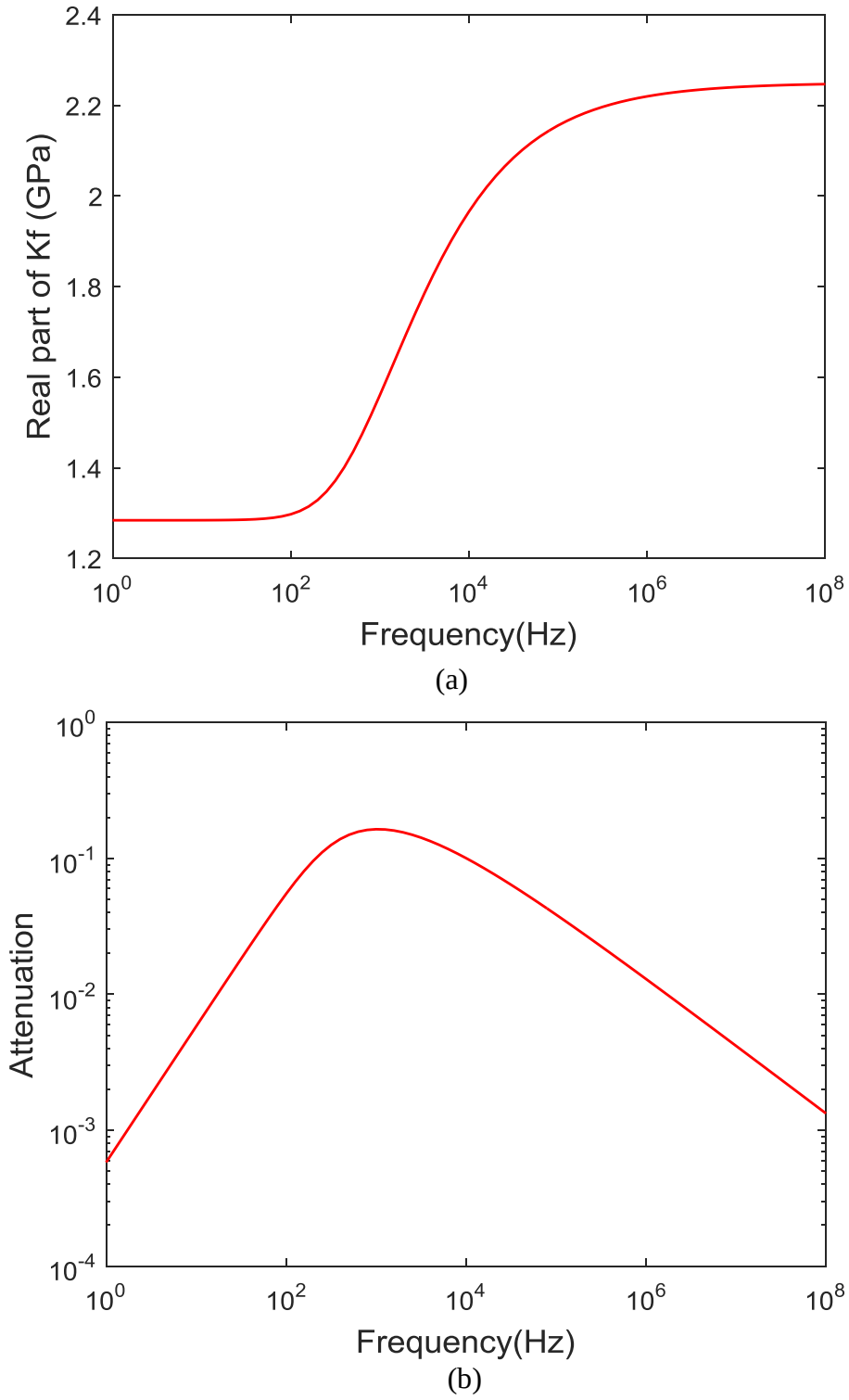

Figure 6-4. Dispersion and attenuation of the fluid bulk modulus.

6.4 Discussion and conclusions

In this chapter, we proposed a hybrid method to quantify the coupling effects of WIFF and wave scattering. Based on the WIFF model proposed in Chapter 3 and the scattering model established in Chapter 5, we combined them through a complex-valued and frequency-dependent fluid bulk modulus. This fluid bulk modulus can be calculated through the relaxation function and the values in the low- and high- frequency limits of WIFF. Then, we can use the frequency-dependent fluid bulk modulus in the boundary conditions and hence the interactions between the WIFF and the scattering can be studied. To illustrate this coupling effect, we consider a P-wave propagating through a saturated porous sandstone with aligned fractures. The results show that the characteristic frequencies for the WIFF and the wave scattering are close to each other in the studied case. Hence, the interplay between the WIFF and wave scattering is significant, which occurs primarily in the Rayleigh scattering regime. To validate the theoretical predictions, the wave propagation numerical simulations based on the low frequency approximation of Biot's dynamic poroelastic equations are also performed, which showed good agreement with the theoretical predictions. The slight shift of the numerically estimated attenuation from the theoretically predicted values may be due to the transmission loss which is not taken into account in the theoretical predictions.

As both the WIFF model and the scattering model assume that the fracture thickness and density are small (usually both are smaller than 0.1), the hybrid approach also requires the low fracture thickness and density. However, both these two values are relatively high (slightly larger than 0.1) in the studied case. The good agreement between the theoretical predictions and the numerical simulations suggests that our approach is applicable even under the relatively high fracture thickness and density, which implies the robustness of this approach. Furthermore, apart from the P-wave perpendicular to the fracture plane, the proposed approach is also capable to calculate the angle-dependence of the P-wave velocity and attenuation. The frequency-dependent anisotropic properties can thus be studied. This work will be carried out in the future. In addition, we only consider the WIFF between the fractures and the background medium (FB-WIFF) in our current model. The effects of WIFF between fractures (FF-WIFF) can also be incorporated into the model in the future work. Finally, it should be noted that, as both the mechanisms of WIFF and wave scattering are complicated, it cannot be guaranteed that the

assumptions behind these two mechanisms are entirely consistent in the proposed hybrid approach. However, the hybrid approach is still very useful due to the fact that the real fractures will cause both effects and hence a simple and efficient method is needed for modelling them.

Chapter 7
Conclusions and future work

7.1 Conclusions

In this thesis, two mechanisms for the seismic dispersion and attenuation, as well as frequency-dependent anisotropy, are studied in the fractured reservoirs. One mechanism is the wave-induced fluid flow, which results in the intrinsic seismic dispersion and attenuation. For the reservoirs with aligned fractures, the effects of the FB-WIFF on the seismic responses were studied, for which the characteristic frequency depends on the diffusivity of the background medium and the fracture geometries. Three types of fractures were considered, i.e., the periodically- and randomly- spaced planar fractures, as well as the penny-shaped cracks. The existing models for P-waves propagating perpendicular to the fracture plane were extended using the branching function approach, which was extended to account for the effects of finite fracture thickness. To study the anisotropic properties, the results were further extended to the full stiffness matrix using two theoretical approaches, one of which involves interpolation between low and high frequency limits of the stiffness tensor using a relaxation function while the other is based on the frequency-dependent effective fracture compliances. The extended models were then validated by comparing to the numerical simulations based on the Biot's quasi-static equations of poroelasticity. The results show that the finite fracture thickness has significant influence on the seismic dispersion and attenuation at high frequencies when the fluid pressure in the fractures does not have enough time to equilibrate with that in the background pores. However, this influence is rather small at low frequencies when the fluid pressure in the fractures has sufficient time to communicate with that in the background pores. The extended models are found to be applicable even for the relatively high fracture density (0.2) for the case with random fracture distributions. This implies the cancellation of the competing effects of stress shielding and amplification under the random fracture distributions, which results in the small fracture interaction effects. For the anisotropic properties, the predictions

given by both theoretical approaches are in good agreement with the numerical simulations. The approach based on the frequency-dependent fracture compliance matrix is particularly attractive in practice as the fracture compliances can be estimated from the seismic data through the standard analysis in the frequency-domain.

When the fractures intersect with each other, the WIFF between the fractures (FF-WIFF) also has significant influence on the seismic dispersion and attenuation. To study these effects, the seismic dispersion and attenuation in the saturated porous rocks with two perpendicular sets of fractures were considered. Two cases were studied, one with intersecting fractures and the other with non-intersecting fractures. Based on the theoretical models for the rocks with aligned fractures, the models for the considered two cases were developed. Furthermore, the characteristic frequencies for the FB-WIFF and FF-WIFF in the studied cases are also given. For the FB-WIFF, the characteristic frequency is same with that for the aligned fracture case, whereas for the FF-WIFF, the characteristic frequency depends on the diffusivity of an effective background medium and geometries of the fractures. The results show that, as expected, for the rocks with non-intersecting fractures, only FB-WIFF occurs and hence there are only two frequency regimes (low- or high- frequency limit) depending on whether or not the fluid pressure in the fractures has enough time to equilibrate with that in the background pores. However, for the rocks with intersecting fractures, apart from the FB-WIFF, FF-WIFF also occurs. This results in an additional intermediate frequency regime where the fractures are hydraulically isolated from the background medium, but are in hydraulically communications with each other. This additional frequency regime is well separated from the low- and high- frequency limits by the characteristic frequencies for the FB-WIFF and FF-WIFF respectively. Due to the effects of the fluid pressure equilibration between the fractures, the magnitude of the seismic dispersion and attenuation due to FB-WIFF is smaller. Furthermore, the velocity anisotropy is also reduced greatly due to variations of the stiffening effects of the fracture fluid in response to FF-WIFF (Rubino et al., 2017). Hence, it is of great importance to consider both manifestations of WIFF when the fractures in the reservoirs are intersecting with each other. This, in turn, provides the potential to extract the information on the fracture connectivity and reservoir effective permeability from the seismic data. To validate the theoretical

predictions, the results are compared to the numerical simulations, which shows good agreement between them.

Another important mechanism for the seismic dispersion and attenuation is the wave scattering by the fractures. When the fractures have similar size with the seismic wavelength, the wave scattering can cause significant seismic dispersion and attenuation. This mechanism is of particular importance in the fracture 'swarms' or 'corridors' as the fracture size in these fractured zones is usually comparable to the seismic wavelength. To study this mechanism, the P-wave scattering by the fluid saturated fractures with finite thickness is investigated in this thesis. The P-wave dispersion and attenuation are first related to the displacement discontinuities across the fractures using the Foldy approximation and the representation theorem. Then, the displacement discontinuities across the fractures are obtained from the boundary conditions and hence the P-wave dispersion and attenuation can be calculated. To illustrate the P-wave scattering effects, a numerical example was then given. The results show that the fracture thickness has significant influence on the dispersion and attenuation, especially in the low frequency regime when the fracture size is smaller than the seismic wavelength. The effects of the fluid bulk modulus are also significant, which are opposite to those of the fracture thickness. However, the effect of the fluid viscosity is found to be negligible for the studied configurations. To validate the proposed model, the theoretical predictions are compared with ultrasonic measurements on fractured samples. The comparison shows overall good agreement between theory and experiment. This work reveals the important influence of fracture thickness and saturating fluid properties on the P-wave scattering dispersion and attenuation. Hence, it shows a potential to extract these parameters from seismic data.

While a lot of research has been done on the WIFF and wave scattering mechanisms, most of them consider these two mechanisms separately and the interplay between them is seldom studied. Hence, in this thesis, the coupling effects between these two mechanisms on the seismic dispersion and attenuation were investigated. By using the complex-valued and frequency-dependent fluid bulk modulus in the boundary conditions, the WIFF effects can be incorporated into the scattering model. The interplay between them can thus be studied. The results show that the interactions between WIFF

and wave scattering are significant when the characteristic frequencies for these two mechanisms are close to each other. Due to the fluid pressure communications between the fractures and the background medium, the velocities in a medium with both the WIFF and scattering effects will be smaller than when only the scattering effects are present. To validate the proposed approach, the wave propagation numerical simulations based on the low-frequency approximation of Biot's dynamic equations of poroelasticity are also performed. Good agreement is found between the theoretical predictions and the numerical simulations. This work allows a more accurate interpretation of the rock properties from the seismic dispersion and attenuation data.

In summary, the study in this thesis provides the basis for developing the seismic attributes for the detection and characterizations of the fractures. Based on the developed theories, it is possible to extract various fracture properties from the seismic data, such as the fracture thickness, saturating fluid properties, and fracture connectivity degree, among many others.

7.2 Future work

In the future, more work can be done on the following aspects:

1) Considering the complexity of the real fractured reservoirs, the models developed in this study may still not be adequate for the fracture detection and characterization. For instance, our current models only consider very simple fracture networks. However, fracture networks in real reservoirs can be very complicated. Hence, it is essential to study the effects of complex fracture networks on the WIFF and wave scattering, and hence on the related seismic dispersion and attenuation, as well as the frequency-dependent anisotropy. This includes various effects, such as the fracture size distributions, fracture orientations, and fracture intersection angles, among many others. Furthermore, the current models assume that the rocks are saturated with a single fluid and the background medium is isotropic. However, the reservoirs are usually saturated with several different types of fluids (such as oil, gas, and water) and the background medium can show anisotropic properties (such as tight sand and shale reservoirs). Hence, it is also important to study these effects on the seismic signatures in the future.

2) The ultimate objective of developing these rock physics models is to apply them in practice. Hence, a major task for the future work is developing the seismic attributes for the characterization of fractured reservoirs and interpretation of corresponding seismic data. To this end, we can first develop several attributes based on our theoretical models, which can then be tested using the synthetic and real seismic data. The most sensitive attributes can thus be selected and improved according to the test results. During this procedure, the recent developed technologies in computer sciences, such as the big data analysis, artificial intelligence, and deep learning, can serve as powerful tools for this purpose. The developed seismic attributes will provide information on fracture properties, especially the fracture thickness and fracture connectivity. This will enable us to estimate the effective permeability of the fractured reservoirs, which is of great importance in the oil/gas exploration and production.

Appendix A

Expressions of T_{jkl}

Expressions of T_{jkl} are given by Kawahara and Yamashita (1992), which are shown as follows:

$$T_{jkl}\left(x_1,x_2\mid\zeta_1,\zeta_2\right)=T^{*}_{jkl}\left(x_1,x_2\mid\zeta_1,\zeta_2\right)$$

$$+\frac{i}{4}\left[\left(\delta_{jl}\frac{\partial^2}{\partial x_k\partial x_2}+\delta_{k2}\frac{\partial^2}{\partial x_j\partial x_l}+\delta_{kl}\frac{\partial^2}{\partial x_j\partial x_2}+\delta_{j2}\frac{\partial^2}{\partial x_k\partial x_l}\right)\right.$$

$$\left.\times H_0^{(1)}\left(k_sR\right)-\frac{4}{k_s^2}\frac{\partial^4}{\partial x_j\partial x_k\partial x_l\partial x_2}\left(H_0^{(1)}\left(k_pR\right)-H_0^{(1)}\left(k_sR\right)\right)\right], \tag{A1}$$

where $R=\left(x_1-\zeta_1\right)^2+\left(x_2-\zeta_2\right)^2$, and

$$T^{*}_{111}\left(x_1,x_2\mid\zeta_1,\zeta_2\right)=\frac{i}{2}\left(1-2\frac{k_p^2}{k_s^2}\right)\frac{\partial^2}{\partial x_1\partial x_2}H_0^{(1)}\left(k_pR\right), \tag{A2}$$

$$T^{*}_{122}\left(x_1,x_2\mid\zeta_1,\zeta_2\right)=T^{*}_{212}\left(x_1,x_2\mid\zeta_1,\zeta_2\right)=T^{*}_{221}\left(x_1,x_2\mid\zeta_1,\zeta_2\right)=T^{*}_{111}\left(x_1,x_2\mid\zeta_1,\zeta_2\right), \tag{A3}$$

$$T^{*}_{112}\left(x_1,x_2\mid\zeta_1,\zeta_2\right)=\frac{i}{4}\frac{k_s^2}{k_p^2}\left(1-2\frac{k_p^2}{k_s^2}\right)\left(\frac{\partial^2}{\partial x_1^2}+\frac{\partial^2}{\partial x_2^2}\right)H_0^{(1)}\left(k_pR\right), \tag{A4}$$

$$T^{*}_{121}\left(x_1,x_2\mid\zeta_1,\zeta_2\right)=T^{*}_{211}\left(x_1,x_2\mid\zeta_1,\zeta_2\right)=0, \tag{A5}$$

$$T^{*}_{222}\left(x_1,x_2\mid\zeta_1,\zeta_2\right)=\frac{i}{4}\frac{k_s^2}{k_p^2}\left[\left(1-2\frac{k_p^2}{k_s^2}\right)^2\frac{\partial^2}{\partial x_1^2}+\left(1-4\frac{k_p^4}{k_s^4}\right)\frac{\partial^2}{\partial x_2^2}\right]H_0^{(1)}\left(k_pR\right). \tag{A6}$$

Appendix B

Numerical calculation of T_{mn}^{jkl}

The expressions of T_{mn}^{jkl} can also be found in Kawahara and Yamashita (1992). They are repeated here for the convenience of the readers as follows:

When $m = n$,

$$T_{nn}^{121} = -\frac{\hat{k}_p^2 - \hat{k}_s^2}{\hat{k}_s^2}\frac{4}{\pi\Delta s} - \frac{\hat{k}_p^4 + \hat{k}_s^4}{\hat{k}_s^2}\frac{i\Delta s}{8}$$

$$+\frac{\Delta s}{4\pi\hat{k}_s^2}\left[\hat{k}_p^4 \log\frac{\hat{k}_p\Delta s}{4} + \hat{k}_s^4 \log\frac{\hat{k}_s\Delta s}{4} + \hat{k}_p^4\left(C - \frac{3}{4}\right) + \hat{k}_s^4\left(C - \frac{5}{4}\right)\right], \tag{B1}$$

$$T_{nn}^{222} = -\frac{\hat{k}_p^2 - \hat{k}_s^2}{\hat{k}_s^2}\frac{4}{\pi\Delta s} - \frac{3\hat{k}_p^4 - 4\hat{k}_p^2\hat{k}_s^2 + 3\hat{k}_s^4}{\hat{k}_s^2}\frac{i\Delta s}{8}$$

$$+\frac{\Delta s}{4\pi\hat{k}_s^2}\left[3\hat{k}_p^4 \log\frac{\hat{k}_p\Delta s}{4} - 4\hat{k}_p^2\hat{k}_s^2 \log\frac{\hat{k}_p\Delta s}{4} + 3\hat{k}_s^4 \log\frac{\hat{k}_s\Delta s}{4} + 2\hat{k}_s^4 \log\frac{\hat{k}_p}{\hat{k}_s}\right.$$

$$\left.+\hat{k}_p^4\left(3C - \frac{5}{4}\right) + \hat{k}_p^2\hat{k}_s^2\left(4C + 2\right) + \hat{k}_s^4\left(3C - \frac{11}{4}\right)\right], \tag{B2}$$

$$T_{nn}^{122} = T_{nn}^{221} = 0; \tag{B3}$$

when $m \neq n$,

$$T_{mn}^{121} = -\frac{i}{4}\hat{k}_s^2\Delta s H_0^{(1)}\left(\hat{k}_s s_{mn}\right) - \frac{i\Delta s}{\hat{k}_s^2}\left[\frac{1}{s_{mn}}\left\{\hat{k}_p^3 H_1^{(1)}\left(\hat{k}_p s_{mn}\right) - \hat{k}_s^3 H_1^{(1)}\left(\hat{k}_s s_{mn}\right)\right\}\right.$$

$$+\frac{3}{s_{mn}^2}\left\{\hat{k}_p^2 H_0^{(1)}\left(\hat{k}_p s_{mn}\right)-\hat{k}_s^2 H_0^{(1)}\left(\hat{k}_s s_{mn}\right)\right\}-\frac{6}{s_{mn}^3}\left\{\hat{k}_p H_1^{(1)}\left(\hat{k}_p s_{mn}\right)-\hat{k}_s H_1^{(1)}\left(\hat{k}_s s_{mn}\right)\right\}\Bigg]$$

$$-\frac{\hat{k}_p^4+\hat{k}_s^4}{4\pi\hat{k}_s^2}\left[\Delta s\log s_{mn}-\int_{s_n-\Delta s/2}^{s_n+\Delta s/2}\log\left|s_m-\hat{\zeta}_1\right|d\hat{\zeta}_1\right]$$

$$-\frac{\hat{k}_p^2-\hat{k}_s^2}{\pi\hat{k}_s^2}\left[\frac{\Delta s}{s_{mn}^2}-\int_{s_n-\Delta s/2}^{s_n+\Delta s/2}\frac{d\hat{\zeta}_1}{\left(s_m-\hat{\zeta}_1\right)^2}\right], \tag{B4}$$

$$T_{mn}^{222}=-\frac{i}{4}\hat{k}_s^2\left(1-2\frac{\hat{k}_p^2}{\hat{k}_s^2}\right)^2\Delta s H_0^{(1)}\left(\hat{k}_p s_{mn}\right)$$

$$-\frac{i\Delta s}{\hat{k}_s^2}\left[\frac{\hat{k}_s^2}{s_{mn}}\left\{\hat{k}_p\left(1-2\frac{\hat{k}_p^2}{\hat{k}_s^2}\right)H_1^{(1)}\left(\hat{k}_p s_{mn}\right)+\hat{k}_s H_1^{(1)}\left(\hat{k}_s s_{mn}\right)\right\}\right.$$

$$\left.-\frac{3}{s_{mn}^2}\left\{\hat{k}_p^2 H_0^{(1)}\left(\hat{k}_p s_{mn}\right)-\hat{k}_s^2 H_0^{(1)}\left(\hat{k}_s s_{mn}\right)\right\}+\frac{6}{s_{mn}^3}\left\{\hat{k}_p H_1^{(1)}\left(\hat{k}_p s_{mn}\right)-\hat{k}_s H_1^{(1)}\left(\hat{k}_s s_{mn}\right)\right\}\right]$$

$$-\frac{3\hat{k}_p^4-4\hat{k}_p^2\hat{k}_s^2+3\hat{k}_s^4}{4\pi\hat{k}_s^2}\left[\Delta s\log s_{mn}-\int_{s_n-\Delta s/2}^{s_n+\Delta s/2}\log\left|s_m-\hat{\zeta}_1\right|d\hat{\zeta}_1\right]$$

$$-\frac{\hat{k}_p^2-\hat{k}_s^2}{\pi\hat{k}_s^2}\left[\frac{\Delta s}{s_{mn}^2}-\int_{s_n-\Delta s/2}^{s_n+\Delta s/2}\frac{d\hat{\zeta}_1}{\left(s_m-\hat{\zeta}_1\right)^2}\right], \tag{B5}$$

$$T_{mn}^{122}=T_{mn}^{221}=0, \tag{B6}$$

where $H_1^{(1)}(\cdot)$ is the first order Hankel function of the first kind; $\hat{k}_s=ak_s$ is the normalized *S*-wave number in the elastic background medium; $C\approx 0.5772$ is Euler's constant; s_n and s_m are equal to $-1+n\Delta s$ and $-1+m\Delta s$, respectively; and $s_{mn}=\left|s_m-s_n\right|$. Note that equations (B3) and (B6) mean:

$$T_{122}\left(x_1,0\,|\,\zeta_1,0\right)=T_{221}\left(x_1,0\,|\,\zeta_1,0\right)=0\,. \tag{B7}$$

Appendix C

Copyright consent

Permission 1:

Publications ▸ Policies and Permissions ▸ Open Access Policy

SEG Policy on Open-access Publishing

SEG provides authors a variety of open-access publishing options, including some "green" and "gold" open-access options.

SEG provides the world's premier vehicles for knowledge exchange in applied geophysics. The Society's publishing program is one such vehicle. To help attract the best scholarship and disseminate it to the widest possible audience through journals, meetings papers, and books, SEG provides authors a variety of open-access publishing options. These include some "green" open-access options that long have been features of the traditional subscription-based business model that has sustained the Society's publishing program.

In 2011, SEG went further by instituting a "gold" open-access option for its journals, transforming them into "hybrid" open-access journals. In exchange for payment of an author publication charge (APC) of US$2,500 plus payment of all applicable voluntary and mandatory page and color charges, SEG agreed to remove access barriers to full-text presentations of the author's paper on SEG publications sites. Standard copyright transfer was required.

Beginning with papers published in 2014, this gold open-access option is expanded with additional copyright and licensing options, and the policy also is extended to meetings papers and book chapters. These changes make all SEG publications compliant with requirements in place and emerging from a variety of research funders and their overseers, such as Research Councils UK (RCUK), the European Commission, and the U.S. Office of Science and Technology Policy. Also, some aspects of SEG's green open-access policy are refined.

In October 2015, the SEG Board of Directors approved a policy change removing the requirement of authors to pay all voluntary charges for open-access papers for papers submitted on or after 15 October 2015. Authors must pay mandatory charges and the $2,500 open-access fee.

Here are features of open-access options available to authors, or in cases of works made for hire, their employers:

Traditional publication (including green open access)

- No author publication charge (APC) is levied, although payment of mandatory page charges are assessed and payment of voluntary charges is requested. Relief from mandatory charges may be requested under SEG's hardship relief policy.
- Copyright is transferred to SEG.
- Authors/employers retain proprietary rights such as the right to patentable subject matter and the right to make oral presentation of the work with full citation and proper copyright acknowledgment.
- Authors/employers enjoy the right to prepare and hold copyright in derivative publications based on the paper provided that the derivative work is published subsequent to the official date of the original paper's publication by SEG.
- Authors/employers may post a final accepted version of the manuscript or the final SEG-formatted version (book chapters excluded) on authors' personal websites, employers' websites, or in institutional repositories operated and controlled exclusively by authors'

employers provided that:

1. the SEG-prepared version is presented without modification;
2. copyright notice and a full citation appear with the paper;
3. a link to the SEG version of record in the SEG Digital Library using Digital Object Identifier (DOI) permalinks is provided;
4. the posting is noncommercial in nature, and the paper is made available to users without charge; and
5. that notice be provided that use is subject to SEG terms of use and conditions.

- Authors/employers may not post their articles in an institutional repository or other site in which the content is required to carry or is implied as carrying a license contrary to SEG copyright and terms of use and terms of this policy.
- Authors/employers may post to their own websites a preprint (a version prior to SEG peer review) of a submitted manuscript provided that the posting is accompanied by prominent notice that the paper is under review for publication by SEG and the publication to which the manuscript has been submitted is identified. Upon publication of the paper by SEG, the author must replace any previously posted electronic versions of the paper with either (a) a full citation to the SEG-published work with a DOI permalink to the paper's abstract or (b) the final version of the manuscript or SEG-formatted version (book chapters excluded) subject to SEG conditions for such posting.
- Authors may reuse all or part of their papers published with SEG in a thesis or dissertation that authors write and are required to submit to satisfy criteria of degree-granting institutions.
- Authors/employers have the nonexclusive right, after publication by SEG, to give permission to third parties to republish print versions of the paper, or excerpts therefrom, without obtaining permission from SEG, provided that:
  1. the SEG-prepared version is not used for this purpose;
  2. the paper is not republished in another journal or book; and
  3. the third party does not charge a fee. Permission must be obtained from SEG for other republication of the paper.

"Gold" open access

- Authors, their employers, or research funders pay an author publication charge (APC) of US$2,500 plus any applicable mandatory page charges. It is SEG's expectation that APCs typically be paid by employers or research funding agencies and, if by the author, from a portion of author's research funds designated for open-access publishing. The fee applies to all journal articles and meeting papers yet may be adjusted for book chapters depending on chapter length, number of chapters, the proportion of open-access material in the whole book, and the anticipated market for the book.
- SEG publishes the paper to its official websites (SEG Digital Library and GeoScienceWorld) without access controls immediately upon publication and in perpetuity. The paper is clearly flagged as Open Access.
- Authors/employers retain copyright and select from among four Creative Commons licenses under which their work is licensed to the public and to SEG. Authors/employers execute an additional licensing agreement extending specific additional rights to SEG. The Creative Commons licenses available for selection by authors/employers are:
  - Creative Commons Attribution license (CC BY): This license lets others distribute, remix, tweak, and build upon the author's work, even commercially, as long as they credit the author and/or licensors for the original creation. This license meets licensing requirements of the RCUK.
  - Creative Commons Attribution-NonCommercial license (CC BY-NC): This license allows the

same uses and has the same attribution requirement as CC BY but excludes commercial use of the paper. Those who reuse the work do not have to adopt the same license for derivative works.
    - Creative Commons Attribution-ShareAlike license (CC BY-SA): This license allows the same uses and has the same attribution requirement as CC BY except that all derivative works must carry the same license, so any derivatives also will allow commercial use. The SEG Wiki and Wikipedia use this license.
    - Creative Commons Attribution-NonCommercial-NoDerivatives license (CC BY-NC-ND): This is the most restrictive of the Creative Commons licenses, allowing others to download and share the author's work with attribution but without the right to create derivatives or to use the work commercially.
- Licensing agreements between SEG and authors/employers extend to SEG worldwide license to publish the paper, all associated supplemental material, and subsequent, if necessary, errata in any SEG publication under the terms of the Creative Commons license selected by authors/employers. Further, authors/employers agree to acknowledge the SEG-published version of the paper as the version of record.
- Licensing agreements between SEG and authors/employers also stipulate that subsequent Discussions and Replies associated with a paper be licensed and published under the same Creative Commons license as the paper itself.
- Licensing agreements between SEG and authors/employers stipulate that further distribution of a paper must maintain attribution to the author(s) and the published paper's title, full citation, and DOI (linked to the SEG official version if in electronic form). SEG states this requirement in the published paper alongside indication of which Creative Commons license has been selected by the authors/employer.
- Licensing agreements between SEG and authors/employers grant to SEG additional rights to enforce rights in the work, on behalf of the author and SEG, against third parties in cases of plagiarism, ethical disputes, and fraud. Such agreements also grant SEG nonexclusive right to extend to third parties content-reuse permissions that exceed the rights granted to third parties under the Creative Commons license selected by the author/employer.
- Author/employer rights and responsibilities defined for traditional publication that are not superseded by these gold open-access policies are applicable to authors/employers electing gold open access.

Applicability to copublished material

The policies herein described apply not only to material published by SEG alone but also to Interpretation, which SEG copublishes with the American Association of Petroleum Geologists. Questions about the applicability of these policies to other work SEG publishes with other organizations should be directed to the SEG publications director.

Subscription pricing

SEG shall annually examine whether gold open access adoption rates merit moderation or reduction in institutional subscription fees and adjust rates accordingly.

Permission 2:

Author Reuse and Self-Archiving

As an author of an Oxford University Press title, published by our Academic, Trade, Reference, Science and/or Medical books groups, there are certain rights granted to you in the area of Reuse and Self Archiving. This policy sets out the way in which you, as authors of these titles, may reuse pre and post publication versions of your work for your own teaching, publishing and self-archiving purposes, without the need to obtain written permission from OUP.

Scope of the policy

The specific parameters set out in this policy relate to the following Global Academic Business (GAB) book publishing groups in the UK, US, India and Canada **ONLY:**

Academic

Trade

Science

Medical

Reference

This **does not** cover authors of titles published by the following GAB publishing groups:

Higher Education

Law

Education - Schools/K-12 (Canada), or

ELT (Canada)

Requests from these areas will continue to be handled on a case-by-case basis by the book's editor.

If you are unsure about which division or publishing group is responsible for publishing your title, please contact your Commissioning/Acquiring Editor.

Authors wishing to reuse work that they have published with **English Language Teaching (ELT) or Oxford Educational (OE)** divisions must contact the respective rights teams directly in order to request permission.

ELT
OXED

Our Journals publishing group has its own author reuse guidelines which may be found on the homepage of each journal.

Rights Granted

Prior to publication

Prior to publication, you retain the right to make a maximum of one chapter (or article where appropriate) of the original pre-copyedited version of your work available on the following, where necessary:

your personal website

the website of your employer and/or

in pre-print servers (i.e. free public servers of original version articles or other content in your subject area)

This is permitted provided that you acknowledge that the content has been accepted for publication by including an acknowledgement as follows:

This is a draft of a chapter/article that has been accepted for publication by Oxford University Press in the forthcoming book [title] by/edited by (Author/editor) due for publication in [year].

After publication Oxford would also ask that you update this record to ensure that the details are accurate, and if possible include links to the OUP catalogue and webpage.

After publication

After publication you may reuse the following portions of your content without obtaining formal permission for the activities expressly listed below:

- one chapter or up to 10% of the total of your single author or co-authored book,
- a maximum of one chapter/article from your contribution to an edited book or collection (e.g. Oxford Handbooks),
- a maximum of one chapter/article of your contribution to an online only, or digital original publication, or
- three figures/illustrations/tables of your own original work

OUP is pleased to grant this permission for the following uses:

- posting on the your own personal website or in an institutional or subject based repository after a **12 month** period for **Science and Medical** titles and a **24 month** period for **Academic, Trade and Reference** titles;
- inclusion in scholarly, not-for-profit derivative reuses, (these can include the extension of your contribution to a book-length work, or inclusion in an edited collection of your own work, or any work of which you are an author or editor);
- reproduction within coursepacks or e-coursepacks for your own teaching purposes, (with the proviso that the coursepacks are not sold for more than the cost of reproduction);
- inclusion within your thesis or dissertation.

Permission for these reuses is granted on the following conditions:

- that the material you wish to reuse is your own work and has already been published by OUP;
- that the intended reuse is for scholarly purposes, for publication by a not-for-profit publisher;
- that full acknowledgement is made of the original publication stating the specific material reused [pages, figure numbers, etc.], [Title] by/edited by [Author/editor], [year of publication], reproduced by permission of Oxford University Press [link to OUP catalogue if available, or OUP website];
- In the case of joint-authored works, it is the responsibility of the authors to obtain permission from co-authors for the work to be reuse/republished.
- that reuse on personal websites and institutional or subject based repositories includes a link to the work as published in an OUP online product (e.g. Oxford Scholarship Online), and/or or to the OUP online catalogue entry; and that the material is not distributed under any kind of Open Access style licences (e.g. Creative Commons) which may affect the Licence between yourself and OUP.

This policy does not cover my intended reuse

If this policy does not cover your intended reuse, either because your material is not published by the subject groups listed above, or falls outside the specific parameters set out here, this does not automatically mean that you will be unable to obtain permission. For all uses not described here, permission may be sought by contacting your Commissioning/Acquiring Editor or by filling in a Permissions Request Form.

We will aim to process your request within 7-10 working days.

FAQ for authors:

Why do I need permission to reuse my own writing?

Our publishing agreement with you enables OUP to make many investments in your work, including editorial review, copyediting, typesetting, design, printing, coding for electronic publication, marketing, distribution, and securing copyright against piracy and plagiarism. Reuse permission protects these investments.

Because I am using less than 10% of my chapter or book, I do not need formal written permission. How should I word the credit?

We ask that you include this wording: "This material was originally published in [Title] by / edited by [Author / Editor], and has been reproduced by permission of Oxford University Press [link to book within an OUP online product and/or http://global.oup.com/academic]. For permission to reuse this material, please visit http://global.oup.com/academic/rights."

I am planning to use a portion of my OUP publication in my thesis or dissertation. Will I be given permission to do so?

Yes. We would appreciate you letting your OUP editor know.

I am planning to use a portion of my OUP publication in a future book. Will I be given permission to do so?

Generally speaking, yes, permission will be granted without charge. We ask that you request formal permission here.

I retained the copyright to my work when I negotiated my contract with OUP. Do I still need to request permission to reuse my content outside of the conditions set forth above?

Your contract grants OUP the exclusive rights to publish your work. This is independent of who holds copyright and so permission to reuse material may be required regardless of whether you retained copyright.

May I have a .pdf of my book or my chapter?

As a means of protecting against piracy, it is not OUP's policy to send out .pdfs of books or chapters except in extraordinary circumstances.

Share:

Permission 3:

MENU

- Guidelines for Permission Request
- ASCE Terms and Conditions for Permissions Requests
- Request Permission Online (Rightslink)
- STM Permission Guidelines
- Reuse Author's Own Material
- Open Access Options and Rights

REUSE AUTHOR'S OWN MATERIAL

As the original author of an ASCE journal article or proceedings paper, you are permitted to reuse your own content for another ASCE or non-ASCE publication.

The following restrictions apply:

- Permission is denied if you request to republish an entire article in an ASCE or a non-ASCE publication.
- Permission is denied if the requested content constitutes more than 25% of your work in a new publication.
- **Internet posting of the *published version* of your article is strictly prohibited.**
- If the request is for an online coursepack, the site must be password-protected.
- If you wish to photocopy your content, the total number of copies cannot exceed 100. If you need more than 100 copies, please contact ASCE Permissions directly.

If the content has been prepared by an employee within the scope of employment, the employer shall enjoy the same rights as the authors.

If the content was prepared under a U.S. government contract, the federal government shall have the rights under the copyright law to the extent required by the contract.

POSTING YOUR ARTICLE OR PAPER ONLINE

Published Article
Authors may post a PDF of the ASCE-published version of their work on their employers' *Intranet* with password protection.

Draft Manuscript
Authors may post the final draft of their work on open, unrestricted Internet sites or deposit it in an institutional repository when the draft contains a link to the bibliographic record of the published version in the ASCE Library or Civil Engineering Database. "Final draft" means the version submitted to ASCE after peer review and prior to copyediting or other ASCE production activities; it does not include the copyedited version, the page proof, or a PDF of the published version. Proceedings papers, with no final draft, may post the abstract.

When posting online, please add the statement: "This material may be downloaded for personal use only. Any other use requires prior permission of the American Society of Civil Engineers. This material may be found at [URL/link of abstract in the ASCE Library or Civil Engineering Database]."

American Society of Civil Engineers

1801 Alexander Bell Drive
Reston, VA 20191-4400
703-295-6300 | 800-548-2723

ASCE LIBRARY

ASCE

SERVICES

Permission 4:

From: Laura van Kal [mailto:lkl@eage.org]
Sent: Wednesday, 7 February 2018 7:02 PM
To: Junxin Guo <junxin.guo@postgrad.curtin.edu.au>
Subject: RE: Copyright permission to reproduce the work in a Ph. D. thesis

Dear Junxin Guo,

Permission to copy and republish the materials is hereby granted, provided that full acknowledgement of the source and copyright is mentioned in the thesis.

Kind regards,

Laura van Kal

Publications Coordinator

European Association of Geoscientists & Engineers (EAGE)

PO Box 59

3990 DB Houten

The Netherlands

Tel: +31 889955055

Fax: +31 30 6343524

Email: lkl@eage.org

From: Junxin Guo [mailto:junxin.guo@postgrad.curtin.edu.au]
Sent: woensdag 7 februari 2018 5:02
To: Laura van Kal <lkl@eage.org>
Subject: Copyright permission to reproduce the work in a Ph. D. thesis

Dear publisher,

My name is Junxin Guo, a Ph. D. student in Curtin University (Australia). Currently, I am writing my doctoral thesis entitled 'Seismic dispersion, attenuation, and frequency-dependent anisotropy of fractured reservoirs'). In this thesis, I would like to reproduce my work (Figures/caption and text)

which has been published in EAGE annual conference and in the journal *Geophysical Prospecting* as follows:

1. Extended abstract

Guo, J., J. G. Rubino, B. Gurevich, S. Glubokovskikh, A. V. Dyskin, and E. Pasternak, 2016, Effects of fracture intersections on seismic dispersion- Theoretical predictions versus numerical simulations: 78th EAGE Conference and Exhibition.

2. Journal paper

Guo, J., J. G. Rubino, S. Glubokovskikh, and B. Gurevich, 2017, Effects of fracture intersections on seismic dispersion: theoretical predictions versus numerical simulations: Geophysical Prospecting, 65, no.5, 1264-1276.

The above materials will be integrated into part of a thesis chapter and hence the format will be different from that of EAGE but follow that of my thesis. Once completed, the thesis will be made available in a hard-copy form in the Curtin library and in a digital form via the Australian Digital Thesis Program. The material will be provided strictly for educational purposes and on a non-commercial basis. Further information on the ADT program can be found at http://adt.caul.edu.au.

I would be most grateful for your consent to the copying and republishing of the material as proposed. Full acknowledgement of the ownership of the copyright and the source of the material will be provided in the thesis. I would be willing to use a specific form of acknowledgement that you may require and to communicate any conditions related to the use of this material.

If you are not the copyright owner of the referred material, I would be grateful for any information you can provide as to who is likely to hold the copyright. I look forward to hearing from you and thank you in advance for your consideration of my request.

Best regards,

Junxin Guo
Ph. D. student | Department of Exploration Geophysics

Curtin University
Mobile | +61 451 620 826

Email | junxin.guo@postgrad.curtin.edu.au

Web | www.curtin.edu.au

CRICOS Provider Code 00301J

Permission 5:

From: Claire.Gibson@csiro.au [mailto:Claire.Gibson@csiro.au]
Sent: Wednesday, 7 March 2018 7:15 AM
To: Junxin Guo <junxin.guo@postgrad.curtin.edu.au>
Subject: RE: Copyright permission to incorporate my ASEG abstract into my Ph. D. thesis

Dear Junxin,

Thank you for your email.

As specified in your Licence to Publish, you retain the right to use your work for further research; and; use the illustrations (line art, photographs, figures, plates) and research data in your own future work.

Kind regards

Claire

Claire Gibson

Rights and Special Sales

CSIRO PUBLISHING

T +61 3 9545 2444
E claire.gibson@csiro.au

From: Junxin Guo [mailto:junxin.guo@postgrad.curtin.edu.au]
Sent: Tuesday, 6 March 2018 11:02 PM
To: PUBLISHING - General Info <info@publish.csiro.au>
Subject: Copyright permission to incorporate my ASEG abstract into my Ph. D. thesis

Dear publisher,

My name is Junxin Guo, a Ph. D. student in Curtin University (Australia). Currently, I am writing my doctoral thesis entitled 'Seismic dispersion, attenuation, and frequency-dependent anisotropy of fractured reservoirs'). I would like to incorporate my ASEG extended abstract into the thesis (the

format will be different from that of ASEG but follow that of my thesis). The details of this abstract are as follows:

Guo, J., S. Glubokovskikh, B. Gurevich, and J. G. Rubino, 2018, Seismic Signatures of Fractured Reservoirs: Theory Versus Numerical Simulations,

https://doi.org/10.1071/ASEG2018abP070

Once completed, the thesis will be made available in a hard-copy form in the Curtin library and in a digital form via the Australian Digital Thesis Program. The material will be provided strictly for educational purposes and on a non-commercial basis. Further information on the ADT program can be found at http://adt.caul.edu.au.

I would be most grateful for your consent to the copying and republishing of the material as proposed. Full acknowledgement of the ownership of the copyright and the source of the material will be provided in the thesis. I would be willing to use a specific form of acknowledgement that you may require and to communicate any conditions related to the use of this material.

If you are not the copyright owner of the referred material, I would be grateful for any information you can provide as to who is likely to hold the copyright. I look forward to hearing from you and thank you in advance for your consideration of my request.

Best regards,

Junxin Guo
Ph. D. student | Department of Exploration Geophysics

Curtin University
Mobile | +61 451 620 826

Email | junxin.guo@postgrad.curtin.edu.au
Web | www.curtin.edu.au

References

Achenbach, J. D., 1973, Wave propagation in elastic solids: Elsevier Science Publishers B.V.

Alasbali, A., R. Pevzner, K. Tertyshnikov, A. Bóna, and B. Gurevich, 2016, Estimation of seismic attenuation and prediction of VTI anisotropy parameters from VSP and log data: a case study from the Middle East: Arabian Journal of Geosciences, **9**, no. 7, 485.

Barbosa, N. D., J. G. Rubino, E. Caspari, J. Guo, B. Gurevich, and K. Holliger, 2017, Hybrid modelling of 3D fractured media based on 2D numerical simulations: aligned fractures case: International Exposition and 87th Annual Meeting, SEG, Extended Abstracts, 4200-4204.

Basir, H. M., A. Javaherian, and M. T. Yaraki, 2013, Multi-attribute an-tracking and neural network for fault detection: a case study of an Iranian oilfield: Journal of Geophysics and Engineering, **10**, 015009.

Basquet, R., L. Rennan, J. Ringen, and O. P. Wennberg, 2008, Fluid flow simulations on core samples containing natural fractures and stylolites: 70st Conference and Exhibition, EAGE, Extended Abstracts, E007.

Bath, M., 1974, Spectral analysis in Geophysics: Elsevier Scientific Publishing Company.

Berryman, J. G., 1985, Scattering by a spherical inhomogeneity in a fluid – saturated porous medium: Journal of Mathematical Physics, **26**, 1408 – 1419.

Biot, M. A., 1941, General theory of three-dimensional consolidation: Journal of Applied Physics, **12**, 155–164.

Biot, M. A., 1956a, Theory of propagation of elastic waves in a Fluid-saturated porous solid. I. Low-frequency range: The Journal of the Acoustical Society of America, **28**, no. 2, 168 – 178.

Biot, M. A., 1956b, Theory of propagation of elastic waves in a Fluid-saturated porous solid. I. Higher frequency range: The Journal of the Acoustical Society of America, **28**, no. 2, 179 - 191.

Biot, M. A., D. G. Willis, 1957, The elastic coefficients of the theory of consolidation: Journal of Applied Mechanics, **24**, 594 – 601.

Biot, M. A., 1962, Mechanics of deformation and acoustic propagation in porous media: Journal of Applied Physics, **33**, 1482 – 1498.

Brajanovski, M., B. Gurevich, and M. Schoenberg, 2005, A model for P-wave attenuation and dispersion in a porous medium permeated by aligned fractures: Geophysical Journal International, **163**, 372-384.

Brajanovski, M., T. M. Müller, and B. Gurevich, 2006, Characteristic frequencies of seismic attenuation due to wave-induced fluid flow in fractured porous media: Geophysical Journal International, **166**, 574-578.

Burns, D. R., M. E.Willis, M. N. Toksöz, and L. Vetri, 2007, Fracture properties from seismic scattering: The Leading Edge, **26**, 1186-1196.

Bush, I., 2010, An integrated approach to fracture characterisation: Oil Review Middle East, **2**, 88 – 91.

Caleap, M., C. Aristégui, and Y. C. Angel, 2009, Effect of crack opening and orientation on dispersion and attenuation of antiplane coherent wave, **177**, 1151-1165.

Carcione, J. M., B. Gurevich, J. E. Santos, and S. Picotti, 2013, Angular and frequency-dependent wave velocity and attenuation in fractured porous media: Pure and Applied Geophysics, **170**, 1673–1683.

Cardona, R., 2002, Two theories for fluid substitution in porous rocks with aligned cracks: 72nd Annual International Meeting, SEG, Expanded Abstracts, 173-176.

Caspari, E., M. Milani, J. G. Rubino, T. M. Müller, B. Quintal, and K. Holliger, 2016, Numerical upscaling of frequency-dependent P- and S- wave moduli in fractured porous media: Geophysical Prospecting, **64**, 1166 – 1179.

Caspari, E., M. Novikov, V. Lisitsa, N. D. Barbosa, B. Quintal, J. G. Rubino, and K. Holliger, 2017, Attenuation mechanisms in fractured fluid-saturated porous rocks: a numerical modelling study: Geophysical Prospecting, submitted.

Chapman, M., 2003, Frequency dependent anisotropy due to mesoscale fractures in the presence of equant porosity: Geophysical Prospecting, **51**, 369-379.

Chapman, M., 2009, Modelling the effect of multiple sets of mesoscale fractures in porous rock on frequency-dependent anisotropy: Geophysics, **74**, no. 6, D97-D103.

Chapman, M., E. Liu, and X.-Y. Li, 2006, The influence of fluid-sensitive dispersion and attenuation on AVO analysis: Geophysical Journal International, **167**, 89-105.

Chapman, M., S. V. Zatsepin, and S. Crampin, 2002, Derivation of a microstructural poroelastic model: Geophysical Journal International, **151**, 427-451.

Che, X., W. Qiao, P. Liu, X. Ju, and J. Lu, 2015, Identification of fractures in carbonates using sonic imaging logs: Example from the central of East European plain: The Journal of the Acoustic Society of America, **137**, 2403.

Clark, R., P. Benson, A. Carter, and C. Guerrero Moreno, 2009, Anisotropic P-wave attenuation measured from a multi-azimuth surface seismic reflection survey: Geophysical Prospecting, **57**, 835–845.

Collet, O., B. Gurevich, M. Madadi, and M. Pervukhina, 2014, Modeling elastic anisotropy resulting from the application of triaxial stress: Geophysics, **79**, no. 5, C135-C145.

Deresiewicz, H., and R. Skalak, 1963, On uniqueness in dynamic poroelasticity: Bulletin of the Seismological Society of America, **53**, 783–788.

Dutta, N. C., and H. Odé, 1979, Attenuation and dispersion of compressional waves in fluid-filled porous rocks with partial gas saturation (White model)-Part I: Biot theory: Geophysics, **44**, 1777-1788.

Endres, A. L., and R. J. Knight, 1997, Incorporating pore geometry and fluid pressure communication into modelling the elastic behaviour of porous rocks: Geophysics, **62**, no. 1, 106-117.

Eriksson, A. S., A. Bostrom, and S. K. Datta, 1995, Ultrasonic wave propagation through a cracked solid: Wave Motion, **22**, 297-310.

Eshelby, 1957, The determination of the elastic field of an ellipsoidal inclusion, and related problems: Proceedings of the Royal Society A: Mathematical, Physical and Engineering Sciences, **241**, no. 1226, 376-396.

Far, M. E., L. Thomsen, and C. M. Sayers, 2013, Seismic characterization of reservoirs with asymmetric fractures: Geophysics, **78**, no.2, N1-N10.

Foldy, L. L., 1945, The multiple scattering of waves I. General theory of isotropic scattering by randomly distributed scatterers: Physical Review, **67**, no. 3 and 4, 107-119.

Gao, D., 2013, Integrating 3D seismic curvature and curvature gradient attributes for fracture characterization: Methodologies and interpretational implications: Geophysics, **78**, no.2, O21-O31.

Galvin, R. J., and B. Gurevich, 2006, Interaction of an elastic wave with a circular crack in a fluid-saturated porous medium: Applied Physics Letter, **88**, 061918.

Galvin, R. J., and B. Gurevich, 2007, Scattering of a longitudinal wave by a circular crack in a fluid-saturated porous medium: International Journal of Solids and Structures, **44**, 7389-7398.

Galvin, R. J., and B. Gurevich, 2009, Effective properties of a poroelastic medium containing a distribution of aligned cracks: Journal of Geophysical Research: Solid Earth, **114**, B07305.

Galvin, R. J., and B. Gurevich, 2015, Frequency-dependent anisotropy of porous rocks with aligned fractures: Geophysical Prospecting, **63**, 141-150.

Ganley, D. C., and E. R. Kanasewich, 1980, Measurement of absorption and dispersion from check shot surveys: Journal of Geophysical Research, **85**, 5219-5226.

Gassmann, F., 1951a, Über die Elastizität poröser Medien: Vier. der Natur. Gesellschaft Zürich, **96**, 1–23.

Gassmann, F., 1951b, Elastic waves through a packing of spheres: Geophysics, **16**, no. 4, 673-685.

Glubokovskikh, S., B. Gurevich, M. Lebedev, V. Mikhaltsevitch, and S. Tan, 2016, Effect of asperities on stress dependency of elastic properties of cracked rocks: International Journal of Engineering Science, **98**, 116-125.

Glubokovskikh, S., B. Gurevich, and N. Saxena, 2016, A dual ‐ porosity scheme for fluid/solid substitution: Geophysical Prospecting, **64**, 1112-1121.

Grechka, V., and M. Kachanov, 2006, Effective elasticity of rocks with closely spaced and intersecting cracks: Geophysics, **71**, D85-D91.

Guéguen, Y., and J. Sarout, 2009, Crack-induced anisotropy in crustal rocks: Predicted dry and fluid-saturated Thomsen's parameters: Physics of the Earth and Planetary Interiors, **172**, 116-124.

Guo, J., S. Glubokovskikh, B. Gurevich, and J. G. Rubino, 2018a, Seismic Signatures of fractured reservoirs: Theory versus numerical simulations: Extended Abstract, ASEG, https://doi.org/10.1071 /ASEG2018abP070.

Guo, J., J. G. Rubino, N. D. Barbosa, S. Glubokovskikh, and B. Gurevich, 2018b, Seismic dispersion and attenuation in saturated porous rocks with aligned fractures of finite thickness: theory and numerical simulations – Part 1: P-wave perpendicular to the fracture plane: Geophysics, **83**, no. 1, WA49-WA62.

Guo, J., J. G. Rubino, N. D. Barbosa, S. Glubokovskikh, and B. Gurevich, 2018c, Seismic dispersion and attenuation in saturated porous rocks with aligned fractures of finite thickness: theory and numerical simulations – Part 2: Frequency-dependent anisotropy: Geophysics, **83**, no. 1, WA63-WA71.

Guo, J., J. G. Rubino, S. Glubokovskikh, and B. Gurevich, 2017a, Effects of fracture intersections on seismic dispersion: theoretical predictions versus numerical simulations: Geophysical Prospecting, **65**, no.5, 1264-1276.

Guo, J., J. G. Rubino, S. Glubokovskikh, and B. Gurevich, 2017b, Effects of fractures and background porosity on seismic dispersion and attenuation: theory versus numerical simulations: 4th International Workshop on Rock Physics.

Guo, J., J. G. Rubino, B. Gurevich, and S. Glubokovskikh, 2017c, Effects of finite fracture thickness on seismic dispersion and attenuation in saturated rocks with aligned penny-shaped cracks: theory versus numerical simulation: 6th Biot Conference on Poromechanics.

Guo, J., J. G. Rubino, S. Glubokovskikh, and B. Gurevich, 2018d, Dynamic seismic signatures of saturated porous rocks containing two orthogonal sets of fractures: Theory versus numerical simulations: Geophysical Journal International, **213**, 1244-1262.

Guo, J., J. G. Rubino, B. Gurevich, and S. Glubokovskikh, 2016a, Fluid flow effects on Seismic Properties of Fractured medium: Theoretical / Numerical modelling: SEG-AGU Workshop: Upper Crust Physics of Rocks.

Guo, J., J. G. Rubino, B. Gurevich, S. Glubokovskikh, A. V. Dyskin, and E. Pasternak, 2016b, Effects of fracture intersections on seismic dispersion- Theoretical predictions versus numerical simulations: 78th EAGE Conference and Exhibition.

Guo, J., D. Shuai, J. Wei, P. Ding, and B. Gurevich, 2018e, P-wave dispersion and attenuation due to scattering by aligned fluid saturated fractures with finite thickness: Theory and experiment: submitted to Geophysical Journal International.

Gurevich, B., 2003, Elastic properties of saturated porous rocks with aligned fractures: Journal of Applied Geophysics, **54**, 203-218.

Gurevich, B., M. Brajanovski, R. J. Galvin, T. M. Müller, and J. Toms-Stewart, 2009, P-wave dispersion and attenuation in fractured and porous reservoirs - poroelasticity approach: Geophysical Prospecting, **57**, 225-237.

Gurevich, B., and S. L. Lopatnikov, 1995, Velocity and attenuation of elastic waves in finely layered porous rocks: Geophysical Journal International, **121**, 933-947.

Gurevich, B., and R. Pevzner, 2015, How frequency dependency of Q affects spectral ratio estimates: Geophysics, **80**, no. 2, A39-A44.

Gurevich, B., and M. Schoenberg, 1999, Interface conditions for Biot's equations of poroelasticity: Journal of the Acoustic Society of America, **105**, 2585-2589.

Gurevich, B., V. B. Zyrianov, and S. L. Lopatnikov, 1997, Seismic attenuation in finely layered porous rocks: Effects of fluid flow and scattering, Geophysics, **62**, no.1, 319-324.

Hudson, J. A., 1981, Wave speeds and attenuation of elastic waves in material containing cracks: Geophysical Journal of the Royal Astronomical Society, **64**, 133-150.

Hudson, J. A., E. Liu, and S. Crampin, 1996, The mechanical properties of materials with interconnected cracks and pores: Geophysical Journal International, **124**, 105-112.

Ishimaru, A., 1978, Wave propagation and scattering in random media: Academic Press.

Jakobsen, M., 2004, The interacting inclusion model of wave-induced fluid flow: Geophysical Journal International, **158**, 1168-1176.

Jakobsen, M., and J. A. Hudson, 2003, Visco-elastic waves in rock-like composites: Studia Geophysica et Geodaetica, **47**, no.4, 793-826.

Jakobsen, M., T. A. Johansen, and C. McCann, 2003, The acoustic signature of fluid flow in complex porous media: Journal of Applied Geophysics, **54**, 219-246.

James, S. R., H. A. Knox, L. Preston, J. M. Knox, M. C. Grubelich, D. K. King, J. B. Ajo-Franklin, T. C. Johnson, and J. P. Morris, 2017, Fracture detection and imaging through relative seismic velocity changes using distributed acoustic sensing and ambient seismic noise: The Leading Edge, **36**, no. 12, 1009 – 1017.

Johnson, D. L., J. Koplik, R. Dashen, 1987, Theory of dynamic permeability and tortuosity in fluid-saturated porous media: Journal of Fluid Mechanics, **176**, 379 – 402.

Johnson, D. L., 2001, Theory of frequency dependent acoustics of patchy-saturated porous media: The Journal of the Acoustic Society of America, **110**, 682-694.

Kachanov, M., 1980, Continuum model of medium with cracks: Journal of the Engineering Mechanics Division, **106**, 1039 – 1051.

Kachanov, M., 1992, Effective elastic properties of cracked solids: critical review of some basic concepts: Applied Mechanics Reviews, **45**, no. 8, 304 – 335.

Kachanov, M., and I. Sevostianov, 2005, On quantitative characterization of microstructures and effective properties: International Journal of Solids and Structures, **42**, 309-336.

Kanasewich, E. R., and S. Phadke, 1988, Imaging discontinuities on seismic sections: Geophysics, **53**, 334 – 345.

Kawahara, J., 1992, Scattering of P, SV waves by random distributions of aligned open cracks: Journal of Physics of the Earth, **40**, 517-524.

Kawahara, J., T. Yamashita, 1992, Scattering of elastic waves by a fracture zone containing randomly distributed cracks: Pure and Applied Geophysics, **139**, 121-144.

Keller, J. B., 1964, Stochastic equations and wave propagation in random media: Proceedings of Symposia in Applied Mathematics, **16**, 145-170.

Keogh, P. S., 1986, High-frequency scattering of a normally incident plane compressional wave by a penny-shaped crack: The Quarterly Journal of Mechanics & Applied Mathematics, **39**, no.4, 535-566.

Kikuchi, M., 1981, Dispersion and attenuation of elastic waves due to multiple scattering from inclusions: Physics of the Earth and Planetary Interiors, **25**, 159-162.

Kong, L., B. Gurevich, Y. Zhang, and Y. Wang, 2017, Effect of fracture fill on frequency dependent anisotropy of fractured porous rocks: Geophysical Prospecting, **65**, no. 6, 1649-1661.

Krenk, S., and H. Schmidt, 1982, Elastic wave scattering by a circular crack: Philosophical Transactions of the Royal Society of London. Series A, Mathematical and Physical Sciences, **308**, 167-198.

Krzikalla, F., and T. Müller, 2011, Anisotropic p-sv-wave dispersion and attenuation due to inter-layer flow in thinly layered porous rocks: Geophysics, **76**, no. 3, WA135-WA145.

Kuster, G. T., and M. N. Toksöz, 1974, Velocity and attenuation of seismic waves in two-phase media: Part I. Theoretical formulations: Geophysics, **39**, 587 – 606.

Lacazette, A., J. Vermilye, S. Fereja, and C. Sicking, 2013, Ambient fracture imaging: A new passive seismic method: Unconventional Resources Technology Conference, URTeC 1582380.

Lambert, G., B. Gurevich, and M. Brajanovski, 2006, Attenuation and dispersion of P-waves in porous rocks with planar fractures: Comparison of theory and numerical simulations: Geophysics, **71**, no.3, N41-N45.

Landa, E., V. Shtivelman, and B. Gelchinsky, 1987, A method for detection of diffracted waves on common – offset sections: Geophysical Prospecting, **35**, 359 – 373.

Liu, E., M. Chapman, Z. Zhang, and J. H. Queen, 2006. Frequency-dependent anisotropy: Effects of multiple fracture sets on shear-wave polarizations: Wave Motion, **44**, 44-57.

Liu, E., and A. Martinez, 2012, Seismic fracture characterization: EAGE Publications bv, Houten, Netherlands.

Mal, A. K., 1970a, Interaction of elastic waves with a penny-shaped crack: International Journal of Engineering Science, **8**, 381-388.

Mal, A. K., 1970b, Interaction of elastic waves with a Griffith crack: International Journal of Engineering Science, **8**, 763-776.

Malin, P. E., J. A. Waller, R. D. Borcherdt, E. Cranswick, E. G. Jensen, and J. Van Schaack, 1988, Vertical seismic profiling of Oroville microearthquakes: Velocity spectra and particle motion as a function of depth: Bulletin of the Seismological Society of America, **78**, 401-420.

Mangriotis, M. D., J. W. Rector, E. F. Herkenhoff, and J. C. Neu, 2013, Scattering versus intrinsic attenuation in the vadose zone: A VSP experiment: Geophysics, **78**, no. 2, B49-B63.

Martin, P. A., 1981, Diffraction of elastic wave by a penny-shaped crack: Proceedings of the Royal Society A, **378**, 263-285.

Martin, P. A., F. J. Rizzo, 1989, On boundary integral equations for crack problems: Proceedings of the Royal Society A, **421**, 341-355.

Masson, Y. J., S. R. Pride, K. T. Nihei, 2006, Finite difference modelling of Biot's poroelastic equations at seismic frequencies: Journal of Geophysical Research: Solid Earth, **111**, B10.

Maultzsch, S., M. Chapman, E. Liu, and X.-Y. Li, 2003, Modelling frequency-dependent seismic anisotropy in fluid-saturated rock with aligned fractures: implication of fracture size estimation from anisotropic measurements: Geophysical Prospecting, **51**, 381-392.

Maultzsch, S., M. Chapman, E. Liu, and X.-Y. Li, 2007, Modelling and analysis of attenuation anisotropy in multi-azimuth VSP data from the Clair field: Geophysical Prospecting, **55**, 627-642.

Mavko, G., T. Mukerji, and J. Dvorkin, 2009, The Rock Physics Handbook: Cambridge University Press.

Milani, M., J. G. Rubino, T. M. Müller, B. Quintal, E. Caspari, and K. Holliger, 2016, Representative elementary volumes for evaluating effective seismic properties of heterogeneous poroelastic media: Geophysics, **81**, no.2, D169-D181.

Milton, G. W., 2002, The theory of composites: Cambridge University Press.

Müller, T. M., B. Gurevich, and M. Lebedev, 2010, Seismic wave attenuation and dispersion resulting from wave-induced flow in porous rocks — A review: Geophysics, 75, no.5, 75A147–75A164.

Müller, T. M., and E. Rothert, 2006, Seismic attenuation due to wave-induced flow: Why Q in random structures scales differently: Geophysical Research Letters, **33**, L16305.

Mura, T., 1987, Micromechanics of defects in solids: Martinus Nijhoff Publishers.

Murai, Y., 2007, Scattering attenuation, dispersion and reflection of SH waves in two-dimensional elastic media with densely distributed cracks: Geophysical Journal International, **168**, 211-223.

Murai, Y., J. Kawahara, and T. Yamashita, 1995, Multiple scattering of SH waves in 2-D elastic media with distributed cracks: Geophysical Journal International, **122**, 925-937.

Nakagawa, S., and M. A. Schoenberg, 2007, Poroelastic modelling of seismic boundary conditions across a fracture: The Journal of the Acoustical Society of America, **122**, 831- 847.

Narr, W., D. S. Schechter, and L. B. Thompson, 2006, Naturally fractured reservoir characterization: Society of Petroleum Engineers.

Nelson R. A., 2001, Geologic analysis of naturally fractured reservoirs: Gulf Professional Publishing.

Nishizawa, O., 1982, Seismic velocity in a medium containing oriented cracks – transversely isotropic case: Journal of the Physics of the Earth, **30**, 331-347.

Norris, A. N., 1985, A differential scheme for the effective moduli of composites: Mechanics of Materials, **4**, 1-16.

Norris, A. N., 1993, Low-frequency dispersion and attenuation in partially saturated rocks: The Journal of the Acoustical Society of America, **94**, 359-370.

Nye, J. F., 1985, Physical properties of crystals: Their representation by tensors and matrices: Oxford University Press.

O'Connell, R. J., and B. Budiansky, 1977, Viscoelastic properties of fluid-saturated cracked solids: Journal of Geophysical Research, **82**, no. 36, 5719-5735.

Peacock, S., C. McCann, J. Sothcott, and T. Astin, 1994, Experimental measurements of seismic attenuation in microfractured sedimentary rock: Geophysics, **59**, 1342-1351.

Plona, T. J., 1980, Observation of a second bulk compressional wave in a porous medium at ultrasonic frequencies: Applied Physics Letter, **36**, 259 – 261.

Pride, S. R., and J. G. Berryman, 2003, Linear dynamics of double-porosity and dual-permeability materials. II Fluid transport equations, Physical Review E, **68**, 036604.

Protasov, M. I., G. V. Reshetova, and V. A. Tcheverda, 2016, Fracture detection by Gaussian beam imaging of seismic data and image spectrum analysis: Geophysical Prospecting, **64**, 68-82.

Questiaux, J-M., G. D. Couples, and N. Ruby, 2010, Fractured reservoirs with fracture corridors: Geophysical Prospecting, **58**, 279 – 295.

Rashid, F., P. W. J. Glover, P. Lorinczi, R. Collier, and J. Lawrence, 2015, Porosity and permeability of tight carbonate reservoir rocks in the north of Iraq: Journal of Petroleum Science and Engineering, **133**, 147-161.

Rosenbaum, J. H., 1974, Synthetic microseismograms: Logging in porous formations: Geophysics, **39**, 14–32.

Rubino, J. G., E. Caspari, M. Milani, T. M. Müller, and K. Holliger, 2015, Seismic anisotropy in fractured low-permeability formations: The effects of hydraulic connectivity: 85th SEG Annual International Meeting, Extended Abstract, 3219-3223.

Rubino, J. G., E. Caspari, T. M. Müller, and K. Holliger, 2017, Fracture connectivity can reduce the velocity anisotropy of seismic waves: Geophysical Journal International, **210**, 223-227.

Rubino, J. G., E. Caspari, T. M. Müller, M. Milani, N. D. Barbosa, and K. Holliger, 2016 , Numerical upscaling in 2D heterogeneous poroelastic rocks: Anisotropic attenuation and dispersion of seismic waves: Journal of Geophysical Research: Solid Earth, **121**, doi:10.1002/2016JB013165.

Rubino, J. G., L. Guarracino, T. M. Müller, and K. Holliger, 2013, Do seismic waves sense fracture connectivity?: Geophysical Research Letter, **40**, 692-696.

Rubino, J. G., T. M. Müller, L. Guarracino, M. Milani, and K. Holliger, 2014, Seismoacoustic signatures of fractures connectivity: Journal of Geophysical Research: Solid Earth, **119**, 2252-2271.

Rubino, J. G., C. L. Ravazzoli, and J. E. Santos, 2009, Equivalent viscoelastic solids for heterogeneous fluid-saturated porous rocks: Geophysics, **74**, no. 1, N1-N13.

Sabina, F. J., V. P. Smyshlyaev, and J. R. Willis, 1993, Self-consistent analysis of waves in a matrix-inclusion composite- I. Aligned spheroidal inclusions: Journal of the Mechanics and Physics of Solids, **41**, 1573-1588.

Sarout, J., 2009, Impact of pore space topology on permeability, cut-off frequencies and validity of wave propagation theories: Geophysical Journal International, **189**, 481-492.

Sassen, D. S., and M. E. Everett, 2009, 3D polarimetric GPR coherency attributes and full-waveform inversion of transmission data for characterizing fractured rock: Geophysics, **74**, no. 3, J23-J34.

Sato, H., M. C. Fehler, and T. Maeda, 2011, Seismic wave propagation and scattering in the heterogeneous earth: Second edition, Springer.

Sayers, C. M., and M. Kachanov, 1995, Microcrack-induced elastic wave anisotropy of brittle rocks: Journal of Geophysical Research, **100**, 4149-4156.

Schoenberg, M., 1980, Elastic wave behavior across linear slip interfaces: Journal of the Acoustical Society of America, **68**, 1516 – 1521.

Schoenberg, M., and J. Douma, 1988, Elastic wave propagation in media with parallel fractures and aligned cracks: Geophysical Prospecting, **36**, 571-590.

Schoenberg, M., and C. M. Sayers, 1995, Seismic anisotropy of fractured rock: Geophysics, **60**, no.1, 204-211.

Sevostianov, I., and M. Kachanov, 1999, Compliance tensors of ellipsoidal inclusions: International Journal of Fractures, **96**, L3-L7.

Smyshlyaev, V. P., and J. R. Willis, 1993a, Self-consistent analysis of waves in a matrix-inclusion composite-II. Randomly oriented spheroidal inclusions: Journal of the Mechanics and Physics of Solids, **41**, 1589-1598.

Smyshlyaev, V. P., and J. R. Willis, 1993b, Self-consistent analysis of waves in a matrix-inclusion composite-III. A matrix containing cracks: Journal of the Mechanics and Physics of Solids, **41**, 1809-1824.

Suzuki, Y., J. Kawahara, T. Okamoto, and K. Miyashita, 2006, Simulations of SH wave scattering due to cracks by the 2-D finite difference method: Earth Planets Space, **58**, 555-567.

Suzuki, Y., T. Shiina, J. Kawahara, T. Okamoto, and K. Miyashita, 2013, Simulations of P-SV wave scattering due to cracks by the 2-D finite difference method: Earth Planets Space, **65**, 1425-1439.

Tang, X. M., M. N. Toksöz, and C. H. Cheng, 1990, Elastic wave radiation and diffraction of a piston source: Journal of the Acoustical Society of America, **87**, no. 5, 1894-1902.

Thomsen, L., 1986, Weak elastic anisotropy: Geophysics, **51**, 1954-1966.

Thomsen, L., 1995, Elastic anisotropy due to aligned cracks in porous rock: Geophysical Prospecting, **43**, 805-830.

Timoshenko, S. P., and J. N. Goodier, 1934, Theory of Elasticity: McGraw-Hill.

Tsingas, C., B. El. Marhfoul, A. Al-Dajani, 2010, Fracture detection by diffraction imaging: Extended abstract, EAGE annual conference.

Tsvankin, I., 1997, Anisotropic parameters and P-wave velocity for orthorhombic media: Geophysics, **62**, no.4, 1292-1309.

Vasconcelos, I., and E. Jenner, 2005, Estimation of azimuthally varying attenuation from wide-azimuth P-wave data: SEG Technical Program Expanded Abstracts, 123-126.

Vlastos, S., E. Liu, I. G. Main, and X.-Y. Li, 2003, Numerical simulation of wave propagation in media with discrete distributions of fractures: effects of fracture sizes and spatial distributions: Geophysical Journal International, **152**, 649-668.

Vlastos, S., E. Liu, I. G. Main, and C. Narteau, 2007, Numerical simulation of wave propagation in 2-D fractured media: scattering attenuation at different stages of the growth of a fracture population: Geophysical Journal International, **171**, 865-880.

Vlastos, S., E. Liu, I. G. Main, M. Schoenberg, C. Narteau, X.-Y. Li, and B. Maillot, 2006, Dual simulations of fluid flow and seismic wave propagation in a fractured network: effects of pore pressure on seismic signature: Geophysical Journal International, **166**, 825-838.

Wang, S., X-Y Li, Z. Qian, B Di, and J. Wei, 2007, Physical modelling studies of 3-D P-wave seismic for fracture detection: Geophysical Journal International, **168**, 745-756.

Wei, J., 2004, A physical model study of different crack densities: Journal of Geophysics and Engineering, **1**, 70-76.

Wei, J., B. Di, and P. Ding, 2013, Effect of crack aperture on P-wave velocity and dispersion: Applied Geophysics, **10**, no. 2, 125-133.

Wenzlau, F., and T. M. Müller, 2009, Finite-difference modelling of wave propagation and diffusion in poroelastic media, Geophysics, **74**, no. 4, T55-T66.

White, J. E., N. G. Mikhaylova, and F. M. Lyakhovitsky, 1975, Low-frequency seismic waves in fluid-saturated layered rocks: Izvestiya, Physics of the Solid Earth, 11, 654-659.

Willis, M. E., D. R. Burns, R. Rao, B. Minsley, M. N. Toksöz, and L. Vetri, 2006, Spatial orientation and distribution of reservoir fractures from scattered seismic energy, Geophysics, **71**, 43 – 51.

Witherspoon, P. A., J. S. Y. Wang, K. Iwai, and J. E. Gale, 1980, Validity of cubic law for fluid flow in a deformable rock fracture: Water resources research, **16**, 1016-1024.

Wu, R., and K. Aki, 1985, Scattering characteristics of elastic waves by an elastic heterogeneity: Geophysics, **50**, no.4, 582-595.

Yamashita, T., 1990, Attenuation and dispersion of SH waves due to scattering by randomly distributed cracks: Pure and Applied Geophysics, **132**, 545-568.

Yang, L., and J. A. Turner, 2005, Wave attenuations in solids with perfectly aligned cracks: Acoustic Research Letters Online, **6**, 99-105.

Zazoun, R. S., 2013, Fracture density estimation from core and conventional well logs data using artificial neural networks: The Cambro-Ordovician reservoir of Mesdar oil field, Algeria: Journal of African Earth Sciences, **83**, 55-73.

Zeeb, C., E. Gomez-Rivas, P. D. Bons, and P. Blum, 2013, Evaluation of sampling methods for fracture network characterization using outcrops, AAPG Bulletin, **97**, no.9, 1545-1566.

Zhang, C. H., and J. D. Achenbach, 1991, Effective wave velocity and attenuation in a material with distributed penny-shaped cracks: International Journal of Solids and Structures, **27**, 751-767.

Zhang, C. H., and D. Gross, 1993a, Wave attenuation and dispersion in randomly cracked solids – I. slit cracks: International Journal of Engineering Science, **31**, 841-858.

Zhang, C. H., and D. Gross, 1993b, Wave attenuation and dispersion in randomly cracked solids – II. penny-shaped cracks: International Journal of Engineering Science, **31**, 859-872.

Zhang, X., T. Li, Y. Shi, and Y. Zhao, 2015, The application of fracture interpretation technology based on ant tracking in Sudeerte Oilfield: Acta Geologica Sinica, **89**, 437-438.

List of Figures

List of Tables